Numerical modeling of turbulent convection in rough Rayleigh-Bénard cell

Mebarek Belkadi

Sorbonne Université

École Doctorale Sciences Mécaniques, Acoustique, Électronique & Robotique

Laboratoire d'Informatique pour la Mécanique
et les Sciences de l'Ingénieur (LIMSI UPR3251)

Numerical modeling of turbulent convection in rough Rayleigh-Bénard cell

Par Mebarek BELKADI

Thèse de doctorat de Mécanique des Fluides

Dirigée par Anne Sergent & Bérengère Podvin

Présentée et soutenue publiquement le 11 Juillet 2019

Devant un jury composé de :

Chillà Francesca	Professeure, ENS Lyon	Rapporteure
Davaille Anne	Directrice de Recherche CNRS, FAST	Examinatrice
Oualli Hamid	Professeur, EMP Alger	Membre invité
Podvin Bérengère	Chargée de Recherche, LIMSI	Co-Directrice de thèse
Rossi Maurice	Directeur de Recherche CNRS, Institut ∂'Alembert	Examinateur
Sergent Anne	Maître de conférences, LIMSI	Directrice de thèse
Vincent Stéphane	Professeur, Université Paris-Est Marne-la-Vallée	Rapporteur

Dedicated to my beloved parents,
Aicha *and* ***Tahar****,*
with love.

Acknowledgements

Foremost, I would like to express my sincere gratitude and thanks to my supervisors : Mrs Anne Sergent and Mrs Bérengère Podvin for the continuous support of my Ph.D study and research, for their patience, motivation, enthusiasm, and immense knowledge. Their guidance helped me in all the time of research and writing of this thesis.

My sincere thanks also goes to M. Yann Fraigneau for sharing his knowledge and experience with me, for his insightful comments and encouragement. Also I would like to thank M. Julien Salort and M. Ronald du Puits for their collaboration and fruitful help.

I thank all my colleagues from LIMSI : Antoine faugaret, Ismail Ben Hassan Saidi, Raphaël Zanella, Elie Saikali, Guy Yoslan Cornejo Maceda, Jiang Nan, Jianfei Song, Hugues Faller, Raksmy Nop, Ziad Youssef, for the stimulating discussions and for all the fun we have had in the last three years.

In addition, I would like to thank my brother and sisters : Amine, Sara, Nesrine and Hanane, you are always there for me. Finally, there are my friends, who were of great support in deliberating over our findings, as well as providing happy distraction.

Contents

Preamble

Turbulent convective flows are ubiquitous in geophysical and engineering topics. The Earth topography influences convective flows occurring in the oceans and in atmosphere. Rough surfaces are often used to promote turbulence and enhance convective heat transfer in multiple industrial applications (Ventola et al., 2014; Kaewchoothong et al., 2017). They are usually used to trigger thermal exchanges and their high efficiency has been proven for thermal systems such as heat exchangers or nuclear fuel rods (Tikadar et al., 2018). In the past years, the investigation of thermally driven turbulence has been the subject of intensive research (Niemela et al., 2000; Grossmann and Lohse, 2000, 2001; Ahlers et al., 2009; Chilla and Schumacher, 2012), in particular for Rayleigh Bénard convection, which is a relevant configuration to study turbulent thermal convection.

In this context, a series of studies has been conducted to study turbulent thermal convection over rough plates experimentally (Du and Tong, 1998, 2000), (Tisserand et al., 2011), (Xie and Xia, 2017) and numerically (Stringano et al., 2006), (Wagner and Shishkina, 2015), (Toppaladoddi et al., 2017; Zhu et al., 2017). Multiple behaviors have been identified within which the heat transfer is getting enhanced or even reduced. In particular, an intermediate regime has been observed for which significant change of the flow dynamics occuring near the rough walls results in intensive heat exchange (Shen et al., 1996; Liot et al., 2017). Various geometries such as cylindrical and box-shaped cells have been tested. Roughness can be introduced either on one plate (the bottom or top plates) leading an asymmetric cell (Salort et al., 2014) or on both sides, leading to a symmetric configuration in the case of Boussinesq approximation (Ciliberto and Laroche, 1999). The overwhelming majority of these studies considers an array of regular roughnesses, such as pyramids, squares, ratchetlike, grooves, waves, etc. Besides the shape of roughnesses, different sizes and geometrical arrangements of roughness can be examined (Xie and Xia, 2017; Zhu et al., 2019).

Even if the influence of roughness has been established, the physical mechanism that leads to the enhancement of the heat transfer is still not well understood. In experiments, in order to observe the heat transfer enhancement in the Ra number range reachable with water

as working fluid, the typical height H_p of roughness embedded in the Rayleigh Bénard cell is smaller than 1% of the cavity height H (Wei et al., 2014; Rusaouën et al., 2018). However, this ratio H_p/H is hardly tractable by simulations. For instance, due to resolution requirements, numerical studies are usually performed with macroscopic scale roughnesses (Shishkina and Wagner, 2011; Zhu et al., 2019) or are either two-dimensional or three-dimensional with a limited number of obstacles (Wagner and Shishkina, 2015).

The objective of this work is to investigate the fluid dynamics around roughness in turbulent thermal convection by carrying out three dimensional direct numerical simulations of an asymmetric Rayleigh-Bénard cell. It specifically aims to clarify the behaviors seen in different regimes of the heat transfer. Simulations are performed with an in-house, massively parallel code *SUNFLUIDH*, running on national high-performance computers. Massive resources are employed in order to provide an adequate spatial resolution and a sufficient long duration of simulation.

In this work, we establish our capability for reproducing numerically the different heat transfer regimes with 3D DNS using an array of 3D plots to model roughness. We show that DNS results compares well with experimental data with both global quantities such as the Nusselt number Nu and local measurements. We provide a detailed description of the complex interactions between the flow and rough surface, and in particular we determine the characteristics of each heat transfer regime.

The present manuscript is organized as follows : § I contains a general review about thermal turbulent convection over smooth and rough surfaces. § II provides a description about the DNS code features. § III describes the numerical modeling of thermal convection over the rough surface in RB cell. § IV details the effect of roughness on the regime of heat transfer, § V investigates the effects of roughness on the boundary layer structure. § VI presents a comparison with experimental study and § VII presents a discussion of roughness effects on coherent thermal plumes.

I – General Introduction

I.1 Natural convection

I.1.1 Physical phenomenon

Thermal convection arises widely in geophysical and astrophysical systems. In spite of its widespread occurrence, the flows are mostly turbulent and the motion of fluid is still difficult to be predicted. Besides that, convection phenomena are of a large scale such as in earth mantle, atmosphere and oceans or even in engineering systems of big sizes. A fluid being heated from below buoyant body forces that can produce vigorous turbulent motion. When buoyancy is the only source of motion, we commonly refer to the resulting flow as natural

convection. This thermal convection is actually the displacement of macroscopic volumes of the fluid (gas or fluid), resulting in a transfer of mass and heat. Owing to the presence of density gradients in the fluid, the potential gravitational energy transforms to energy motion under the action of buoyancy forces. Understanding the physics of thermal flow have been the subject of theories, laboratory experiments and numerical simulations.

I.1.2 Flow physics near boundaries

Viscosity effects are important near boundaries where velocity changes from zero at the wall to the free stream value away from the surface, this thin layer is known as the kinetic boundary layer (KBL). In thermal problems, we have a second layer near the top and the bottom walls where the gradient of temperature is concentrated, this layer is known as thermal boundary layer (TBL). The background region outside of boundary layers is often called the bulk. When convection takes place, it ensures a sufficient mixing of species so that the bulk region is relatively homogeneous in temperature. The thickness of the viscous and thermal BLs are denoted by δ_u and δ_θ resp. These thicknesses roughly depend on the fluid properties, mainly the Prandtl number (Pr) which is is the ratio of the viscous to the thermal diffusions rates expressed as the ratio of kinematic viscosity to the thermal diffusivity. A high viscosity leads to a thick viscous boundary layer (high Prandtl number $Pr >> 1$), and a high thermal diffusivity should give a thick thermal boundary layer (small Prandtl number $Pr << 1$). (see detailed investigations on Pr number in turbulent flow by Cebeci and Bradshaw (1984)).

I.2 Rayleigh Bénard convection

In practice, turbulent thermal convection is usually studied in a simplified model system. At the laboratory small scale, experiments are conducted and take some assumptions in consideration to simplify the problem. In this work, we are interested in studying the Rayleigh-Bénard model (RB) for multiple reasons : (i) it is a quite simple model but essentially successful to describe thermal convection for a wide range of physics problems involving heat transfer. (ii) It is mathematically well-posed problem with simple boundary conditions. (iii) It is a closed system, thus the heat transport properties could be related to the energy dissipation rates. It is accessible through theoretical, experimental and numerical simulations with basic geometries. It provides a rich and helpful discussion to our understanding.

I.2.1 From a model to a cavity

Early studies were mostly qualitative. Henri Bénard was the first to perform quantitative experiments about convection mode (Bénard, 1900a,b). In his work, he studied the stability of a thin fluid layer open to air and submitted to a vertical temperature gradient. He was interested by the self-organizing processes of hexagonal pattern (more details are provided

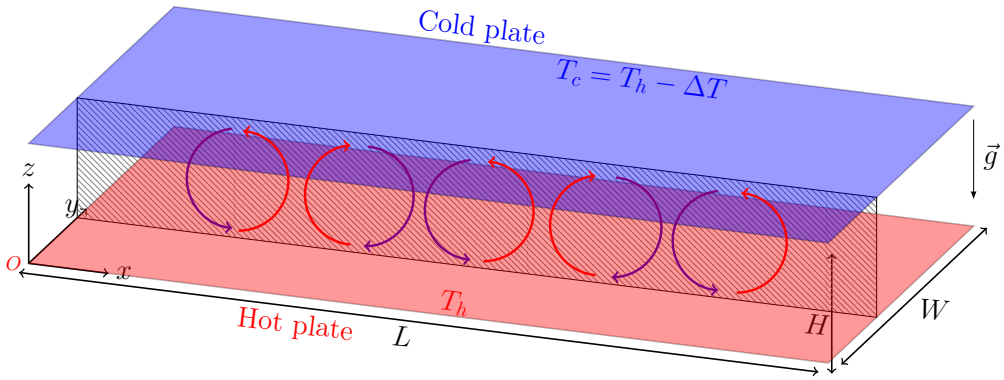

Fig. I.1 Ideal case of the Rayleigh-Bénard model, T_h and T_c are temperature of bottom and upper plates resp. The two plates are extended to infinity (L and W$\longrightarrow \infty$). convective rolls take place between two horizontal plates at different temperatures.

by Bergé and Dubois (1984); Daniels (1993); Getling (1998)) and the formation of those cells that take his name today. An interpretation was given by Rayleigh (1916) who showed that cells could appear even without imposing zero velocity on the walls. His theory of feedback coupling resting on buoyancy (further explanations are given e.g. by Mutabazi et al. (2006)).

This configuration is now referred to as Rayleigh Bénard model, as sketched in figure (I.1). Theoretically, it consists of two infinite horizontal flat plates distanced vertically. The bottom plate is maintained at a higher temperature than the top plate, thus generating a vertical temperature gradient that oppose the gravity force. In fact, most fluids become less dense as their temperature increases, the accumulation of hotter fluid below colder one generates an instability above a critical temperature difference when the buoyancy force overcomes the stabilizing effects of viscosity and heat diffusivity. The motionless state is then replaced by an array of convection cells. This ideal configuration can be approximated numerically by periodic boundaries or experimentally with large length size.

The configuration that we consider in the flowing work is a box shaped cell (figure I.2). Is has a height H, a depth D and a length L. The system is controlled via the Rayleigh and Prandtl numbers (Ra, Pr) and two aspect ratios $\Gamma_\mathrm{x} = L/H$ and $\Gamma_\mathrm{y} = D/H$. The temperatures of hot bottom and cold top plates are denoted resp. by T_h and T_c.

I.2.2 Equations of motion

The thermodynamic coupling is behind the motion of the fluid in the RBC, naturally because of buoyancy force which causes the fluid flow. The Navier-Stokes equations which describes the transport of mass, momentum and energy could be given in the differential formulation,

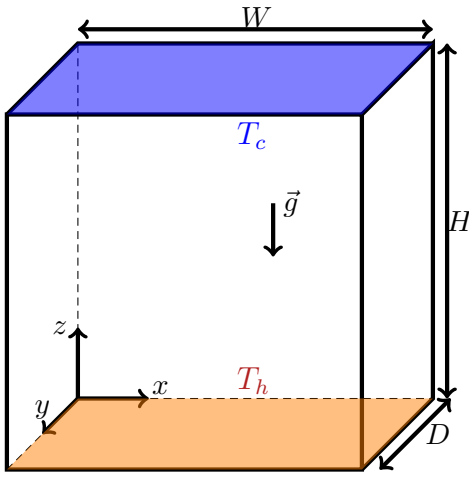

Fig. I.2 Sketch of Rayleigh Bénard cell (RBC) with nomenclature and coordinate system.

Continuity equation

$$\frac{\partial \rho}{\partial t} + \overrightarrow{\nabla} \cdot (\rho \boldsymbol{u}) = 0 \tag{I.1}$$

Momentum equation

$$\frac{\partial (\rho \boldsymbol{u})}{\partial t} + \overrightarrow{\nabla} \cdot (\rho \boldsymbol{u} \otimes \boldsymbol{u}) = -\overrightarrow{\nabla} p + \overrightarrow{\nabla} \cdot \overline{\overline{\tau}} + \rho \overrightarrow{f} \tag{I.2}$$

Energy equation

$$\rho C_p \frac{\partial T}{\partial t} + \boldsymbol{u} \cdot \overrightarrow{\nabla} T = \overrightarrow{\nabla} \cdot (k \overrightarrow{\nabla} T) + \alpha T \frac{Dp}{Dt} + \overrightarrow{\nabla} \boldsymbol{u} : \overline{\overline{\tau}} \tag{I.3}$$

In these equations :

$\boldsymbol{x} = (x, y, z)$ vector of positions $[m]$

$\boldsymbol{u} = (u, v, w)$ vector of Eulerian velocities $[m\ s^{-1}]$

ρ denotes the density of the fluid $[Kg\ m^{-3}]$

t represents the time $[s]$

p is the pressure $[Pa]$

$\overline{\overline{\tau}} = \tau_{ij} = \mu[\overrightarrow{\nabla} \boldsymbol{u} + (\overrightarrow{\nabla} \boldsymbol{u})^t - \frac{2}{3}(\overrightarrow{\nabla} \cdot \boldsymbol{u})\overline{\overline{I}}]$ is the tensor of viscous stresses $[Pa]$

$\overrightarrow{f}$ denotes the resultant of external forces exerted on the fluid per unit of mass $[m\ s^{-2}]$. In our problem, it refers to gravity acceleration $\overrightarrow{g}[m\ s^{-2}]$ ported by the vertical axis $\overrightarrow{e_z}$ and directed in the opposite direction ($\overrightarrow{g} = -g\overrightarrow{e_z}$).

T is the temperature $[K]$

$\alpha = -\frac{1}{\rho} \left.\frac{\partial \rho}{\partial T}\right|_P$ is the coefficient of expansion of the fluid at constant pressure.

k means thermal conductivity $[W\ m^{-1}\ K^{-1}]$

μ is the dynamic viscosity of the fluid, expressed in $[kg\ m^{-1}\ s^{-1}]$

$\overrightarrow{\nabla} \cdot$ is the divergence operator

$\frac{D}{Dt}$ indicates the material derivative

I.2.3 The Boussinesq approximation

Boussinesq (1903) formulated an hypothesis in which he consider all physical properties of the fluid independent of the temperature variations except for density. This latter dependency is only manifested in the buoyancy term insofar as it gives rise to gravitational force. Hence, the continuity equation (I.1) could be simplified to a constant density form,

$$\overrightarrow{\nabla}.\boldsymbol{u} = 0 \tag{I.4}$$

We introduce ρ_{ref} as the reference density evaluated at a reference state (T_{ref}, p_{ref}). In the following work, the reference temperature is taken as $T_{ref} = T_c$. The density variations could be written as

$$\rho = \rho_{ref} + \Delta\rho \tag{I.5}$$

If all acceleration involved in the flow are small compared with gravitational one, the variation of density in time and space in terms other than buoyancy will be negligible. Under this hypothesis, we could assume a linear dependence of the density on the temperature,

$$\Delta\rho = -\alpha\rho_{ref}\Delta T \tag{I.6}$$

With $\Delta T = T - T_{ref}$ is the imposed temperature difference.

If we introduce the driven pressure P^* defined as difference between thermodynamic and hydrostatic pressures,

$$\overrightarrow{\nabla} P^* = \overrightarrow{\nabla} p - g\rho_{ref} \tag{I.7}$$

The applicability of the Boussinesq approximation is based on the following criteria,

$$\alpha\Delta T \ll 1 \tag{I.8a}$$

(I.8b)

$$g\rho bL \ll 1 \tag{I.8c}$$

(I.8d)

$$g\alpha H/C_p \ll 1 \tag{I.8e}$$

Where b is the isothermal compressibility and C_p is the specific heat at constant pressure.

The condition (I.8a) requires that the imposed temperature differences should not produce excessive density variations. Conditions (I.8c) and (I.8e) require a negligible compressibility effects and a small system scale compared with scale heights over which various parameters change by a fraction of order unity. (more details are provided from Tritton (1977).p.180 and Getling (1998),p.10). In these circumstances, the Boussinesq momentum equation is reduced,

$$\frac{\partial \boldsymbol{u}}{\partial t} + \boldsymbol{u}.\overrightarrow{\nabla}\boldsymbol{u} = -\frac{\overrightarrow{\nabla} P^*}{\rho_{ref}} + \nu\overrightarrow{\nabla}^2\boldsymbol{u} - g\alpha(T - T_{ref}) \tag{I.9}$$

Where $\nu = \mu/\rho_{ref}$ is the kinematic viscosity of the fluid.

The energy equation (I.3) can also be simplified by neglecting the two source terms due to pressure gradients and viscous dissipation due to low fluid velocities,

$$\frac{\partial T}{\partial t} + \boldsymbol{u}.\overrightarrow{\nabla} T = \kappa\overrightarrow{\nabla}^2 T \tag{I.10}$$

Where $\kappa = \dfrac{k}{\rho_{ref} C_p}$ is the thermal diffusivity.

I.2.4 Dimensionless equations

The characteristic scales used for length $[L]$, mass $[M]$, temperature $[\Theta]$ and velocity $[U]$ are

$$[L] = H\ , \qquad [M] = \rho_{ref}[L]^3\ , \qquad [\Theta] = \Delta T = T_h - T_c\ , \qquad [U] = \frac{\kappa}{H}(\sqrt{Ra}) \tag{I.11}$$

We can define dimensionless temperature θ, ranging in [0-1],

$$\theta = \frac{(T - T_{ref})}{(T_h - T_c)} \tag{I.12}$$

The Boussinesq equations (I.4),(I.9) and (I.10) could be written in dimensionless form as

$$\overrightarrow{\nabla}.\boldsymbol{u} = 0 \tag{I.13}$$

$$\frac{\partial \boldsymbol{u}}{\partial t} + \boldsymbol{u}.\overrightarrow{\nabla}\boldsymbol{u} = -\overrightarrow{\nabla} P^* + \frac{Pr}{\sqrt{Ra}}\overrightarrow{\nabla^2}\boldsymbol{u} + Pr\theta e_z \tag{I.14}$$

$$\frac{\partial \theta}{\partial t} + \boldsymbol{u}.\overrightarrow{\nabla}\theta = \frac{1}{\sqrt{Ra}}\overrightarrow{\nabla}^2\theta \tag{I.15}$$

The equation (I.15) requires a boundary conditions for the temperature field. We impose the Dirichlet condition on temperature for top and bottom plates. The no slip condition is used for all boundaries. The sidewalls are adiabatic.

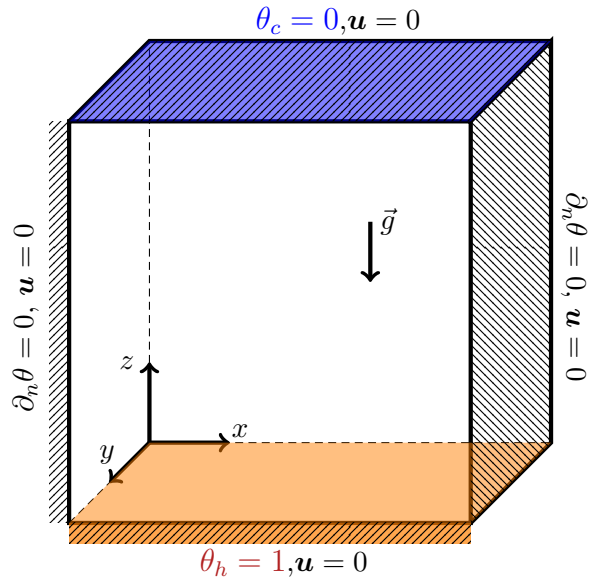

Fig. I.3 Boundary conditions of temperature and velocity fields.

I.2.5 Boundary layers and coherent structures

Inside the RB cavity, the thermal BLs are localized near the top and bottom surfaces. The region outside of thermal and viscous BLs is commonly referred to as the bulk as shown schematically in figure (I.4a). As the temperature difference $(\theta_h - \theta_c)$, imposed across the cell increases, coherent structures get detached from top and bottom plates. These small structures shown in figure (I.4b) are often called thermal plumes. They play a critical role in transporting energy (Zocchi et al., 1990). Xi et al. (2004) have shown that plumes are responsible for the onset of the large scale circulation in Rayleigh Bénard turbulent convection. According to numerical study of Shishkina and Wagner (2008), the local heat flux and the vertical vorticity component are found be the highest in the regions where plumes interact and merge with each other.

The studies of RBC include (i) the scalings of global heat transport Nu, (ii) the dynamics of kinetic and thermal boundary layers, and (iii) the interaction between the large scale circulation (LSC) and the small scale motions generated by thermal plumes (Ahlers et al., 2009). For this purpose, it is necessary to know about the system response regarding the input parameters of the configuration.

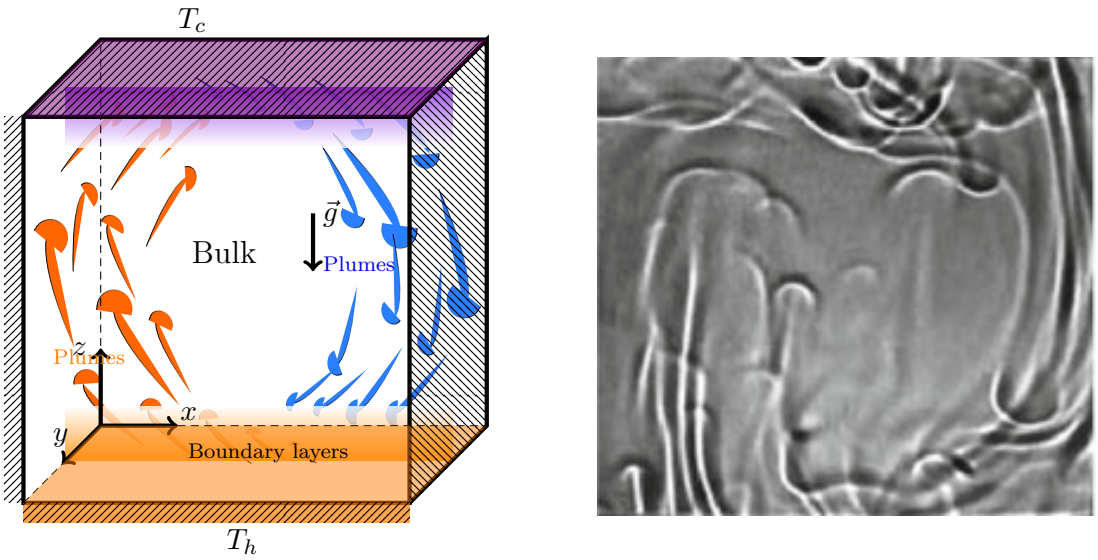

(a) (b)

Fig. I.4 (a) Sketch of boundary-bulk-plumes interaction in Rayleigh Bénard problem. Bursts of plumes from thin thermal boundary layers drive a large-scale flow. The behavior of the system is affected by the ability of the plates to produce plumes which affect the motion of the LSC. (b) Shadowgraph visualization of rising and falling plumes (Xi et al., 2004), the flow motion organize into a large scale circulation.

I.2.6 System parameters and responses

The dynamic behavior inside the RBC is determined by (i) its geometry, usually cylindrical or box-shaped, (ii) the physical properties of the fluid, and (iii) temperature differences between top and bottom plates. In the classical RBC with smooth boundaries, the problem is controlled by four dimensionless parameters : the Prandtl number Pr which describes the ratio between viscous and thermal diffusions, the Rayleigh number Ra which describe the ratio of inertial forces to viscous forces and eventually two aspect ratios (Γ_x, Γ_y) :

$$\begin{cases} Pr &= \dfrac{\nu}{\kappa} \\ Ra &= \dfrac{\alpha g \Delta T H^3}{\kappa \nu} \\ \Gamma_x &= L/H \\ \Gamma_y &= W/H \end{cases} \tag{I.16}$$

Where ν is the kinematic viscosity, κ is the thermal diffusivity, α is the thermal expansion coefficient, ΔT is an imposed temperature difference and (W, D, H) define the length, depth and height of the cavity.

In the following work, $\langle x \rangle_S$ and $\langle x \rangle_V$ denote respectively the space average of x, where S refers to the horizontal surface (plane (x, y)) and V denotes the total volume. The over line $\overline{x}$ denotes the time average of x.

The response of the RBC system is usually characterized by the dimensionless form of the heat flux is defined by the Nusselt number Nu. It expresses the ratio between total and purely conductive heat flux. We also define the Reynolds number based on the height H and a characteristic velocity U which express the ratio of inertial to viscous forces.

$$\begin{cases} Nu &= \dfrac{Q}{\kappa \Delta T/H} = \dfrac{\langle \overline{wT} \rangle_S - \kappa \dfrac{\partial \langle \overline{T} \rangle_S}{\partial z}}{\kappa \Delta T/H} \\ \\ Re &= \dfrac{HU}{\nu} \end{cases} \tag{I.17}$$

a) Other definitions for Nusselt number

The dimensionless form of the heat flux is defined as the Nusselt number Nu. It can be expressed in the dimensionless form as

$$Nu(z) = \sqrt{Ra} \langle \overline{w\theta} \rangle_S - \partial_z \langle \overline{\theta} \rangle_S (z) \tag{I.18}$$

1) Nusselt number for horizontal planes

Adiabatic sidewalls allow the total heat transport through the entire cavity. Thus, the time-space average of the Nusselt number is no longer dependent on the z component. We define the Nusselt number for the bottom surface at $z = 0$ denoted by Nu_{bot} and the Nusselt number for the top surface Nu_{top} at $z = 1$, directly given by the conductive heat flux $\langle \partial_z \theta \rangle_{S,t}$. We define also a mid-plane Nusselt number Nu_{mid} at $z = 0.5$,

$$\begin{cases} Nu_{bot} = \partial_z \langle \overline{\theta} \rangle_{S,z=0} \\ Nu_{top} = \partial_z \langle \overline{\theta} \rangle_{S,z=H} \\ Nu_{mid} = \sqrt{Ra} \langle \overline{w\theta} \rangle_{S,z=0.5} - \partial_z \langle \overline{\theta} \rangle_{S,z=0.5} \end{cases} \tag{I.19}$$

2) Bulk Nusselt number

As the sidewalls are adiabatic, the Nusselt number is statistically preserved through the vertical direction. Therefore, we to define a volumetric Nusselt which we called bulk Nusselt number Nu_{bulk}, the time-space average in the hole cavity of a volume V must be equal to the three previous Nusselt's.

$$Nu_{bulk} = \sqrt{Ra} \langle \overline{w\theta} \rangle_V - \partial_z \langle \overline{\theta} \rangle_V \tag{I.20}$$

3) Exact relations for dissipations rates

The thermal dissipation rate $\epsilon_\theta(\boldsymbol{x},t)$ and the viscous dissipation rate $\epsilon_u(\boldsymbol{x},t)$ are defined as Chilla and Schumacher (2012) by

$$\epsilon_\theta(\boldsymbol{x},t) = \kappa \sum_i \left(\frac{\partial \theta}{\partial x_i}\right)^2 \tag{I.21}$$

$$\epsilon_u(\boldsymbol{x},t) = \frac{\nu}{2} \sum_{i,j} \left(\frac{\partial u_i}{\partial x_j} + \frac{\partial u_j}{\partial x_i}\right)^2 \tag{I.22}$$

Following Shraiman and Siggia (1990), two exact formula could be derived from the Boussinesq equations. By averaging the dimensionless energy equation (I.15) and taking into account the adiabatic sidewall hypothesis, the Nusselt number could be related to the thermal dissipation rate $\langle\overline{\epsilon_\theta}\rangle_V$, hence

$$\langle\overline{\epsilon_\theta}\rangle_V = \kappa \frac{H^2}{\Delta\theta^2} Nu_{\epsilon_\theta} \tag{I.23}$$

Also, the averaged viscous dissipation rate balances the conversion of potential energy to kinetic energy in equation (I.14). One can thus extract the second relation between the Nusselt number and the viscous dissipation rate $\langle\overline{\epsilon_u}\rangle_V$ as follows

$$\langle\overline{\epsilon_u}\rangle_V = \frac{\nu^3}{H^4}(Nu_{\epsilon_u} - 1) RaPr^{-2} \tag{I.24}$$

We respectively call Nu_{ϵ_θ} and Nu_{ϵ_u} the Nusselt numbers of thermal and viscous dissipations. We could derive their expression as follows

$$Nu_{\epsilon_\theta} = \frac{\Delta\theta^2}{\kappa H^2} \langle\overline{\epsilon_\theta}\rangle_V \tag{I.25}$$

$$Nu_{\epsilon_u} = Ra^{-1} Pr^2 \frac{H^4}{\nu^3} \langle\overline{\epsilon_u}\rangle_V + 1 \tag{I.26}$$

Based on previous numerical investigations made by Wagner and Shishkina (2013) or Kaczorowski et al. (2014), the convergence between previous Nusselt numbers Nu_{bot}, Nu_{top}, Nu_{mid}, Nu_{bulk}, Nu_{ϵ_θ} and Nu_{ϵ_u} is a criterion to verify the global convergence in the system.

b) Reynolds numbers

It provides a measure of the importance of advective effects relative to viscous effects. In the following, we construct various definitions for the Reynolds number by changing the velocity and length scales. A first definition that we use is based on the maximal horizontal velocity U_{max} and the height of the cell H. The idea is to characterize the flow patterns in the large scale.

$$Re_U = HU_{max}/\nu \tag{I.27}$$

We aim to check the influence of the roughness elements on the flow (see the description of the rough/smooth cell in (§ III.1)). We define a Reynolds number based on the roughness scale. We chose H_p^* and $U|_{z=H_p^*}$ as characteristic length and velocity scales to determine the flow patterns regarding the small scale.

$$Re_U^* = H_p^* U|_{z=H_p^*}/\nu \tag{I.28}$$

We also use another definition for Re to analyze the effect on turbulent fluctuations at roughness scale by considering the vertical velocity rms w_{rms} as a characteristic velocity scale.

$$Re_{w_{rms}} = H_p^* w_{rms}|_{z=H_p^*}/\nu \tag{I.29}$$

I.3 Scaling regimes of thermal convection with smooth boundaries

First investigations such as Deardorff and Willis (1967) have focused on properties of turbulent convection, when others were interested in the transition to turbulence for a given Prandtl number, e.g. Krishnamurti (1973) showed that several distinct transitions occur at certain distinct Rayleigh numbers. In the following we will be interested on the trend of variation of the system responses as a function of its control parameters.

I.3.1 Theories review

Older theories concepted for Rayleigh-Bénard cavity with smooth boundaries predict power laws dependencies in between (Nu, Re) and (Ra, Pr),

$$Nu \sim c\ Ra^{\beta} Pr^{\gamma} \tag{I.30}$$

$$Re \sim c_2\ Ra^{\beta_2} Pr^{\gamma_2} \tag{I.31}$$

Three regime can be identified :

The classical regime : $Nu \sim Ra^{1/3}$

The theory proposed by Malkus (1954) for large Ra numbers and $\mathrm{Pr} = 1$ assumed that diffusive boundary layers are marginally stable at a thickness that depends only on the temperature drop and thus the heat flux would be independent of the cavity height H,

$$Q = Nu\frac{\kappa\Delta T}{H} \nsim H \tag{I.32}$$

In this circumstance, we could immediately derive a $Nu \propto Ra$ scaling relation from equations (I.16) and (I.17). Since, $Ra \sim H^3$ the existence of such stability condition requires that the heat flux vary as

$$Nu \sim Ra^{1/3} \tag{I.33}$$

The argument given for this scaling is limited to the case of thin boundary layers. It does not hold for small Prandtl numbers for which the thermal boundary layer thickness is likely significant.

The hard turbulence regime $Nu \sim Ra^{2/7}$

Castaing et al. (1989) developed a mixing layer theory which was later extended by Cioni et al. (1997) to include Prandtl's dependencies. Their concept is based on the existence of a mixing layer in which the fluid namely thermal plume is accelerated to the velocities of the bulk region. This layer is assumed to be much thicker than the BL but thin compared with the height of the cell. They assumed that thermal plumes retain a thickness similar to the BL thickness and moving toward bulk region because of buoyancy force with a characteristic velocity $u_c = g\alpha\Delta T\delta_\theta^2/\nu$. The BL is considered as purely conductive, hence $\delta_\theta \sim \kappa\Delta T/H$. Assuming a Prandtl number of the order of unity and solving the system equations, they predicted a scaling exponent $\beta = 2/7$. This scaling is close to those reported in experiments. It is in good agreement with all experiments conducted with gases.

The same exponent is obtained based on dimensional arguments in the work of Shraiman and Siggia (1990). They argued by the presence of a mean flow to derive an exact relation between kinetic dissipation rate and the heat flux. By using turbulent boundary layer theory and assuming $Nu \sim 1/\delta_\theta$ together with the kinetic energy dissipation estimated in turbulent shear flow in channels $Pr\langle(\nabla\mathbf{u})^2\rangle_V \sim u_c^3$ where u_c is the characteristic velocity. Combining all terms will yield the following scaling law

$$Nu \sim 0.27 Ra^{2/7} Pr^{-1/7} \tag{I.34}$$

The Ultimate regime : $Nu \sim Ra^{1/2}$

For high Rayleigh numbers, the buoyancy is fully compensated by advection so that the heat transfer no longer depends on the molecular properties, the shear stress at the wall leads to the destabilization of the viscous boundary layers which become turbulent. From there, Kraichnan (1962) deduces that the thermal behavior is affected and passes asymptotically towards a law with $\beta = 1/2$ known as the *ultimate regime of thermal convection*.

As an alternative approach Howard (1972), Busse (1978) proved the existence of upper bounds for Nu. Later, Doering and Constantin (1996) derived mathematically a strict upper bound given by $Nu \leq 0.16 Ra^{1/2} - 1$ building on the equations of motion relative to a steady state. This method is based on the decomposition of the energy dissipation into a background and a fluctuating component, the background part yields an upper bound if the fluctuation term satisfies a certain non-negativity condition, mainly a spectral constraint.

We note that in a similar configuration to the RBC consist of a recent experimental study of the heat transport in a radiatively driven convection by Bouillaut et al. (2019) have reported a transition to the ultimate scaling regime $Nu \sim Ra^{1/2}$ for high absorption length.

I.3.2 Experiments and simulations review

Various experiments have studied the scaling of Nu with Ra in turbulent thermal convection such as Chu and Goldstein (1973) in water for $10^5 < Ra < 10^8$, Threlfall (1975) used gaseous helium in a cylindrical vessel for $Ra < 10^9$, Heslot et al. (1987); Wu and Libchaber (1992) in a cylindrical cell filled with helium gas, Solomon and Gollub (1991) in mercury flow. These studies suggested a smaller exponent approximately $\beta = 2/7$, values that are consistently lower than the classical prediction of $1/3$. Otherwise, Goldstein et al. (1990); Fleischer and Goldstein (2002) suggested that the reduced exponent may be due to the limited range in Ra of some previous experiments. They described an experimental study of high Ra, in which an exponent $1/3$ was found.

In the past years, noticeable numerical improvement allowed to perform full 3D simulations. Through direct numerical simulation (DNS) (Kerr, 1996) achieved $Ra = 2 \times 10^7$ for $Pr = 0.7$ and found an effective power law $Nu \sim Ra^{0.28}$. Later, Verzicco and Camussi (2003), Stringano and Verzicco (2006) have explored a high Ra range up to 2×10^{11} in a slender cell with $\Gamma = 1/2$ and $Pr = 0.7$. Beyond $Ra = 10^{10}$ their numerical data are consistent with $Nu \sim Ra^{1/3}$. Computing facilities allowed to Amati et al. (2005) to reach very high Rayleigh

numbers in the order of 10^{14} thus finding that the Nusselt number varies nearly as the 1/3 power of Ra. Wagner et al. (2012) considered cylindrical RB cells with air as working fluid $Pr = 0.786$. They conducted highly resolved DNS up to Ra^9 and obtained effective scaling exponent $\beta = 0.298$. Recently, Zhu et al. (2018) reached a very high Rayleigh up to 10^{14} for Prandtl number Pr = 1 by performing two-dimensional simulations and reported a transition to the ultimate regime where the local Nusselt number has an effective scaling $Nu \sim Ra^{0.38}$.

There is some confusion about the relevant values of the prefactors and exponents of equation (I.30) which could vary according to the chosen coupling $(Ra - Pr)$, but it also depends on aspect ratios. The experiments conducted at large numbers of Rayleigh have diversified results and indicate that a single universal regime is not easy to achieve, (more discussion details are provided e.g reviews of Ahlers et al. (2009) and Chilla and Schumacher (2012)). A first inspection confirmed what has been said before, a good agreement is observed for a Rayleigh number less than 10^{12}, all experiments exhibit a behavior in $Ra^{2/7}$. For a larger number of Rayleigh, remarkable differences appear and can be triggered by the different flow states. Several behaviours are observed, (Niemela et al., 2000), pass through a $Ra^{1/3}$, (Chavanne et al., 2001) and (Roche et al., 2010) pass to $Ra^{1/2}$ scaling at $Ra \approx 10^{11}$. It becomes hard to define a common scaling law especially for high Ra range, indeed, researchers still debating on this behaviours, questioning if it is due to Non-Boussinesq effect or experiment setups or other negligible sources that could modify the system response.

I.3.3 The unifying theory of Grossmann & Lohse

The Grossmann−Lohse theory (Grossmann and Lohse, 2000, 2001, 2004) is one of the first successful theories to describe the Nu and Re dependence on Ra and Pr over a wide range of parameters. This theory is applicable for the Prandtl-Blasius laminar BL scaling and suggests no pure power laws. The main approach of this unifying theory is based on the decomposition of the energy dissipation rate into boundary layer and bulk contributions. Naturally, they separate viscous dissipation ϵ_u and thermal dissipation ϵ_θ into two parts :

$$\epsilon_u = \epsilon_{u,BL} + \epsilon_{u,bulk} \tag{I.35}$$

$$\epsilon_\theta = \epsilon_{\theta,BL} + \epsilon_{\theta,bulk} \tag{I.36}$$

The modeling of those dissipation rates is obeying the Boussinesq equations. It is also assumed that the layer has a Blasius type. All assumptions are detailed in (Grossmann and Lohse, 2000, 2001). Depending on whether the viscous BL is within the thermal BL or not, i.e depending on the Pr number, one can gets the following correlations,

$$\epsilon_{u,BL} \sim \frac{\nu 3}{H^4} \frac{Re^2}{g(\sqrt{Re_L/Re})} \tag{I.37a}$$

$$\epsilon_{u,bulk} \sim \frac{\nu 3}{H^4} Re^3 \tag{I.37b}$$

$$\epsilon_{\theta,BL} \sim \kappa \frac{\Delta T^2}{H^2} Re \Pr \left\{ f \left[\frac{2Nu}{\sqrt{Re_L}} g \left(\sqrt{\frac{Re_L}{Re}} \right) \right] \right\}^{1/2} \tag{I.37c}$$

$$\epsilon_{\theta,bulk} \sim \kappa \frac{\Delta T^2}{H^2} Re \Pr f \left[\frac{2Nu}{\sqrt{Re_L}} g \left(\sqrt{\frac{Re_L}{Re}} \right) \right] \tag{I.37d}$$

where f and g are cross-over functions ($f(x) = (1 + x^n)^{-1/n}$ and $g(x) = x * (1 + x^n)^{-1/n}$, with $n = 4$) introduced as corrections for the transitions from small to large Prandtl numbers and Re_L is a critical Reynolds number.

By incorporating the modeling assumptions (I.37a),(I.37b),(I.37c),(I.37d) into the dissipations equations (I.35),(I.36) and taking into account the exact relations that Shraiman and Siggia (1990)) derived for ϵ_u and ϵ_θ, GL obtained the final two implicit equations for $Nu(Ra, Pr)$ and $Re(Ra, Pr)$ with six free parameters a,Re_L, and $c_i, i = 1, 2, 3, 4$:

$$\begin{aligned} (Nu - 1) RaPr^{-2} &= c_1 \frac{Re^2}{g(\sqrt{Re_L/Re})} + c_2 Re^3 \\ Nu - 1 &= c_3 Re^{1/2} Pr^{1/2} \left\{ f \left[\frac{2aNu}{\sqrt{Re_L}} g \left(\sqrt{\frac{Re_L}{Re}} \right) \right] \right\}^{1/2} \\ &\quad + c_4 PrRef \left[\frac{2aNu}{\sqrt{Re_L}} g \left(\sqrt{\frac{Re_L}{Re}} \right) \right] \end{aligned} \tag{I.38}$$

As showed in figure (I.5a), the GL theory provides a $Ra - Pr$ parameter-space mapping for Nu with multiple scaling laws. The fit is based on extensive experimental and numerical data. (Stevens et al., 2013) used new data points and gave an updated fit in a much larger parameter space. As figure (I.5b) shows the Nu number scaling with Ra is well-predicted by the GL theory, therefore, can be used as a good reference. We note Grossmann and Lohse (2011) made an extension of the GL theory to very large Ra and made predictions for the multiple scaling in the ultimate regime.

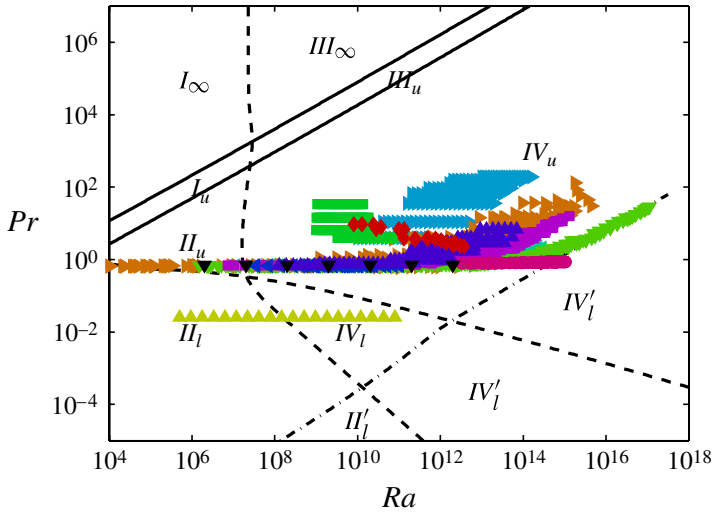

(a)

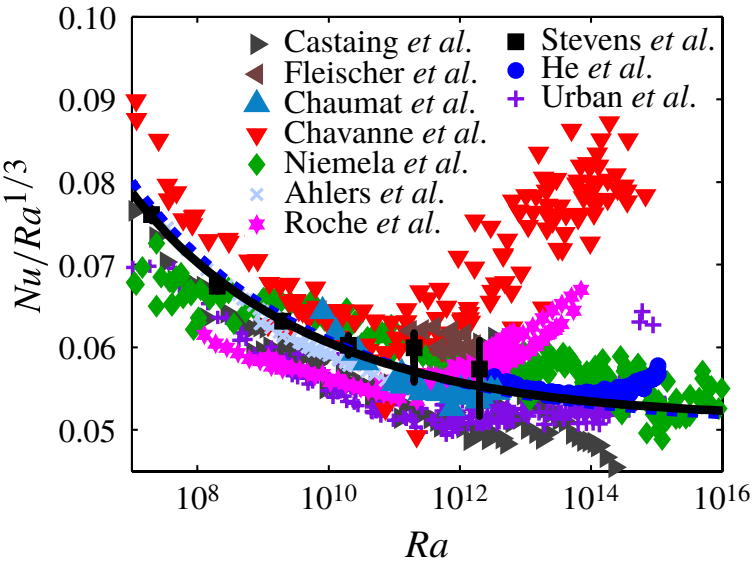

(b)

Fig. I.5 Rayleigh Bénard convection phase diagram in the Ra-Pr space according to the GL model for $\Gamma = 1/2$. The upper solid line means $Re = 1$; the lower nearly parallel solid line corresponds to $\epsilon_{u,BL} = \epsilon_{u,bulk}$; the curved solid and dashed line is $\epsilon_{\theta,BL} = \epsilon_{\theta,bulk}$; and along the long-dashed line $\delta_u = \delta_\theta$. The dash-dotted line indicates where the laminar kinetic BL is expected to become turbulent. The data are from (Castaing et al., 1989), (Chavanne et al., 1997), (Glazier et al., 1999), (Niemela et al., 2000), (Ahlers and Xu, 2001), (Chaumat et al., 2002), (Ahlers et al., 2009), (Burnishev et al., 2010), (Roche et al., 2010), (Urban et al., 2011), (Urban et al., 2012), (He et al., 012b), (Stevens et al., 2010a) and (Stevens et al., 2011). (b) compensated heat transport as a function of the Rayleigh number. Figures are taken from (Stevens et al., 2013).

I.4 Rough boundaries in thermal convection

We have seen that, until now, scaling theories exist for convective flows occurring over smooth boundaries. However, the real flows are in general much more turbulent than those studied in laboratories and they occur over strongly rough surfaces. In the nature, thermal turbulence mostly occurs over rough topographies, such as in the atmosphere and over the deep ocean, see figure (I.6a).

The influence of roughnesses has been established for some engineering topics. Ribs are used on heat exchange surfaces to promote turbulence and enhance convective heat transfer. Applications include fuel rods of gas-cooled nuclear reactors, inside cavities of turbine blades, and internal surfaces of pipes used in heat exchangers. According to Ventola et al. (2014), rough surfaces could enhance the heat transfer for electronics cooling. Numerous investigations exist for this purpose. Chang et al. (2008) examined rectangular channel fitted with V-shaped ribs. Cernecky et al. (2014) used an area roughness in forced convection channel. Recently, Kaewchoothong et al. (2017) have been studying the effect V-shaped ribs on cooling channel for internal cooling of gas turbine blades, see figure (I.6b), thus finding a remarkable heat transfer intensification. According to the author, the secondary flow is formed in between the ribs an contribute mainly in transferring the heat into the system.

A fruitful approach to gain insight into the mechanism for turbulent heat transport is to alter the boundary conditions of the cell and find out how the convective flow responds to BL perturbations.

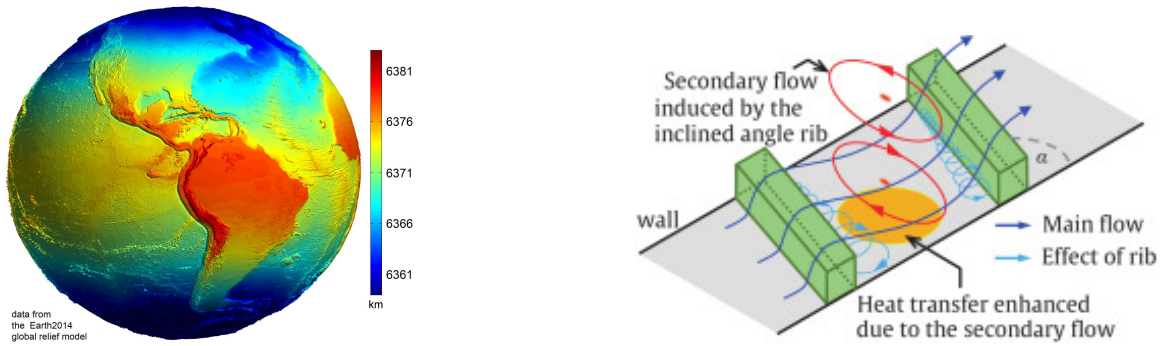

(a) (b)

Fig. I.6 (a) Earth shape, as given by the Earth2014 global relief model. Shown are distances between relief points and the geocentre (www.wikimedia.org). (b) Rib-roughened walls induce local heat transfer enhancement in a stationary channel (Kaewchoothong et al., 2017).

I.4.1 Experiences and simulations review for RBC with roughened walls

From an efficiency standpoint, roughness has an apparent impact on enhancing the heat transfer. However, the mechanism by which this behaviour is reached is probably not well known. Shen et al. (1996) were perhaps the first to make experimental study of turbulent thermal convection over rough surfaces in RB cavity. By using rough upper and lower plates with regularly spaced pyramids, they identified a critical Rayleigh number Ra_c beyond which the heat transfer gets increased, suggesting that thermal boundary layer thickness become lower than roughness height Hp. In their study, we should mention that δ_θ is quantified just via the relation $\delta_\theta = H/(2Nu)$. The Nu is enhanced but without changing of the power law exponent β. According to the authors, this is due to extra thermal plumes produced by the surface roughness. Flow visualization were carried out by Subudhi and Arakeri (2012) in turbulent free convective flow for both the smooth and grooved surface in an open cavity filled with water. In agreement with Shen et al. (1996), they reported an intermittent detachment of thermal plumes near roughnesses moving randomly and merging with each other may contribute to the heat enhancement.

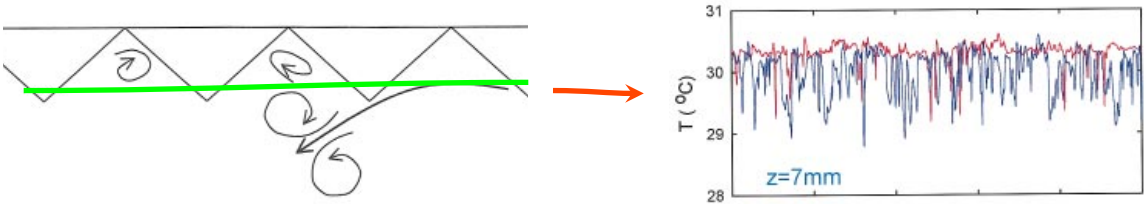

(a) (b)

Fig. I.7 (a) Sketch of the flow field near the rough surface, a secondary flow is created inside the groove region. (b) Typical time series measurements of temperature fluctuations near the upper walls (green line). A red line color for smooth whereas blue line is used for rough surface, (Du and Tong, 2000).

The experiment of Du and Tong (1998, 2000) was conducted in a cylindrical cell filled with water. They used a similar apparatus to Shen et al. (1996) and found that Nu increases by 76% when $\delta_\theta < H_p$, which exceeds increase due to the larger effective contact area of the fluid with the rough surface. Here also the $Nu \sim Ra^\beta$ scaling remains unchanged. According to them, large scale circulation (LSC) interacts with the surface roughness as sketched in figure (I.7a) and produces more energetic thermal plumes from the tip of pyramids that can survive for longer times and penetrate vertically into the bulk region, thus enhances the heat transport. The measure of temperature fluctuations near pyramids demonstrates change of the flow dynamics. Indeed, emission of thermal plumes is found to be higher near roughnesses, see figure (I.7b). Some of these results were reconfirmed in a different experiment by Ciliberto

and Laroche (1999). They tested several setups of roughnesses made of glass spheres with variable diameters and deduced that the exponent β is sensitive to the presence of a obstacles and could be strongly modified depending on the geometric distribution of those roughnesses.

Later, Roche et al. (2001) used cylindrical cell with rough boundaries. They claimed to have reached the ultimate regime. They reported a transition to the power law $Nu \sim Ra^{1/2}$ which has spread considerable discussion since then.

The effect roughened wall in thermal turbulent convection boundary has also been studied through numerical simulations. It gives a full access to the flow field and could provide more key answers and help to improve the roughness effects. Through 3D DNS, Stringano et al. (2006) studied turbulent thermal convection in a cylindrical cell confined by plates with axisymmetric grooves for $Pr = 0.7$ with Ra number ranging in $[2 \times 10^6, 2 \times 10^{11}]$. Similarly, a transition to an enhanced regime beyond a critical Rayleigh Ra_c is founded, however, the scaling exponent increased to $\beta = 0.37$. They estimated local TBL thickness and found $\delta_\theta < H_p$ for $Ra > Ra_c$, a consistent results with previous works.

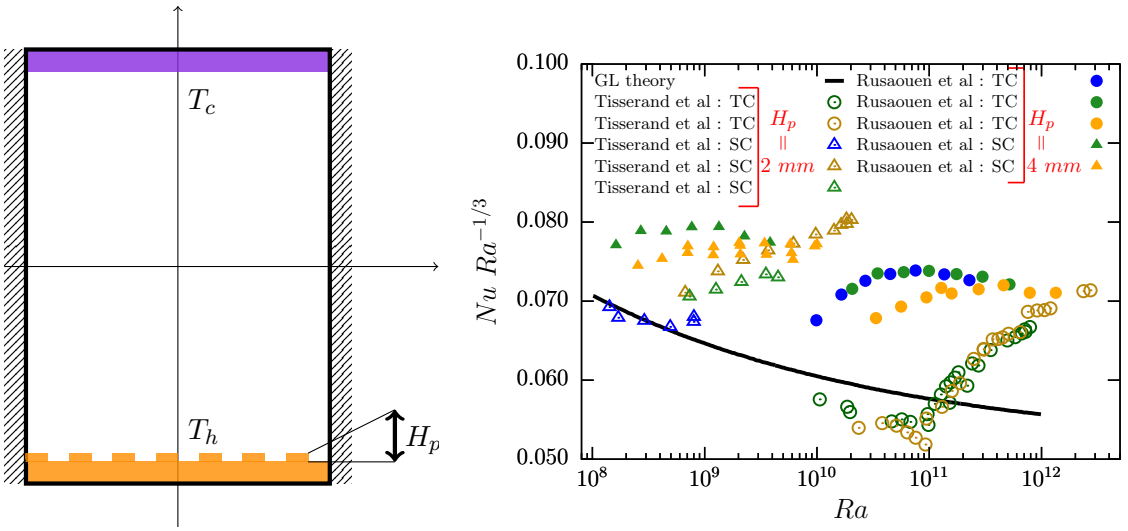

(a) (b)

Fig. I.8 (a) Asymmetric rough Rayleigh-Bénard cavity. (b) compensated Nu number in rough cavities. Color code for bulk temperature : (blue,25^oC or 30^oC), (green,40^oC), (orange,60^oC) and (brown,70^oC), (Rusaouën et al., 2018).

Massive experimental studies were conducted at ENS Lyon using an asymmetric RB cell with a rough lower surface with square based plots as sketched in figure (I.8a). By assuming an independent behavior between the opposite plates, Tisserand et al. (2011) found that on the one hand, the smooth plate is behaving almost like a classical RBC with an scaling

exponent $\beta = 1/3$. On the other hand, rough plate showed a transition to enhanced regime characterized by a scaling exponent in some cases up to $\beta = 1/2$. Once again, they clearly showed that additional heat exchange surface is not the only cause of Nu enhancement. Later, Salort et al. (2014) used a rectangular cell filled with water and confirmed the transition when $\delta_\theta > H_p$. Furthermore, their local temperature measurements revealed that thermal BL was thinner on top of plots and suggested a local enhancement of the heat transfer.

To explain this observation, Liot et al. (2016, 2017) carried out high-resolution PIV measurements near the roughness elements. They suggested that viscous BL on the top of plots transitions from laminar to turbulent state. In continuation of previous works, Rusaouën et al. (2018) provide an extension to Tisserand et al. (2011) measurements with twice higher roughnesses. By doing so, different scaling regime are identified for the rough plate. Most importantly in tall cell, a saturated regime is found with a scaling law similar to smooth plate $Nu \sim Ra^{1/3}$ as can be seen in figure (I.8b). This study demonstrates clearly the effect of roughness height as a control parameter in the system.

The experiment of Tisserand et al. (2011) in tall cells with small H_p shows that the heat transfer is reduced comparing with GL model when $Ra < 10^{11}$. According to the authors, it is due to thermal resistance induced by motionless fluid in between the roughness elements. In parallel, a numerical investigation made by Zhang et al. (2018) confirmed this behaviour. According to this study, accumulation of the heat between the rough elements leads to a much thicker TBL, thus reduce the global heat transfer.

Other works have focused on the roughness effect on heat transfer properties. Wei et al. (2014) have tested experimentally configurations in which upper and lower surface could be smooth or roughened with square based pyramids. According to them, smooth plate can influence the opposite rough plate but it can not be influenced, whereas, rough plate is found to be sensitive to boundary condition (BC) of the facing plate. The explanation is that boundary layers are thinner than roughness height, i.e. therefore obstacles are within to the bulk flow, which impacts the rough plate properties. This study shows the importance of the LSC in the global and local heat transfer. Recent numerical investigation on this subject made by Jiang et al. (2018) who used a rough cell with ratchet structures confirm the LSC orientation effect. Indeed, the emission of thermal plumes is found to be affected by LSC-BL's interaction which directly impacts the heat transfer efficiency.

Simple analytical models were proposed to represent the effect of rough boundaries. They are based on 2D Prandtl-Blasius BL theory (Shishkina and Wagner, 2011) and were extended to 3D configuration (Wagner and Shishkina, 2015). The shortfall of those models is their

limited ability to handle complex geometries only as regular parallelepiped roughness can be considered. Moreover, a few number of relatively high obstacles are used in those study but generally it could predict the Nu enhancement approximatively. Beside that, they highlight the effect of spacing between obstacles on Nu, which could be counted as a control parameter as well. The interesting result is the scaling exponent β dependence on the aspect ratio of roughness but also on their geometrical arrangement.

The effect of roughnesses geometric properties (size, spacing) were studied by Toppaladoddi et al. (2017) through numerical simulation of a 2D symmetric RB rectangle with both rough plates for $Pr = 1$ and Ra ranging in $[4 \times 10^6 - 3 \times 10^9]$. As shown in figure (I.9) a sinusoidal form is used to model roughness and found an optimal wavelength value ((defined as the ratio of roughness width to the total height) $\lambda_p = W_p/H$) for which the heat transfer scaling exponent is maximized and claimed to have reached the ultimate regime. However, by using a very similar 2D DNS configuration, Zhu et al. (2017) reached high Ra number up 10^{12} and showed that the onset of $Nu \sim Ra^{1/2}$ is a transitional regime after which another behavior for the scaling law with $Nu \sim Ra^{1/3}$ is reported. We note that this kind of saturation was also found in Taylor-Coutte flow with roughness boundaries, more details are provided by Zhu et al. (2016).

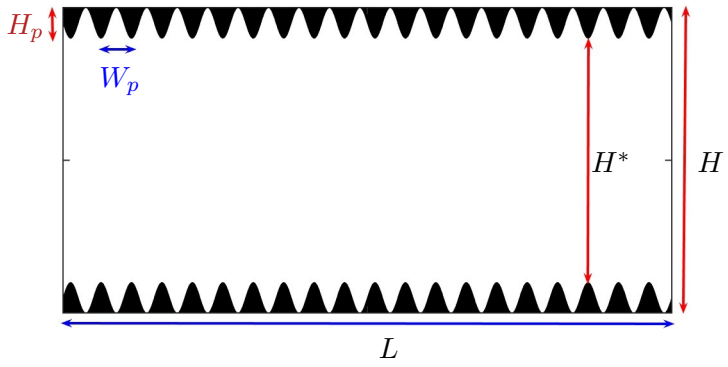

Fig. I.9 Geometry of 2D rough rectangular cell from (Toppaladoddi et al., 2017).

Recently, experiment made by Xie and Xia (2017) in RBC with rough bottom and upper plates with pyramid-shaped for Ra ranging in $[7.5 \times 10^7, 1.31 \times 10^{11}]$ has been focused on the heat transport dependence on roughness geometry by varying the ratio λ_p (defined here as the height of a pyramid over its base width). The scaling exponent β get increased with λ_p. Besides that, they reported two transitions, firstly, from regime I to enhanced regime II due to a thermal BL thinner than roughness height, a consistent result with previous studies, whereas the second is resulted of a viscous BL thickness becoming thinner roughness.

I.4.2 ENS Lyon models

Model 1 : BL totally destabilized

Salort et al. (2014) developed this model based on the destabilization of the laminar boundary layer because of roughness. By defining a shear Reynolds number Re_{sh} based on viscous BL thickness and a critical Péclet number Pe_T and considering the case of a thermal BL thinner than the viscous one,

$$Re = \frac{\delta_u U}{\nu} \tag{I.39a}$$

$$Pe_T = \frac{U\delta_\theta^2}{\kappa\delta_u} \tag{I.39b}$$

The Nusselt number is defined as $Nu = H/(2\delta_\theta)$, yield the so called rough Nusselt number Nu_R which represent the heat transfer in a cell with both top and bottom plates being rough

$$Nu_R = \frac{1}{2}\frac{RePr^{1/2}}{(Pe_T Re_{sh})^{1/2}} \tag{I.40}$$

They assumed that the transition to enhanced regime occurs when $\delta_\theta \sim H_p$, thus the critical value of Péclet, shear Reynolds and Nusselt numbers are

$$Re_{sh} = \frac{\delta_{u,c} U_c}{\nu} \tag{I.41a}$$

$$Pe_T = \frac{U_c H_p^2}{\kappa\delta_{u,c}} \tag{I.41b}$$

$$Nu_c = \frac{H}{2H_p} \tag{I.41c}$$

Where U_c is mean velocity and $\delta_{u,c}$ viscous BL thickness at the transition.

We can deduce that $Pe_T Re_{sh} = (H_p/H)^2 \,\mathrm{Pr}\, Re_c^2$ with $Re_c = HU_c/\nu \sim Ra_c^{1/2}\,\mathrm{Pr}^{-3/4}$. Therefore, we could obtain

$$Nu_R = \frac{H}{2H_p}\frac{Ra^{1/2}}{Ra_c^{1/2}} \tag{I.42}$$

Where $Ra_c = (Nu_c/\sigma)^3$ with σ is a prefactor. Finally the equation model for rough Nusselt number is given by

$$Nu_R = 0.5(2\sigma)^{3/2}(H_p/H)^{1/2} Ra^{1/2} \tag{I.43}$$

Model 2 : BL partially destabilized

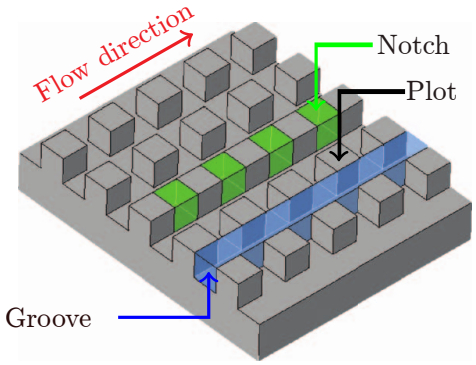

Fig. I.10 Sketch of the rough plate from the study of Salort et al. (2014)

A prediction model for the rough Nusselt number Nu_R was also proposed by Salort et al. (2014). It based on the contribution from different geometrical zones. According to their geometry, three zone could be considered : plot, notch and groove. Depending on the surface that occupy each part, the rough Nusselt number is constructed from those contributions is given by

$$Nu_R = s_p Nu_{plot} + s_n Nu_{notch} + s_g Nu_{groove} \tag{I.44}$$

Where s_p,s_n and s_g are the surface proportions of plots, notches and grooves in the rough plates with $s_p + s_n + s_g = 1$.

The authors assumed a fully transited BL on top of plots. Moreover, the notch zone is considered as a small convection cell, reasoning on the order magnitude at this small scale, a definition is given whether before or after the transition. The groove zone is considered as a smooth plate with taking the contribution from side roughnesses into account. Therefore, we may express those assumptions as following

$$Nu_{plot} = 0.5(2\sigma)^{3/2}(H_p/H)^{1/2}Ra^{1/2} \tag{I.45}$$

$$\begin{cases} Nu_{notch} &= f_{GL}(Ra) & \text{if } \; Nu < H/(2H_p) \\ Nu_{notch} &= \dfrac{H}{2H_p} f_{Ch}(\dfrac{1}{2}(\dfrac{H_p}{H})^3 Ra) & \text{if } \; Nu > H/(2H_p) \end{cases} \tag{I.46}$$

$$Nu_{groove} = \left(1 + \frac{H_p}{H}\right) f_{GL}(Ra) - \frac{H}{2l} \tag{I.47}$$

Where f_{GL} is the prediction with Grossmann-Lohse model Stevens et al. (2013), f_{Ch} is an interpolation from Chavanne et al. (2001) experiment. l is the width of roughness element.

I.4.3 Göttingen models

Model 1 : Two dimensional case

A two dimensional model for rectangular roughness elements is developed by Shishkina and Wagner (2011). By using the approximation made by Pohlhausen (1921), they assumed a boundary layer of Prandtl-Blasius type. By taking into account the increased surface of roughened plates, they derive a linear combination of the contributions to the heat transfer from horizontal and vertical surfaces of the rough plate,

$$Nu_R = C(\Psi_h + \Psi_v) \tag{I.48}$$

where Ψ_h and Ψ_v are the proportional contributions to Nu_R from horizontal and vertical surfaces. $C = Nu_S/((T_h - T_c)H^3)^{1/4}$ with Nu_S the Nusselt number of smooth cell.

Model 2 : Three dimensional case

Wagner and Shishkina (2015) have also proposed a prediction model for three dimensional geometry. Simply, this model handle with rectangular roughness extruded from the previous 2D geometry. Here, we are particularly interested is some proposed formulations that we will use later in our work. We mention their approximation based on their DNS data that gives

$$Nu_R \approx Nu_S \left(1 + C_1 \left(\frac{H_p}{H}\right) + C_2 \left(\frac{H_p}{H}\right)^2 f(W_p/H)\right) \tag{I.49}$$

Where C_1 and C_2 are constants. f is a function which depends on the roughness width W_p.

Another approximation based on Pohlhausen (1921) to quantify the contribution from vertical surfaces. Assuming that roughness elements are infinitively slender ($W \to 0$). The obtained prediction model could be written as following

$$Nu_R \approx Nu_S \left(1 + C \left(\frac{H_p}{H}\right)^{3/4}\right) \tag{I.50}$$

Where the coefficient C depends on Ra. It is estimated with $C = \frac{A_R - A_S}{A_S}(2Nu_S)^{3/4}$. A_R and A_S are relative surface of rough and smooth plates.

The 2D model gives a good approximation with respect to the 2D geometry. Otherwise, as reported is those studies, it cannot predict the enhanced regime for the 3D configuration. According to their 3D DNS, if the distance between roughnesses is larger, the later area would be more washed by the flow which probably enhance further the heat transfer.

I.5 Motivations and objectives

Through this thesis, we will be interested in studying the effects of roughened boundary in turbulent Rayleigh Bénard convection. The aim is to improve our understanding of the various issues and observations of roughness effects most importantly seen in experiments. Thus, we conduct a three dimensional direct numerical simulations to permit quantitative measures that are not accessible in experimental studies. A wide range of Rayleigh numbers is explored to capture eventual changes of the heat transfer regime. Massive parallel computing resources are deployed to construct a numerical database in which the statistical fields and measured quantities are converged. A post-processing code written in Fortran-90 is developed to handle with the big data analysis.

The present manuscript is organized as follows,

Chapter § II is a description of the numerical code. We detailed the resolution methods of the governing equations, the parallel computing and the immersed boundary method. The scalability tests for the used solvers are presented as well to characterize performances of the code together with two validation cases are presented.

Chapter § III is a description of the asymmetric Rayleigh Bénard cell with bottom rough and top smooth surfaces, the system parameters and responses. We present the methodology used to separate the behaviors of the rough and smooth plates. We also details various definitions useful for the characterization of boundary layers.

Chapter § IV focus on the study of roughness effects on the heat transfer regime. We Compare our data with multiple 2D and 3D models. A description of the heat flux at the roughness scale is discussed.

Chapter § V is dedicated to the local description of mean profiles and boundary layers structures near roughnesses comparing with the smooth case.

Chapter (§ VI) is a comparison between 3D DNS and experimental works. We compare local mean profiles at the roughness scale and effects of the large scale circulation on flow structures near roughness.

Chapter § VII focus on roughnesses effects on thermal plumes properties. Temporal monitoring on the coherent structures is made to reveal their characteristics. In addition, a numerical ombroscopy is performed. We discuss and compare the presence of dissipative structures close to the rough and smooth plates.

II – NUMERICAL CODE : SUNFLUIDH

II.1 Introduction

SUNFLUIDH is a finite volume code written in Fortran and developed at LIMSI by Yann Fraigneau (2013) for the simulation of incompressible unsteady flows. The code allows the numerical simulation of a wide range of flows (forced, natural, mixed,...) or low Mach number flows ($Ma < 0.1$). It is able to treat flows with heat transfer in transient or turbulent regimes.

In the present chapter, we first detail the numerical discretization opted in this work. We then present (i) the immersed boundary method used to embed solids inside the computational domain, (ii) the multigrid solvers of the Poisson equation and (iii) the parallelization strategies. Secondly, we discuss about the performance of the code when using two different multigrid solvers. Finally, the code will be validated using two cases (i) 3D smooth RBC and (ii) 2D RB with immersed roughness elements.

II.2 Numerical methods

We consider the Boussinesq equations for incompressible flow written in dimensionless form

$$\begin{aligned} \overrightarrow{\nabla}.\boldsymbol{u} &= 0 \\ \frac{\partial \boldsymbol{u}}{\partial t} + \boldsymbol{u}.\overrightarrow{\nabla}\boldsymbol{u} &= -\overrightarrow{\nabla}P^* + \frac{Pr}{\sqrt{Ra}}\overrightarrow{\nabla^2}\boldsymbol{u} + Pr\theta e_z \\ \frac{\partial \theta}{\partial t} + \boldsymbol{u}.\overrightarrow{\nabla}\theta &= \frac{1}{\sqrt{Ra}}\overrightarrow{\nabla}^2\theta \end{aligned} \tag{II.1}$$

The conservative formulation is used for the discretization of operators,

$$\begin{aligned} \frac{\partial \mathbf{u}}{\partial t} + Op_a(\mathbf{u}) &= -\frac{1}{\rho_{ref}}\nabla P + Op_v(\mathbf{u}) + F \\ \frac{\partial \theta}{\partial t} + Op_a(\theta) &= Op_T(\theta) \end{aligned}$$

If we consider that Op_v is the operator associated to the viscous term, thus

$$Op_a(\mathbf{u}) = \nabla(\mathbf{u}^t \cdot \mathbf{u}) \tag{II.2}$$

II.2.1 Staggered meshgrid and spatial discretization

Discretization of different quantities is carried out on Cartesian staggered meshgrid (Harlow and Welch, 1965). The reference mesh is associated with scalar quantities where the velocity components are defined on its interfaces as sketched in figure (II.1). It ensures a numerical stability comparing with a discretization on collocated grid. This type of meshing leads to the definition of ghost cells outside the computational domain that are reserved for the management of the boundary conditions. A second order finite volume approach in time and space is applied for the discretization of the governing equations. A second order accurate centered schemes are used for all space derivatives. The spatial discretization is carried out on the staggered meshgrid. Velocity components are expressed at the mesh cell interfaces via a linear interpolation.

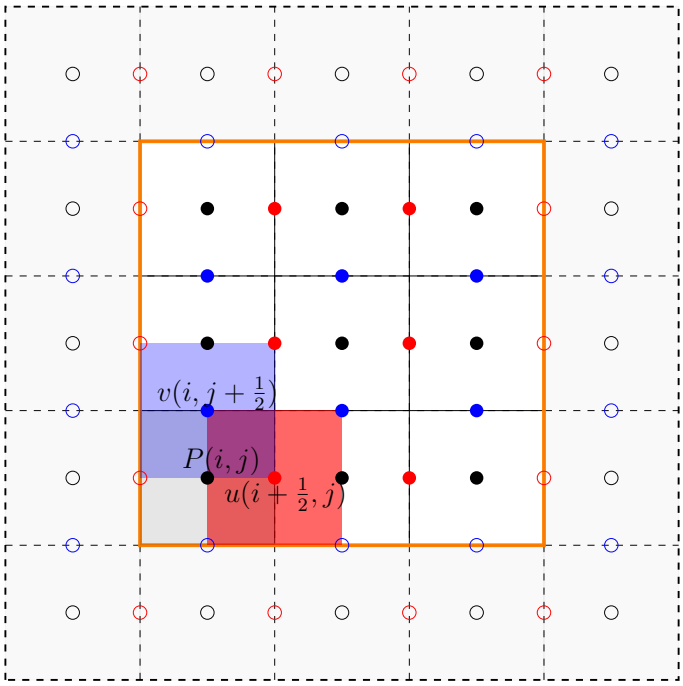

Fig. II.1 2D staggered meshgrid. (•) scalar quantities. (•) horizontal and (•) vertical velocity components. Control volumes associated with velocity are sketched with red and blue areas whereas scalar quantities with black. Nodes inside the computation domain (full circles), nodes in ghost cells are associated to the boundary conditions (open circles).

II.2.2 Temporal discretization scheme

A delayed Euler scheme or backward differentiation formula (BDF2) is used for temporal discretization. If we assume a constant time step Δt, the time derivative term can be written as follows

$$\partial_t u_i^{n+1} = \frac{3u_i^{n+1} - 4u_i^n + u_i^{n-1}}{2\Delta t} + O(\Delta t^2) \tag{II.3}$$

The viscous terms are implicitly considered, whereas the convective terms are explicitly evaluated and approximated using a second order Adams Bashforth scheme. This approach makes it possible to enhance the numerical stability which is mainly related to the CFL condition.

$$\partial_j (u_j u_i)^{n+1} = 2\partial_j (u_j u_i)^n - \partial_j (u_j u_i)^{n-1} \tag{II.4}$$

The discretization of equations (II.1) is as follow

$$\partial_i u_i^{n+1} = 0 \tag{II.5a}$$

$$\frac{3u_i^{n+1} - 4u_i^n + u_i^{n-1}}{2\Delta t} + \partial_j (2u_i^n u_j^n - u_i^{n-1} u_j^{n-1}) = -\partial_i p^n + \Pr Ra^{-\frac{1}{2}} \partial_j^2 u_i^{n+1} + \Pr \theta^{n+1} \delta_{ij} \tag{II.5b}$$

$$\frac{3\theta^{n+1} - 4\theta^n + \theta^{n-1}}{2\Delta t} + \partial_j (2u_j^n \theta^n - u_j^{n-1} \theta^{n-1}) = Ra^{-\frac{1}{2}} \partial_j^2 \theta^{n+1} \tag{II.5c}$$

We first resolve the equation (II.5c) to find a solution for θ^{n+1}. We need to solve the following Helmholtz-Poisson problem

$$\theta^{n+1} - \tfrac{1}{A} Ra^{-1/2} \partial_j^2 \theta^{n+1} = \tfrac{1}{A} Q_\theta^n \tag{II.6a}$$

$$Q_\theta^n = \tfrac{4\theta^n - \theta^{n-1}}{2\Delta t} - (2\partial_j (u_j \theta)^n - \partial_j (u_j \theta)^{n-1}) \tag{II.6b}$$

Where $A = \frac{3}{2\Delta t}$ and Q_θ^n is the source term relative to θ.

Due to the incompressibility condition and the pressure gradient involved, the velocity pressure coupling is more complex. We use an incremental pressure correction scheme (for more details see Chorin (1969); Guermond et al. (2006)). In this scheme, the pressure term in the momentum equation (II.5b) is treated explicitly to obtain a provisional velocity field $\mathbf{u}^*$ which may not be divergence free. This is the so called prediction step.

$$Au_i^* - PrRa^{-1/2}\partial_j^2 u_i^* = Q_{u_i}^n - \partial_i p^n \tag{II.7a}$$

$$Q_{u_i}^n = \frac{4u_i^n - u_i^{n-1}}{2\Delta t} - (2\partial_j(u_j u_i)^n - \partial_j(u_j u_i)^{n-1}) + Pr\theta^{n+1} \tag{II.7b}$$

The problems are reduced to the solution of one 3D Helmholtz-Poisson problem for each primitive variable (u, v, w and θ). Therefore we obtain solution for θ^{n+1} and u_i^*.

Because of hard convergence, for each of the $3D$ Helmholtz-Poisson problems, the Douglas-Rachford Alternating Direction Implicit (ADI) method is used to separate the operators into one dimensional components and split the scheme into one sub step for each coordinate. Consider the following model equation of the form

$$(1 - D\partial_j^2)\phi^{n+1} = Q \tag{II.8}$$

Where ϕ represents the primitive variables $\phi = \{\mathbf{u}, \theta\}$, D the corresponding diffusion coefficients $D = \{\frac{2\Delta t}{3}PrRa^{-1/2}, \frac{2\Delta t}{3}Ra^{-1/2}\}$, and $Q = \{Q_\theta^n, Q_{u_i}^n\}$ the source terms. The ADI method is based on the factorization of the left hand side of our model equation as the product of one dimensional operators as follows (Ferziger and Peric, 2002).

By neglecting $O(\Delta t^2)$, i.e. D^2 and D^3 terms, we obtain the following simplified expression

$$Q = (1 - D\partial_x^2)(1 - D\partial_y^2)(1 - D\partial_z^2)\phi^{n+1} \tag{II.9}$$

Using a multi-step approach leaves a 1-D Helmholtz problem for each ADI sub-step

$$\begin{aligned} (1 - D\partial_x^2)\tilde{\phi} &= Q \qquad \text{with BC on } e_x \\ (1 - D\partial_y^2)\tilde{\tilde{\phi}} &= \tilde{\phi} \qquad \text{with BC on } e_y \\ (1 - D\partial_z^2)\phi^{n+1} &= \tilde{\tilde{\phi}} \qquad \text{with BC on } e_z \end{aligned} \tag{II.10}$$

In the projection step, we assume that $(u_i^{n+1} - u_i^*)$ derives from potential field Π. We can obtain the following Poisson equation by applying the divergence operator to the momentum equation

$$\partial_i^2 \Pi = \frac{3}{2\Delta t}\partial_i u_i^* \qquad \text{with} \qquad \partial_n \Pi = 0 \;\; \text{on the solid boundaries} \tag{II.11}$$

In correction step, the velocity u_i^{n+1} and pressure p^{n+1} will be evaluated using provisional velocity u_i^* and the potential function Π

$$u_i^{n+1} = u_i^* - \frac{1}{A}\partial_i \Pi \tag{II.12}$$

$$p^{n+1} = p^n + \frac{1}{A}\partial_i \Pi - PrRa^{-1/2}\partial_i u_i^* \tag{II.13}$$

We note that each ADI sub-step takes the form of a tridiagonal system that can be solved directly using the Thomas algorithm. In this work, we used the multigrid method for solving the Poisson problem (II.11)) (Brandt, 1977; Strang, 2007). The time step is fixed to ensure that $CFL = 0.3$ is verified

$$\left(\frac{u}{\Delta x} + \frac{u}{\Delta y} + \frac{u}{\Delta z}\right) \leqslant CFL \tag{II.14}$$

Where Δx, Δy, and Δz correspond to the dimensions of the control volume along the x, y and z directions, respectively.

II.2.3 Immersed boundary method

In Sunfluidh code, we can introduce a solid body inside the computational domain Ω by defining its geometry, size and location. In our case, we use a parallelepiped shape. This immersed body (IB) has to be aligned with the mesh interfaces as shown in figure (II.2).

We used a loop truncation method to compute only over the fluid cells Ω_{fluid}. Each immersed body could be identified by an indexation of its minimal and maximal border cells for all space directions ($i \in [i_{min}^{IB}\ i_{max}^{IB}]$; $j \in [j_{min}^{IB}\ j_{max}^{IB}]$; $k \in [k_{min}^{IB}\ k_{max}^{IB}]$) This essentially leads to skip the solid body Ω_{solid} in the computing process. This indexation is local, it is made relatively to the subdomain meshgrid to which the immersed body belongs to.

We refers by the subscript SD to the indexation loop inside a subdomain. Let us take an example of a computing process passing through one immersed body. We give details only for $\overrightarrow{i}$ direction as follow

1. Pre-computing step : attribution of local indexation for the immersed body inside the subdomain

$$\text{First cell} \longmapsto i_{min}^{IB} \qquad \text{Last cell} \longmapsto i_{max}^{IB}$$

2. Computing on fluid cells for $i_{SD} : 1 \longmapsto i_{min}^{IB} - 2$

3. Update of west cell $i_{SD} = i_{min}^{IB} - 1$ with respect to boundary conditions on the west face of immersed body,

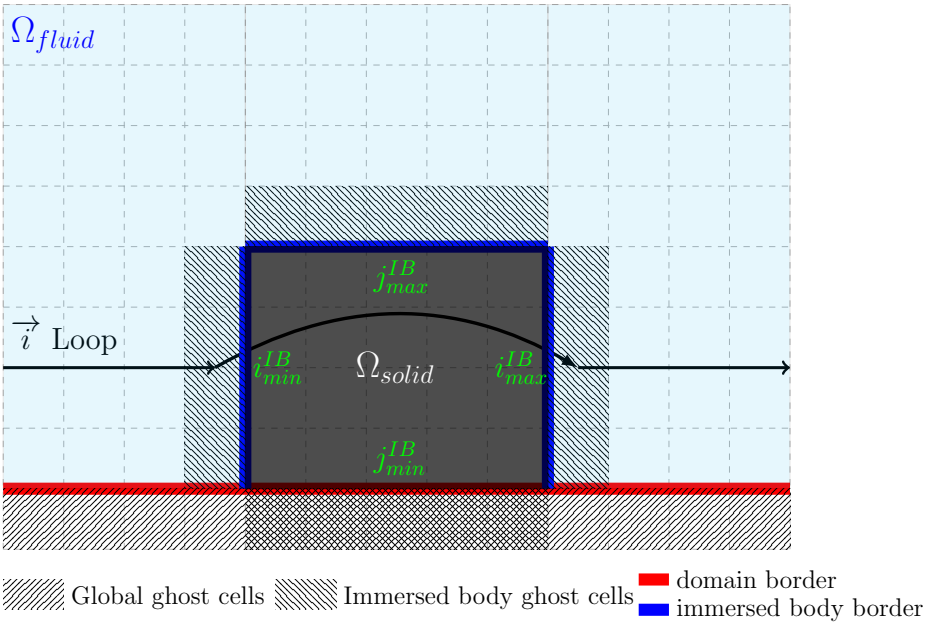

Fig. II.2 2D Immersed body in the computational domain. Its borders are recognized by means of a local indexation in the subdomain. I-direction $[i^{IB}_{min}\ i^{IB}_{max}]$. J-direction $[j^{IB}_{min}\ j^{IB}_{max}]$

4. Loop stop at $i_{SD} = i^{IB}_{min} - 1$. and restart directly from $i_{SD} = i^{IB}_{max} + 1$

5. Update of east cell $i_{SD} = i^{IB}_{max} + 1$ with respect to boundary conditions on the east face of immersed body,

6. Computing on fluid cells for $i_{SD} : i^{IB}_{max} + 2 \longmapsto end$

Each immersed body has its own kinematic and thermal boundary conditions. In our case, the no slip condition is applied for velocity and Dirichlet condition for temperature. The so called immersed body ghost cells are actually belonging to the computational domain. They are updated in the way the imposed boundary condition will be respected exactly on fluid/solid interface (see blue border in figure (II.2)). We mention here that the computing process skip the solid cells.

II.2.4 Resolution of Poisson equation by Multigrid method

In order to solve the Poisson's equation in accordance to immersed boundary method, two solvers are tested and used in the performed simulations.

a) I-SOR solver

The first method is a Successive Over-Relaxed method (SOR) coupled with a nV-cycle multigrid method in order to accelerate the convergence. We used a SOR solver based on a "Red-Black" preconditioning (Bailey et al., 1995) optimized for the domain decomposition approach (MPI-parallel computations). It has the advantage of being independent of the decomposition of the computational domain, therefore it gives a reproducible results. This method is directly implemented in the code and no external library is required.

Through multigrid algorithm, we evaluate the errors made on the approximate solution, which are essentially attributable to the low convergence rate of the large scale modes. Those errors are calculated recursively on coarser discretization grids in order to increase the convergence rate of the solution. The level of the finest grid is $n_g = 1$, corresponds to the main computing grid. For next levels ($n_g > 1$), the spatial resolution scale (in each direction) is divided by 2 between two successive levels.

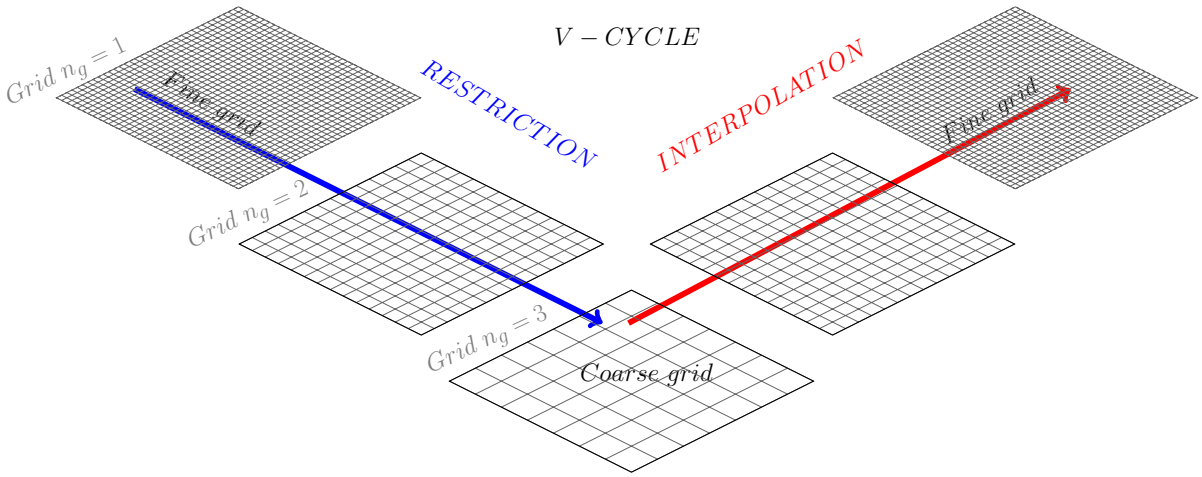

Fig. II.3 Three grid level of a V-cycle in multigrid solver. In each V-cycle, the grid is smoothed and a residual is computed and propagated to the coarser grid. At the coarsest level, a direct solver is applied, and the solution is then iteratively interpolated to finer grids.

The set up of parameters to be used in this method are : maximum number of grids (levels) N_{Grid}, maximal number of V-cycles N_{cycle}, number of iterations performed by the SOR solver during the restriction step itr_{F-C}, on the coarsest grid itr_C or during the interpola-

tion step itr_{C-F} of each V-cycle of the multigrid algorithm (Brandt, 1977). The coefficient of over-relaxation $c_{sor} = 1$ is used, i.e a pure Gauss-Seidel algorithm. More details on multigrid method are provided by Wesseling (1992); Strang (2007).

Lot of types of multigrid methods exist. In our case, as shown in figure (II.3), we used an nV-cycle multigrid method. It is based on two steps :

1. **Restriction** (from the finest to coarsest grid) :
   - We iterate on $A_{n_g}\phi_{n_g} = b_{n_g}$ to reach an approximate solution ϕ_{n_g}. A is the original matrix and b is the source term. During this step, the SOR iterative solver is used with a fixed number of iterations itr_{F-C}.
   - We restrict the residual $r_{n_g} = b_{n_g} - A_{n_g}\phi_{n_g}$ to the coarser grid by

     $$r_{n_g+1} = R_{n_g}^{n_g+1} r_{n_g}$$

     Where $R_{n_g}^{n_g+1}$ is the restriction matrix.

   - We approximate the coarser grid error E_{n_g+1} by solving

     $$A_{n_g+1}E_{n_g+1} = r_{n_g+1}$$

   At the end of this step, we determine on each grid, from the finest to the coarsest an estimation of the error committed on the lower grid level $n_g + 1$. The number of iterations performed with SOR solver that we use on the coarsest grid itr_C is relatively higher than that during the restriction itr_{F-C}.

2. **Interpolation** (from the coarsest to finest grid) :
   - We interpolate E_{n_g+1} back to E_{n_g} on the finer grid

     $$E_{n_g} = I_{n_g+1}^{n_g} E_{n_g+1}$$

     Where $I_{n_g}^{n_g+1}$ is the interpolation matrix
   - Reconstruct the solution on the finer grid from the evaluation of these errors

     $$\phi_{n_g}^* = \phi_{n_g} + E_{n_g}$$

   - We iterate using SOR solver starting from improved solution ($\phi_{n_g}^*$) using a fixed number of iterations itr_{C-F} on

     $$A_{n_g}\phi_{n_g} = r_{n_g+1}$$

We note that the correction of error on finer grid is done by means of a linear interpolation. This choice makes possible to greatly simplify the calculation procedures and brings a substantial gain of computing time. The precision of the solution obtained ϕ_{n_g} is estimated using the convergence criterion fixed on the L_2-norm of the residual. If the criterion is not satisfied, we start again a new V-cycle taking ϕ_{n_g} as initial condition.

b) HYPRE solver

The second method to solve the Poisson equation is to use a high performance preconditioners (HYPRE) library tools (Falgout et al., 2005, 2006), which is an external library of algebraic multigrid algorithms and software for extreme-scale parallel supercomputers. It provides a high performance parallel multigrid preconditioners for both structured and unstructured grid problems. The SMG method is used as preconditioner, it is a parallel Semicoarsening Multigrid Solver for the linear systems. It is a particularly robust method, for more details, see (Falgout and Jones, 2000; Brown et al., 2000; Schaffer, 1998).

II.2.5 Parallelization strategies in SUNFLUIDH code

a) Parallelization API OpenMP

OpenMP (Open Multi-Processing) is an application programming interface (API) firstly introduced in 1997. It supports multi-platform shared memory multiprocessing programming. This method is mainly used to increase the performance of the code by using the multi-threading architecture. We use a fine grain parallelism method which mainly consist in parallelizing the loops and distribute their iterations over multiple threads.

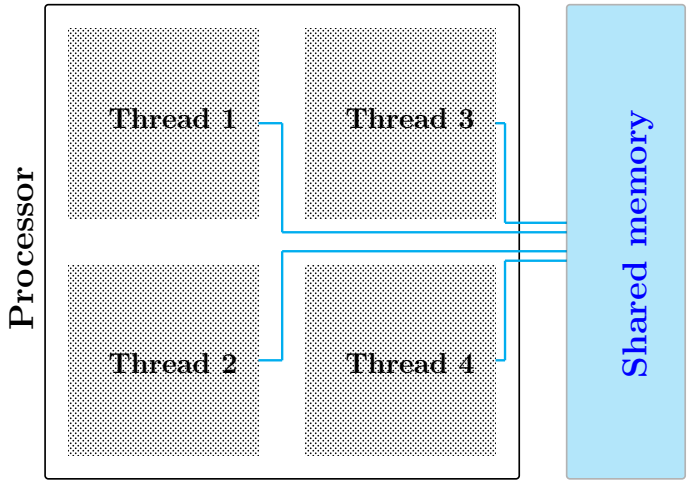

Fig. II.4 Schematic representation of Open Multi-Processing.

b) Parallelization MPI

The parallelization with Message Passing Interface (MPI) (Pacheco, 1996) consists on the decomposition of the computational domain into subdomains (*SD*). Each *SD* is assigned to a processor via an MPI process. Each processor has its own memory and cannot access the memory of other processors. The code can handle with structured mesh grid. A Cartesian topology is used for the decomposition into subdomains. The boundary of a *SD* could be either a part of the border of the computational domain or a communication interface with a neighbor sub-domain.

The mesh on each of the subdomains is defined in the same way as on the complete domain. It consists of inner subdomain cells and ghost cells that serve as overlapping between two neighboring subdomains. They are used for Network communication managed by the MPI implementation. The treatment of domain decomposition with respect to the numerical methods is treated in different ways

- For the calculation of the explicit terms of the equations : at each time step, local ghost cells are updated.
- For solving the Poisson equation using the iterative method SOR : local ghost cells are updated at each iteration.
- For the resolution of tridiagonal systems resulting from the ADI method : we use Schur complement (Schur, 1917; Haynsworth, 1968) coupled with the algorithm of Thomas.

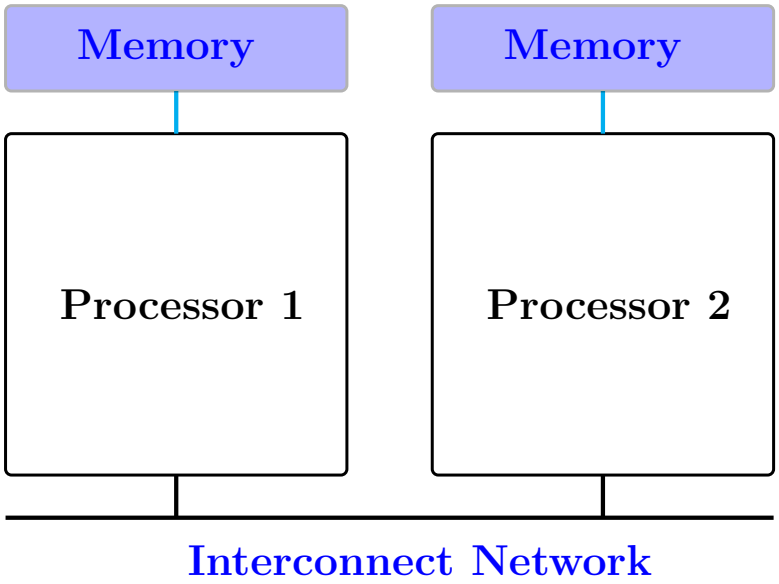

Fig. II.5 Schematic representation of MPI parallelization. In this example, the computational domain is divided among 2 MPI processors

c) Parallelization Hybrid MPI/OpenMP

It is a combination of the two previous parallelization methods. It is based on the addition of a local sub-parallelization of each MPI process. Two level of parallel architectures : i) processor associated with the distributed memory implementation (MPI approach) and ii) threads associated with the shared memory implementation (OpenMP approach).

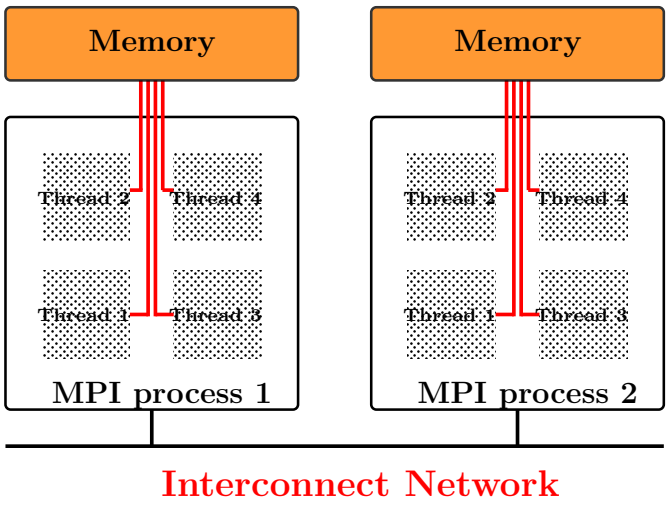

Fig. II.6 Schematic representation of Hybrid parallelization. In this example, the computational domain is divided among 2 MPI processors, each one is decomposed with 4 threads.

In this work, we first opted for MPI parallelization. Recently, developments of the code with the implementation of hybrid parallelization allowed us to perform hybrid parallel computing for the case of highest turbulent flow ($Ra = 10^{10}$).

II.3 Performances

Our simulations are performed on the Turing supercomputer (IBM Blue Gene/Q) at IDRIS (Institute for Development and Resources in Intensive Scientific Computing). It has a massively parallel architecture. This machine is intended for high degree of parallelism in which the available memory is of 1 GiB per processor. To better use Sunfluidh code on Turing, series of tests are performed for a moderate Rayleigh number $Ra = 10^6$ and a Prandtl number $Pr = 4.38$.

We measured the relative speedup (S) which is the ratio between the reference time on the restitution and the time with p processors and the efficiency (E). These measures are related to a reference simulation case of 8 processors,

$$\text{Strong scaling :} \quad S(p) = \frac{t_r(8)}{t_r(p)} \quad E(p) = 8 \times \frac{S(p)}{p} \tag{II.15}$$

$$\text{Weak scaling :} \quad S(p) = \frac{p}{8} \times \frac{t_r(8)}{t_r(p)} \quad E(p) = 8 \times \frac{S(p)}{p} \tag{II.16}$$

p the number of processor and $t(p)$ is the time of restitution for a test case using p processor.

The following tests are performed on a 3D smooth Rayleigh Bénard cavity with an aspect ratio $\Gamma_y = 1/2$. Regular mesh is used in different spatial directions. The HYPRE and I-SOR Poisson equation solvers that are described previously are tested in both strong and weak scaling. For the strong scaling, varied mesh per sub-domain are used and the global mesh size remains constant 256^3, it measures the ability of the code to execute more quickly when the number of processors increases. The total number of operations is kept constant, while the network communications is increased. In the other hand, weak scaling is carried out using a constant mesh size per subdomain 64^3 where the global mesh size increases. It measures the ability of the code to keep its speed of execution. both operations and network communications are increased. Here we mention that we are more concerned with the weak scaling, since in our problematic, an increase of the Ra number requires the increase of global mesh size. In addition, more decomposition of the computational domain will not be fruitful because of the immersed bodies.

Here, we note that the structure of classes on Turing machine is configured to give access for high paralleled computing jobs. There is a limited elapsed time of 30 min for simulations which use less than 16 compute nodes (namely 256 processors), this is why we selected a moderate iteration numbers to make the test possible even for simulations with low processor numbers. The performed time iterations number is 40 for strong scaling cases and 100 for weak scaling whatever the multigrid solver. The number of compute nodes N_{nodes} reserved on Turing machine must be in the order of 2^n, the MPI processes is ranging from 8 to 4096 while the decomposition of the domain varied from low parallelization $(2 \times 2 \times 2)$ to a higher level $(16 \times 16 \times 16)$. We measured the elapsed time t_r (time of restitution in seconds). First, we discuss the tests performed on with HYPRE solver then we will show the obtained scalability results with the internal solver (I-SOR) directly implemented in the code.

II.3.1 Scalability of the HYPRE solver

The multigrid algorithm is managed implicitly by the SMG-HYPRE solver. We only choose a convergence criterion and the number of iteration N_{iter} that we keep constant to make a pure scalability tests.

For the strong scaling, we observe that the t_{wall} time decreases significantly when the number of MPI processes increases (see table [II.1]). However, more than 256 MPI processes leads to decrease the efficiency under 40% as shown in figure (II.7). Additionally, measures of the divergence with the L2-norm show a very satisfying convergence in term of incompressibility constraint (see table [II.2]).

For the weak scaling, we observe in figure (II.8) that the speedup remains very close to ideal cases. Efficiency remains above 70% and a very good scalability is obtained up until 4096 MPI processes. It shows then the robustness of the HYPRE solver to keep its speed of execution. Divergence measured with L2 norm is always less than 10^{-10} which is a very satisfying values in regarding the physical problem (for details see tables [II.3] and [II.4]).

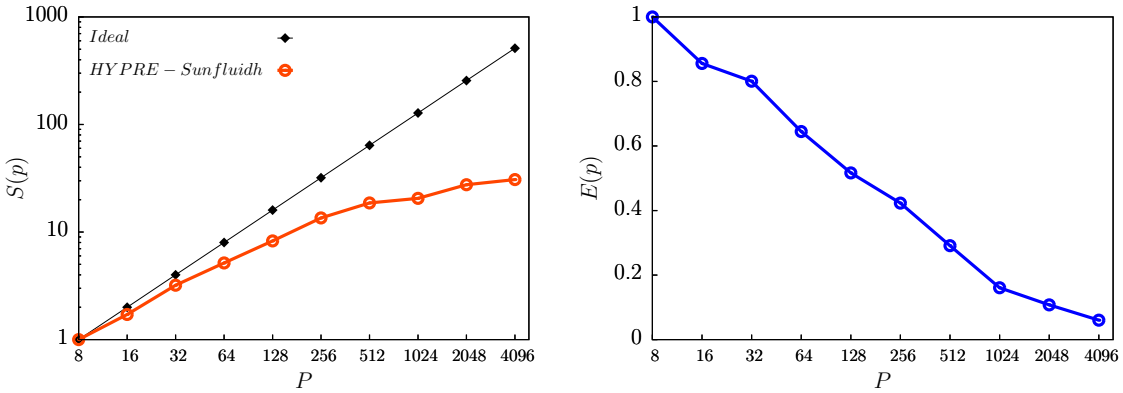

Fig. II.7 Strong scalability of the SMG-HYPRE solver. (a) Speedup and (b) efficiency as a function of processors number. The global mesh size is 256^3.

Table II.1 Strong scaling of HYPRE solver. Parameters : N_{proc}, number of processors ; N_{nodes} number of nodes ; $\frac{N_{proc}}{node}$ number of processor used per node ; N_{SD} number of subdomains in each spatial direction ; $(N_x \times N_y \times N_z)_{SD}$ mesh size used for a subdomain ; t_{wall} performance wall time (s/cell/time-step) ; t_r is the time of restitution.

N_{proc}	Node	$\frac{N_{proc}}{node}$	N_{SD}	$(N_x \times N_y \times N_z)_{SD}$	t_{wall}	t_r (s)	Speedup	Efficiency
8	2	4	$2 \times 2 \times 2$	$128 \times 128 \times 128$	2.626E-06	1762.20	1.00	1.000
16	2	8	$4 \times 2 \times 2$	$64 \times 128 \times 128$	1.534E-06	1029.40	1.71	0.856
32	4	8	$4 \times 2 \times 4$	$64 \times 128 \times 64$	8.199E-07	550.22	3.20	0.801
64	4	16	$4 \times 4 \times 4$	$64 \times 64 \times 64$	5.091E-07	341.65	5.15	0.645
128	8	16	$8 \times 4 \times 4$	$32 \times 64 \times 64$	3.177E-07	213.20	8.26	0.517
256	16	16	$8 \times 4 \times 8$	$32 \times 64 \times 32$	1.940E-07	130.19	13.54	0.423
512	32	16	$8 \times 8 \times 8$	$32 \times 32 \times 32$	1.409E-07	94.55	18.64	0.291
1024	64	16	$16 \times 8 \times 8$	$16 \times 32 \times 32$	1.277E-07	85.69	20.56	0.161
2048	128	16	$16 \times 8 \times 16$	$16 \times 32 \times 16$	9.543E-08	64.04	27.52	0.108
4096	256	16	$16 \times 16 \times 16$	$16 \times 16 \times 16$	8.541E-08	57.31	30.75	0.060

Table II.2 Strong scaling of HYPRE solver. Parameters : N_{iter}, number of iterations performed by the SMG method ; $div - L2$ is the divergence of u^{n+1} measured with L2 norm ; $div - Linf$ the divergence measured with L_{inf} norm.

N_{proc}	N_{iter}	$div - L2$	$div - Linf$
8	6	8.0235568E-10	5.2078959E-08
16	6	8.0235568E-10	5.2078958E-08
32	6	8.0235568E-10	5.2078965E-08
64	6	8.0235568E-10	5.2078965E-08
128	6	8.0235567E-10	5.2078963E-08
256	6	8.0235567E-10	5.2078966E-08
512	6	8.0235568E-10	5.2078963E-08
1024	6	8.0235568E-10	5.2078960E-08
2048	6	8.0235567E-10	5.2078964E-08
4096	6	8.0235567E-10	5.2078957E-08

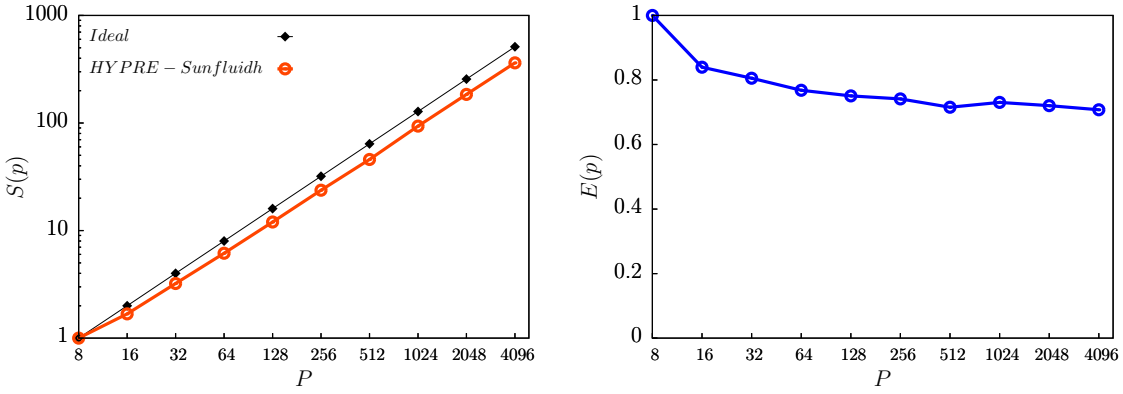

Fig. II.8 Weak scalability of the SMG-HYPRE solver. (a) Speedup and (b) efficiency as a function of processors number.

Table II.3 Weak scaling of HYPRE solver. Parameters : N_{proc}, number of processors ; N_{nodes} number of nodes ; $\frac{N_{proc}}{node}$ number of processor used per node ; N_{SD} number of subdomains in each spatial direction ; t_{wall} performance wall time (s/cell/time-step) ; t_r is the time of restitution.

N_{proc}	Node	$\frac{N_{proc}}{node}$	Dec_D	Global Mesh	t_{wall}	t_r (s)	Speedup	Efficiency
8	1	8	$2 \times 2 \times 2$	$128 \cdot 128 \cdot 128$	3.112E-06	652.63	1.00	1.000
16	1	16	$4 \times 2 \times 2$	$256 \cdot 128 \cdot 128$	1.853E-06	777.20	1.69	0.839
32	2	16	$4 \times 2 \times 4$	$256 \cdot 128 \cdot 256$	9.658E-07	810.17	3.22	0.806
64	4	16	$4 \times 4 \times 4$	$256 \cdot 256 \cdot 256$	5.064E-07	849.60	6.15	0.768
128	8	16	$8 \times 4 \times 4$	$512 \cdot 256 \cdot 256$	2.591E-07	869.40	12.01	0.751
256	16	16	$8 \times 4 \times 8$	$512 \cdot 256 \cdot 512$	1.312E-07	880.47	23.72	0.741
512	32	16	$8 \times 8 \times 8$	$512 \cdot 512 \cdot 512$	6.796E-08	912.14	45.79	0.715
1024	64	16	$16 \times 8 \times 8$	$1024 \cdot 512 \cdot 512$	3.290E-08	893.22	93.52	0.731
2048	128	16	$16 \times 8 \times 16$	$1024 \cdot 512 \cdot 1024$	1.687E-08	905.70	184.47	0.721
4096	256	16	$16 \times 16 \times 16$	$1024 \cdot 1024 \cdot 1024$	8.589E-09	922.24	362.32	0.708

Table II.4 Weak scaling of HYPRE solver. Parameters : N_{iter}, number of iterations ; $div-L2$ is the divergence of u^{n+1} measured with L2 norm ; $div - Linf$ the divergence measured with L_{inf} norm.

N_{proc}	N_{iter}	$div - L2$	$div - Linf$
8	6	6.3444156E-10	2.0521171E-08
16	6	5.6416210E-10	3.7842240E-08
32	6	6.1898965E-10	3.9791835E-08
64	6	1.6866189E-09	2.8906462E-07
128	6	1.2649190E-09	6.5759813E-08
256	6	2.1369029E-10	1.8275432E-08
512	6	8.1276509E-11	8.2439632E-09
1024	6	6.1486271E-11	9.6157582E-09
2048	6	3.5608864E-11	7.9691636E-09
4096	6	3.7939101E-11	8.3110186E-09

II.3.2 Scalability of the I-SOR solver

We make the same scalability tests that are performed for the HYPRE solver. However, the set up of parameters for the I-SOR solver is different. Indeed, we had to choose manually the number of grids N_{Grid}, maximal number of V-cycles N_{cycle}, number of iterations performed by the I-SOR solver during the restriction step itr_{F-C}, on the coarsest grid itr_C or during the interpolation step itr_{C-F} of each V-cycle of the multigrid method. A coefficient of over-relaxation $\beta_r = 1$ is used for the following test cases. Here, we mention that two types of tests are effectuate : we called "pure scalability" the tests of I-SOR solver regardless the incompressibility constraint. In the second tests, we look for convergence in term of satisfying the incompressibility constraint. It will be our basis for a future use of the I-SOR solver with immersed boundary method.

a) Strong scaling

First, we made pure scalability take by keeping the same I-SOR multigrid solver parameters. We used : $N_{Grid} = 4$, $N_{cycle} = 5$, $itr_{F-C} = 3$, $itr_C = 15$ and $itr_{C-F} = 20$. As we can see in figure (II.9), the solver shows a good scalability until 1024 MPI processes. More than 512 MPI processes leads to decrease the efficiency under 40% (see details in table [II.5]).

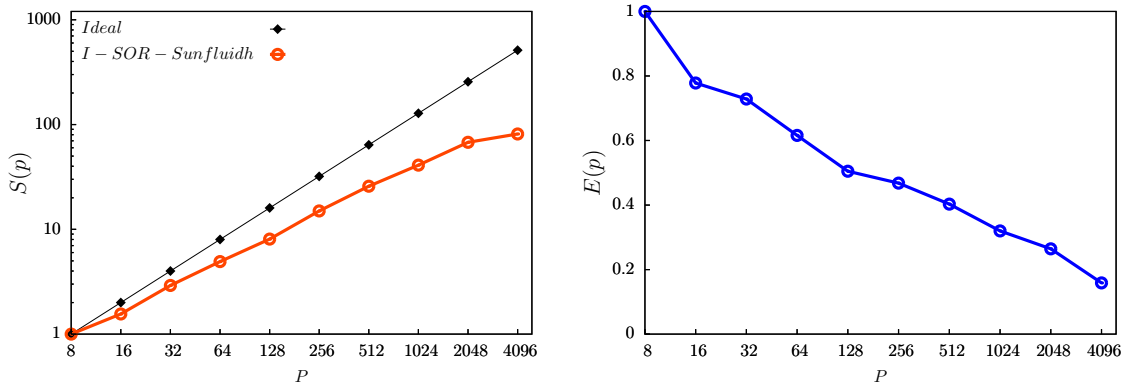

Fig. II.9 Pure scalability tests. Strong scaling of the I-SOR solver. (a) Speedup and (b) efficiency as a function of processors number.

Table II.5 Pure scalability : strong scaling of I-SOR solver. Parameters : N_{proc}, number of processors ; N_{nodes} number of nodes ; $\frac{N_{proc}}{node}$ number of processor used per node ; N_{SD} number of subdomains ; $(N_x \times N_y \times N_z)_{SD}$ mesh size used for a subdomain ; t_r time of restitution.

N_{proc}	N_{nodes}	$\frac{N_{proc}}{node}$	Dec_D	$(N_x \times N_y \times N_z)_{SD}$	t_{wall}	t_r (s)	Speedup	Efficiency
8	1	8	$2 \times 2 \times 2$	$128 \cdot 128 \cdot 128$	1.849E-06	1240.82	1.00	1.00
16	1	16	$4 \times 2 \times 2$	$64 \cdot 128 \cdot 128$	1.187E-06	797.13	1.56	0.78
32	2	16	$4 \times 2 \times 4$	$64 \cdot 128 \cdot 64$	6.345E-07	425.81	2.91	0.73
64	4	16	$4 \times 4 \times 4$	$64 \cdot 64 \cdot 64$	3.754E-07	251.93	4.93	0.62
128	8	16	$8 \times 4 \times 4$	$32 \cdot 64 \cdot 64$	2.290E-07	153.65	8.08	0.50
256	16	16	$8 \times 4 \times 8$	$32 \cdot 64 \cdot 32$	1.235E-07	82.87	15.97	0.47
512	32	16	$8 \times 8 \times 8$	$32 \cdot 32 \cdot 32$	7.170E-08	48.12	25.79	0.40
1024	64	16	$16 \times 8 \times 8$	$16 \cdot 32 \cdot 32$	4.515E-08	30.30	40.95	0.32
2048	128	16	$16 \times 8 \times 16$	$16 \cdot 32 \cdot 16$	2.731E-08	18.33	67.69	0.26
4096	256	16	$16 \times 16 \times 16$	$16 \cdot 16 \cdot 16$	2.275E-08	15.27	81.26	0.16

b) Strong scaling with respect of incompressibility constraint

We aim to introduce immersed bodies for the future works. This will have an impact on the way we use the I-SOR solver. More decomposition of the computational domain leads to use reduced grid number in multigrid algorithm. Through this tests, we look for a compromise between a good scalability and acceptable convergence in terms of respecting the incompressibility constraint.

For the strong scaling, we observe in figure (II.10) that the speedup is influenced by the number of grid level used in the multigrid method. Actually, more we decompose the computational domain, less are the available grids to perform a V-cycle. Consequently, more cycle and especially more iterations on the coarsest grid and during the interpolation step are needed to obtain a satisfying convergence (details are in table [II.6]).

The dependence on grid numbers could be seen clearly on the efficiency. It remains almost constant for the same grid number, otherwise, it changes significantly. We can see in table (II.7) that a mesh size lower than 64^3 per subdomain is not adequate for the code's performances, convergence becomes very hard. In general, the solver I-SOR shows a good scalability when it comes to use large number of grids in the multigrid algorithm which means more refinement of the mesh inside the subdomain.

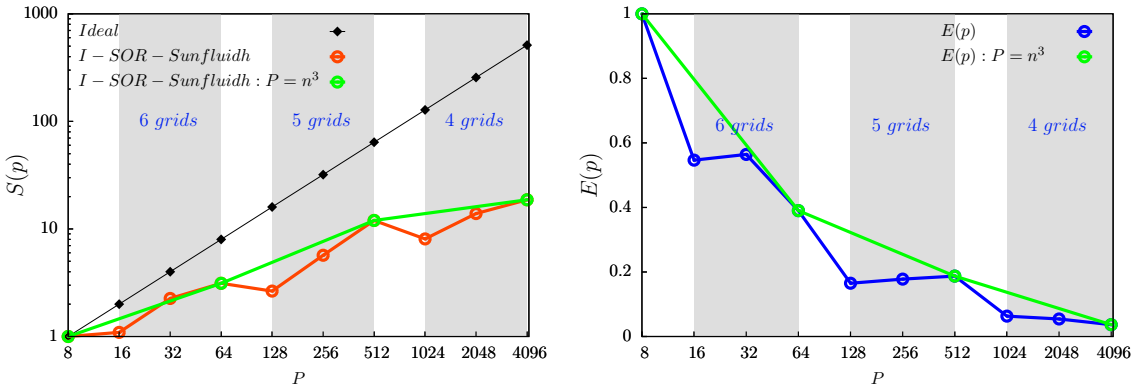

(a) (b)

Fig. II.10 Strong scalability of the I-SOR solver. (a) Speedup and (b) efficiency as a function of processors number. Green line correspond to homogeneous domain decomposition of a type $P = (2^n)^3$ with similar grid number in all space direction.

Table II.6 Strong scaling of ISOR solver. Parameters : N_{proc}, number of processors ; N_{nodes} number of nodes ; $\frac{N_{proc}}{node}$ number of processor used per node ; N_{SD} number of subdomains in each spatial direction ; $(N_x \times N_y \times N_z)_{SD}$ mesh size used for a subdomain ; t_{wall} performance wall time (s/cell/time-step) ; t_r is the time of restitution.

N_{proc}	N_{nodes}	$\frac{N_{proc}}{node}$	Dec_D	$(N_x \times N_y \times N_z)_{SD}$	t_{wall}	t_r (s)	Speedup	Efficiency
8	1	8	$2 \times 2 \times 2$	$128 \cdot 128 \cdot 128$	1.679E-06	1263.89	1.00	1.000
16	1	16	$4 \times 2 \times 2$	$64 \cdot 128 \cdot 128$	1.723E-06	1156.29	1.09	0.547
32	2	16	$4 \times 2 \times 4$	$64 \cdot 128 \cdot 64$	8.343E-07	559.89	2.26	0.564
64	4	16	$4 \times 4 \times 4$	$64 \cdot 64 \cdot 64$	6.036E-07	405.07	3.12	0.390
128	8	16	$8 \times 4 \times 4$	$32 \cdot 64 \cdot 64$	7.129E-07	478.42	2.64	0.165
256	16	16	$8 \times 4 \times 8$	$32 \cdot 64 \cdot 32$	3.311E-07	222.20	5.69	0.178
512	32	16	$8 \times 8 \times 8$	$32 \cdot 32 \cdot 32$	1.571E-07	105.43	11.99	0.187
1024	64	16	$16 \times 8 \times 8$	$16 \cdot 32 \cdot 32$	2.331E-07	156.43	8.08	0.063
2048	128	16	$16 \times 8 \times 16$	$16 \cdot 32 \cdot 16$	1.354E-07	90.87	13.91	0.054
4096	256	16	$16 \times 16 \times 16$	$16 \cdot 16 \cdot 16$	1.008E-07	67.65	18.68	0.037

Table II.7 Strong scaling of ISOR solver. Parameters : N_{Grid}, number of grid ; N_{cycle} number of cycles ; itr_{F-C} number of iterations from fine to coarse grid ; itr_C iteration on coarsest grid ; itr_{C-F} number of iterations from coarse to fine grid. $div - L2$ is the divergence of u^{n+1} measured with L2 norm ; $div - Linf$ the divergence measured with L_{inf} norm.

N_{proc}	N_{Grid}	N_{cycle}	itr_{F-C}	itr_C	itr_{C-F}	$div - L2$	$div - Linf$
8	7	5	3	20	15	5.7218662E-13	3.5833558E-12
16	6	6	3	25	20	2.9251854E-09	6.0757239E-09
32	6	6	3	25	20	2.9251854E-09	6.0757216E-09
64	6	6	3	25	20	2.9251854E-09	6.0757203E-09
128	5	6	5	75	45	3.7829788E-09	7.7050833E-09
256	5	6	5	75	45	3.7829788E-09	7.7050771E-09
512	5	6	5	75	45	3.7829788E-09	7.7050798E-09
1024	4	10	20	95	65	6.0538819E-07	1.7215731E-06
2048	4	10	20	95	65	6.0538819E-07	1.7215731E-06
4096	4	10	20	95	65	6.0538819E-07	1.7215731E-06

c) Weak scaling

By keeping the same set up for the I-SOR multigrid solver : $N_{Grid} = 4$, $N_{cycle} = 5$, $itr_{F-C} = 3$, $itr_C = 15$ and $itr_{C-F} = 20$. We test the pure scalability according to weak scaling. As we can see in figure (II.11), the solver shows an excellent scalability up until 4096 MPI processes. The code keep well its speed of execution with an efficiency around 70% (see details in table [II.8]).

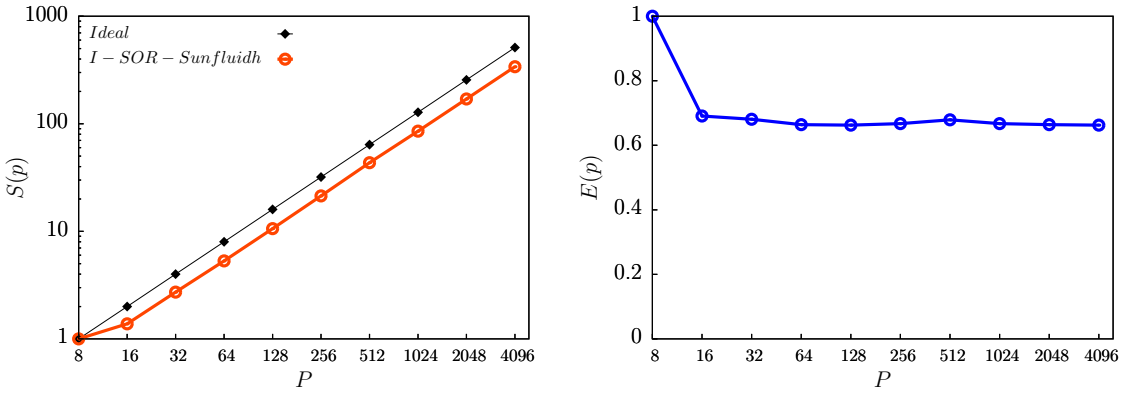

(a) (b)

Fig. II.11 Pure scalability tests. Weak scaling of the I-SOR solver. (a) Speedup and (b) efficiency as a function of processors number.

Table II.8 Pure scalability : weak scaling of ISOR solver. Parameters : N_{proc}, number of processors ; N_{nodes} number of nodes ; $\frac{N_{proc}}{node}$ number of processor used per node ; N_{SD} number of subdomains in each spatial direction ; t_{wall} performance wall time (s/cell/time-step) ; t_r is the time of restitution.

N_{proc}	N_{nodes}	$\frac{N_{proc}}{node}$	Dec_D	Global Mesh	t_{wall}	t_r (s)	Speedup	Efficiency
8	1	8	$2 \times 2 \times 2$	$128 \cdot 128 \cdot 128$	2.291E-06	480.53	1.00	1.00
16	1	16	$4 \times 2 \times 2$	$256 \cdot 128 \cdot 128$	1.610E-06	675.38	1.38	0.69
32	2	16	$4 \times 2 \times 4$	$256 \cdot 128 \cdot 256$	8.113E-07	680.57	2.72	0.68
64	4	16	$4 \times 4 \times 4$	$256 \cdot 256 \cdot 256$	4.147E-07	695.73	5.31	0.66
128	8	16	$8 \times 4 \times 4$	$512 \cdot 256 \cdot 256$	2.076E-07	696.69	10.60	0.66
256	16	16	$8 \times 4 \times 8$	$512 \cdot 256 \cdot 512$	1.052E-07	706.04	21.35	0.67
512	32	16	$8 \times 8 \times 8$	$512 \cdot 512 \cdot 512$	5.273E-08	707.81	43.45	0.68
1024	64	16	$16 \times 8 \times 8$	$1024 \cdot 512 \cdot 512$	2.683E-08	720.30	85.39	0.67
2048	128	16	$16 \times 8 \times 16$	$1024 \cdot 512 \cdot 1024$	1.348E-08	723.73	169.97	0.66
4096	256	16	$16 \times 16 \times 16$	$1024 \cdot 1024 \cdot 1024$	6.754E-09	725.26	339.23	0.66

d) Weak scaling with respect of incompressibility constraint

The goal is to find a compromise between convergence with respect of incompressibility constraint and a good performance. We fixed the local mesh size at 64^3, then, the number of grid levels is constant, only the cycle number and iterations number during restriction and interpolation steps, eventually on the coarsest grid are to be changed to obtain a satisfying convergence (see table (II.10) fore more details).

We observe in figure (II.12) that the speedup is good comparing to ideal cases. Efficiency drops lower than 30% if we use more than 512 MPI processes (see also table (II.9)). This behavior is expected because if we combine the local coarsest grid in each direction, we obtained a finner global coarsest grid, thence, convergence need more iterations and this is what affect the performance. Efficiency drops when at least the number of subdomain increases in a given direction. From this point of view, we suggest a decomposition of the computational domain in the order of $8 \times 8 \times 8$ to obtain an efficiency up to 40%.

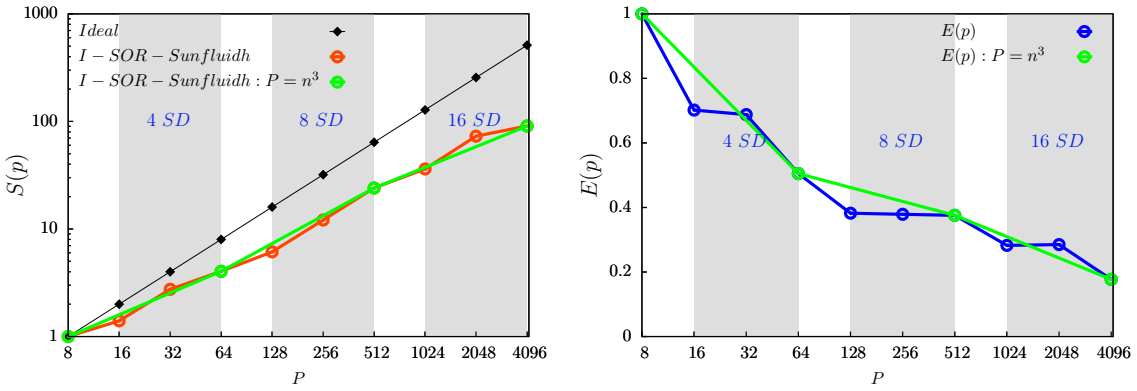

Fig. II.12 Weak scalability of the I-SOR solver. (a) Speedup and (b) efficiency as a function of processors number. Green line correspond to homogeneous domain decomposition of a type $P = (2^n)^3$ with similar grid number in all space direction. A decomposition is made with 4 SD, 8 SD, 16 SD subdomain at least in one given direction.

SMG-HYPRE versus I-SOR solvers

- **SMG-HYPRE** : for the strong scaling, a good performance is obtained for a mesh size 64^3 per subdomain. The efficiency is up to 60%. For the weak scaling, a very good performance is obtained with an efficiency around 80% for up to 4096 process.
- **I-SOR** : regarding the strong scaling (for pure scalability), good performance is obtained when using a mesh size 64^3 per subdomain. Likewise, for the week scaling, it keeps an efficiency around 70% for up to 4096 processors.
- The wall times founded for both HYPRE and I-SOR (with pure scaling) slovers are very comparable. Their performances are similar.
- Regarding the incompressibility constraint : (i) for the strong scaling, the performance

Table II.9 Weak scaling of ISOR solver. Parameters : N_{proc}, number of processors ; N_{nodes} number of nodes ; $\frac{N_{proc}}{node}$ number of processor used per node ; N_{SD} number of subdomains in each spatial direction ; t_{wall} performance wall time (s/cell/time-step) ; t_r is the time of restitution.

N_{proc}	N_{nodes}	$\frac{N_{proc}}{node}$	Dec_D	Global Mesh	t_{wall}	t_r (s)	Speedup	Efficiency
8	1	8	$2 \times 2 \times 2$	$128 \cdot 128 \cdot 128$	2.092E-06	438.63	1.00	1.000
16	1	16	$4 \times 2 \times 2$	$256 \cdot 128 \cdot 128$	1.490E-06	625.01	1.40	0.702
32	2	16	$4 \times 2 \times 4$	$256 \cdot 128 \cdot 256$	7.601E-07	637.66	2.75	0.688
64	4	16	$4 \times 4 \times 4$	$256 \cdot 256 \cdot 256$	5.177E-07	868.56	4.04	0.505
128	8	16	$8 \times 4 \times 4$	$512 \cdot 256 \cdot 256$	2.611E-07	876.11	6.12	0.382
256	16	16	$8 \times 4 \times 8$	$512 \cdot 256 \cdot 512$	1.124E-07	754.30	12.12	0.379
512	32	16	$8 \times 8 \times 8$	$512 \cdot 512 \cdot 512$	8.699E-08	1167.56	24.04	0.376
1024	64	16	$16 \times 8 \times 8$	$1024 \cdot 512 \cdot 512$	5.785E-08	1552.90	36.15	0.283
2048	128	16	$16 \times 8 \times 16$	$1024 \cdot 512 \cdot 1024$	2.868E-08	1539.75	72.93	0.285
4096	256	16	$16 \times 16 \times 16$	$1024 \cdot 1024 \cdot 1024$	2.308E-08	2478.20	90.62	0.177

Table II.10 Weak scaling of ISOR solver. Parameters : N_{Grid}, number of grid ; N_{cycle} number of cycles ; itr_{F-C} number of iterations from fine to coarse grid ; itr_C iteration on coarsest grid ; itr_{C-F} number of iterations from coarse to fine grid. $div - L2$ is the divergence of u^{n+1} measured with L2 norm ; $div - Linf$ the divergence measured with L_{inf} norm.

N_{proc}	N_{Grid}	N_{cycle}	itr_{F-C}	itr_C	itr_{C-F}	$div - L2$	$div - Linf$
8	6	4	3	20	15	1.3411084E-11	9.3945962E-11
16	6	4	3	20	15	5.7525534E-11	4.3229461E-10
32	6	4	3	20	15	4.3274937E-10	9.0622931E-10
64	6	5	3	25	20	8.1631667E-09	1.6960520E-08
128	6	5	3	25	20	3.3400365E-09	7.0056967E-09
256	6	6	3	30	25	9.4428353E-10	2.3578709E-09
512	6	6	3	30	25	7.0695860E-07	1.4598972E-06
1024	6	6	5	50	35	2.9709250E-07	6.1852577E-07
2048	6	6	5	50	35	9.8570845E-07	1.9762036E-06
4096	6	8	7	75	45	9.1519032E-07	1.8423253E-06

of the I-SOR solver are reduced especially when we decompose the computational domain more than 4 time in one direction. This effect is expected since the available grids for multigrid algorithm is also reduced, thus reaching good convergence will be hard. (ii) For the weak scaling, the wall time is increased especially for higher mesh size bigger than 512^3 where the efficiency drops to 20% because of communication time between MPI process. From this point of view, using the SMG-HYPRE solver gives a better convergence and keeps a good performance.

- **Note** : for the simulation of rough RB cavity presented in next chapter (§ *III*), problems of compatibility occur between the SMG-HYPRE solver and the immersed boundary method for $Ra \geqslant 5 \times 10^7$. Therefore, we use instead the I-SOR solver.

II.4 Validation cases

II.4.1 case 1 : Rayleigh Bénard with smooth boundaries

A rectangular Rayleigh−Bénard cavity with smooth boundaries is used to validate the Sunfluidh code. The cavity has a length W, a height H and a depth D characterized by an aspect ratio $\Gamma_x = L/H$ and $\Gamma_y = D/H$. Our benchmark stands on numerical studies carried by Wagner and Shishkina (2013) and Kaczorowski et al. (2013, 2014). Concluding remarks from (Shishkina et al., 2010) have been taken into consideration to estimate the grid resolution requirement for boundary layers resolution.

In this case, we perform DNS for two Prandtl numbers. First, by using Pr = 0.786 with an aspect ratio Γ_y ranging from 1/4 to 1/2 for a Ra number ranging from 10^5 to 3×10^6. Secondly, using $Pr = 4.38$ with fixed aspect ratio $\Gamma_y = 1/2$ for Ra number ranging from 10^5 to 5×10^7. Boundary conditions are those of a confined box ; impermeability condition is used for all walls while the side ones are set to be adiabatic. Dirichlet condition is imposed for lower and upper surfaces which are considered isothermal. The table [*II*.11] summarizes the different input parameters of our simulations.

Table II.11 Parameters : Pr, Prandtl number ; Ra, Rayleigh number ; Γ_y, aspect ratio ; Δt, time step ; $N_x \times N_y \times N_z$ number of grid points in spacial directions ; $(N_x \times N_y \times N_z)^{ref}$ number of grid points in spacial directions used in literature ; n_θ, number of grid points used in the thermal boundary layer ; h_z, first grid line in the vertical direction e_z ; τ, amount of time unit used for average unsteady cases ; n_θ^{ref}, n_u^{ref} numbers of grid points used in thermal and viscous boundary layers (Wagner and Shishkina, 2013) and (Kaczorowski et al., 2014).

Pr	Ra	Γ_y	Δt	$N_x \times N_y \times N_z$	n_θ	h_z	τ	$(N_x \times N_y \times N_z)^{ref}$	n_θ^{ref}	n_u^{ref}
	10^5	1/4	–	$96 \times 32 \times 96$	21	5×10^{-3}	–	$64 \times 32 \times 64$	14	13
	10^6	1/3	$1.85.10^{-2}$	$96 \times 64 \times 96$	25	10^{-4}	500	$96 \times 32 \times 96$	16	15
	10^5	1/2	–	$96 \times 32 \times 96$	25	10^{-3}	–	$64 \times 64 \times 64$	12	11
0.786	3.10^5	1/2	$2.65.10^{-2}$	$96 \times 64 \times 96$	32	10^{-4}	305	$96 \times 64 \times 96$	20	19
	10^6	1/2	$2.3.10^{-2}$	$96 \times 64 \times 96$	25	10^{-4}	700	$96 \times 64 \times 96$	16	15
	2.10^6	1/2	$1.65.10^{-2}$	$96 \times 64 \times 96$	25	10^{-4}	1180	$96 \times 64 \times 96$	14	13
	3.10^6	1/2	$7.5.10^{-3}$	$192 \times 128 \times 192$	26	10^{-4}	450	$192 \times 128 \times 192$	17	16
	10^6	1/2	$1.4.10^{-2}$	$192 \times 96 \times 192$	39	5.10^{-4}	420	–	–	–
	5.10^6	1/2	6.10^{-3}	$192 \times 96 \times 192$	34	5.10^{-4}	350	–	–	–
4.38	10^7	1/2	5.10^{-3}	$192 \times 96 \times 192$	31	10^{-4}	365	$178 \times 90 \times 194$	14	21
	2.10^7	1/2	5.10^{-3}	$192 \times 96 \times 192$	28	10^{-4}	450	–	–	–
	5.10^7	1/2	$3.5.10^{-3}$	$192 \times 96 \times 192$	24	10^{-4}	350	–	–	–

We compare in table [II.12] different Nusselt numbers (definitions are given in section (§ I.2.6)). The convergence between all Nusselt numbers is a criterion to verify the global convergence in the system. The results show a good agreement with (Wagner and Shishkina, 2013) performed for a Pr = 0.786, for different Rayleigh numbers ranging from 10^5 to 3×10^6. It is also consistent with Kaczorowski et al. (2014) result for the case of $Pr = 4.38$ and $Ra = 10^7$ where all the Nusselt have converged roughly to the same value.

Table II.12 Nusselt numbers : Nu_{top} at the top ; Nu_{bot} at the bottom ; Nu_{mid} at the median plane ; Nu_{bulk}, in the cavity ; Nu_{ϵ_u} of viscous dissipation, Nu_{ϵ_θ} of thermal dissipation and Nu_{ref}, reference Nusselt number from (Wagner and Shishkina, 2013; Kaczorowski et al., 2014) ; γ, the standard deviation.

Pr	Ra	Γ_y	Nu_{top}	Nu_{bot}	Nu_{mid}	Nu_{bulk}	Nu_{ϵ_u}	Nu_{ϵ_θ}	γ	Nu_{ref}
	10^5	1/4	2.997	2.997	2.997	2.997	2.998	2.984	0.005	2.99
	10^6	1/3	8.432	8.432	8.431	8.431	8.436	8.441	0.003	8.44 ± 0.01
	10^5	1/2	3.641	3.641	3.641	3.641	3.629	3.631	0.005	3.63
0.786	3×10^5	1/2	5.754	5.754	5.753	5.753	5.755	5.760	0.002	5.73 ± 0.01
	10^6	1/2	8.771	8.772	8.777	8.775	8.739	8.776	0.013	8.74 ± 0.01
	2×10^6	1/2	10.795	10.795	10.794	10.795	10.854	10.800	0.021	10.78 ± 0.02
	3×10^6	1/2	11.759	11.755	11.774	11.770	11.612	11.778	0.058	11.69 ± 0.10
	10^6	1/2	8.824	8.824	8.825	8.824	8.479	8.829	0.054	–
	5×10^6	1/2	12.815	12.814	12.834	12.833	12.605	12.821	0.081	–
4.38	10^7	1/2	15.828	15.829	15.823	15.828	15.814	15.830	0.005	15.9
	2×10^7	1/2	19.639	19.611	19.617	19.608	19.662	19.660	0.022	–
	5×10^7	1/2	26.035	26.037	26.069	26.056	26.301	26.060	0.093	–

The transport of heat in RBC at a stationary regime which corresponds to $Ra = 10^5$ and $Pr = 0.786$ is illustrated in figure (II.13) for two aspect ratios. The heat is being transported especially in the corners of the cavity and carrying the hot fluid upwards and cold fluid downwards. In those cases, only one convection roll filled the cell. For $Pr = 0.786$, the flow becomes unsteady at $Ra = 3\times10^5$.

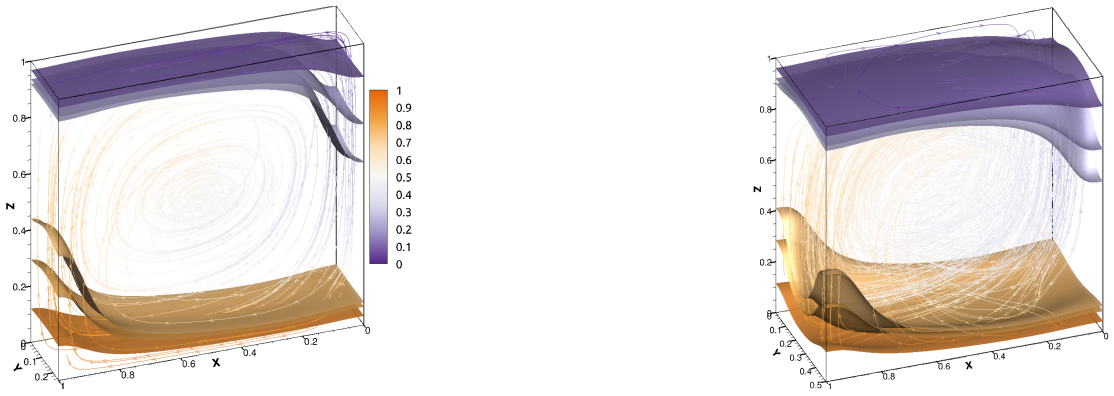

(a) $\Gamma_y = 1/4$ (b) $\Gamma_y = 1/2$

Fig. II.13 Isosurfaces of instantaneous temperature and velocity streamlines for $Ra = 10^5$ and $Pr = 0.786$ for two different aspect ratios.

We construct a second validation criterion based on spectral analysis of the Nusselt number time series through a fast Fourier transformation. The idea is to compare the frequency spectrum for a specific test case using similar numerical simulation parameters of Wagner and Shishkina (2013), which are a Rayleigh number 10^6, a Prandtl number 0.786 and an aspect ratio $\Gamma_y = 1/3$. The flow is this case is quasi periodic. The figure (II.14) presents the time evolution of Nu_{bot} and Nu_{top} with the corresponding frequency spectrum. Results are very consistent with reference data. Indeed, the dominant frequency evaluated by Sunfluidh code is $f = 0.121$. It is the same frequency found by Wagner and Shishkina (2013).

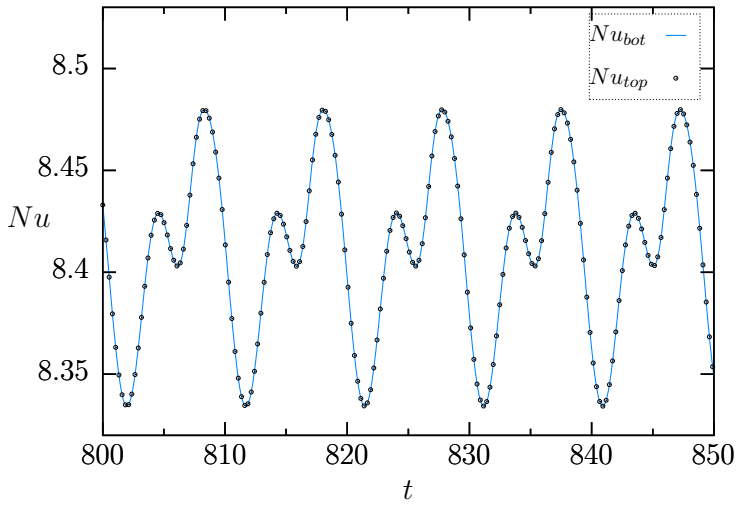

(a)

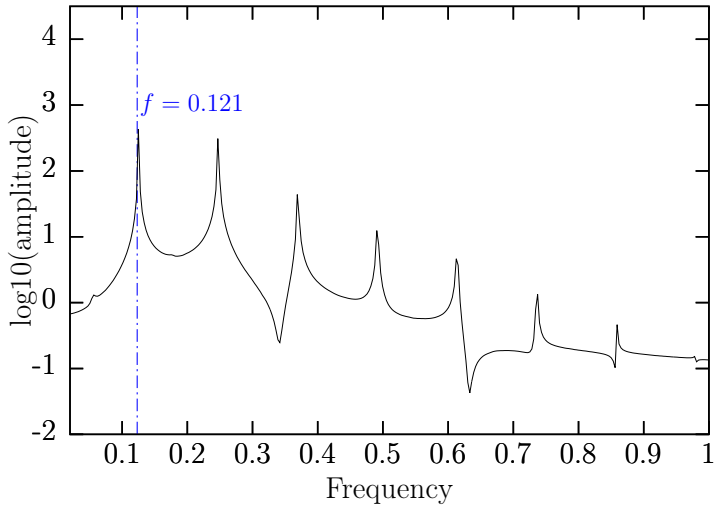

(b)

Fig. II.14 Sunfluidh results : (a) Time series of Nu_{bot} and Nu_{top} for $Ra = 10^6$, $Pr = 0.786$ and $\Gamma_y = 1/3$, (b) corresponding frequency spectra.

II.4.2 case 2 : 2D Rough Rayleigh Bénard cell

This test case is conducted to validate the capability of Sunfluidh code to deal with immersed solid boundaries in the computing domain. A benchmark based on the comparison with two dimensional numerical simulations is done for three configurations similar to Shishkina and Wagner (2011), i.e a square RB cell with rough elements. We use the same parameters with Rayleigh and Prandtl numbers ($Ra = 10^8, \mathrm{Pr} = 1$). The computational mesh used is 600×400. A set of four rectangular elements is used on both top and bottom plates equidistantly distributed. We use the classic boundary conditions, constant temperatures on hot and cold plate including immersed roughnesses where sidewalls are adiabatic.

Three configuration are considered. We change the height H_p and the width D_p of the roughness elements (see figure (II.15)). The geometrical parameters are listed for the 4 cases in table [II.13] comparable with Shishkina and Wagner (2011) and the classic RBC as reference. The response of the system is quantified via the Nusselt number Nu.

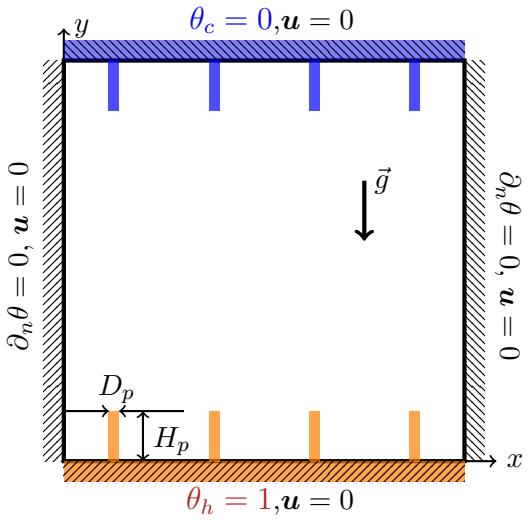

Fig. II.15 Sketch of the 2D convection cell with immersed solids equidistantly distributed with typical height H_p and width d_p, located at the hot and cold plates. The height and width of the cell are H and D, resp.

Table II.13 Geometrical parameters of the roughness elements of a height H_p and width D_p. The 2D cell has a height H and a width D. Nu are Nusselt numbers obtained by Sunfluidh code (definitions are given in section (§ I.2.6)). Nu^{ref} reference data from Shishkina and Wagner (2011). Case S_0 is the classical smooth RBC.

Case	D_p/D	H_p/H	Nu_{mid}	Nu_{bulk}	Nu_{ϵ_u}	Nu_{ϵ_θ}	Nu	$err_r\%$	Nu^{ref}
S_0	–	–	23.57	23.60	23.69	23.19	23.51 ± 0.19	0.82	23.59
1	0.025	0.125	26.59	26.70	26.58	26.10	26.49 ± 0.23	0.87	26.40
2	0.125	0.025	22.88	22.40	22.73	22.79	22.70 ± 0.18	0.81	22.56
3	0.125	0.125	23.18	22.90	23.25	23.31	23.16 ± 0.16	0.68	23.05

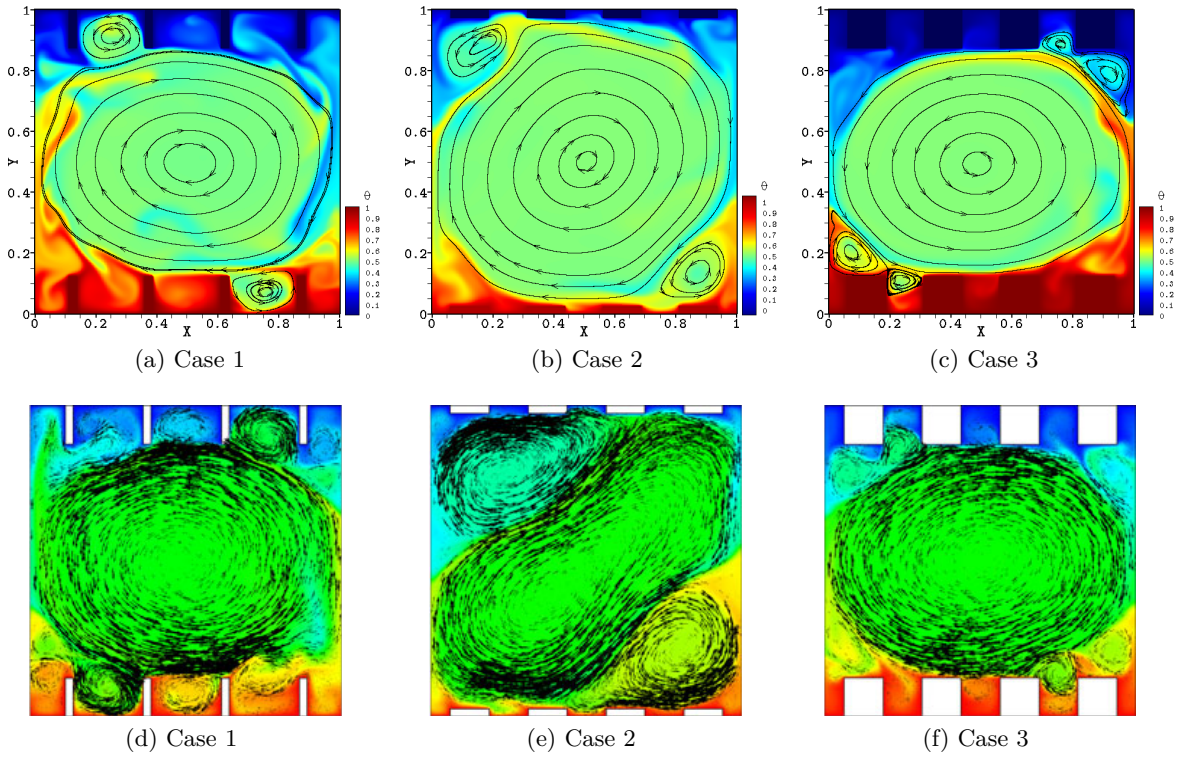

(a) Case 1 (b) Case 2 (c) Case 3

(d) Case 1 (e) Case 2 (f) Case 3

Fig. II.16 Instantaneous temperature fields with velocity streamline for $Ra = 10^8$, Pr = 1 and roughness types (a,d) $H_p/H = 0.125, D_p/D = 0.025$ (b,e) $H_p/H = 0.025, D_p/D = 0.125$ and (c,f) $H_p/H = 0.125, D_p/D = 0.125$. (a,b,c) 2D DNS performed with Sunfluidh code. (d,e,f) Reference 2D numerical simulation conducted by Shishkina and Wagner (2011).

A rapid comparison between the present DNS results and reference data shows a strong agreement about the effect of roughness elements on the system response. Actually, we obtained very close Nusselt numbers to those of Shishkina and Wagner (2011) data. The relative error is less than 1%.

In figure (II.16) we present a qualitative comparison with available results from Shishkina and Wagner (2011) for the three configurations considered. The instantaneous temperature field with superimposed velocity streamlines is plotted for each case. We can observe a similar temperature distribution (with respect to the direction of rotation in the bulk flow). A large scale circulation is formed in all cases in the regions between the upper edges of the heated roughness elements and the lower edges of the cooled elements.

In case 1, a secondary rolls appear mainly in between roughness. Clearly, two rolls are positioned diagonally opposite each other. The case 2 is similar to a classical RBC, two secondary rolls formed in the corners. In case 3, the large scale circulation in maintained in the bulk, small secondary eddies appear from time to time near the corners.

Through this global visualization of the flow, we validate the implementation of the immersed boundary method. The thermal and kinetic boundary conditions relative to the wall-roughness are successfully respected.

In figure (II.17), we plot the time average of temperature field for the three cases. We may identify the same observations as for instantaneous fields. The point is to validate our method by comparing the mean temperature profiles in the vertical direction at $x/D = 0.5$, in between solids. This constitutes another criterion to verify the robustness of the immersed boundary method. As shown in figure (II.18), excellent agreement is obtained. The mean temperature profiles are nicely superposed with the reference data.

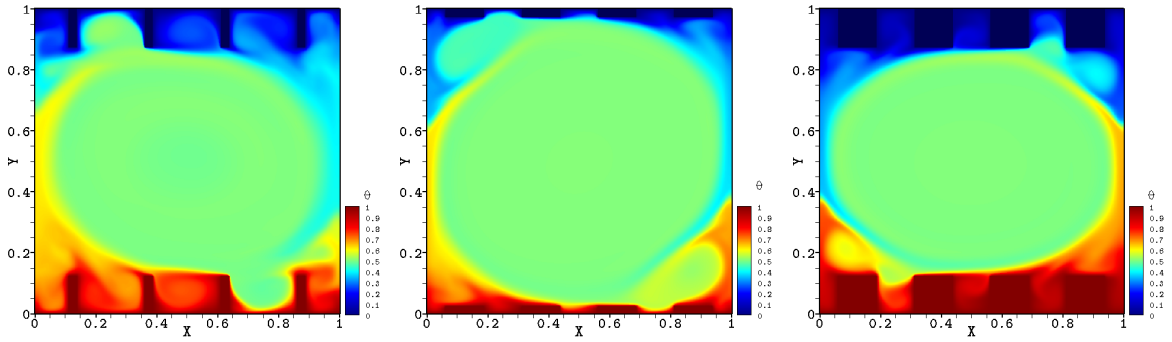

(a) Case 1 (b) Case 2 (c) Case 3

Fig. II.17 Time average temperature fields for $Ra = 10^8$, Pr $= 1$.

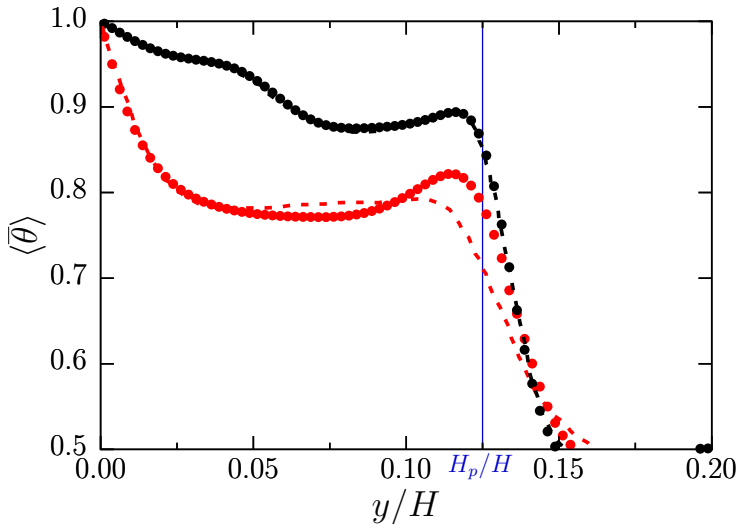

Fig. II.18 Time averaged temperature profiles in the vertical direction at the center $x/D = 0.5$ of the square cell near the heated horizontal plate for Pr $= 1$ and $Ra = 10^8$. Red : case 1. Black : case 3. Full circles : DNS results of the Sunfluidh code. The dashed lines : reference DNS data from Shishkina and Wagner (2011).

II.5 Conclusion

At the present time, the scalability of the code has been tested using the SMG-HYPRE and I-SOR solvers. The performance is good enough to perform simulations with a reasonable computing time. We also validate the numerical methods implemented in the code in particular the immersed boundary method. The code is robust and provides all functionalities required for our following work. In the next chapter (§ III), we will use SUNFLUIDH to built the numerical database to investigate the fluid dynamics inside a rough Rayleigh Bénard cavity.

III – Physical problem & characteristic quantities

In this chapter, we describe the geometric setup and numerical requirements for the study of Rayleigh Bénard convection with rough boundary. Based on the results of previous experimental works, the arrangement of immersed bodies is carefully organized. Details will be provided on the mesh structure and the resolution requirements in the bulk region of the cell and near the boundary layers. We also discuss the specification of parallel computing with the presence of solids inside the computational domain, in particular how do we ensure the compatibility between mesh distribution and the multi-grid solver.

III.1 Numerical configuration of RBC with roughness elements

III.1.1 Physical problem

We study the fluid flow occurring in an asymmetric Rayleigh Bénard cavity with a rough bottom plate as sketched in figure (III.1). It is a rectangular cell with a height H, a depth D and a length W. The aspect ratios used for the following work are $\Gamma_x = W/H = 1$ and $\Gamma_y = D/H = \frac{1}{2}$. The temperature of hot bottom (resp. cold top) plate is denoted by θ_h (resp. θ_c). The Prandtl number ($\mathrm{Pr} = 4.38$) corresponds to water at 40^o Celsius. In what follows, only the Ra number will be varied. One advantage of the asymmetric cell is to make

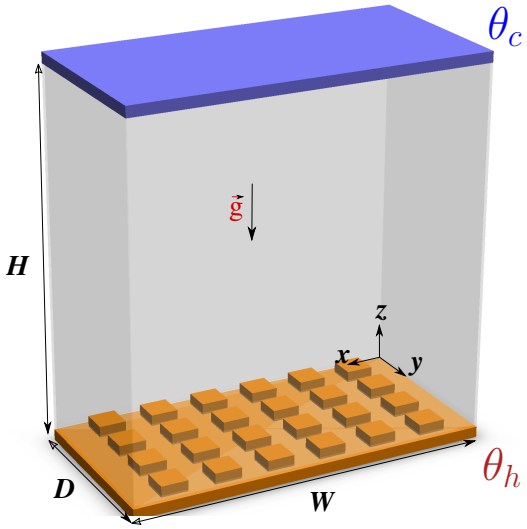

Fig. III.1 Asymmetric rough Rayleigh Bénard cavity (R/S).

possible comparison of interactions between the rough and smooth plates with the same bulk flow. Numerically, it reduces costs because from a single simulation, we can define two equivalent symmetric cavities in which we would have two identical horizontal plates ,i.e. smooth/smooth or rough/rough boundaries. We refer to this cavity as R/S in what follows.

The roughness elements are modeled by a set of parallelepiped solid blocks with square bases. The first thing is to find typical sizes of roughness (height H_p, width W_p and depth D_p) and space distribution of those plots (D_r,W_r) regarding the involved phenomena noticed in the literature (Ciliberto and Laroche (1999), Stringano et al. (2006), Salort et al. (2014) and Liot et al. (2016)). The community now agrees on the fact that enhancement of heat transfer appears when the thickness of thermal boundary layer δ_θ reaches the height of the roughness elements ($\delta_\theta \approx H_p$).

Choice of roughness height H_p and Ra range

Our study aims to clarify the different regimes of heat transfer seen in literature especially beyond the transition to enhanced ones. Previous works (for example (Du and Tong, 2000; Tisserand et al., 2011)) report an increase of the Nusselt number Nu when the thermal boundary layer thickness becomes in the order of roughness height. Thus, we seek to obtain an enhancement of Nu at relatively low Ra number (of the order of 10^7) to reduce computational coast and make simulations possible for even higher Ra. Our DNS of classical Rayleigh Bénard cavity with smooth boundaries at $Ra = 10^7$ shows a thickness of the thermal boundary layer around $\delta_\theta = (H/2Nu) \approx 0.032$. This is the reason why the height of the roughness elements in the asymmetrical cell is set up to $H_p = 0.03$. Thus, the range of Ra number considered in this work is five decades $[10^5 : 10^{10}]$. This configuration is maintained in what follows. It will be studied in the next chapters (§ IV,§ V,§ VI and § VII).

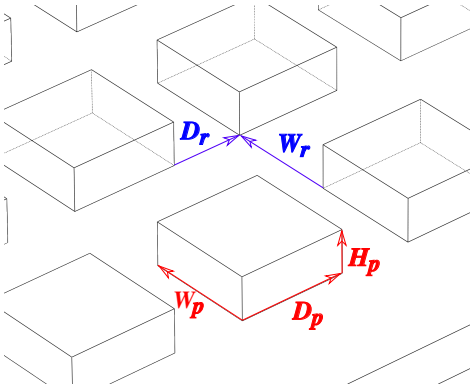

Fig. III.2 Sketch near the rough plate shows geometrical distribution of roughness elements. Each plot has a dimension of ($W_p \times D_p \times H_p = 0.075 \times 0.075 \times 0.03$) and are distributed equidistantly using ($W_r, D_r = 0.075, 0.05$).

Surface of heat exchange and distribution of roughnesses

Our computational solver SUNFLUIDH is developed to handle parallelepipedic immersed bodies. The experiences of Salort et al. (2014) represent the closest asymmetric Rayleigh Bénard cavity that we can model. Thus, we retain an equivalent distribution and shape of plots. We align four rows of roughnesses in the transversal direction $\overrightarrow{e_y}$, each row includes six plots, a total set up of $N_{plots} = 24$ square based plots. A single plot has a dimension of $W_p \times D_p \times H_p = 0.075H \times 0.075H \times 0.03H$. Plots are regularly distributed over the horizontal plate as sketched in figure (III.2)). Introducing roughness elements adds an additional surface of heat exchange. The ratio of both heat exchange surfaces C_s between fully asymmetric rough and symmetric smooth cavities is equal to

$$C_s = \frac{A_{R/S}}{A_S} = \frac{A_R^{hot} + A_S^{cold}}{A_S^{hot} + A_S^{cold}} = 1.216 \tag{III.1}$$

Where A_R and A_S are the total areas of heat exchange surface in rough and smooth cavities.

Boundary conditions in rough RB cell

In our cavity, the non slip condition is used for all walls including those of roughness elements. Side walls are considered to be adiabatic, so we use the homogeneous Neumann boundary condition on the temperature filed. The lower and upper surfaces are isothermal, then we impose Dirichlet condition on temperature.

$$\begin{cases} \underline{u} & = 0 \quad \text{on all walls} \\ \theta_h & = 1 \quad \text{on lower hot plate including plots faces} \\ \theta_c & = 0 \quad \text{on upper cold plate} \\ \dfrac{\partial \theta}{\partial \overrightarrow{n}} & = 0 \quad \text{on sidewalls} \end{cases} \tag{III.2}$$

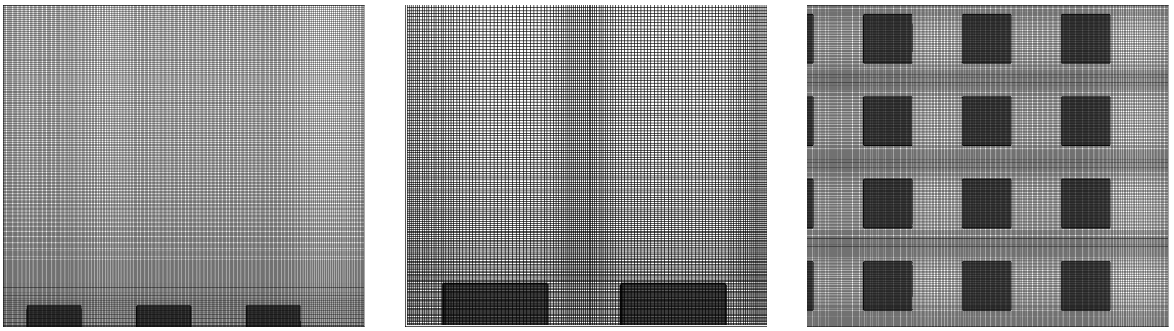

(a) XZ plane (b) YZ plane (c) XY plane

Fig. III.3 Cartesian staggered grid near roughness elements for $Ra = 5 \times 10^8$. An adequate refinement is applied, the maximum variation of the size ratio in between two adjacent mesh cells is lower than 3%. The number of nodes in between roughnesses is in the order of 2^n.

III.1.2 Mesh structure and resolution requirements

For the SUNFLUIDH code, spatial discretization of the equations is carried out on a cartesian staggered grid as shown in figure (III.3). In our work, we built an irregular mesh-grid per subdomain in all spatial direction by means of distribution laws such as the hyperbolic tangent function. The mesh is finer near the walls in particular along the adjacent walls of roughness elements. Mainly, we regard three important points : (i) resolution requirements in the whole cavity namely in the bulk region, (ii) resolution needed for boundary layers or side walls and (iii) from a purely technical viewpoint, we need for a mesh adaptation in between roughnesses for the construction of grids used in multigrid I-SOR solver in particular in the case of the domain decomposition used for parallel computing. Simulation are performed fo 16 Ra numbers using the corresponding mesh determined with these criteria as showed in figure (III.4) (Numerical resources and mesh details are given in table [III.1]).

a) Bulk resolution

In order to obtain accurate results, one should use a suitable mesh grid resolution. In DNS, the local mesh size should be smaller than the local Kolmogorov scale $\eta_K(\underline{x}, t)$ (Kolmogorov, 1941) and Batchelor scale $\eta_B(\underline{x}, t)$ (Batchelor, 1959) as described by Paterson (1976). It is found that $\eta_B(\underline{x}, t) = \eta_K(\underline{x}, t)Pr^{-1/2}$, consequently for Prandtl number $Pr = 4.38$, the Batchelor scale becomes the most restrictive criterion. As viscosity effects balances the inertial effects at Kolmogorov length scale whereas advection and thermal diffusion balance at Bachelor scale, a definition of the global Kolmogorov η_K and Batchelor η_B lengths using viscous energy dissipation rate are given by Shishkina et al. (2010) as follows

$$\eta_K = \frac{\nu^{3/4}}{\langle \overline{\epsilon_u} \rangle_V^{1/4}} \tag{III.3}$$

$$\eta_B = \frac{\nu^{1/4} \kappa^{1/2}}{\langle \overline{\epsilon_u} \rangle_V^{1/4}} \tag{III.4}$$

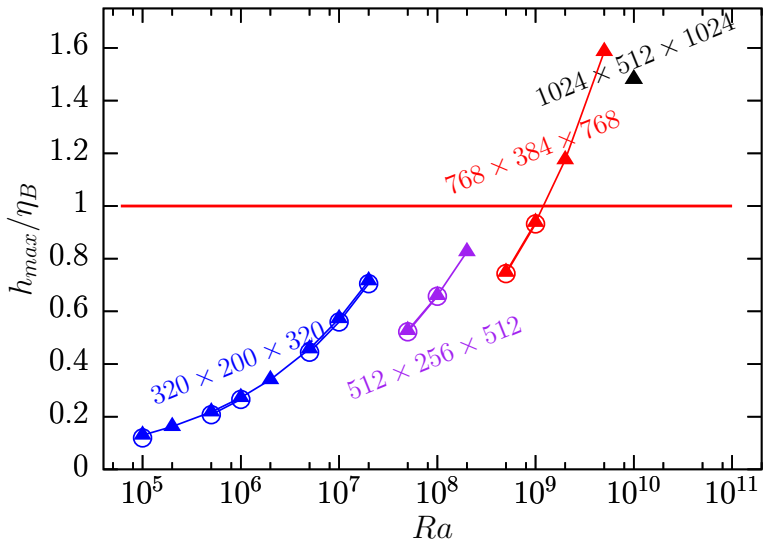

Fig. III.4 Comparison between the maximum size h_{max} in the 3D mesh and the Batchelor global length scale η_B for different Ra numbers. Colors refer to the meshgrid : (▲,○)→(320 × 200 × 320), (▲,○)→(512 × 256 × 512), (▲,○)→(768 × 384 × 768), (▲)→(1024 × 512 × 1024). Full triangles refer to estimations based on GL theory where for open circles are based on our DNS data of the smooth RB cavity.

Consequently, the criterion to be respected is that the admissible local mesh size h_{max} in the whole cavity should be smaller than the following Batchelor length scale (Grötzbach, 1983),

$$h_{max} \leqslant \eta_B \qquad \text{with} \quad \eta_B = \frac{H}{[Ra\ (Nu-1)]^{1/4}} \tag{III.5}$$

In order to evaluate the Batchelor length in equation (III.5), we estimate the heat flux Nu with two methods : (i) a priori using the Grossmann-Lohse theory (Grossmann and Lohse, 2004, 2011; Stevens et al., 2013), (ii) using our DNS data of the symmetric smooth cavity as an approximation for Nu in an asymmetric cavity.

In figure (III.4), we compare the ratio of the local mesh size h_{max} in the R/S cavity and the Batchelor length scale. Clearly, the ratio is lower than unity until $Ra = 10^9$, hence the different resolutions used are fine enough regarding the Batchelor scale except for the cases $Ra \geqslant 2 \times 10^9$ where the ratio exceeds slightly the unity. Nevertheless, over the whole mesh, the local mesh size is smaller than η_B. We consider that the defined mesh respects mostly the bulk criterion.

b) Boundary layers resolution

Several studies done on turbulent Rayleigh-Bénard convection have shown that a fine resolution of the boundary layer structure is of high importance for the accuracy of numerical results. We use requirements from the study of Shishkina et al. (2010) to estimate necessary number of nodes. They used the laminar Prandtl- Blasius boundary layer theory to determine relative thicknesses of the thermal and kinetic boundary layers as function of Prandtl number. Indeed, they estimated that the minimum number of nodes in the thermal boundary layer $N_{th,BL}$ and in the viscous boundary layer $N_{u,BL}$ as follows

$$\begin{cases} N_{th,BL} & \geq \sqrt{2}\ a\ Nu^{1/2} Pr^{-3/4}\ b^{3/2} \\ N_{u,BL} & \geq \sqrt{2}\ a\ Nu^{1/2} Pr^{1/3}\ b^{1/2} \end{cases} \qquad \text{for} \qquad Pr > 3 \tag{III.6}$$

Where a and b are empirical parameters.

As suggested by Verzicco and Camussi (2003) and Stevens et al. (2010b), we also increase the number of nodes that should be placed in the thermal and kinetic boundary layers to capture more accurately the sufficient thermal dissipation and consequently better estimate the Nusselt number.

c) Decomposition of computational domain with immersed bodies

The decomposition of computational domain is not obvious as one must take care of the construction of meshgirds for the I-SOR Poisson solver. On the one hand, we know from chapter (*II*) that the use of higher number of grids gives a better convergence, however this number in related to the mesh points available in the fluid volume in each subdomain. On the other hand, to get a good performance of the code, we have to choose an adequate parallelization. More we decompose the computational domain in a given direction, smaller is the available number of mesh grids. So the question is to find a good compromise between convergence and performance. In addition, the number of grids is limited by several conditions that we have to respect simultaneously,

1. The number of subdomains must be in order of 2^n on the Turing/IDRIS machine,
2. The number of grids N_{grid} is the same in each space direction,
3. Mesh points must be in the order of 2^n in every subdomain,
4. Decomposition technique of the computational domain leads to subdomains which involve immersed bodies, i.e coexistence of fluid and solid parts within the same subdomain. However, the SUNFLUIDH code resolves only the fluid parts. The conditioning of multi grids applies to all subdomains, the number of mesh points must be in the order of 2^n in every fluid zone between roughness elements or between the plot and the border of the subdomain, (more details are available in the table (III.2).

Table III.1 Parameters : Ra, Rayleigh number ; N_{thread} number of threads ; N_{MPI} number of MPI processes ; N_{OP} number of openMP processes ; $d^{i;j;k}$ number of subdomains in each direction (i,j,k) ; $N_x \times N_y \times N_z$ global mesh size ; Δt, time step ; T_u total simulated time units at the concerned Ra. (1) For $Ra = 10^9$ and $Ra = 5 \times 10^9$ simulation are started from $Ra = 5 \times 10^8$ at $t = 31$ and $t = 48$ resp. (2) For $Ra = 2 \times 10^9$, the simulation is started from $Ra = 10^9$ at $t = 255$. (3) For $Ra = 10^{10}$, a massively parallel hybrid MPI/OpenMP computing, It is started from $Ra = 2 \times 10^8$ at $t = 635$ by performing an interpolation technique.

Ra	N_{thread}	N_{MPI}	$\frac{N_{MPI}}{node}$	N_{OP}	$d^i \times d^j \times d^k$	$N_x \times N_y \times N_z$	$(N_x \times N_y \times N_z)_{SD}$	Δt	T_u
1×10^5	256	16	16	1	$8 \times 4 \times 8$	$320 \times 200 \times 320$	$40 \times 50 \times 40$	$2.55e-3$	700
2×10^5	256	16	16	1	$8 \times 4 \times 8$	$320 \times 200 \times 320$	$40 \times 50 \times 40$	$2.55e-3$	200
5×10^5	256	16	16	1	$8 \times 4 \times 8$	$320 \times 200 \times 320$	$40 \times 50 \times 40$	$2.50e-3$	700
1×10^6	256	16	16	1	$8 \times 4 \times 8$	$320 \times 200 \times 320$	$40 \times 50 \times 40$	$2.40e-3$	1000
2×10^6	256	16	16	1	$8 \times 4 \times 8$	$320 \times 200 \times 320$	$40 \times 50 \times 40$	$2.40e-3$	1000
5×10^6	256	16	16	1	$8 \times 4 \times 8$	$320 \times 200 \times 320$	$40 \times 50 \times 40$	$2.00e-3$	760
1×10^7	256	16	16	1	$8 \times 4 \times 8$	$320 \times 200 \times 320$	$40 \times 50 \times 40$	$1.80e-3$	700
2×10^7	256	16	16	1	$8 \times 4 \times 8$	$320 \times 200 \times 320$	$40 \times 50 \times 40$	$1.60e-3$	700
5×10^7	256	16	16	1	$8 \times 4 \times 8$	$512 \times 256 \times 512$	$64 \times 64 \times 64$	$9.00e-4$	746
1×10^8	256	16	16	1	$8 \times 4 \times 8$	$512 \times 256 \times 512$	$64 \times 64 \times 64$	$8.50e-4$	728
2×10^8	256	16	16	1	$8 \times 4 \times 8$	$512 \times 256 \times 512$	$64 \times 64 \times 64$	$8.00e-4$	700
5×10^8	512	32	16	1	$8 \times 8 \times 8$	$768 \times 384 \times 768$	$96 \times 48 \times 96$	$5.50e-4$	397
1×10^9	512	32	16	1	$8 \times 8 \times 8$	$768 \times 384 \times 768$	$96 \times 48 \times 96$	$5.00e-4$	399^1
2×10^9	512	32	16	1	$8 \times 8 \times 8$	$768 \times 384 \times 768$	$96 \times 48 \times 96$	$5.00e-4$	252^2
5×10^9	512	32	16	1	$8 \times 8 \times 8$	$768 \times 384 \times 768$	$96 \times 48 \times 96$	$4.50e-4$	372^1
1×10^{10}	32768	2048	1	16	$16 \times 8 \times 16$	$1024 \times 512 \times 1024$	$64 \times 64 \times 64$	$2.50e-4$	255^3

As listed in table [III.1], the spatial resolution of different meshes are relatively fine. The domain is decomposed to compute in parallel all subdomains. As a reminder about the architecture of the supercomputer Turing, a single node contains 16 processors. The number of allocated nodes varies between 16 and 32 for a pure MPI approach whereas a set of 2048 nodes is used for a hybrid MPI/openMP approach. For $Ra \leqslant 5 \times 10^8$, simulation are initiated with a fluid at rest and a temperature $\theta = \theta_h + \theta_c)/2$, i.e ($\mathbf{u} = 0; \theta = 0.5$ in the whole cavity). We note that the simulations for $Ra \geqslant 10^9$ are initiated from lower Ra numbers because of high turbulence level and to gain considerable time of computing.

The choice of the spatial decomposition of the computational domain is based on our performance tests presented in section [II.3]. For Ra in $[10^5 : 2 \times 10^8]$, we used a decomposition of $8 \times 4 \times 8$ subdomains for which good scalability is obtained for both hypre library and I-SOR solvers. Similarly, we choose a decomposition with $8 \times 8 \times 8$ subdomains for $[5 \times 10^8 : 5 \times 10^9]$ which give a good compromise between performance and convergence. Implementation of the Hybrid MPI/OpenMP parallelization technique in the SUNFLUIDH has been done during this work by F. FRAIGNEAU. It enabled us to reach higher turbulent level (here $Ra = 10^{10}$).

Table III.2 Multigrid solver parameters : N_{iter}, number of iterations performed by the Hypre solver ; N_{Grid}, number of grids ; N_{cycle} maximal number of V-cycles ; itr_{F-C} number of iterations from fine to coarse grid ; itr_C iteration on coarsest grid ; itr_{C-F} number of iterations from coarse to fine grid.

Ra	Solver	N_{iter}	N_{Grid}	N_{cycle}	itr_{F-C}	itr_C	itr_{C-F}
$1 \cdot 10^5$	Hypre	3	-	-	-	-	-
$2 \cdot 10^5$	Hypre	3	-	-	-	-	-
$5 \cdot 10^5$	Hypre	6	-	-	-	-	-
$1 \cdot 10^6$	Hypre	6	-	-	-	-	-
$2 \cdot 10^6$	Hypre	6	-	-	-	-	-
$5 \cdot 10^6$	Hypre	6	-	-	-	-	-
$1 \cdot 10^7$	Hypre	6	-	-	-	-	-
$2 \cdot 10^7$	Hypre	6	-	-	-	-	-
$5 \cdot 10^7$	I-SOR	-	6	5	3	20	15
$1 \cdot 10^8$	I-SOR	-	6	5	3	20	15
$2 \cdot 10^8$	I-SOR	-	6	5	3	20	15
$5 \cdot 10^8$	I-SOR	-	4	5	4	22	17
$1 \cdot 10^9$	I-SOR	-	4	5	4	22	17
$2 \cdot 10^9$	I-SOR	-	4	5	4	22	17
$5 \cdot 10^9$	I-SOR	-	4	5	4	25	20
$1 \cdot 10^{10}$	I-SOR	-	7	5	4	20	20

In table [III.2], we summarize the parameters of the hypre library and I-SOR multigrid solvers. It has been chosen with care in order to obtain good convergence and reasonable wall times. We note that all the simulations begin with a $CFL = 0.3$. Once the transitory regime is passed, a constant time step Δt is chosen (see table [III.1]), hence we begin to build-up the statistics. We mention here that problems of computing with the HYPER solver for large mesh grids in the present cases with embedded solids. This is the reason why we opt for the second solver I-SOR.

III.1.3 System responses and convergence of simulations

The convergence between Nusselt numbers of the bottom and top plates with volumetric Nusselt numbers based on viscous and thermal dissipation stands as strong criterion to verify the global convergence of the system responses (Stevens et al., 2010b; Shishkina et al., 2010). In the following table [III.3], a summary of various Nusselt numbers directly calculated in the R/S cavity is given (see the definitions in subsection (III.2.2)). Due to the presence of roughnesses which have non adiabatic sides, Nu_{bot} will be measured at the height equals to the upper bound H_p. Thus it could be compared with other definitions as well. We define $Nu_{R/S}$ the Nusselt number of the asymmetric cavity as the arithmetic average of all Nusselt numbers, it represents a direct quantification of the heat flux inside the R/S cavity,

$$Nu_{R/S} = \frac{Nu_{bot}^{H_p} + Nu_{top} + Nu_{mid} + Nu_{bulk} + Nu_{\epsilon_u} + Nu_{\epsilon_\theta}}{6} \tag{III.7}$$

By measuring the standard deviation γ among all Nusselt definitions, we can measure the rate of dispersion. Thus, we define err_r, the relative error as follows

$$err_r = \frac{100\ \gamma}{Nu_{R/S}} \tag{III.8}$$

We can see from table [III.3] that $err_r < 1\%$ for all Ra. This low error indicates that all Nu tend to be close to $Nu_{R/S}$. Thus our system response could be considered as statistically converged as suggested by Stevens et al. (2010b) and Shishkina et al. (2010). We highlight that the time of computing varies depending on Ra between 1 and 8 months. Beyond which, DNS cost becomes very extensive to further expand our statistics. Recently, hybrid computing with MPI/OpenMP technique allows us to simulate $Ra = 10^{10}$. It is a massively parallel case in which 32768 threads are deployed, thus reducing considerably the computing time.

Table III.3 Convergence of Nusselt numbers : $Nu_{bot}^{H_p}$ at the bottom plate at H_p ; Nu_{top} at the top ; Nu_{mid} at the median plane ; Nu_{bulk}, in the bulk of cavity ; Nu_{ϵ_u} of viscous dissipation, Nu_{ϵ_θ} of thermal dissipation. γ is the standard deviation and err_r is relative error.

Ra	$Nu_{bot}^{H_p}$	Nu_{top}	Nu_{mid}	Nu_{bulk}	Nu_{ϵ_u}	Nu_{ϵ_θ}	$Nu_{R/S}$	γ	$err_r\%$
1×10^5	3.793179	3.793180	3.793180	3.793180	3.791804	3.722969	3.781249	0.028053	0.74
2×10^5	4.779906	4.779906	4.779906	4.779910	4.777614	4.730978	4.771370	0.019437	0.41
5×10^5	6.360257	6.356722	6.360427	6.363180	6.354198	6.241600	6.339397	0.047099	0.74
1×10^6	7.989253	7.993813	7.993175	7.988624	7.981578	7.846551	7.965499	0.057462	0.72
2×10^6	10.071277	10.045540	10.078614	10.013367	10.043307	10.000377	10.042080	0.027970	0.28
5×10^6	13.558428	13.547054	13.567512	13.571744	13.546621	13.334637	13.520999	0.090338	0.67
1×10^7	17.901206	17.871703	17.901769	17.918378	17.875445	17.605264	17.845627	0.116437	0.65
2×10^7	23.086897	23.124660	23.096158	23.124836	23.147507	22.784217	23.060712	0.136705	0.59
5×10^7	31.935568	31.932221	31.915269	31.686430	32.169418	31.571214	31.868354	0.208954	0.66
1×10^8	40.698299	40.516712	40.682049	40.644892	41.003708	40.212016	40.626279	0.256721	0.63
2×10^8	51.033254	50.730497	51.028237	50.820200	51.638343	50.472201	50.953789	0.393393	0.77
5×10^8	68.395442	68.248637	68.181979	68.758019	68.249916	68.735443	68.428239	0.256058	0.37
1×10^9	86.849683	85.021588	86.763164	85.514926	85.700314	85.487365	85.889507	0.608996	0.71
2×10^9	106.950532	106.208407	107.386193	107.650807	107.317361	106.415460	106.988127	0.573045	0.54
5×10^9	144.303197	143.674557	144.307216	144.465074	145.132092	145.509202	144.565223	0.645340	0.45
1×10^{10}	181.658789	178.914375	179.053660	179.914266	178.991167	178.699248	179.538584	0.594992	0.33

III.2 Separation of rough/smooth plates

We follow Tisserand et al. (2011) and Salort et al. (2014) assumption to separate the effects of rough and smooth plates. By considering that the thermal behavior of the cell is independent of its height, the hot and cold plates could be considered as independent from each other. The separation of the R/S cavity into equivalent rough cell (denoted by R) and smooth cell (denoted by S) is sketched in figure (III.5).

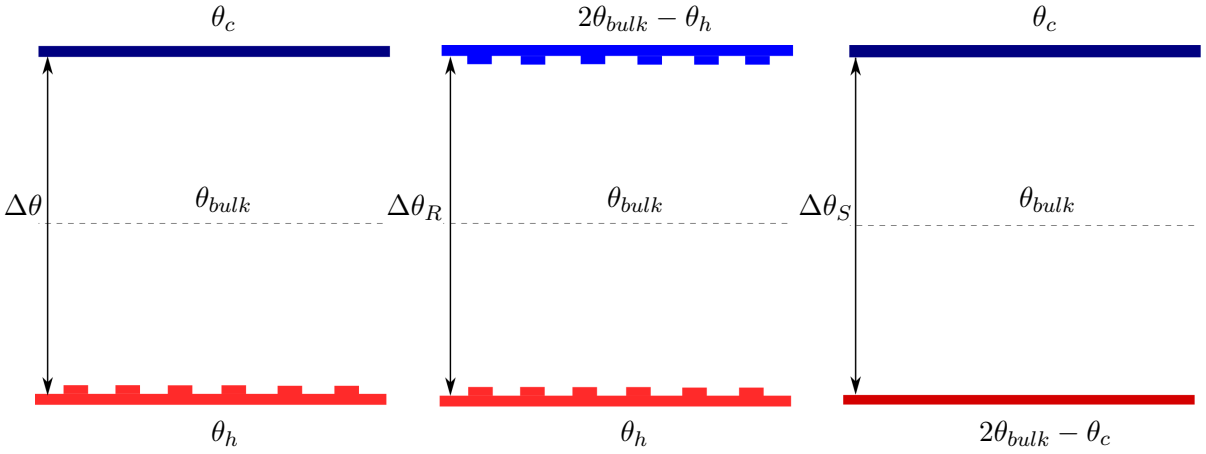

(a) R/S (b) Equivalent rough cell : R (c) Equivalent smooth cell : S

Fig. III.5 Separation of rough and smooth plates. (a) asymmetric Rayleigh Bénard cell : R/S that we used for our DNS. Equivalent symmetric cells : (b) rough cell : R and (c) smooth cell : S. The temperature of hot bottom (resp. cold top) plate are denoted by θ_h (resp. θ_c). θ_{bulk} is bulk temperature. $\Delta\theta_R$ and $\Delta\theta_S$ are temperature differences between the plates of equivalent cells.

.

III.2.1 Estimation methodology of bulk temperature

Bulk temperature in necessary to calculate the temperature differences $\Delta\theta_R$ and $\Delta\theta_S$. By definition, the bulk is a region where the mean temperature remains practically constant. The spatial average of mean thermal field inside the bulk region is considered to be the bulk temperature. As shown in figure (III.6a), θ_{bulk} is estimated using mean temperature profile,

$$\theta_{bulk} = \frac{1}{z_{max} - z_{min}} \int_{z_{min}}^{z_{max}} \langle \overline{\theta} \rangle_S dz \tag{III.9}$$

Where $[z_{min} : z_{max}]$ is the part where mean temperature is almost constant along vertical direction. Regions where $(z < z_{min})$ or $(z > z_{max})$ are characterized by a high temperature gradient, the outer region is considered as the bulk. z_{min} and z_{max} are defined by means of a threshold ϵ_z on temperature vertical gradient profile by,

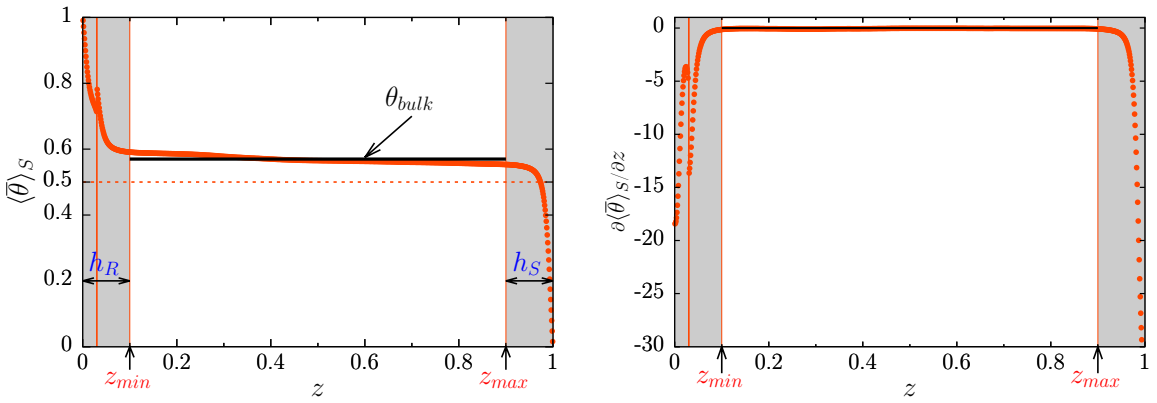

(a) $\langle\overline{\theta}\rangle_S(z)$ (b) $\partial\langle\overline{\theta}\rangle_S/\partial z$

Fig. III.6 Estimation methodology of θ_{bulk}. (a) Mean temperature profile at $Ra = 5 \times 10^7$ in the R/S cell. (b) Profile of corresponding temperature gradient in vertical direction. $h_R = z_{min}$ and $h_S = (H - z_{max})$ are thicknesses of the regions outside the bulk. The vertical red line represent the height of roughness elements.

$$\begin{cases} z_{min} \equiv z\left(|\partial\langle\overline{\theta}\rangle_S/\partial z|_{[0-\frac{H}{2}]}| < \epsilon_z\right) \\ \\ z_{max} \equiv z\left(|\partial\langle\overline{\theta}\rangle_S/\partial z|_{[\frac{H}{2}-H]}| < \epsilon_z\right) \end{cases} \quad \text{with} \quad \epsilon_z = 10^{-3} \tag{III.10}$$

Once the bulk temperature θ_{bulk} within the R/S cell is known, we could define a temperature difference between upper and lower plates associated to equivalent symmetrical cells R and S. We denote by $\Delta\theta_S$ the double temperature difference between the top smooth plate and the bulk region, likewise, $\Delta\theta_R$ is the double temperature difference between the bottom rough plate and the bulk as sketched in figure (III.7).

$$\Delta\theta_S = 2 \times (\theta_{bulk} - \theta_c) \tag{III.11}$$

$$\Delta\theta_R = 2 \times (\theta_h - \theta_{bulk}) \tag{III.12}$$

III.2.2 Definition of quantities relative to rough and smooth cells

Because of geometrical asymmetry, we can see in figure (III.7) that bulk temperature is no longer equal to the arithmetic mean between smooth and rough temperatures ($\theta_{bulk} \neq \frac{\theta_h+\theta_c}{2}$) which means that the temperature difference $\Delta\theta_R$ would be different from $\Delta\theta_S$. In this case, from the same numerical simulation, one can define corresponding Rayleigh and Nusselt numbers for each equivalent cell. We denote by Ra_S and Nu_S the Rayleigh and Nusselt numbers related to the smooth plate.

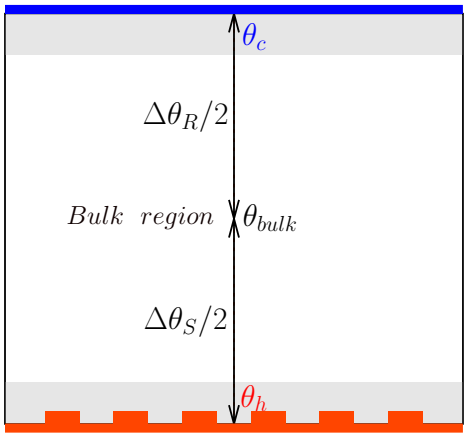

Fig. III.7 Definitions of temperature differences $\Delta\theta_S/2$ and $\Delta\theta_R/2$ relative to smooth and rough plates with respect to bulk temperature.

$$\begin{cases} Ra_S &= \dfrac{g\alpha\Delta T_S H^3}{\nu\kappa} &= Ra_{R/S} \times \Delta\theta_S \\ Nu_S &= \dfrac{QH}{\kappa\Delta T_S} &= Nu_{R/S}/\Delta\theta_S \end{cases} \tag{III.13}$$

The Nusselt number Nu_S is equivalent to that which would have a cavity of the same height H with symmetric smooth boundaries subjected to the same heat flux Q and whose bulk temperature would be θ_{bulk}. In the same way, it is possible to define equivalent Rayleigh number Ra_R and Nusselt number Nu_R related to the rough plate for which we would have a cavity of the same height H with two symmetric rough plates.

$$\begin{cases} Ra_R &= \dfrac{g\alpha\Delta T_R H^3}{\nu\kappa} &= Ra_{R/S} \times \Delta\theta_R \\ Nu_R &= \dfrac{QH}{\kappa\Delta T_R} &= Nu_{R/S}/\Delta\theta_R \end{cases} \tag{III.14}$$

From the equations (III.13) and (III.14), we can deduce the following equalities :

$$\begin{cases} Nu_{R/S} &= Nu_S \times \Delta\theta_S &= Nu_R \times \Delta\theta_R \\ Nu_S \times Ra_S &= Nu_R \times Ra_R \end{cases} \tag{III.15}$$

III.3 Analysis of boundary layers

Estimation of the thickness of thermal and kinetic boundary layers is essential to characterize the flow. We give here definitions of different quantification methods used in literature. We note here that the following methods are developed for the case of smooth plates.

III.3.1 Thermal boundary-layer thicknesses

The thermal boundary layer thickness could be defined in five ways :

a) Approximated value of thermal BL thickness

The heat transfer near horizontal surfaces is mainly ensured by conduction, the contribution of convection is negligible. Assuming that the bulk of the cavity is isothermal at the mean temperature, one can derive an approximation of the thermal boundary layer thickness as a function of Nusselt number for smooth boundaries (see for example (Grossmann and Lohse, 2000) or section 2 of (Shishkina et al., 2010)),

$$\delta_\theta^M \equiv \frac{H}{2Nu} \tag{III.16}$$

b) Thermal diffusive sublayer

We use the classical definition via the slope of temperature profile at the plate (also called first gradient method, see for example Ahlers et al. (2006)). As sketched in figure (III.8), the distance from the plate where the tangent to the mean temperature profile at $z = 0$ reaches the bulk temperature is taken to be a definition of thermal boundary layer thickness,

$$\delta_\theta^g = z \left(\left. \frac{\partial \langle \overline{\theta} \rangle_S}{\partial z} \right|_{z=0} \equiv \theta_{bulk} \right) \tag{III.17}$$

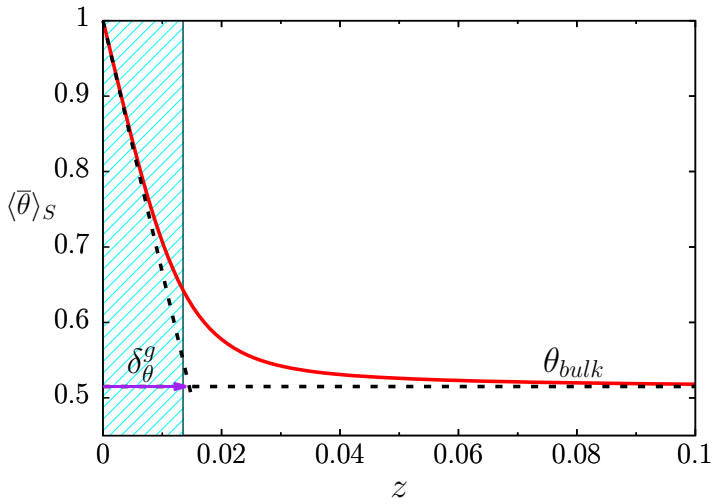

Fig. III.8 Sketch of mean temperature profile $\langle \overline{\theta} \rangle_S(z)$ (red line). Intersections between the tangent at $z = 0$ and the straight line at θ_{bulk} (black dashed lines) defines the thickness of thermal diffusive sublayer.

c) Turbulent thermal layer (rms-based)

As shown in figure (III.9), the temperature rms profile shows that temperature fluctuations are mostly important near horizontal side walls, the vertical position of the peak is taken to be a measure of thermal boundary layer thickness (see for example Kerr (1996)).

$$\delta_\theta^{rms} = z(max[\theta^{rms}]) \tag{III.18}$$

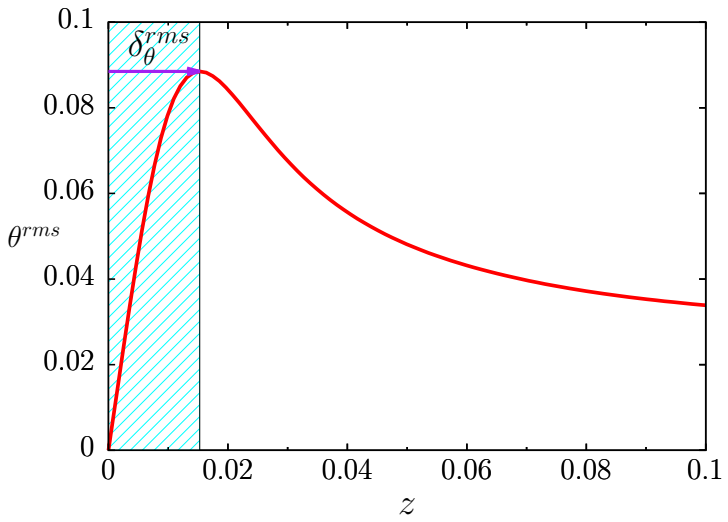

Fig. III.9 Sketch of mean temperature r.m.s profile θ^{rms} (red line). Location of maximal fluctuations is defined as a thermal boundary layer thickness.

d) Thermal displacement thickness

By definition, it is the distance by which the wall surface would have to be moved in the vertical direction to give the same integrated temperature as occurs between the wall and the reference plane for bulk region,

$$\delta_\theta^* = \int_{wall}^{bulk} \left(\frac{\langle \overline{\theta} \rangle_S(z) - \theta_{bulk}}{\theta_h - \theta_{bulk}} \right) dz \tag{III.19}$$

III.3.2 Kinetic boundary layers thicknesses

The kinetic boundary-layer thickness could be defined in similar ways. In the following, we give short description of each method.

a) Viscous diffusive sublayer

The approach that we use here is similar to the one seen in section (§ III.3.1). The distance from the plate where the tangent to the mean velocity profile at $z = 0$ reaches the maximal velocity u_0 is taken to be a kinetic boundary layer thickness.

$$\delta_u^g = z\left(\left.\frac{\partial\langle\overline{u}\rangle_S}{\partial z}\right|_{z=0} \equiv u_0\right) \qquad \text{with} \qquad u_0 = max|\langle\overline{u}\rangle_S| \quad \text{and} \quad z_0 = z(u = u_0) \tag{III.20}$$

b) Turbulent flow fluctuation layer (rms-based)

Velocity fluctuations are mostly important near horizontal side walls, the vertical position of the nearest peak is taken to be a definition of kinetic boundary layer thickness (see for example Kerr (1996)).

$$\delta_u^{rms} = z(max(u^{rms})) \tag{III.21}$$

c) kinetic displacement thickness

The displacement thickness δ_u^* is the distance by which the inviscid outer flow is displaced outwards by the drops in velocity in boundary layer" (Schlichting and Gersten, 2000). It is useful in determining the reduction of volume flux ($u_0\delta_u^*$) due to the action of viscosity in boundary layer.

$$\delta_u^* = \int_0^{z_0}\left(1 - \frac{\langle\overline{u}\rangle_S(z)}{u_0}\right)dz \tag{III.22}$$

d) kinetic momentum thickness

The momentum thickness δ_u^M is defined as the loss of momentum in the boundary layer as compared with that of potential flow. The distance from the wall by which solid boundary would have to be moved parallel to itself towards inviscid flow (Schlichting and Gersten, 2000). It is useful in determining the skin friction, i.e. give us a measure of the reduction of momentum transport in the boundary layer

$$\delta_u^M = \int_0^{z_0}\frac{\langle\overline{u}\rangle_S(z)}{u_0}\left(1 - \frac{\langle\overline{u}\rangle_S(z)}{u_0}\right)dz \tag{III.23}$$

e) kinetic energy thickness

The energy thickness δ_u^E is the distance by which the streamlines of the outer flow are displaced from the solid boundary to have the same amount of kinetic energy. It useful in determining the flux of defect of kinetic energy $\rho u_0^3 \delta_u^E$ (Schlichting and Gersten, 2000).

$$\delta_u^E = \int_0^{z_0} \frac{\langle \overline{u} \rangle_S(z)}{u_0} \left(1 - \frac{\langle \overline{u} \rangle_S(z)^2}{u_0^2} \right) dz \tag{III.24}$$

III.4 Conclusion

In this chapter, we construct a numerical data basis for the rough Rayleigh Bénard convection and give the definitions of the different quantities for data analysis. It will be used in the next chapters for the study of the successive regimes of heat transfer (§ IV) and roughness effects on mean profiles and boundary layer structure (§ V), for the comparison of the DNS data with experiment results § VI and the characterization of thermal plumes § VII.

IV – Successive regimes of heat transfer in an asymmetric rough RBC

IV.1 Introduction

In this chapter, we are interested in studying the roughness effects on the heat transfer in rough RBC, i.e scaling law for $Nu \sim f(Ra)$. We first give a global description of the heat transfer over a wide range of Ra number and compare our results with the literature. We conduct a comparison between the rough and smooth plates behaviors within the same RB cell. Scaling laws are discussed and compared with existing models for rough RBC. We then focus our analysis on the area over and around roughness elements by performing a spatial (solid/fluid) and physical (conductive/convective) decompositions of the heat flux.

IV.2 Roughness effect on the global heat transfer

We compare in figure (IV.1) the compensated Nusselt number as function of the Rayleigh number in the smooth cavity denoted by S/S and the asymmetric cavity R/S. We have performed a few simulations for the cavity with smooth top and bottom plates (see details in

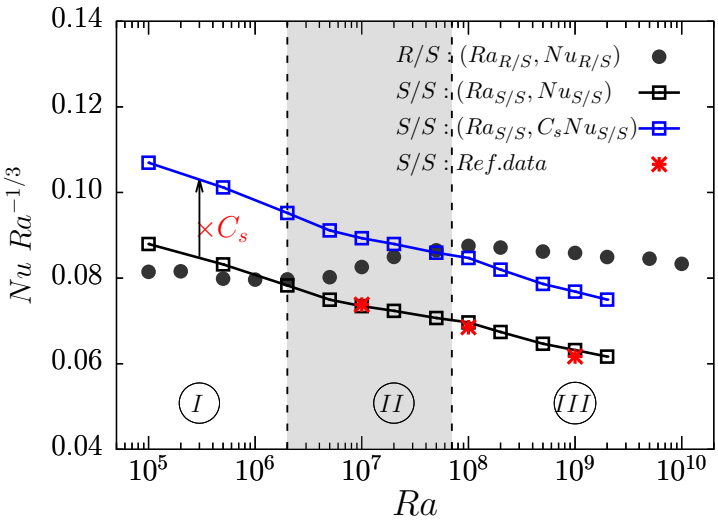

Fig. IV.1 (a) Compensated Nusselt number as a function of Rayleigh number. (–□–) Symbols refer to the S/S cavity. (–■–) is the relative surface increase in S/S cavity with a factor of $C_s = 1.216$. Red stars are reference data taken from numerical results of Kaczorowski et al. (2014) in a symmetric smooth cell with $\Gamma_y = 1/2$ and Pr = 4.38. The transitional regime II is qualitatively represented by gray zone.

chapter *II*). For the smooth cell, the results are in very good agreement with the DNS from Kaczorowski et al. (2014) for a similar cavity with an aspect ratio $\Gamma_y = 1/2$ and using water as a working fluid with Pr = 4.38. The relative error between our and their Nu numbers is very low with less than 1%.

Three successive regimes of heat transfer are found for the asymmetric cell :

1. Regime I : a reduction of Nusselt number $Nu_{R/S}$ comparing with $Nu_{S/S}$ is observed at low Rayleigh numbers for one decade in the range $10^5 \leqslant Ra \leqslant 10^6$. This phenomenon has already been seen by Zhang et al. (2018) using two-dimensional simulations. According to the authors, this reduction is a consequence of heat accumulation in between roughness elements, leading to a much thicker thermal boundary layer and thus impeding the overall heat flux through the system.

2. Regime II : is a transitional regime (marked with gray band). We report an enhancement of $Nu_{R/S}$ beyond $Ra \simeq 3 \times 10^6$. For now, we does not know precisely its limits bounds, i.e the Ra number that belongs to this regime. For instance, the probable Ra for which the change of heat transfer regime occurs is sketched by dashed black lines.

3. Regime III : $Nu_{R/S}$ still increases but less rapidly than regime II. It exceeds the relative increase due to additional surface induced by roughness elements as reported in previous works like Tisserand et al. (2011).

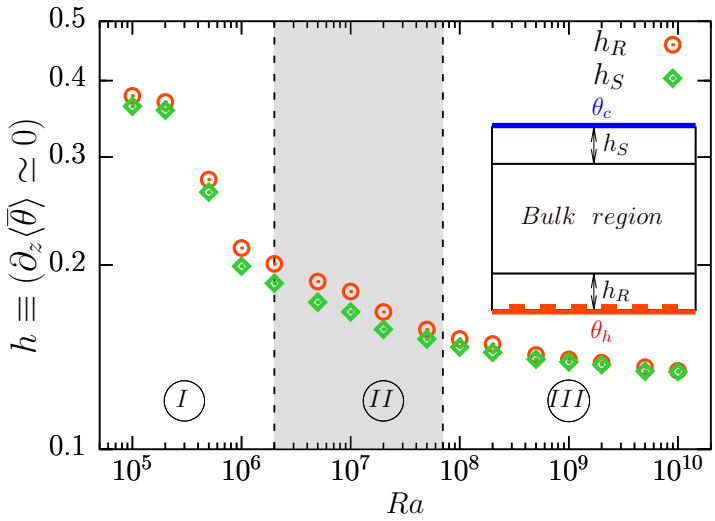

Fig. IV.2 Thickness of the zones outside the bulk region : h_R and h_S relative to rough and smooth sides as a function of Ra number (measures are given in appendix, table [A.1]).

IV.3 Roughness effect on bulk properties

We analyze the roughness effects on the location of the bulk region and on the bulk temperature with increasing Ra number. The thickness of the region outside of the bulk near rough and smooth plates are respectively $h_R = z_{min}$ and $h_S = H - z_{max}$ which are estimated using equations (III.10). As shown in figure (IV.2), h_R and h_S are becoming smaller with increasing Ra number. It means that the bulk region is widening inside the cell and seems to reach a constant size beyond $Ra = 10^8$. We note here that h_R is slightly bigger than h_S particularly during the intermediate regime, i.e the bulk region is a bit pushed up towards the smooth plate. For high Rayleigh numbers greater than 10^8, differences between h_R and h_S are negligible indicating that bulk region is vertically centered in the cell. We define θ_{center} as the mean temperature in the horizontal mid-plane at $z = H/2 = 0.5$ ($\theta_{center} = \langle\overline{\theta}\rangle_S|_{z=0.5}$). In classical RBC, θ_{center} is found to be equal to the arithmetic mean between cold and hot plate temperatures that we denote by $\theta_m = (\theta_h + \theta_c)/2 = 0.5$.

Figure (IV.3a) shows the evolution of θ_{bulk} (see equation [III.9]) and θ_{center} depending on Ra number. In regime I, both of θ_{bulk} and θ_{center} remain around θ_m. In regime II, we observe that θ_{bulk} begins to increase significantly while θ_{center} keeps increasing with slow rate before joining θ_{bulk} at around $Ra \approx 10^7$. However, differences between θ_{bulk} and θ_{center} are particularly remarkable in the range of $2 \times 10^6 \leqslant Ra \leqslant Ra10^7$. This behavior could be linked with the fact of measuring θ_{bulk} reflects the whole bulk temperature whereas θ_{center} is simply a measure at the middle plan. In regime III, we found that θ_{bulk} and θ_{center} saturate at the same temperature. The geometric asymmetry of the cell affects on bulk region which becomes 20% hotter comparing with classic RBC.

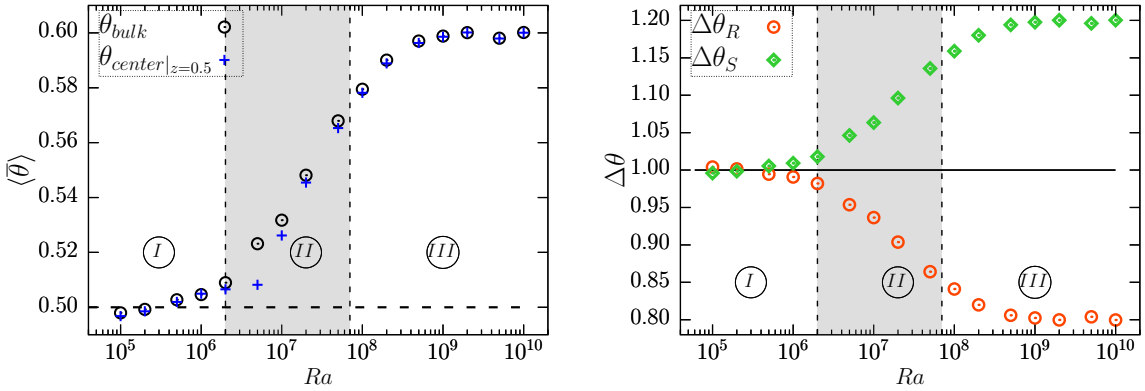

Fig. IV.3 (a) Bulk and mid plane temperatures θ_{bulk}, θ_{center} as a function of Ra number. (b) Double the temperature difference relative to rough side : $\Delta\theta_R = 2(\theta_h - \theta_{bulk})$; smooth side : $\Delta\theta_S = 2(\theta_{bulk} - \theta_c)$. (measures are given in appendix, table [A.2]).

Figure (IV.3b) shows the equivalent temperature differences associated to rough or smooth sides separately. As expected, those differences are close to 1 for Ra in $[10^5 : 10^6]$. Beyond that, temperature differences regarding the bulk region appear. Passing through regimes II to III, θ_{bulk} increases and the bulk region becomes hotter. Consequently temperature difference seen by the smooth top plate $\Delta\theta_{top}$ enhances. On the other plate, temperature difference seen by the rough bottom plate $\Delta\theta_{bot}$ drops. Those variations seems to saturate for higher Ra numbers. It is not clear if θ_{bulk} remains saturated for a further increase of Ra. For the highest reached Ra, we see a slight decrease of the bulk temperature. The process by which those differences vary as a function of Ra is not studied in detail in what follows.

IV.4 Scaling laws based on plate separation analysis

We use the plate separation method (§ III.2) to identify relative behaviors of the rough and smooth surfaces. The resulting (Ra_S, Nu_S) and (Ra_R, Nu_R) are given in figure (IV.4a) (Table is also given in appendix A.4). These results are in agreement with the measurements of Tisserand et al. (2011); Salort et al. (2014); Rusaouën et al. (2018). A transition toward regimes of enhanced heat transfer is observed on the rough plate beyond $Ra \simeq 3 \times 10^6$. In figure (IV.4b) we plotted $Nu \sim f(Ra)$ in log-log scale. It shows that smooth plate follows a unique power law whereas three scaling laws are identified for the rough plate. It must be noted that Nu_R is enhanced in a range of Ra that correspond to the global enhancement of the heat transfer $Nu_{R/S}$ in regimes II and III. The variation of Nu_R is highly correlated with $Nu_{R/S}$. This confirms that the intensification of heat transfer is mainly due to the rough part of our cell.

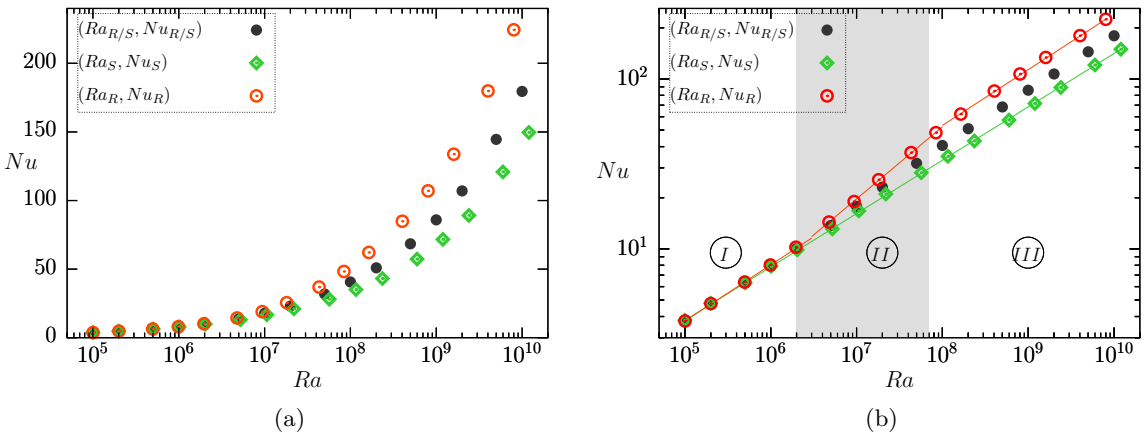

Fig. IV.4 Nusselt numbers as a function of Ra. Subscripts S and R refer to related quantities to smooth or rough plates. The dashed lines represent power-law fits. For the smooth plate, $Nu_S \sim 0.1 Ra_S^{0.315}$. For the rough plate, (i) regime I : $Nu_R \sim 0.083 Ra_R^{0.33}$, (ii) regime II : $Nu_R \sim 0.021 Ra_R^{0.424}$ and (iii) regime III : $Nu_R \sim 0.119 Ra_R^{0.33}$

A compensated Nusselt with Rayleigh number $Nu\ Ra^{-\beta}$ is plotted in figures (IV.5). The smooth plate has a unique behavior, only one scaling $Nu_S \sim c Ra_S^{\beta_S}$ over five-decades of Ra with an unchanged prefactor $c = 0.1$ and exponent $\beta_S = 0.315$. For the rough plate, we can distinguish two transitions separating three successive regimes of heat transfer. It matches the three regimes already identified in section (§ IV.3) :

1. Regime I : rough plate has a similar behavior as the smooth one, a nearby scaling exponent is obtained $\beta_R = 1/3$ whereas the prefactor is smaller. It means that the heat transfer is reduced consistent with 2D DNS of Zhang et al. (2018),
2. Regime II : is only transitional, the scaling exponent is increased to $\beta_R = 0.42$ during practically 2 decades. The increasing behavior or β_R is consistent with numerical studies such as 2D DNS of rough sinusoidal shape roughnesses by Zhu et al. (2017) reporting $\beta_R = 0.49$. Recently, 2D DNS by Zhu et al. (2019) has extended this transitional regime i.e. the Ra range with enhanced exponent by employing multiscale roughness. The results are in agreement as well with experiments like Xie and Xia (2017) who report an enhancement of β_R,
3. Regime III : the heat transfer still increases but at a slower rate. We find again the classic scaling law with $\beta = 1/3$. However the prefactor c is increased 20% comparing with the smooth plate (see the caption of figure (IV.5) for scaling coefficients). It confirms that the enhancement of the heat transfer in regime II could not be considered as the ultimate regime as reported by Toppaladoddi et al. (2017) as it is not maintained beyond $Ra = 10^8$.

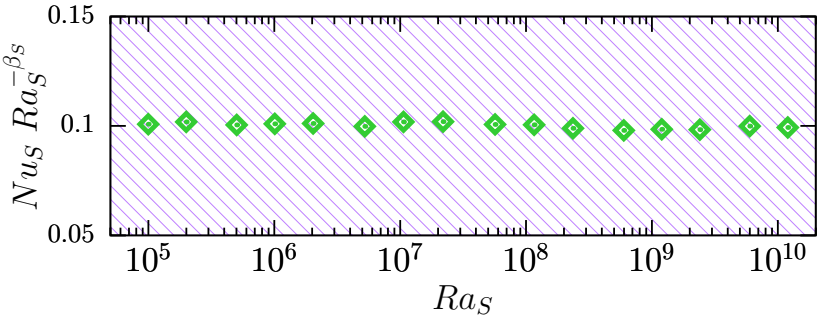

(a) Smooth plate : $\beta_S = 0.315$

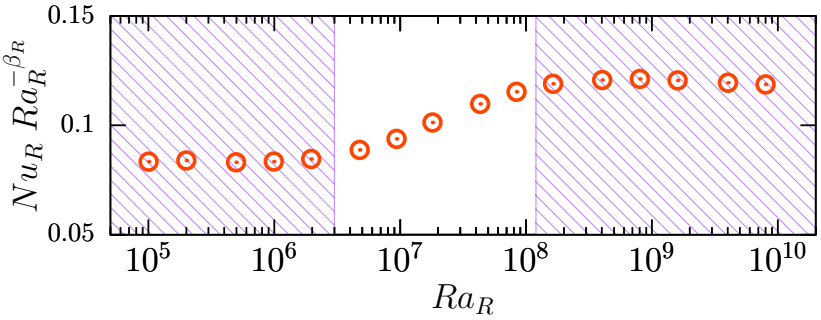

(b) Rough plate : $\beta_R = 1/3$

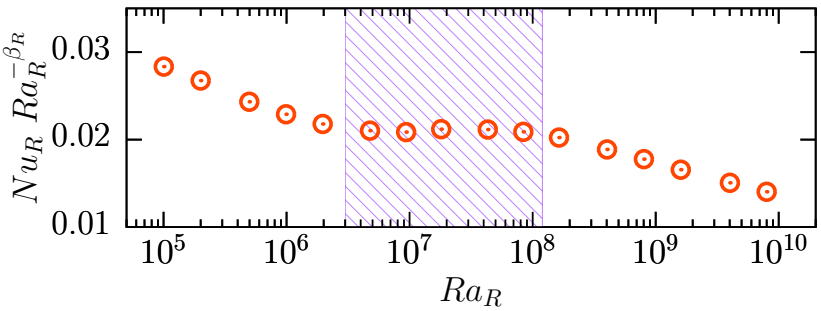

(c) Rough plate : $\beta_R = 0.42$

Fig. IV.5 Compensated plots of Nu_S and Nu_R respectively fitted with Ra_S and Ra_R. Hatched magenta area represents the range of Ra numbers used to perform linear regression. β_S and β_R are the scaling exponents relative to the smooth or rough plate. Best fit for the scaling laws are : (a) smooth plate : $Nu_S \sim 0.1 Ra_S^{0.315}$ in all regimes. (b,c) Rough plate : $Nu_R \sim c Ra_R^{\beta_R}$ with $(c = 0.083, \beta_R = 1/3)$ in regimes I, $(c = 0.021, \beta_R = 0.42)$ in regimes II and $(c = 0.119, \beta_R = 1/3)$ in regime III.

Through this analysis, one can deduce the limit of each regime more precisely as follows :

1. Regime I : $Ra \leqslant 3 \times 10^6$
2. Regime II : $3 \times 10^6 \leqslant Ra \leqslant 10^8$
3. Regime III : $10^8 \leqslant Ra$

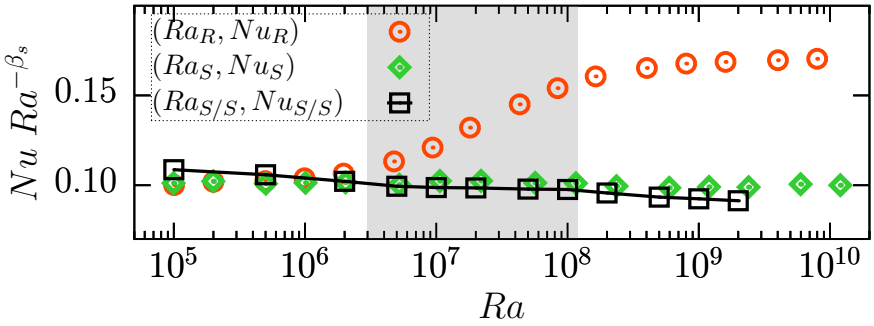

Fig. IV.6 Slight difference between smooth sides in S/S and R/S cells. (Nu_R, Ra_R), (Nu_S, Ra_S) and $(Nu_{S/S}, Ra_{S/S})$ plotted using best fit for smooth plate of R/S cell with scaling exponent $\beta_S = 0.315$.

Figure (IV.6) shows that the compensated Nusselt number on the smooth side $Nu \sim Ra^{\beta_S}$ remains constant over the three regimes. In the case of perfectly smooth cavity (S/S), we find again the classic scaling law as $Nu_{S/S} \sim 0.129 Ra^{0.299}$. The scaling exponent is slightly smaller comparing with smooth plate of R/S cell. However, it is not clear whether if this difference is an artifact or not. This result is generally consistent with Wei et al. (2014) experimental observations on the fact that the smooth plate of the R/S cavity seems to be insensitive to the presence of a rough plate on the opposite side.

IV.4.1 Comparison with the GL theory

The Grossman Lohse model (Grossmann and Lohse, 2000, 2001) has been developed for cavities with smooth boundaries. In the following, we use it to normalize and compare our results with numerical simulations and experimental data. We use the recent updated prefactor from (Stevens et al., 2013) to evaluate Nu_{GL} as,

$$Nu_{GL} = f_{GL}(Ra)$$

Where f_{GL} is the function that gives the Nusselt number for a given Rayleigh number in the GL model detailed in section (§ I.3.3) by resolving equations (I.38).

a) Smooth plate

The Nusselt number relative to smooth plate is plotted against the Rayleigh number as shown in figure (IV.7). It has been found in previous experimental work by Tisserand et al. (2011) and Rusaouën et al. (2018) that the thermal transfer from to the smooth plate was not modified by the presence of roughnesses on the bottom surface. According to their experiments performed at $Ra > 10^8$, the ratio Nu_S/Nu_{GL} relative to the smooth plates collapses

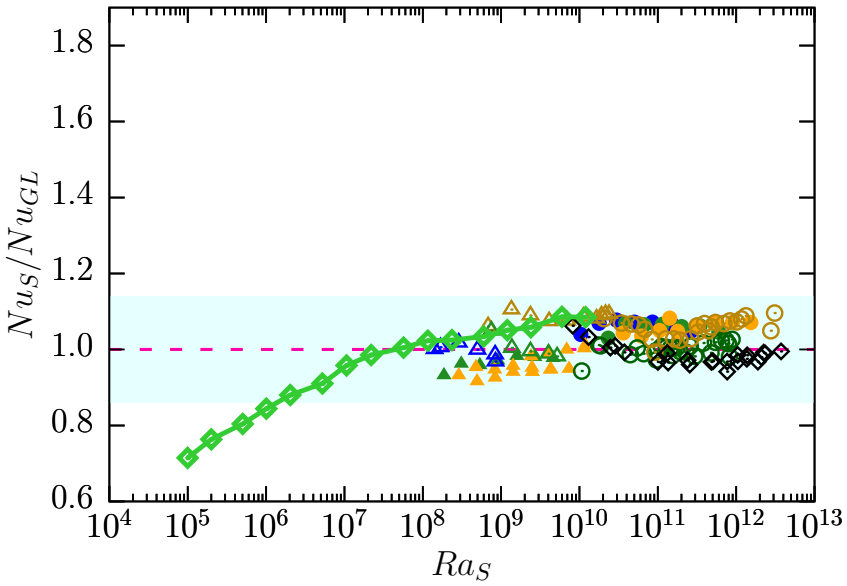

Fig. IV.7 Nu_S normalized by Nu_{GL} as a function of smooth Rayleigh Ra_S. Our DNS data are plotted with green diamond line (– ◇ –). The Nu_{GL} is estimated with the Grossmann - Lohse theory with updated prefactors (Stevens et al., 2013). Experimental results with de-ionized water : $H_p = 2mm$: small cell ($H = 0.2m$) (△ △ △), tall cell ($H = 1m$) (○○) from Tisserand et al. (2011) ; $H_p = 4mm$: small cell (▲ ▲), tall cell (●●●) and S/S cell as reference (◇) from Rusaouën et al. (2018).

on a single horizontal line (in the order of unity) with a dispersion of about 10%. DNS data for $Ra > 3\times10^6$ falls within this range and therefore shows a good agreement with GL model.

We note that $Nu_S \lesssim Nu_{GL}$ for smooth Rayleigh numbers less than $Ra_S \simeq 3 \times 10^6$. Indeed, this range of Rayleigh is poorly investigated especially by experiments that have been focused on relatively high Rayleigh numbers which are generally bigger than 10^8. The relative discrepancy with the GL model for low Rayleigh numbers $< 10^7$ is mainly due to the non-validity of this model for this range of Ra but also because of heat flux reduction due to insulating effects of roughness.

In figure (IV.8), we compare our DNS data in S/S cell with others numerical studies from (Wagner et al., 2012; Wagner and Shishkina, 2013; Kaczorowski et al., 2013, 2014) in the smooth cavities. It is clear that the GL model over estimates the DNS data for $Ra < 10^7$ for both $Pr = 0.786$ and $Pr = 4.38$ and different aspect ratios from the other DNS results. The GL model does not take into account the high dependence on the aspect ratio for low Ra numbers. Moreover, it is scaled based on experimental and numerical data mostly at high Ra numbers. This could be a reason that might explain the over prediction of the GL theory for small Ra numbers.

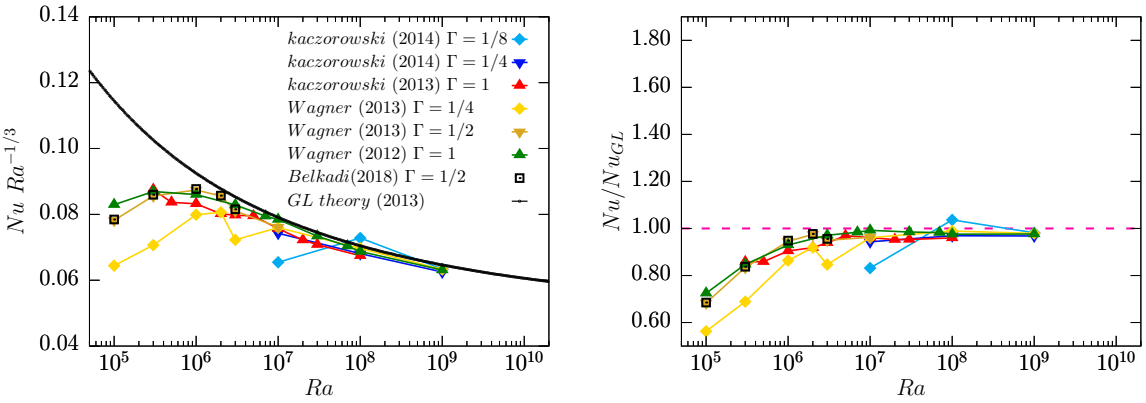

(a) $Pr = 0.786$ (b) $Pr = 0.786$

(c) $Pr = 4.38$ (d) $Pr = 4.38$

Fig. IV.8 Compensated Nusselt number as a function of Rayleigh number. Comparison of our numerical study and results from (Wagner et al., 2012; Wagner and Shishkina, 2013; Kaczorowski et al., 2013, 2014) with the GL model with updated prefactor (Stevens et al., 2013) for a smooth Rayleigh Bénard cavity for two Prandtl numbers (a) $Pr = 0.786$ and (b) $Pr = 4.38$.

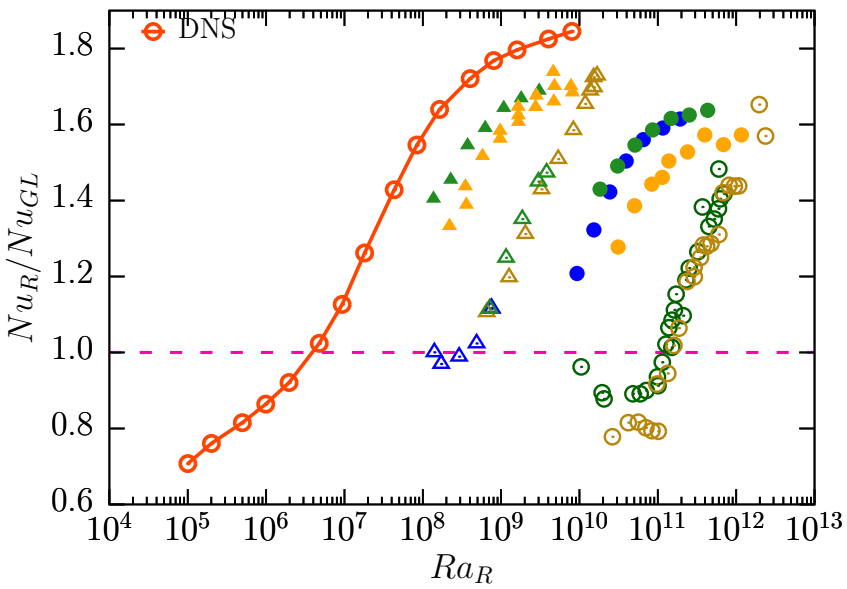

Fig. IV.9 Nu_R normalized by Nu_{GL} as a function of rough Rayleigh number Ra_R. Experimental results with de-ionized water : $H_p = 2mm$: small cell ($H = 0.2m$) (△ △ △), tall cell ($H = 1m$) (○○) from Tisserand et al. (2011) ; $H_p = 4mm$: small cell (▲ ▲), tall cell (●●●). DNS data are plotted with dotted line (– ● –).

b) Rough plate

The Nusselt number Nu_R of the rough plate is plotted as a function of Ra_R in figure (IV.9). We compare our results with experimental data from Tisserand et al. (2011) (open symbols) who used a roughness height $H_p = 2mm$ and from Rusaouën et al. (2018) (full symbols) who recently used taller roughnesses $H_p = 4mm$. Two asymmetric RB cells are used for both studies, a small cell ($H = 0.2m$) used for low Ra and a tall cell ($H = 1m$) is used to reach high Ra numbers.

As shown in figure (IV.7), the behavior of rough plates is considerably different from the smooth ones. The comparison between experimental sets shows a dispersed data, i.e. for the same rough RB cell, it shows different behaviors depending on the roughness height H_p. Tisserand et al. (2011) data goes from slightly reduced to an enhanced regime. The use of roughness elements twice higher by Rusaouën et al. (2018) results in an earlier enhancement of the heat transfer. It also shows a trend towards saturation at high Ra. The authors suggested that data are not scaled correctly and have proposed that the proper space scale is roughness height. The argument is that the enhancement takes place when the thermal BL thickness becomes on the order of roughness height. Consequently, the use of higher elements enhances the heat transfer at earlier Ra.

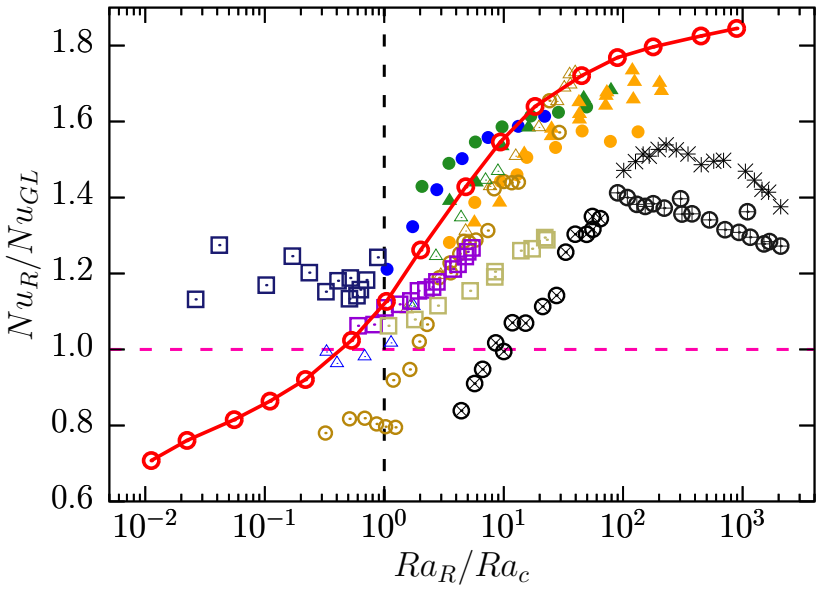

Fig. IV.10 Nu_R normalized by the Grossmann - Lohse model as a function of rough Rayleigh Ra_R normalized by critical Rayleigh number Ra_c. Our DNS data for Pr = 4.38 are plotted with dotted line (– • –). The Nu_{GL} and $Ra_c = f_{GL}^{-1}(H/(2H_p^*))$ is estimated with the Grossmann - Lohse theory with updated prefactors (Stevens et al., 2013). $H_p = 2mm$: small cell (△ △ △), tall cell (○○) from Tisserand et al. (2011) ; $H_p = 4mm$: small cell (▲ ▲) and tall cell (●●●) from Rusaouën et al. (2018) ; $H_p = 3mm$ R/S (⊗) and $H_p = 8mm$ S/R (⊕) and $H_p = 8mm$ R/S (∗) cylindrical asymmetric cell with pyramid-shaped roughness elements from Wei et al. (2014), rectangular cell $H_p = 2mm$ (□□□) from Salort et al. (2014).

In our case, despite the fact that our DNS are performed at quite smaller Ra numbers than in their experiments (a gap of 3 decades), consistent results with respect to experiments are obtained. Indeed, we reproduce the same trend of enhancement of Nu_R for a fixed geometrical configuration by varying only the Ra number. We can see a reduced Nu_R for ($Ra_R < 10^7$), following by an enhanced regime, then a tendency towards saturation, i.e $Nu_R/Nu_{GL} \longmapsto Cst$. The transition to enhanced heat transfer regimes in our case occurs at much lower Ra number than is experiments. This is because our roughnesses are the highest, among all cases. We have the largest ratio $H_p^* = H_p/H$ which means that the thermal BL becomes thinner than roughness height at a lower Ra than in the experiments.

The previous works have suggested that transition to enhanced regimes occurs when the thermal boundary layer thickness δ_θ becomes of the same size as roughness elements. Thus, the height of roughnesses H_p could be considered as a control parameter in the system. Following (Salort et al., 2014; Rusaouën et al., 2018), we define the critical Nusselt and Rayleigh numbers (Nu_c and Ra_c) for $H_p = 0.03$ based on the approximation given with the equation (III.16).

$$Nu_c = \frac{H}{2H_p} = 16.67 \tag{IV.1}$$

The critical Rayleigh number Ra_c can be estimated from Nu_c using GL model as

$$Ra_c = f_{GL}^{-1}(Nu_c) = 8.97 \times 10^6. \tag{IV.2}$$

Figure (IV.10) shows different data gathered from recent Rayleigh Bénard experiments with rough boundaries using either cylindrical cells Tisserand et al. (2011); Wei et al. (2014); Rusaouën et al. (2018) or rectangular shape cavities Salort et al. (2014). Globally, estimating Ra_c allows the authors to collapse data which shows the same trend from a reduced heat transfer regime for $Ra_R < Ra_c$ to an intensified regime. We could highlight some exceptions which may be due to other factors like experimental cell setup such as Prandtl number or roughness geometrical configuration that could impact highly the value of Nusselt number.

The present DNS is in fair agreement with this assumption. Normalization by relative Ra_c for each experiment setup allows to bring together most experimental results including our numerical data which fit the same trend of Nu increase especially those of Lyon. This results was expected since we used a very similar shape and distribution of roughness. Even if the height of roughness peep out as a crucial input in the system, we believe that for different geometric shapes of roughness elements, 3D flow dynamics around plots are not the same. A particular decreasing behavior of Nu for $Ra_R/Ra_c \geqslant 10^2$ is reported by Wei et al. (2014) (see figure IV.10), when using a cylindrical asymmetric cell in which $H_p = 8mm$. This could be related to the use of pyramid-shape roughness.

IV.4.2 Comparison with Salort et al. (2014) models : rough plate

b) Model 1 : BL totally destabilized

The first model given by Salort et al. (2014) is based on the destabilization of the laminar boundary layer (see the description in section (§ I.4.2)). Due to the roughnesses, their experimental results support the idea that the transition to enhanced regime II occurs when the thermal boundary layer thickness reaches the height of roughness. In this model based on the transition of BL to the turbulent state, the Nu number is related to Ra as follows

$$Nu_R = 0.5(2\sigma)^{3/2}(H_p/H)^{1/2}Ra^{1/2}, \tag{IV.3}$$

where σ a prefactor that we determine from the GL model as,

$$\sigma = Nu_c/Ra_c^{1/3}. \tag{IV.4}$$

As can be seen from the figure (IV.11), the description given by Salort et al. (2014) about a fully transited roughness-induced turbulent structure of the boundary layer is in agreement with enhancement of the effective scaling exponent beyond Ra_c. DNS results, as

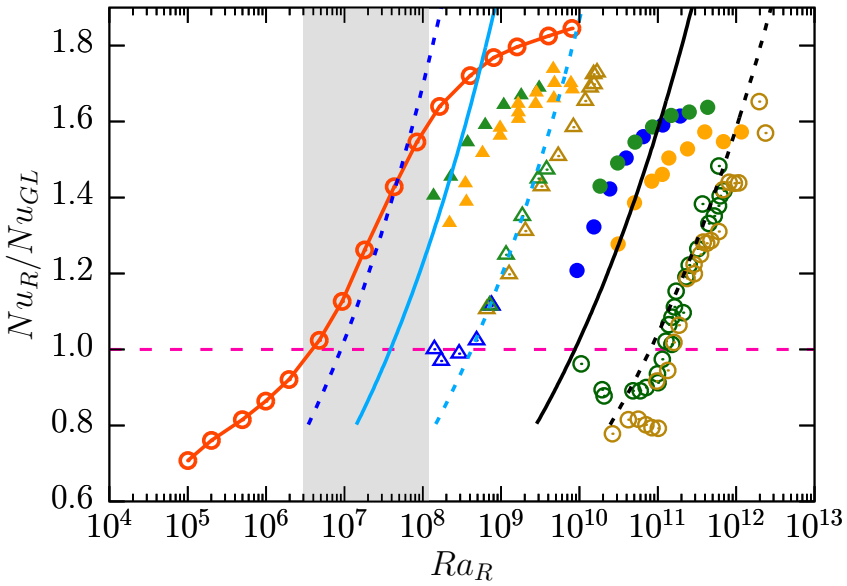

Fig. IV.11 Thermal transfer of the rough plate : Nu_R normalized by Nu_{GL} as a function of rough Rayleigh Ra_R. Symbol and color choices are the same as figure (IV.7). Our DNS data for are plotted with (– • –). Lines stand for equation (IV.3) : blue dotted line stand for our numerical cell with $\sigma = 0.0802$ for $H_p = 0.03$, cyan lines for small cell, black lines for tall cell, full lines are for $H_p = 4mm$ and dashed lines for $H_p = 2mm$ from Rusaouën et al. (2018).

well as experimental data from previous observations made by Tisserand et al. (2011) and Rusaouën et al. (2018) follow partially the model equation (IV.3) for specific range of Ra. In fact, this model uses a law with a scaling exponent $\beta = 1/2$ of a fully transited BL regime. However, for our DNS, there are substantial differences in the Ra range outside $[10^7 : 10^8]$. Deviations from this model are also apparent for Rusaouën et al. (2018) data (full symbols for $H_p = 4mm$) due to the decrease of the scaling exponent in regime III to $\beta_R = 1/3$.

b) Model 2 : BL partially destabilized

Salort et al. (2014) have also suggested that roughness elements could destabilize partially the boundary layers. A predictive model for rough Nusselt number Nu_R was proposed, based on geometrical contribution from different zones (details are given in section (§ I.4.2)). A comparison with this model for our case is shown in figure (IV.12). Reduced variables are used to withdraw roughness height dependence. For reference, the smooth Nusselt number and GL model are also plotted.

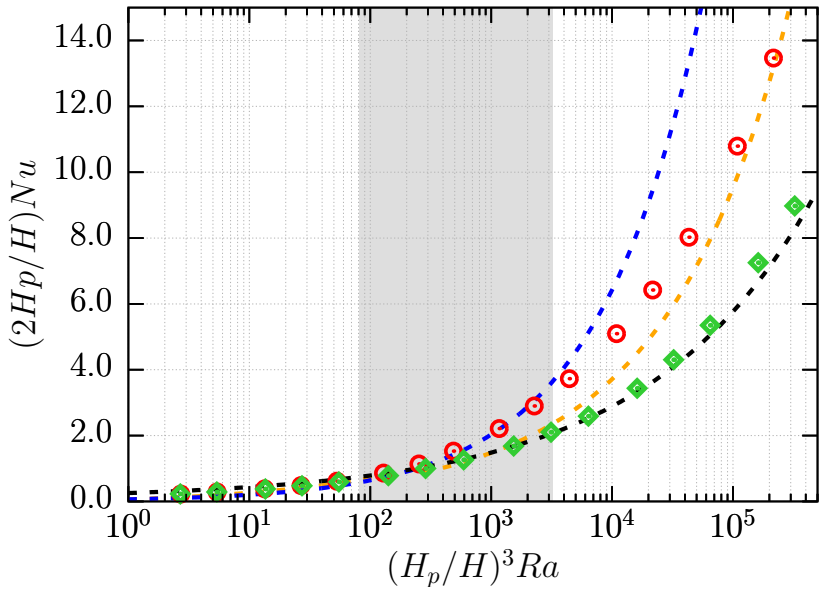

Fig. IV.12 Comparison of heat transfer data in reduced variables with theoretical models. Our DNS data for the rough half cell (○) and smooth half cell (♦). Blue dotted line stand for equation (IV.3), orange dotted line for the model prediction based on a change in the boundary layer structure (Salort et al., 2014), black dashed line : theoretical prediction for a smooth cell with the GL model (Stevens et al., 2013).

DNS data are in good agreement with the prediction model for low Rayleigh numbers mostly in regime I where roughnesses are inactive. However, it underestimates the rough Nu_R number in regime II where our results are much closer to the fully turbulent model from equation (IV.3). In regime III, data are getting closer to the Salort et al. (2014) second model, with a nearby increasing trend. The model seems more appropriate for high Ra numbers.

IV.4.3 Comparison with Göttingen models

First, we present application of the models of Shishkina and their coworkers before comparing with our DNS data.

a) 2D Model

In the following, we first compare results of the present DNS against the analytical two-dimensional model from Shishkina and Wagner (2011) (see the details in section (§ I.4.3)). It is based on the assumption of Prandtl Blasius BL to estimate the heat flux enhancement due to distinct regularly distributed obstacles as

$$Nu_R = Nu_S \left(\frac{1}{4} + \frac{3}{4}\frac{H_{esw}}{H} + \left(\frac{\xi}{2}\right)^{1/4} \frac{\Delta S}{S} \left(\frac{H_p}{H}\right)^{3/4} \right) \tag{IV.5}$$

Where H_{esw} is the equivalent smooth wall height (defined such that the volume of the convection cell with rough horizontal walls is equal to the volume of a cell with the height H_{esw} and smooth walls), ξ the obstacle rarity coefficient and $\Delta S/S$ is the relative increase of the total area covering the rough surface with respect to the area of smooth one.

In our case, the roughness elements are located relatively close to each other, we can approximate ξ a priori by taking $b = 0.3$, thus, $\xi = \frac{bW_p}{H_p} \approx \frac{3}{4}$. Here, $H_{esw} = H - \frac{2mW_pD_pH_p}{WD}$ and $\Delta S/S = \frac{4mW_pH_p}{WD}$ where the number of roughness elements is $m = 24$. We can rewrite the equation model (IV.5) as $Nu_R \sim aNu_S$. We will estimate a by taking $H_{esw} \approx H$, $\xi \approx 3/4$ and $\Delta S/S \approx 1$, thus the rough Nusselt number is approximated as follows

$$Nu_R \approx Nu_S \left(1 + 0.75 \left(\frac{H_p}{H}\right)^{3/4}\right) \tag{IV.6}$$

b) 3D Model

Similarly, we compare our data with Wagner and Shishkina (2015) 3d models developed to estimate the heat flux increase in the case of 3D obstacles larger than the mean thickness of the thermal boundary layer (details are provided in in section (§ I.4.3)). They proposed an empirical function for Nu_R based on their DNS data as,

$$Nu_R \approx Nu_S \left(1 + 5.84 \left(\frac{H_p}{H}\right) - 5.87\exp(7.42W_p/W) \left(\frac{H_p}{H}\right)^2\right) \tag{IV.7}$$

They also proposed a theoretical expression in the limiting case for slender obstacles ($W \to 0$) to estimate an upper bound for the ratio Nu_R/Nu_S

$$Nu_R \approx Nu_S \left(1 + C \left(\frac{H_p}{H}\right)^{3/4}\right) \tag{IV.8}$$

Where the coefficient C depends on Ra number and could be estimated with

$$C = \frac{A_R - A_S}{A_S}(2Nu_S)^{3/4}$$

c) Results and discussion

The comparison with equations models (IV.6),(IV.7) and (IV.8) is presented in figure (IV.13). It shows that the two dimensional model (cyan line) underestimates the enhancement of heat transfer in regimes II and III. Indeed, the relative increase of the total covering area or volume of the roughness obstacles cannot be a measure of the rough Nusselt number. The later results have been also reported in 3D configuration study by Wagner and Shishkina (2015). As expected, the 2D model is based on the enhancement of the prefactor in the scaling relation $Nu_R \sim CRa^{\beta}$. Thus, it does not predict an enhancement of the scaling exponent in the regime II that we have obtained in the present DNS, also reported in 2D numerical studies by Toppaladoddi et al. (2017) or Zhu et al. (2017, 2019).

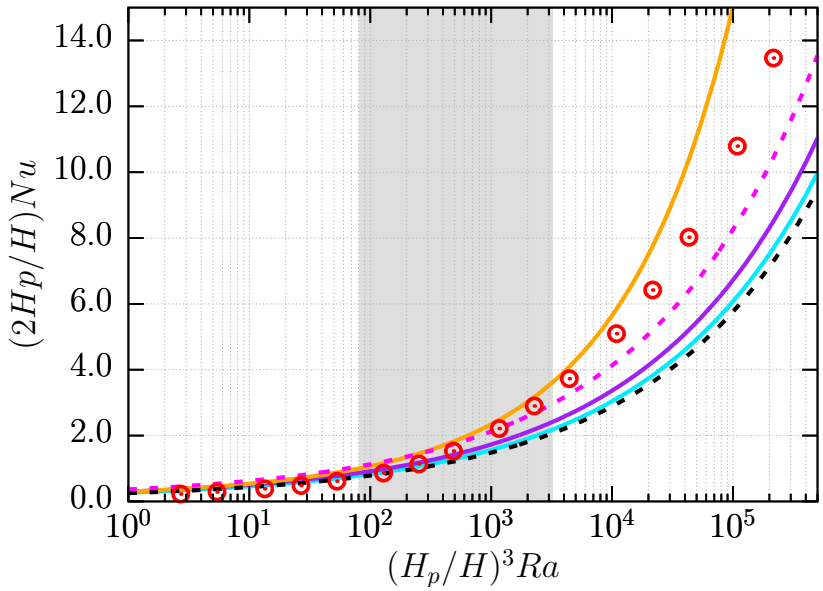

Fig. IV.13 Comparison of heat transfer data in reduced variables with theoretical models from Göttingen (Shishkina and Wagner, 2011; Wagner and Shishkina, 2015). The present DNS data for rough half side (○). Cyan line stand for equation (IV.6) for 2D rough model. Violet line stand for empirical function (IV.7). Orange line represent the upper bound prediction (IV.8). Black dashed line : theoretical prediction for a smooth cell with the GL model (Stevens et al., 2013). Magenta dashed line : heat transfer resulting for the pure increasing of the exchange surface in the case of symmetric rough cell.

It should be noted that the 2D model is constructed based on Pohlhausen (1921) theory for infinite vertical heated surfaces that neglects thermal plumes effects, contrary to what has been found by Du and Tong (2000) who used pyramids or Stringano et al. (2006) who used circular grooved surface. Both papers report an extra detachment of plumes near the top of roughnesses. One more reason for the underestimation of Nu_R could be the differences between two and three dimensional flow structures. Indeed, the interaction of the large scale circulation with the flow in between roughness elements is likely weaker in 2D case.

Additionally, figure (IV.13) shows that the prediction of rough Nusselt number with 3D empirical function (equation (IV.7)) (violet line) is considerably underestimated. It is far smaller than the heat transfer resulting from surface increase. Likewise, the upper bound prediction (orange line) deviates as we expected, it overestimates our DNS data in particular regime III. Those differences could be explained by the fact that the 3D model does not account for the spacing between obstacles in the transversal direction. Thus, the fluid in between roughnesses is not fully washed by the large scale circulation, unlike our case, where it can flow around obstacles, thus boosting the convective heat transfer.

IV.5 Description of the heat flux at roughness scale

In order to determine more precisely the effect of roughness on the heat transfer close to the wall, we analyze the heat transfer behavior in the R/S cavity and its evolution with the height z. We have $Nu(z < H_p) < Nu_{R/S}$ due to the horizontal contribution from vertical surfaces of roughness. Otherwise, $Nu(z > H_p) = Nu_{R/S}$ because vertical sides of the cavity are adiabatic. Our approach is based on the decomposition of the global heat flux $Nu_{R/S}$ measured inside the asymmetric cavity but outside the roughness region ($z > H_p$) into two contributions : a conductive heat flux will be denoted by Nu^{cd} and a convective heat flux with Nu^{cv} as follows

$$Nu_{R/S} = Nu^{cd}_{R/S}(z) + Nu^{cv}_{R/S}(z) \text{ with } z \geqslant H_p \tag{IV.9}$$

$$Nu^{cd}_{R/S}(z) = \int_S -\partial\langle\overline{\theta}\rangle_S/\partial z ds \tag{IV.10}$$

$$Nu^{cv}_{R/S}(z) = \int_S \sqrt{Ra}\ \langle\overline{w\theta}\rangle_S(z) ds \tag{IV.11}$$

IV.5.1 Relative contribution to the heat flux near roughness

We determine the relative contribution from conduction and convection to the increase of Nu number. Figure (IV.14) shows the contribution of vertical conduction and convection as function of the height z for different Ra numbers corresponding to the three regimes previously identified. We normalize with $Nu_{R/S}$ to compare the behavior at different Ra.

In regime I, as shown in figures (IV.14a) and (IV.14b), heat transfer is dominated by conduction on roughness in the $z < H_p^*$ region. Convection has a minor contribution less than 4% which shows that the fluid surrounding obstacles is mostly at rest. Heat is accumulated and is not transported into bulk region which reduces the heat transfer inside the system. This is consistent with the recent numerical study of Zhang et al. (2018) who links this effect to an additional thermal resistance created by motionless fluid between the roughness elements. We also notice that the conductive heat flux at the bottom wall $z = 0$ is quasi constant $Nu_{bot} = 38\%\ Nu_{R/S}$. We can deduce that the contribution from vertical wall of roughness is important.

In regime II, as shown in figures (IV.14c) and (IV.14d), the contribution of conduction term decreases rapidly inbetween roughness for $\frac{H_p^*}{3} < z < H_p^*$, while convection motion increases significantly with increasing Ra number. In this regime, we can highlight a switch of the heat transfer dominant mode from conductive to convective. A significant amount of heat around roughness is transported efficiently into the bulk region which enhances the global heat transfer. However, it is unclear how these changes could explain the enhancement of the scaling exponent β in the relation $Nu \sim Ra^{\beta}$, but we conjecture that a connection exists between the change of contribution from conduction/convection and the scaling law. During this regime, we notice that the contribution of Nu_{bot} increase from 38% to 64% with increasing Ra.

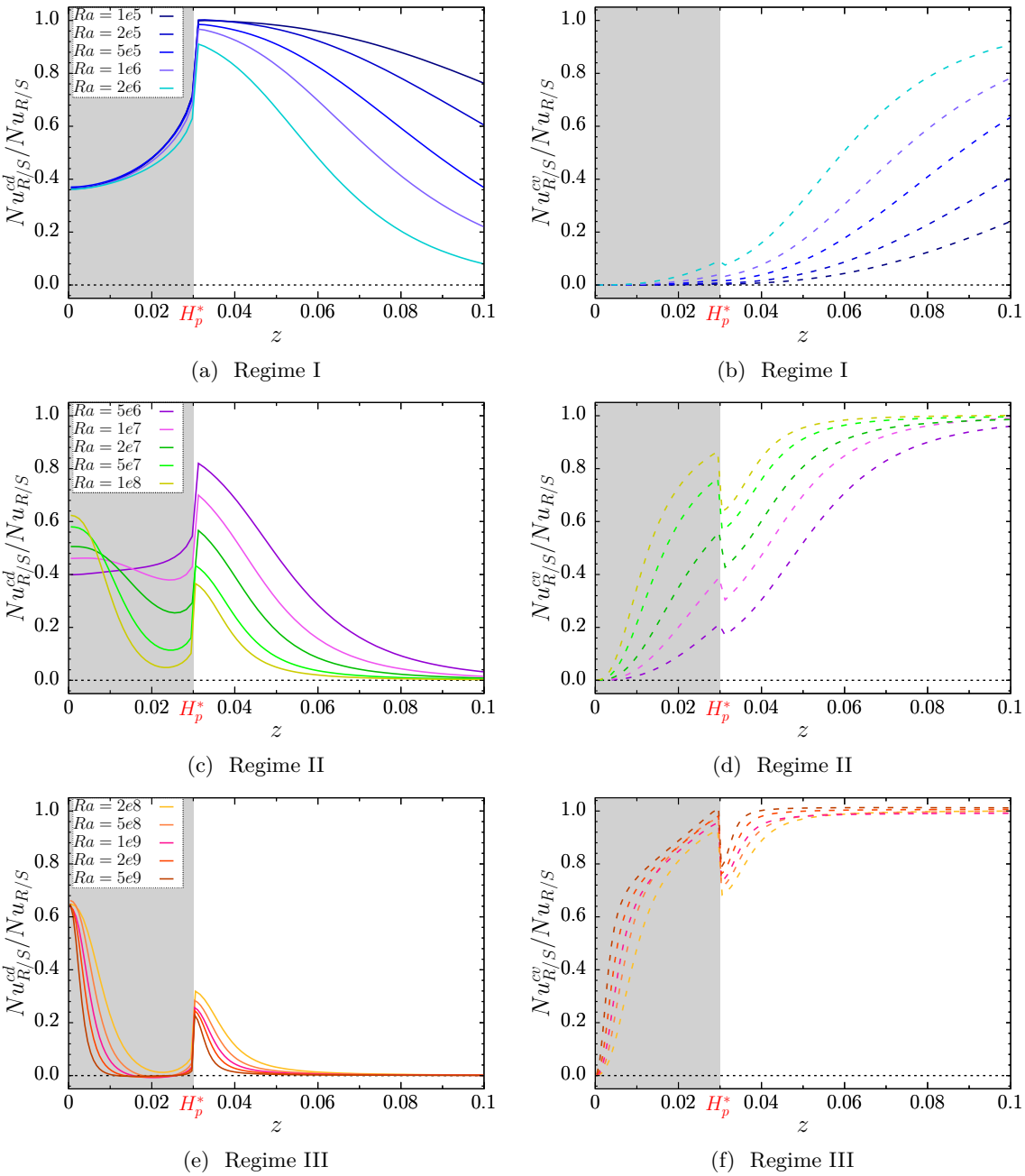

(a) Regime I (b) Regime I

(c) Regime II (d) Regime II

(e) Regime III (f) Regime III

Fig. IV.14 (a,c,e) Normalized vertical conductive and (b,d,f) normalized convective heat flux as function of Ra number in (a,b) regime I, (c,d) regime II and (e,f) regime III.

In regime III, as shown in figures (IV.14e) and (IV.14f), the conductive heat flux contribution decreases to less than 3% in the fluid between roughness elements. Convective mode is dominant near obstacles. The zone around roughnesses is getting fully washed by the large scale circulation. It is noticeable that Nu_{bot} becomes again constant around $64\% Nu_{R/S}$.

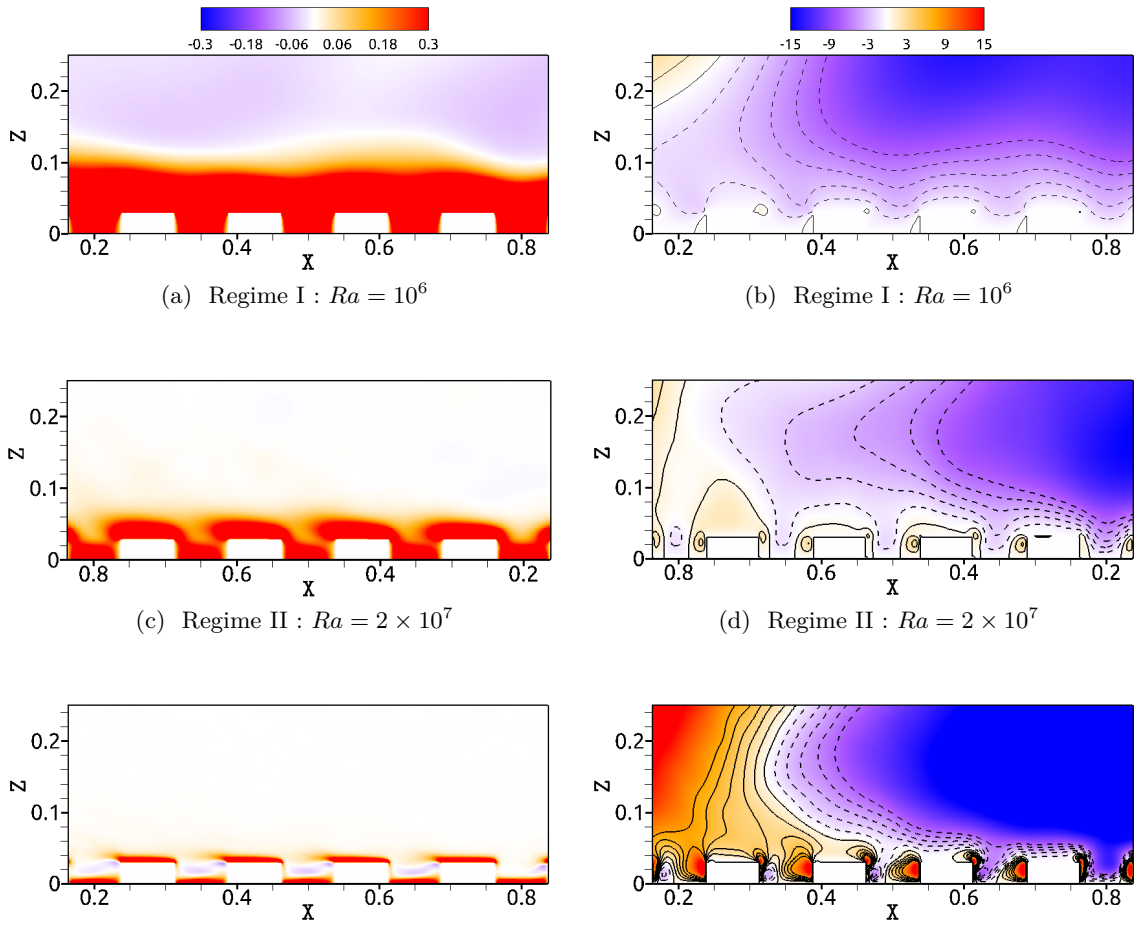

(a) Regime I : $Ra = 10^6$ (b) Regime I : $Ra = 10^6$

(c) Regime II : $Ra = 2 \times 10^7$ (d) Regime II : $Ra = 2 \times 10^7$

(e) Regime III : $Ra = 10^9$ (f) Regime III : $Ra = 10^9$

Fig. IV.15 Slice section near roughness elements at $y = 0.1875$. (a,c,e) Normalized mean vertical conductive heat transfer $Nu^{cd}/Nu_{R/S}$ and (b,d,f) normalized mean convective heat flux $Nu^{cv}/Nu_{R/S}$. Black lines are positive isovalues of mean convective heat flux $\overline{w}\overline{\theta}$, black dashed lines are for negative isovalues.

In order to clarify better the process of thermal transfer near roughnesses we have selected a representative Ra number for each regime. Figure (IV.15) shows a slice section of vertical conductive and convective heat flux in the plane (x, z) passing through the obstacles. In regime I, roughnesses are fully submerged inside the conductive zone (figure (IV.15a)) and we can see a very weak convective motion between roughnesses (figure(IV.15b)). This behavior could be associated with a thermal resistance that reduces the heat transfer. In regime II, a thick conductive layer is observed on top of and in between roughnesses (figure (IV.15c)), it takes the shape of obstacles such as moving waves with the direction of the mean flow. The heat inbetween roughness is getting convected (figure (IV.15d)), especially near the vertical surfaces of roughness where the vertical convective motion has enough strength to

transfer the accumulated heat from the inner to bulk region. Thus, it contributes to the enhancement of thermal transfer. In regime III, the conductive layer becomes thinner than the roughness height. It is still localized on top of roughness and on the bottom plate at $z = 0$ (figure (IV.15e)). We can also see the formation of a thin opposing conductive layer, i.e. an adverse gradient of temperature in the inner region which reveals that heat is getting partially transferred via conduction from the bulk to inner region. As shown in figure (IV.15f), the bulk flow penetrates the inner region that becomes fully convective notably near vertical edges of roughness. However, the heat ejection process is damped by an intense bulk flow. A connexion may exist between this effect and the return to the classical scaling with $\beta = 1/3$.

IV.5.2 Geometric separation of the heat flux at roughness height

The heat transfer regime depends strongly on the height of roughness elements. In the purpose of understanding mechanisms of heat exchanges at the roughness scale, we decompose the heat flux $Nu_{R/S}$ measured at $z = H_p^*$ in different manners.

Conductive versus convective heat flux

We firstly represent the two contributions from conduction and convection as sketched in figure (IV.16) : (i) the vertical conductive heat flux from fluid and the top surface of roughness elements is denoted $Nu^{cd}_{R/S}|_{H_p^*}$ and (ii) the convective heat flux from the fluid is denoted $Nu^{cv}_{R/S}|_{H_p^*}$,

$$Nu_{R/S} = Nu^{cd}_{R/S}|_{H_p^*} + Nu^{cv}_{R/S}|_{H_p^*} \tag{IV.12}$$

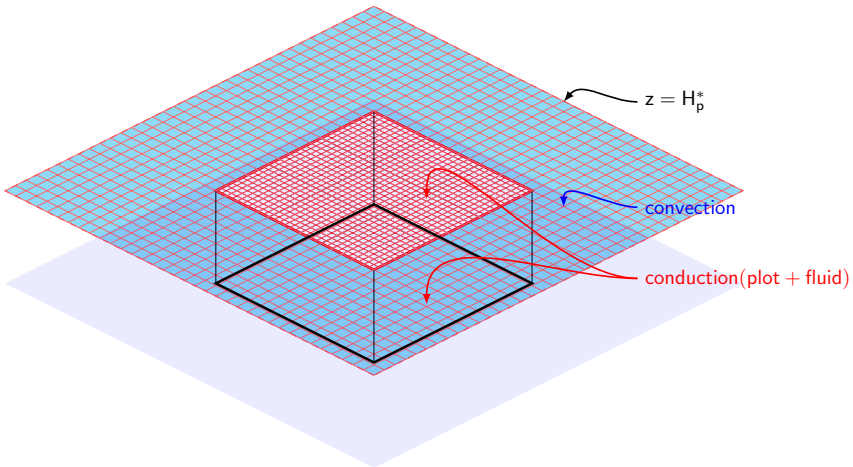

Fig. IV.16 Sketch representing physical decomposition of global heat flux $Nu_{R/S}$ at $z = H_p^*$ into convective flux $Nu^{cv}|_{H_p^*}$ and conductive flux $Nu^{cd}|_{H_p^*}$ contributions.

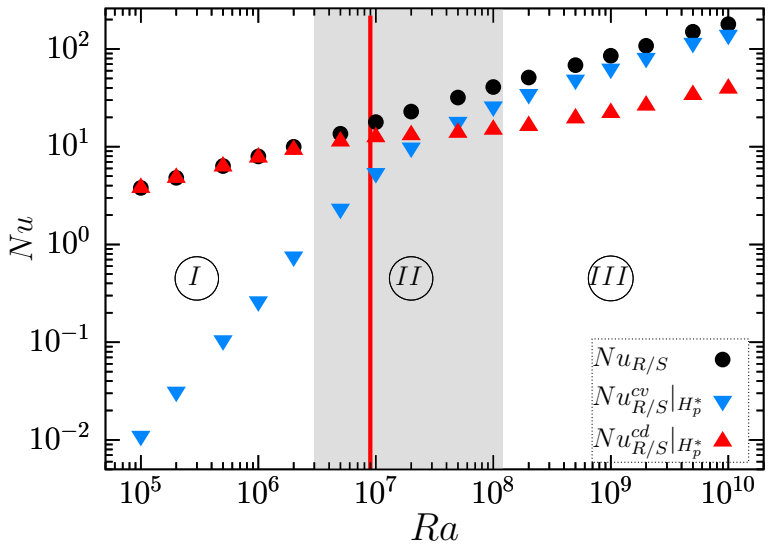

Fig. IV.17 Physical decomposition of global heat flux $Nu_{R/S}$ at $z = H_p^*$ into convective $Nu^{cv}_{R/S}|_{H_p^*}$ and vertical conductive $Nu^{cd}_{R/S}|_{H_p^*}$ contributions. Vertical red line correspond to critical Rayleigh number Ra_c of the present physical configuration.

We can see from figure (IV.17) that the heat transfer in regime I is strongly conductive $Nu^{cd}_{R/S}|_{H_p^*} \gg Nu^{cv}|_{H_p^*}$, the fluid surrounding roughnesses is most probably at rest since $Nu^{cv}_{R/S}|_{H_p^*} < 1$. The contribution of convection keeps growing up in regime II and $Nu^{cv}_{R/S}|_{H_p^*}$ becomes larger than $Nu^{cd}_{R/S}|_{H_p^*}$ around $Ra = Ra_c$. In regime III, convective mode becomes dominant with a contribution to the global heat flux larger than 90%.

Fluid versus plot

Another possibility is to decompose geometrically the global heat flux $Nu_{R/S}$ as sketched in figure (IV.18) into two contributions : (i) one from the top of roughness elements (which is only diffusive owing to the velocity being zero) denoted by $Nu_{R/S}|^{plot}_{H_p^*}$ and (ii) one from the fluid (which includes both convective and diffusive effects) and will be denoted by $Nu_{R/S}|^{fluid}_{H_p^*}$ as follows

$$Nu_{R/S} = Nu_{R/S}|^{fluid}_{H_p^*} + Nu_{R/S}|^{plot}_{H_p^*} \tag{IV.13}$$

The contribution from each part is estimated with

$$Nu_{R/S}|^{fluid}_{H_p^*} = \int_S \sqrt{Ra}\ \langle\overline{w\theta}\rangle_S ds + \int_S -\partial_z\langle\overline{\theta}\rangle_S ds \qquad \text{with} \qquad S \equiv fluid \tag{IV.14}$$

$$Nu_{R/S}|^{plot}_{H_p^*} = \int_S -\partial_z\langle\overline{\theta}\rangle_S ds \qquad \text{with} \qquad S \equiv plot \tag{IV.15}$$

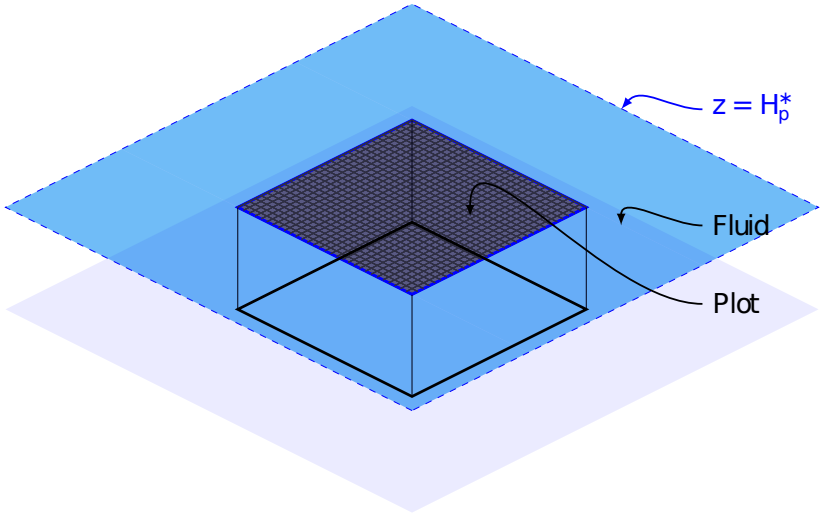

Fig. IV.18 Sketch representing geometrical decomposition of global heat flux $Nu_{R/S}$ at $z = H_p^*$ into contribution from the fluid $Nu_{R/S}|_{H_p^*}^{fluid}$ and a contribution from the up surface of plots $Nu_{R/S}|_{H_p^*}^{plot}$.

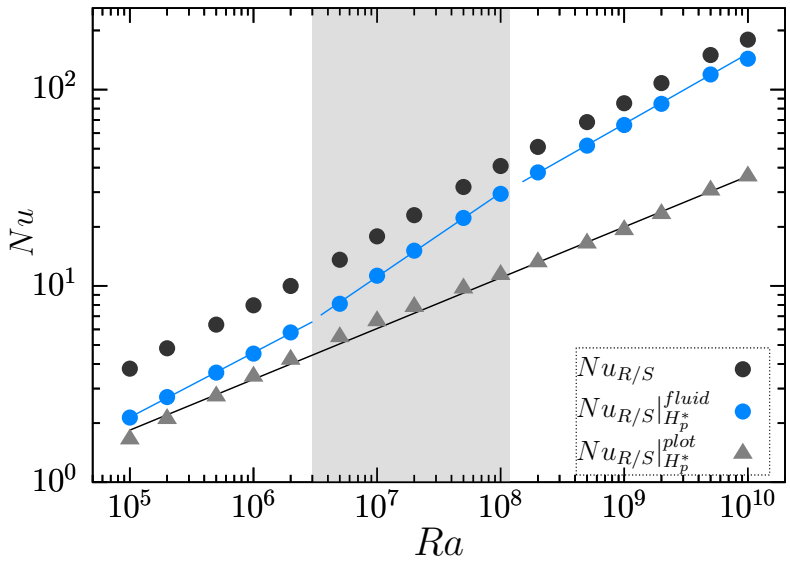

Fig. IV.19 Decomposition of global heat flux $Nu_{R/S}$ at $z = H_p^*$ into contribution from the fluid area $Nu_{R/S}|_{H_p^*}^{fluid}$ or top side of plots $Nu_{R/S}|_{H_p^*}^{plot}$. The lines represent power-law fits given in table [IV.1].

Following this separation, the individual behavior of plot and fluid zones is shown in figure (IV.19). A unique scaling exponent could be assigned to the plot zone while noticeable change of the scaling law could be viewed in the fluid zone (coefficients of the scaling laws are provided in table (IV.1)). This shows that the heat transfer regimes is strongly dependent on the behavior of the fluid zone.

Table IV.1 Scaling laws for Nusselt numbers relative to fluid or plot zones.

Regime	$Nu_{R/S} \sim cRa^{\beta}$	
	$Nu_{R/S}\|_{H_p^*}^{plot}$	$Nu_{R/S}\|_{H_p^*}^{fluid}$
I	$\downarrow$	$0.048\ Ra^{0.329}$
II	$0.091\ Ra^{0.260}$	$0.011\ Ra^{0.428}$
III	$\downarrow$	$0.042\ Ra^{0.356}$

Based on previous results, we separate heat flux from the fluid (equation (IV.14)) into a contribution of conduction $Nu_{R/S}^{cd}|_{H_p^*}^{fluid}$ and another from convection $Nu_{R/S}^{cv}|_{H_p^*}^{fluid}$ as follow

$$Nu_{R/S}^{fluid}|_{H_p^*} = Nu_{R/S}^{cd}|_{H_p^*}^{fluid} + Nu_{R/S}^{cv}|_{H_p^*}^{fluid} \tag{IV.16}$$

The contribution from each part is estimated with

$$Nu_{R/S}^{cd}|_{H_p^*}^{fluid} = \int_S -\partial_z \langle \overline{\theta} \rangle_S ds \qquad \text{with} \qquad S \equiv fluid \tag{IV.17}$$

$$Nu_{R/S}^{cv}|_{H_p^*}^{fluid} = \int_S \sqrt{Ra}\ \langle \overline{w\theta} \rangle_S ds \qquad \text{with} \qquad S \equiv fluid \tag{IV.18}$$

This decomposition in represented in figure (IV.20a). It seems that $Nu_{R/S}^{cd}|_{H_p^*}^{plot} \sim Ra^{\beta}$ has a unique scaling law with an exponent $\beta \approx 2/7$ in all regimes. Therefore, the plot zone follows the hard turbulence regime (Castaing et al., 1989; Cioni et al., 1997) that supposes a purely conductive BL. It confirms that successive transitions are probably not due to a change of plot zone behavior.

For the fluid zone, different behaviors were identified :

1. Regime I : the growth rate of $Nu_{R/S}^{cv}|_{H_p^*}^{fluid}$ is higher with $\beta = 7/5$ but with a very weak prefactor $c = 10^{-9}$. Conduction mode is still dominant with an exponent β around 2/7 similar to the plot zone but with a greater prefactor c, which means that conduction is more important from the fluid. This behavior is due to heat accumulation owing to low velocities around roughness elements.
2. Regime II : the identification of a scaling law is not obvious as the heat transfer switches from a dominant conductive to convective mode during this regime. We note that all contributions to the heat flux become roughly equal at Ra_c, i.e $Nu_{R/S}^{cv}|_{H_p^*}^{fluid} \approx Nu_{R/S}^{cd}|_{H_p^*}^{fluid} \approx Nu_{R/S}^{cd}|_{H_p^*}^{plot}$. This confirms that roughness height is a decisive factor. It should also be noted that the fluid conduction decreases towards an apparently asymptotic value.
3. Regime III : the exchange of heat at $z = H_p^*$ is largely ensured via convection mode, while the fluid conduction remains constant around $Nu_{R/S}^{cd}|_{H_p^*}^{fluid} \approx 3$.

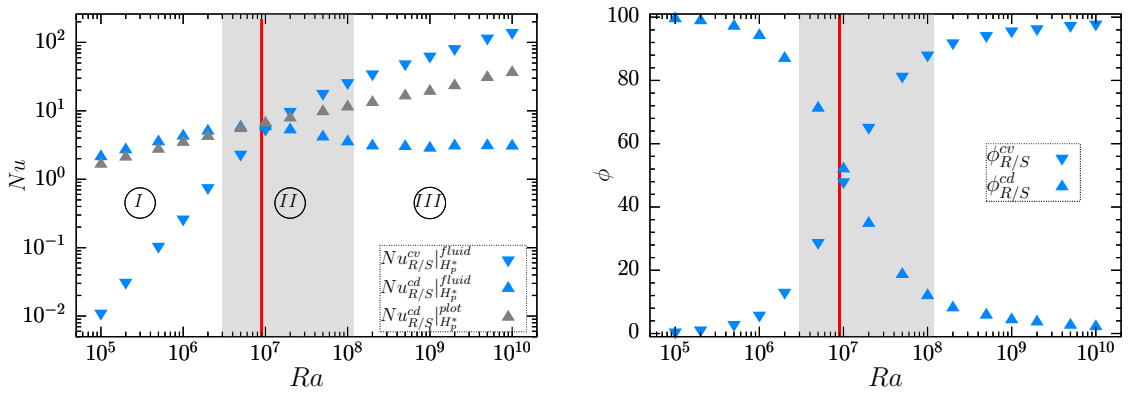

(a) (b)

Fig. IV.20 (a) Decomposition of global heat flux $Nu_{R/S}$ at $z = H_p^*$ into contribution from fluid area : $Nu^{cv}_{R/S}|^{fluid}_{H_p^*}$ (eq.IV.18) and $Nu^{cd}_{R/S}|^{fluid}_{H_p^*}$ (eq.IV.17) and the top side of plots : $Nu^{cd}_{R/S}|^{plot}_{H_p^*}$ (eq.IV.15). (b) Contribution of conductive (eq.IV.19) and convective (eq.IV.20) heat fluxes to the heat transfer in the fluid. Vertical red line is Ra_c.

We compare relative contribution of conduction and convection to the total fluid part via the ratio ϕ as follows

$$\phi^{cd}_{R/S} = Nu^{cd}_{R/S}|^{fluid}_{H_p^*}/Nu_{R/S}|^{fluid}_{H_p^*} \tag{IV.19}$$

$$\phi^{cv}_{R/S} = Nu^{cv}_{R/S}|^{fluid}_{H_p^*}/Nu_{R/S}|^{fluid}_{H_p^*} \tag{IV.20}$$

As shown in figure (IV.20b), the heat transfer in fluid is mostly conductive in regime I with a contribution upper than 90%. The two contributions become similar at Ra_c. In regime III, the contribution from conduction part becomes lower than 10%.

Relative responses of the rough plate based on the separation of plates

The previous results illustrate the strong dependence of the global Nusselt number $Nu_{R/S}$ on the behavior of the fluid zone around the roughnesses. This means that to understand the change in scaling exponent, it is necessary to focus on the rough plate rather than the full asymmetrical cell. Therefore, it is more convenient to use separation of plates to express all the quantities relatively to the rough plate. We can deduce from equations (III.14), (IV.14) and (IV.15) the following relations,

$$\begin{cases} Nu_R & = Nu_R|^{fluid}_{H_p^*} + Nu_R|^{plot}_{H_p^*} \\ Nu_R|^{fluid}_{H_p^*} & = Nu_{R/S}|^{fluid}_{H_p^*}/\Delta\theta_R \\ Nu_R|^{plot}_{H_p^*} & = Nu_{R/S}|^{plot}_{H_p^*}/\Delta\theta_R \end{cases} \tag{IV.21}$$

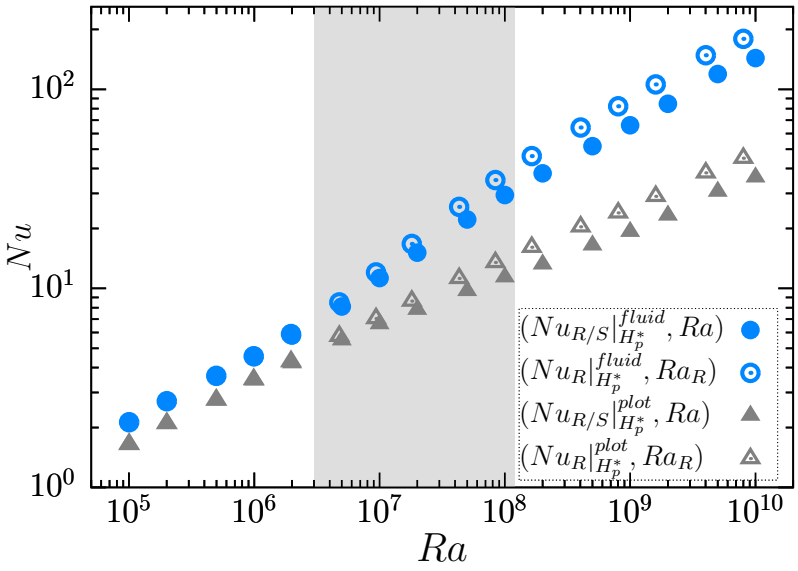

Fig. IV.21 Separation of plates gives the relative rough Nusselt numbers : a contribution from fluid $Nu_R|^{fluid}_{H_p^*}$ and from plot $Nu_R|^{plot}_{H_p^*}$ (open symbols). Decomposition in the case of R/S cell : a contribution from fluid $Nu_{R/S}|^{fluid}_{H_p^*}$ and from plots $Nu_{R/S}|^{plot}_{H_p^*}$ (full symbols)

Figure (IV.21) compares the expressions in equation (IV.21). In regime I, rough Nusselt numbers are similar to those in R/S cell. In regime II, the growth rate of $Nu_R|^{fluid}_{H_p^*}$ is bigger than $Nu_{R/S}|^{fluid}_{H_p^*}$ while the increase of $Nu_R|^{plot}_{H_p^*}$ becomes weaker. In regime III, scaling laws for rough plate are similar to those of R/S cell.

The individual behavior of plot and fluid zones is shown in figure (IV.22). The rough Nusselt number Nu_R is also plotted to evince differences of power-laws fit. Practically, plot zone has only one scaling law in all regimes with an exponent $\beta \approx 0.30$. The behavior of rough fluid Nusselt number $Nu_R|^{fluid}_{H_p^*}$ is correlated with global rough Nusselt number Nu_R. In regime I, a scaling law with $\beta \approx 1/3$ is obtained, then, an enhancement of the scaling exponent in regime II to $\beta \approx 1/2$, later, in regime III, we can observe a reduction of scaling exponent $\beta \approx 0.36$ (details are provided in table (IV.2)).

Table IV.2 Scaling laws for rough Nusselt numbers relative to fluid and plot zones.

Regime	$Nu_R \sim cRa_R^\beta$	
	$Nu_R\|^{plot}_{H_p^*}$	$Nu_R\|^{fluid}_{H_p^*}$
I	$\downarrow$	$0.0429\ Ra^{0.338}$
II	$0.059\ Ra^{0.295}$	$0.0043\ Ra^{0.493}$
III	$\downarrow$	$0.0469\ Ra^{0.364}$

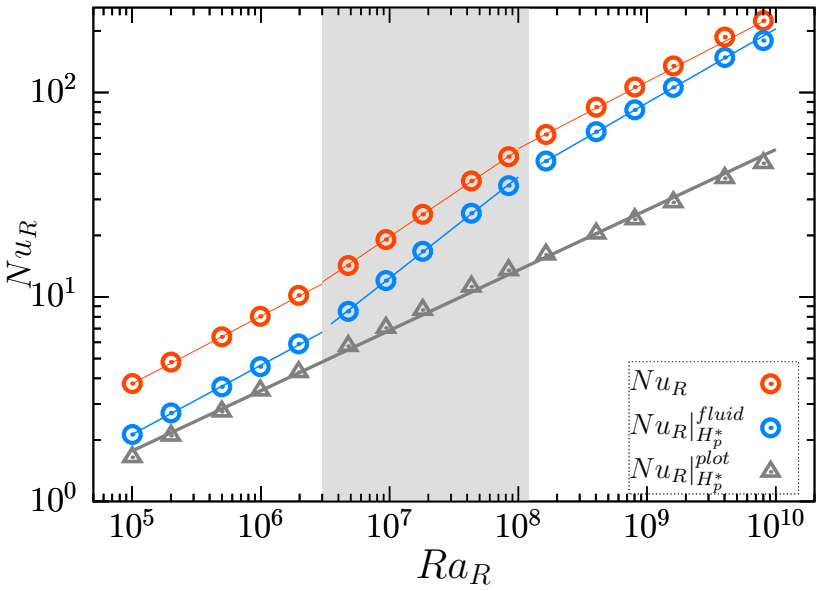

Fig. IV.22 Decomposition of rough heat flux Nu_R at $z = H_p^*$ into contribution from fluid $Nu_R|^{fluid}_{H_p^*}$ and from plots $Nu_R|^{plot}_{H_p^*}$. The Lines represent power-law fits given in table [IV.2].

The enhanced regime II is characterized by a local increase of the scaling law exponent to $\beta = 1/2$ which has predicted by Kraichnan (1962) theory and observed in experimental results from Roche et al. (2010) by implementing V-shaped axis symmetrical grooves. Our DNS shows this behavior but only in the fluid zone. The two dimensional DNS studies from Toppaladoddi et al. (2017) and Zhu et al. (2017) who used sinusoidally rough plates have observed an effective scaling exponent $\beta = 1/2$ in the whole cavity for particular roughness wavelengths. Recently, it was reported by Zhu et al. (2019) 2D DNS using multi scale roughnesses. This dependence on the spacing inbetween obstacles could also be explained by the dependence on the fluid behavior in between roughnesses.

Conductive versus convective heat fluxes relative to the rough plate

Likewise, we use the separation of plates to identify and isolate the roughness effects and contribution to the rough Nusselt number Nu_R. We can deduce from equations (III.14), (IV.10) and (IV.11) the following relations,

$$\begin{cases} Nu_R & = Nu_R^{cd}|_{H_p^*} + Nu_R^{cv}|_{H_p^*} \\ Nu_R^{cd}|_{H_p^*} & = Nu_{R/S}^{cd}|_{H_p^*}/\Delta\theta_R \\ Nu_R^{cv}|_{H_p^*} & = Nu_{R/S}^{cv}|_{H_p^*}/\Delta\theta_R \end{cases} \tag{IV.22}$$

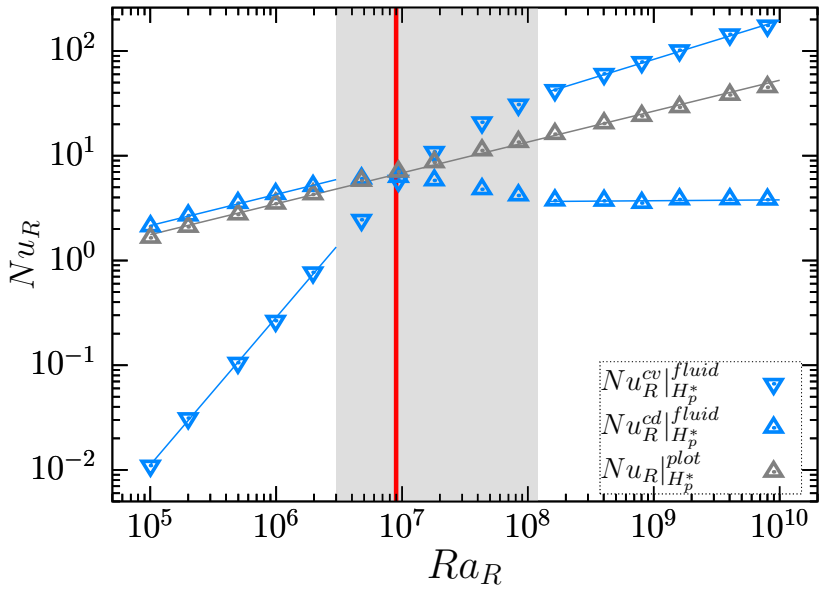

Fig. IV.23 Decomposition of rough heat flux Nu_R at $z = H_p^*$ into contribution from fluid area : $Nu_R^{cv}|_{H_p^*}^{fluid}$ and $Nu_R^{cd}|_{H_p^*}^{fluid}$ or top side of plots : $Nu_R^{cd}|_{H_p^*}^{plot}$. Vertical red line is Ra_c. The lines represent power-law fits given in table [IV.3].

We can also deduce from equations (IV.16) and (IV.22),

$$\begin{cases} Nu_R^{cd}|_{H_p^*}^{fluid} &= Nu_{R/S}^{cd}|_{H_p^*}^{fluid}/\Delta\theta_R \\ \\ Nu_R^{cd}|_{H_p^*}^{plot} &= Nu_{R/S}^{cd}|_{H_p^*}^{plot}/\Delta\theta_R \end{cases} \tag{IV.23}$$

The results of this decomposition are presented in figure (IV.23). The behavior of the Nusselt numbers associated with rough plate is strongly correlated with those related to R/S cell. By performing a linear regression, we identify scaling laws related to rough plate as summarized in table [IV.3]. We note that the identification of scaling laws is not obvious in regime II.

Table IV.3 Scaling laws for rough conductive and convective Nusselt numbers.

Regime	$Nu_R^{cd} \sim cRa_R^{\beta}$		$Nu_R^{cv} \sim cRa_R^{\beta}$
	plot	fluid	
I	$\downarrow$	$0.07\ Ra^{0.297}$	$10^{-9}\ Ra^{1.41}$
II	$0.059\ Ra^{0.295}$	/	/
III	$\downarrow$	≈ 3.5	$0.031\ Ra^{0.38}$

How conduction and convection effect on the scaling laws is not easy to establish. The

important points here are : (i) the non-dependence of the heat transfer regimes to the plot zone which have a smooth cell scaling with $\beta \approx 0.30$, (ii) the change of heat transfer regime is mainly linked to fluid characteristics. As shown in figure (IV.23), in regime I, the heat flux is strongly conductive and convection is negligible. In regime II, convection increases and balances the conduction contribution at critical Rayleigh number. In regime III, the convective heat flux from the fluid is larger than the conduction from the top of plot. In addition, we note a higher scaling exponent $\beta = 0.38$ for the convective heat flux which keeps increasing where the conductive one remains almost constant.

IV.6 Conclusion

A global description of the heat transfer in the asymmetric cell R/S is discussed. We have identified three successive regimes of heat transfer : (i) a thermally resistant regime I where $Nu_{R/S}$ is reduced comparing with $Nu_{S/S}$, (ii) an enhanced intermediate regime II and (iii) a regime III in which the increase of $Nu_{R/S}$ is larger than relative increase of surface due to roughness. By separating the smooth and rough plates, we found only one scaling law exponent for the smooth plate $\beta_S = 0.315$. Two scaling exponents could be associated with the rough plate, i.e. in regimes I and III we found $\beta_R = 1/3$ while it get increased to $\beta_R = 0.43$ in regime II.

Through the decomposition of rough Nusselt number into conductive and convective parts, we showed that conduction is the dominant mode in regime I. The fluid surrounding roughnesses is practically at rest which reduces the heat transfer. Convection contribution becomes important in regime II, it matches with the other contributions of conduction parts from the plot and fluid zones at critical Rayleigh number. In the regime III, convection becomes the dominant mode.

Through the spatial decomposition of the rough Nusselt number at the roughness height H_p into fluid and plot parts, we found a unique scaling law for the top of roughness that behaves like a smooth plate. Otherwise, the behavior of the fluid zone is strongly correlated with the global behavior of Nu_R, i.e three regimes are also identified for the fluid zone. Our results confirm that the heat transfer regime depends on the roughnesses height and on the flow dynamics around these obstacles. As the heat transfer is initiated inside the boundary layers, it suggests details of the flow structure near the roughened surface in particular over the surrounding fluid. Therefore, in the next chapter § V, the decomposition plot/fluid will be maintained and we will focus our analysis on the study of boundary layers.

V – Effect of roughnesses on the flow structure and statistics

V.1 Introduction

We have seen in chapter (§ IV) that different heat transfer regimes exist. We also showed that the surface on the top of roughness differs from the behavior of the surrounding fluid zone. We then expect the characteristics of the flow to be different, and specifically the boundary layers to be modified, a change in the wind patterns near the rough wall would be expected. In the present chapter, we first characterize how the mean profiles are modified by roughness. We then study in detail the effect of roughness on the BL using different definitions from the literature given in section (§ III.3). Finally we discuss the effect of roughness on the turbulent fluctuations.

V.2 Effects of roughness on mean profiles

V.2.1 Global effect

As shown in figure (V.1), vertical profiles of mean temperature are plotted for the different Ra numbers of previous simulations in the R/S cell. Profiles that correspond to the same regime of heat transfer identified in [§ IV] are gathered within the same sub-figure.

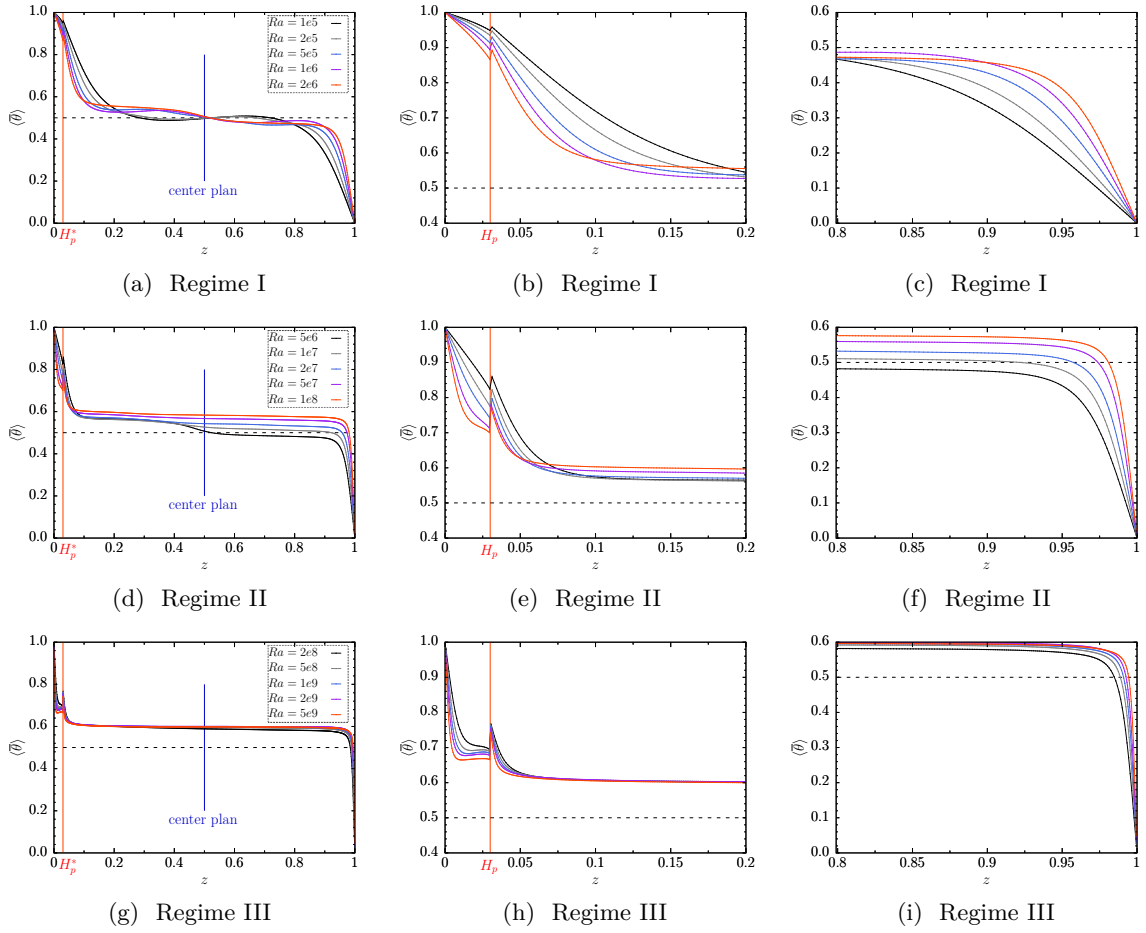

(a) Regime I (b) Regime I (c) Regime I

(d) Regime II (e) Regime II (f) Regime II

(g) Regime III (h) Regime III (i) Regime III

Fig. V.1 (a,d,g) Profiles of mean temperature $\langle\overline{\theta}\rangle_S$ in the vertical direction in different heat transfer regimes. (b,e,h) zoom near the rough plate, (c,f,i) near the smooth plate. For $z \leqslant H_p$ the averaging in the z-direction is performed only over the fluid regions, which leads to discontinuities at the roughness height $z = H_p$ denoted by vertical red line. Black dashed horizontal line at $\langle\overline{\theta}\rangle = 0.5$ represents the theoretical mean temperature between the top and bottom plates.

In regime I, the presence of roughness elements does not affect the distribution of temperature. We note that the cases of $Ra = 10^5, 2\times10^5$ correspond to stationary flows. We notice in figure (V.1a) that mean temperature profiles near rough or smooth plates are symmetrical about $\langle\overline{\theta}\rangle = 0.5$. Roughness are inactive, the temperature of bulk region is similar to classic

RB cell. During regime II, as the bulk temperature θ_{bulk} increase, diffusion in the inner zone $z < H_p$ decreases rapidly. We also can remark the decrease of temperature near roughness $H_p < z < 2H_p$, However, it increase for $z \gtrsim 2H_p$. Therefore, the bulk region becomes more hotter with increasing Ra in particular near rough side ($z < 0.5$). In the other side ($0.5 < z$), the temperature get increase gradually. The bulk region becomes thermally homogeneous at $Ra = 10^8$. In regime III, as the increase of θ_{bulk} is saturated, $\langle\overline{\theta}\rangle_S$ profiles come closer essentially in the bulk region. We notice in figure (V.1h) an isothermal layer take place in the inner region in consistence with numerical observation from Shishkina and Wagner (2011).

As shown in figure (V.2), vertical profiles of mean longitudinal velocity $\langle\overline{u}\rangle_S$ in the R/S cell are plotted for the different regimes. We can observe that geometrical center of the large scale circulation filling the cavity is pushed slightly upwards to $z > 0.5$ because of immersed bodies. Figures (V.2b) and (V.2e) reveal that velocity magnitude in the inner region is very low in regimes I and II. The fluid is practically at rest. In regime III, velocity is increased in the inner region by mean of bulk flow that penetrates within roughnesses.

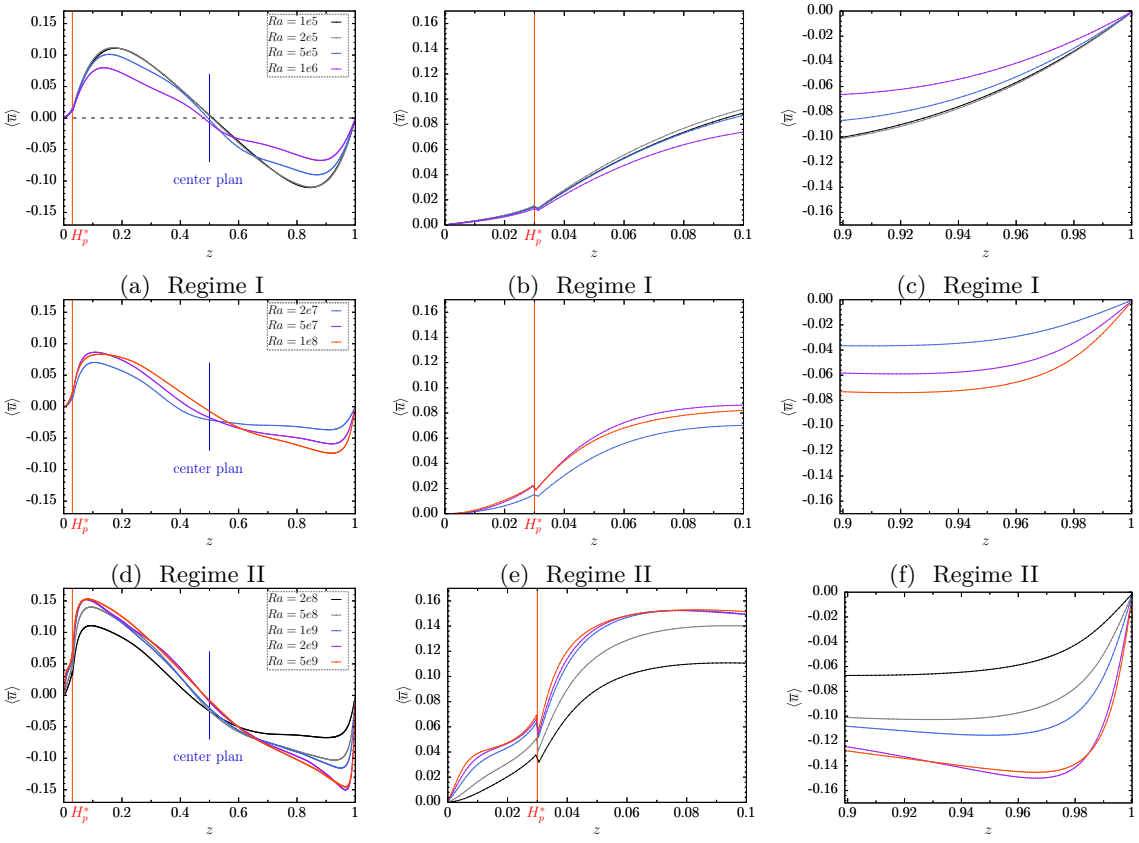

(a) Regime I (b) Regime I (c) Regime I

(d) Regime II (e) Regime II (f) Regime II

(g) Regime III (h) Regime III (i) Regime III

Fig. V.2 (a,d,g) Profiles of mean longitudinal velocity $\langle\overline{u}\rangle_S$ in the vertical direction in different heat transfer regimes. (b,e,h) zoom near the rough plate, (c,f,i) near the smooth plate. Vertical red line represent the height of roughness.

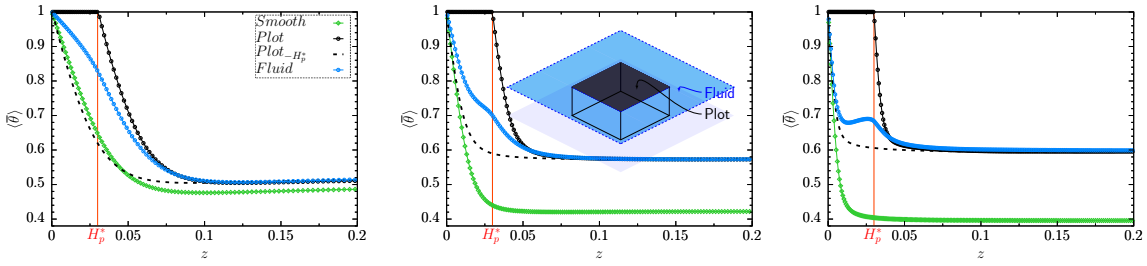

(a) Regime I :$Ra = 2 \times 10^6$ (b) Regime II : $Ra = 5 \times 10^7$ (c) Regime III : $Ra = 10^9$

Fig. V.3 Mean temperature profiles near the plot, fluid and smooth surface for particular Ra belonging to different regimes. plot$_{-H_p^*}$: profiles near plots shifted downward by H_p^*. The sketch represent the geometrical decomposition near roughness into plot/fluid zones.

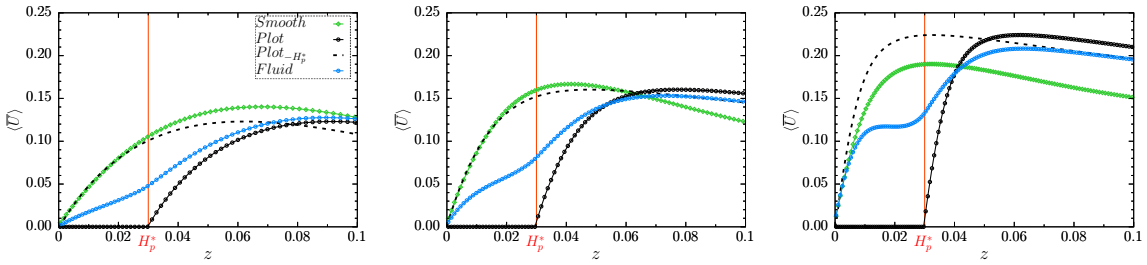

(a) Regime I : $Ra = 2 \times 10^6$ (b) Regime II : $Ra = 5 \times 10^7$ (c) Regime III : $Ra = 10^9$

Fig. V.4 Mean horizontal velocity $U = \sqrt{u^2 + v^2}$ profiles near plots, fluid and smooth surface at different regimes. plot$_{-H_p^*}$ are the profiles near plots shifted downward with H_p^*.

V.2.2 Local effect

We have seen in section [§ IV.5.2] that fluid and te top of roughness have different behaviors. We therefore continue our discussion following this geometrical decomposition. In the figures below are plotted the mean temperature $\langle\overline{\theta}\rangle_S$ and horizontal velocity $U = \sqrt{u^2 + v^2}$ profiles along the vertical direction. We computed those profiles using spatial conditional averages over the fluid, plot and near the top smooth surface.

For clarity reason, we show the results for Ra numbers belonging to the three regimes. Figure (V.3) shows a similar decay rate of the temperature near the wall over the plot and smooth plate. The differences seen with increasing z are due to the increase of bulk temperature. By comparing figures (V.3a) and (V.3b), we can see that the temperature profile associated with the fluid zone is more skewed to the wall, i.e the transition from regime I to II is linked with a rapid increase of the temperature gradient at the wall. In regime III, (V.3c) , the temperature in the fluid is nearly constant within a layer in the inner zone. The profiles above plots are shifted downward, showing a very close shape compared with the profiles near smooth plates. Through all regimes, the wall temperature gradient is higher above plots, which mean the local heat transfer is more intense above roughness.

From figures (V.4), we observe that profiles of horizontal velocity above plots coincide partially with those near the smooth plate. This behavior reflect that the surface on top of roughness is like a smooth plate. The major change could be seen in the fluid zone, wall velocity gradient is growing up significantly from regime II to III. The velocity increases remarkably in the inner zone at regime III. The effect of roughness is clear namely on temperature and velocity in the fluid surrounding the roughness which suggests a destabilization of thermal and kinetic boundary layers.

The immersed bodies that we use in this work are relatively large. One may expect an intense effect on the fluid flow by means of drag friction. The profiles of mean horizontal velocity over roughness and in the surrounding fluid are shown in figure (V.5). The intensity of the mean flow increase with increasing Ra number.The presence of roughnesses is a brake that modify the thermal flow around roughness elements which exerts an opposite force the the motion of fluid which results in a strong drag force that slows the fluid flow in the inner zone $z < H_p^*$. However, in regime III, a second boundary layer appears corresponds to a zone of almost constant velocity.

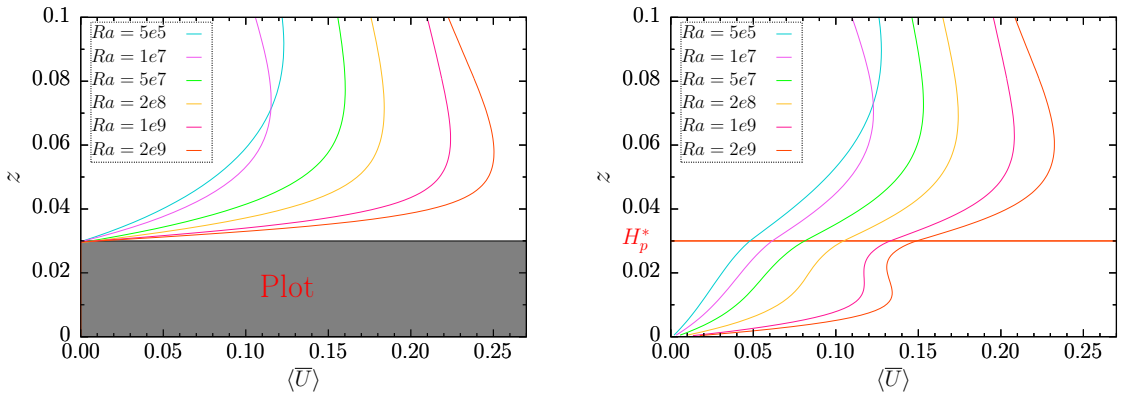

Fig. V.5 Profiles of mean horizontal velocity $\langle \overline{U} \rangle = \langle \sqrt{\overline{u}^2 + \overline{v}^2} \rangle$ over (a) roughness,(b) fluid.

V.2.3 Reynolds number measurement

Roughness has an effect on the bulk turbulence as reported by Xie and Xia (2017). In their work, they showed that Re number (equation (I.27)) scaling with Ra, changes when using different roughness geometries. However, no transition is found from regimes II to to III in $Re_U \sim Ra^n$ scaling law. Figure (V.6a) shows that roughness has no effect on the large scale turbulence comparing the bottom and top plates. We perform a linear regression over almost five decade of Ra to evince $Re_U \sim Ra^n$ scaling law (see table [V.1] for the fitted power laws). We found roughly the scaling exponent $n \approx 1/2$ for both smooth and fluid

zone. By employing pyramid shape roughnesses, Wei et al. (2014) has also compared rough and smooth cells and reported a weak increase of the Reynolds number in the rough cell but the same scaling exponent remains unchanged $n \approx 1/2$. We observe no clear change for the $Re_U \sim Ra^n$ scaling law in agreement with Xie and Xia (2017) observations. The authors report a very much closer power law $Re \sim Ra^{0.551\pm0.001}$. In the experiment of Wei et al. (2014), pyramid shape roughnesses are used. They also reported nearby scaling law $Re \sim Ra^{0.45\pm0.01}$ but fitted only over one decade and a half of Ra.

At the roughness height H_p^*, figure (V.6b) shows that the Reynolds number relative to the fluid zone (equation (I.28)) is overall lower than that of smooth plate as a result of frictional effects of roughness. When $Ra \geqslant Ra_c$ we observe that $Re_U^* \geqslant 1$, i.e. the advective effects are higher than the viscous one. The exponent n increases in regime II, but gets closer to the smooth plate unique scaling with $n \approx 0.58$ in regime III. Indeed, the ratio $[Re_U^*]^{fluid}/[Re_U^*]^{smooth}$ increases rapidly from regime II to III. The later result could be understood as a transition. It shows that the thermal flow is weakly perturbed by roughness elements in regime III.

However, based on Re measurements, it seems that the behaviors of the smooth and the fluid part are quite similar in particular regarding the large scale. However, We highlight some useful details : (i) $Re_U|_{rough} < Re_U|_{smooth}$, (ii) the roughness effects decrease with increasing Re numbers notably in regime III and (iii) in particular, for $Ra > Ra_c$, we note that $Re_U^* > 1$, convective effects are dominant on the fluid surface of roughness. Nevertheless, it is interesting to compare with measurements in S/S cell rather than the top smooth plate to check if roughnesses effect the whole asymmetric cell which deserves further investigation.

Table V.1 Scaling law of the Reynolds number Re in regimes II and III regarding conditional average zones. The Reynolds number is defined as $Re = Hf/\nu$ with f a reference velocity. f could be replaced by U_{max} or $U|_{z=H_p^*}$ which are resp. the maximum mean horizontal velocity and mean horizontal velocity at $z = H_p^*$.

Regime	smooth	fluid	smooth	fluid
	$Re_{U_{max}} \sim Ra^n$		$Re_{U\|_{z=H_p^*}} \sim Ra^n$	
(I)	|	|	|	$Ra^{0.637}$
(II)	$Ra^{0.524}$	$Ra^{0.526}$	$Ra^{0.585}$	$Ra^{0.683}$
(III)	↓	↓	↓	$Ra^{0.598}$

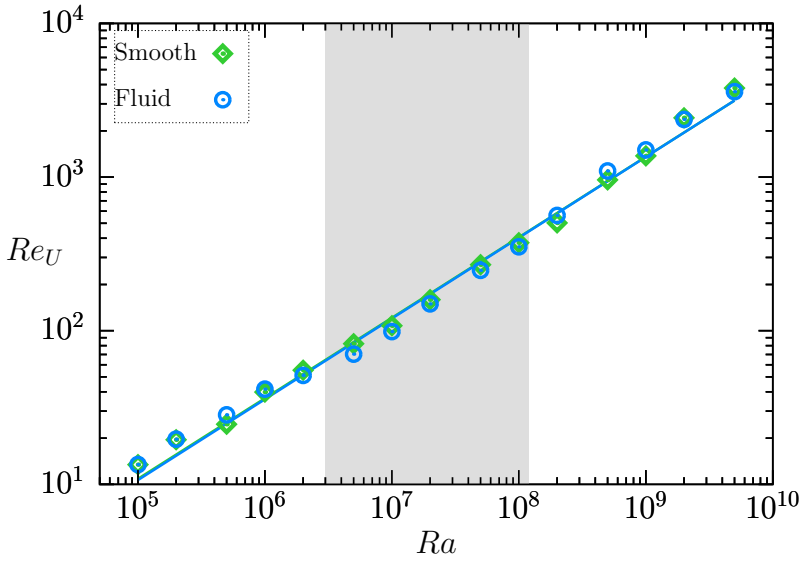

(a) $Re_U = HU_{max}/\nu$

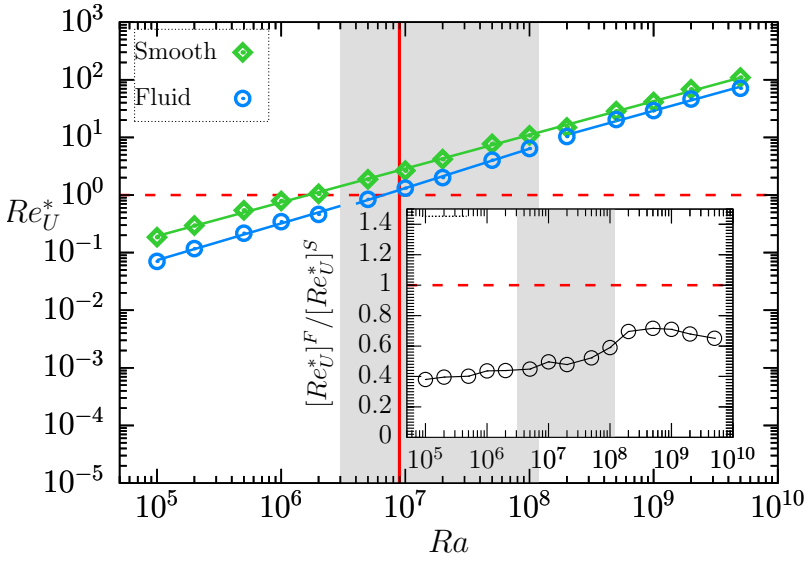

(b) $Re_U^* = H_p^* U|_{z=H_p^*}/\nu$

Fig. V.6 Reynolds number Re as a function of Ra in the R/S cavity. See table [V.1] for the fitted power laws.

V.3 Effect of roughness on boundary layers structure

V.3.1 Thermal and viscous diffusive sublayers

We used the theoretical definition based on the slope of the temperature profile given by equation (III.17). This definition is applied with the respect to mean local temperature profiles above the top roughness surface $\langle\overline{\theta}\rangle_S|_{plot}$ $(z = H_p^*)$ or to the profiles associated with the surrounding fluid $\langle\overline{\theta}\rangle_S|_{fluid}$ from the plate $(z = 0)$ to illustrate the development of thermal boundary layer regarding solid boundaries.

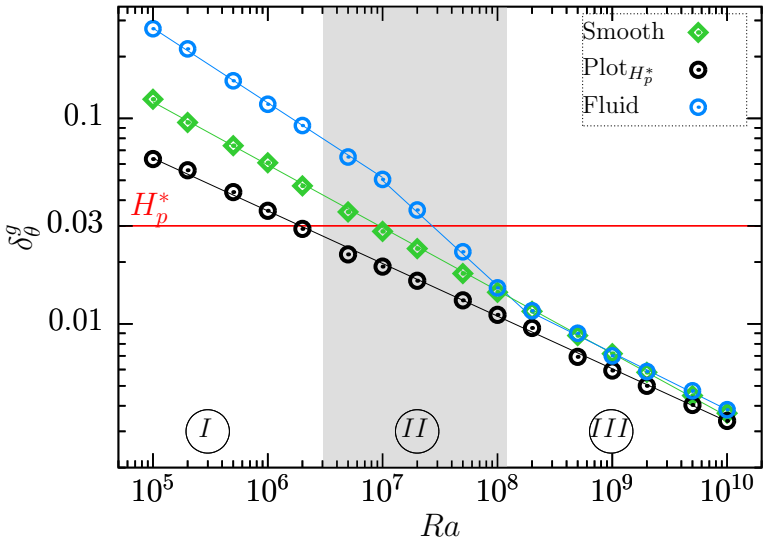

Fig. V.7 Thermal diffusive sublayer thickness δ_θ as function of Ra number. Thicknesses are estimated using spatial conditioning over corresponding areas to smooth, plot or fluid zone and using first gradient method on mean temperature profiles. H_p^* is the height of plots.

As shown in figure (V.7), the TBL is thinner on top of roughness elements with respect to the smooth plate regardless the Ra number. This result is consistent with experimental observations of Salort et al. (2014); Liot et al. (2017) and DNS over grooved plate from Stringano et al. (2006) . One possible explanation is the fact that roughness elements are exposed to the bulk flow which results in higher wind forcing above top surface of roughness. All scaling laws ($\delta_\theta^g \sim Ra^{-\beta_\theta}$) are given in table [V.2]. The smooth plate has a unique scaling law with $[\delta_\theta^g]^{smooth} \sim Ra^{-1/3}$ similar to classic RBC. Plot zone has also a unique scaling but with reduced prefactor α_θ and weaker exponent β_θ. For fluid zone, we find three scaling laws matching more or less with the convection regimes seen in section [§ IV.5]. The first transition appears in regime II with a fast decrease of $[\delta_\theta^g]^{fluid}$. In regime III, BL thicknesses of all zones get closer to each other, yielding to a homogeneous TBL thickness regarding solid boundaries.

By using the same approach, we quantify the thickness of viscous diffusive sublayer (equation III.20) as shown in figure (V.8). The distance from the plate where the tangent to the mean horizontal velocity profile U at $z = 0$ for fluid zone and smooth plate, or at $z = H_p^*$ for plot zone, reaches the maximum velocity is considered to be the local KBL thickness $\delta_u^g = z\,(\partial_z u|_{z\equiv wall} \equiv max(U))$. We found one scaling law per zone (see table [V.2]). Clearly the plot and smooth zones have the same decreasing behavior however the prefactor α_u is smaller for plot zone, i.e $[\delta_u^g]^{plot}$ is thinner. For fluid zone, $[\delta_u^g]^{fluid}$ decreases faster and becomes smaller than the height of roughness elements in regime III. This finding agrees with the experimental study of Xie and Xia (2017) employing pyramid shape roughness. Actually, the authors report the transition to regime III when viscous boundary layer becomes thinner than roughness. However their measures reposes on mean velocity profiles in z-direction by averaging over the whole horizontal surface passing through roughness, i.e their pyramids surface have no upper surface as we do with top of plot. On this purpose, our DNS shows that $\delta_u^g < H_p^*$ in regime III is locally stand only for the fluid zone.

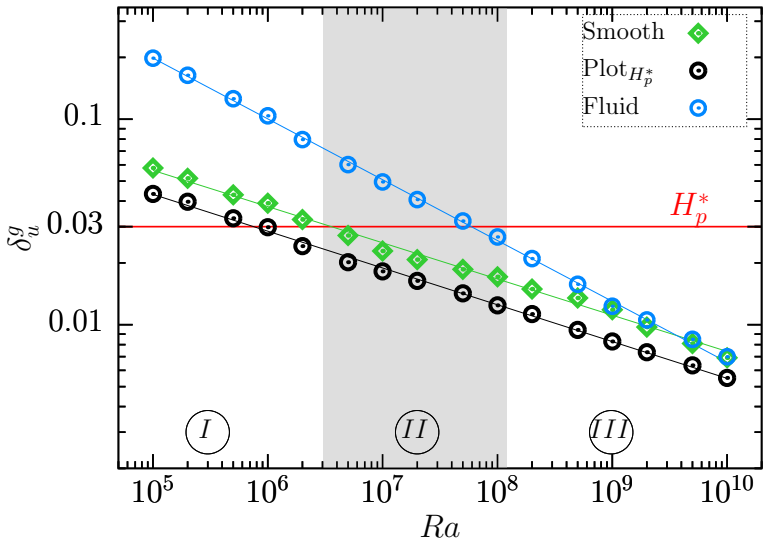

Fig. V.8 Viscous diffusive sublayer thickness δ_u as function of Ra estimated using spatial conditioning over corresponding areas : smooth plate, plot or fluid zone.

Table V.2 Local scaling law for TBL $\delta_\theta^g \sim \alpha_\theta Ra^{-\beta_\theta}$ and kBL $\delta_u^g \sim \alpha_u Ra^{-\beta_u}$

	Regime	$\delta_\theta^g \sim \alpha_\theta Ra^{-\beta_\theta}$		
		smooth	plot	fluid
Thermal BL	(I)			$1.90\ Ra^{-0.37}$
	(II)	$4.06\ Ra^{-0.31}$	$1.24\ Ra^{-0.26}$	$2.46\ Ra^{-0.53}$
	(III)			$2.59\ Ra^{-0.28}$
		$\delta_u^g \sim \alpha_u Ra^{-\beta_u}$		
Viscous BL	through-all	$0.43\ Ra^{-0.18}$	$0.34\ Ra^{-0.18}$	$6.00\ Ra^{-0.30}$

V.3.2 Displacement thicknesses

The measures of the thermal and kinetic boundary layer thicknesses using the slope of mean profile at the wall are indicators about thermal and kinetic diffusions along the plate. It does not take into account the deflection seen essentially in mean vertical profiles above the fluid zone in the inner zone ($z \leqslant H_p$). The displacement thickness given by equations (III.19) and (III.22) can give a more accurate measure of the BL thicknesses computed from solid boundaries.

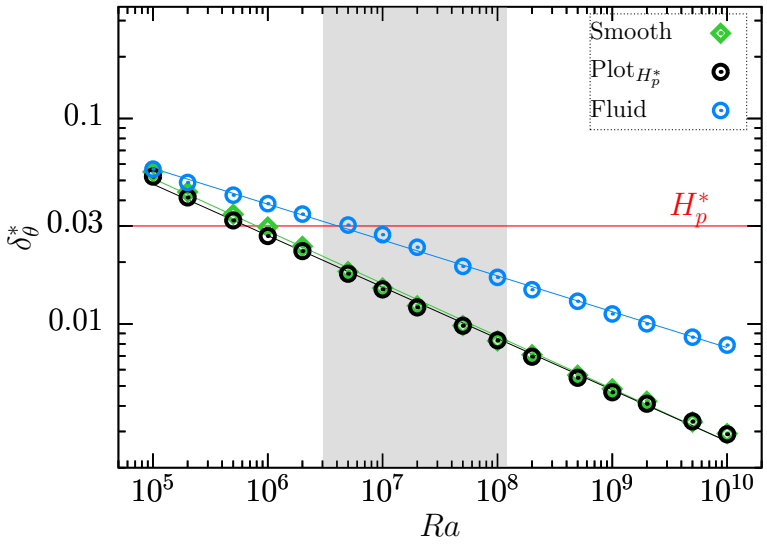

Fig. V.9 Thermal boundary layer thickness δ_θ^* as function of Ra. Thicknesses are estimated using spatial conditioning over corresponding areas to smooth, plot or fluid zones and using displacement method on mean temperature profiles. The lines represent power-law fits given in table [V.3].

As shown in figure (V.9), some previous observations are reproduced here. Generally speaking, the TBL is thinner above roughness rather than in fluid zone. One local scaling law $\delta_\theta^* \sim Ra^{-\beta_\theta}$ is found per zone as given in table [V.3]. The plot and smooth plates have almost the same scaling, which confirms the similar behavior of the top roughness surface and the smooth plate. Beside that, the present measure shows a TBL becoming locally thinner than roughness height in fluid zone from regime II in agreement with earlier investigations with different roughness shapes such as (Du and Tong, 2000) using pyramids, (Tisserand et al., 2011; Salort et al., 2014) using square based plots or from numerical study of Stringano et al. (2006) using grooved plates.

The deviation observed for $\delta_\theta^*|_{fluid}$ from $\delta_\theta^*|_{plot}$ is due to the strong thermal diffusion in the fluid in regime I whereas it is due to the isothermal layer where the temperature

$\langle\overline{\theta}\rangle \approx 0.7 > \theta_{bulk}$ could be considered as the effective thermal boundary condition in the fluid. Regime II is likely a combination between the two previous effects.

Figure (V.10) shows the kinetic displacement thickness δ_u^* as function of Ra also computed from the solid boundaries. Likewise, it shows a decreasing behavior comparing with kinetic diffusive sublayer. It is similar for plots and smooth surfaces, for which close scaling laws are founded using both definitions (see table [V.3]). Here also, we can check that KBL thickness of the fluid zone becomes thinner than roughness height in regime III in agreement with Xie and Xia (2017).

The deviation observed for $\delta_u^*|_{fluid}$ from $\delta_u^*|_{plot}$ could be related to intensive viscous diffusion in the fluid inner zone through regime I and II. In regime III, roughness elements are more exposed to the external flow, which results in significant deviation in horizontal velocity profiles, yield from an intense drag friction.

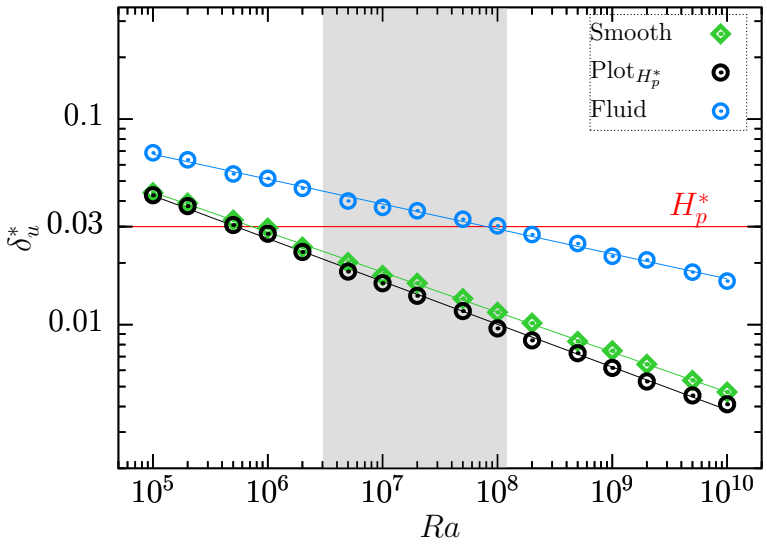

Fig. V.10 Kinetic displacement thickness δ_u^* as function of Ra. Thicknesses are estimated using spatial conditional average over corresponding areas : smooth plate, plot or fluid zone. The lines represent power-law fits given in table [V.3].

Table V.3 Scaling laws for the boundary layer based on the relative displacement thickness to smooth, plot and fluid. (a) thermal BL : $\delta_\theta^* \sim \alpha_\theta Ra^{-\beta_\theta}$. (b) kinetic BL : $\delta_u^* \sim \alpha_u Ra^{-\beta_u}$.

	$\delta_\theta^* \sim \alpha_\theta Ra^{-\beta_\theta}$		
	smooth	plot	fluid
Thermal BL	$1.01\ Ra^{-0.26}$	$0.89\ Ra^{-0.25}$	$0.43\ Ra^{-0.18}$
	$\delta_u^* \sim \alpha_u Ra^{-\beta_u}$		
Kinetic BL	$0.41\ Ra^{-0.19}$	$0.49\ Ra^{-0.21}$	$0.27\ Ra^{-0.12}$

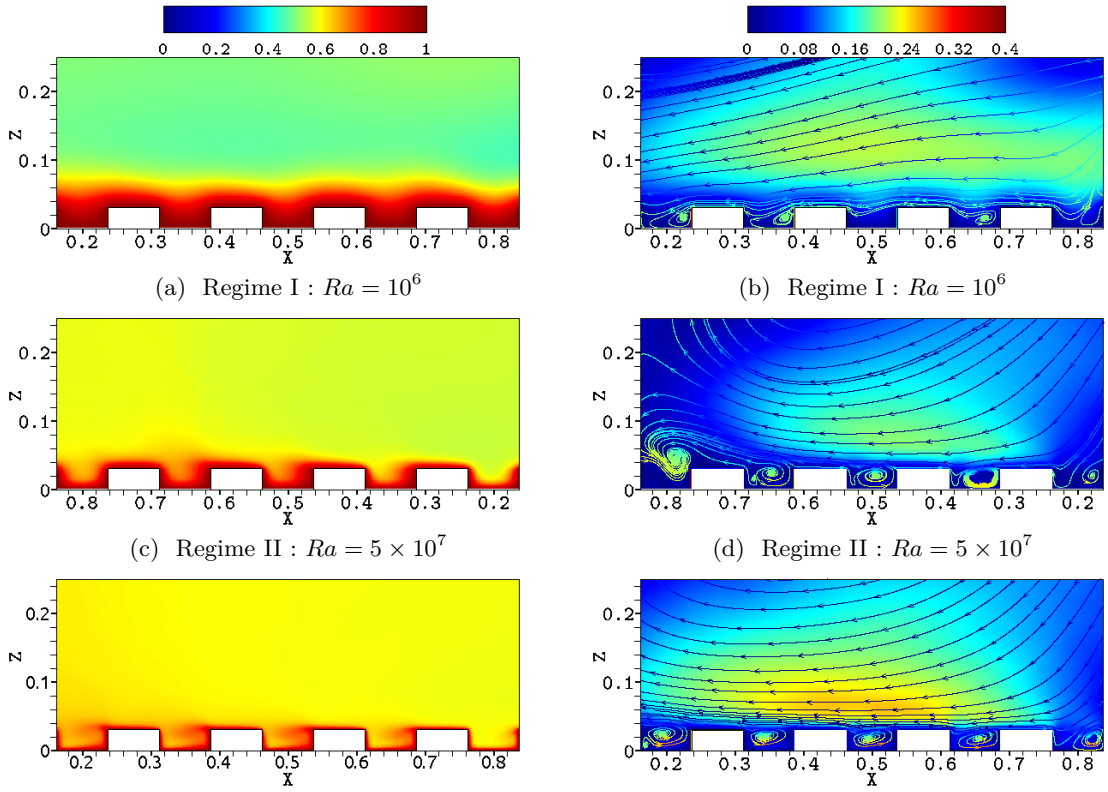

(a) Regime I : $Ra = 10^6$ (b) Regime I : $Ra = 10^6$

(c) Regime II : $Ra = 5 \times 10^7$ (d) Regime II : $Ra = 5 \times 10^7$

(e) Regime III : $Ra = 10^9$ (f) Regime III : $Ra = 10^9$

Fig. V.11 Slice section near roughness elements at $y = 0.3125$ for 3 representative Ra numbers in (a,b) regime I , (c,d) regime II and (e,f) regime III. (a,c,e) mean temperature field $\overline{\theta}$. (b,d,f) mean horizontal velocity field $\overline{U}$ superimposed with 2D velocity streamlines.

In order to describe the flow structure near rough boundary, we plotted in figures (V.11) the mean temperature and horizontal velocity fields for three Rayleigh numbers belonging to different regimes. In regime I, roughness elements are immersed inside the thermal and viscous BLs, δ_θ becomes of the same order of H_p^* on top of plots (figure (V.11a)). One can also remark that velocity magnitudes are relatively weak in the inner zone (figure (V.11b)). Once more, this proves a dominant diffusion and heat accumulation in the inner zone, as a consequence, it reduces the heat transfer. In regime II, we have $\delta_\theta < H_p^*$, the TBL begins an adaptation to roughness shape. Here, the flow is entrained through convective mode in competition with thermal conduction mode as we demonstrate before. Secondary rolls take place and partially-filled the region in between roughness. It essentially wash and release the fluid from inner to outer zone. In regime III, the LSC interact heavily with roughnesses elements, visibly the thermal BL here takes perfectly the shape of the solid boundary as reported by many works such as Stringano et al. (2006); Zhu et al. (2017); Xie and Xia (2017). The convection in the inner region is dominant, we can see the recirculation eddies fully-filled the region in between plots.

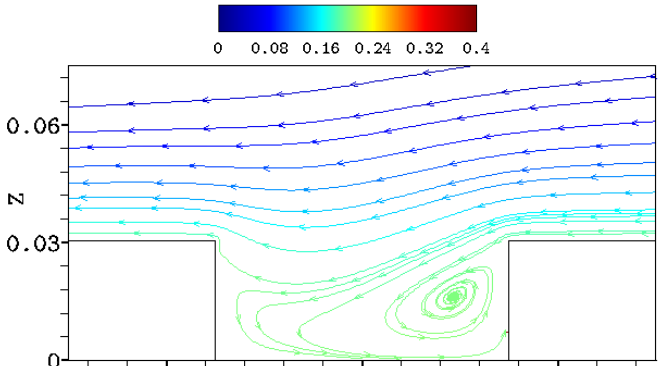

(b) Regime I : $Ra = 10^6$

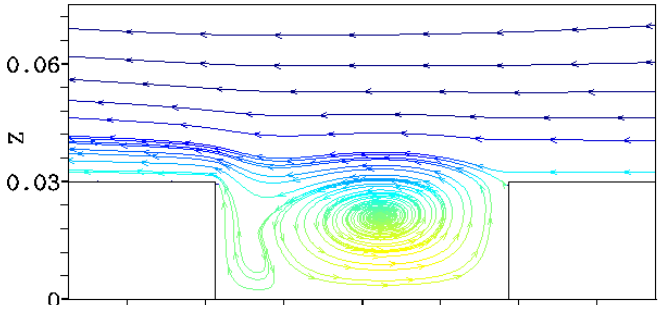

(c) Regime II : $Ra = 5 \times 10^7$

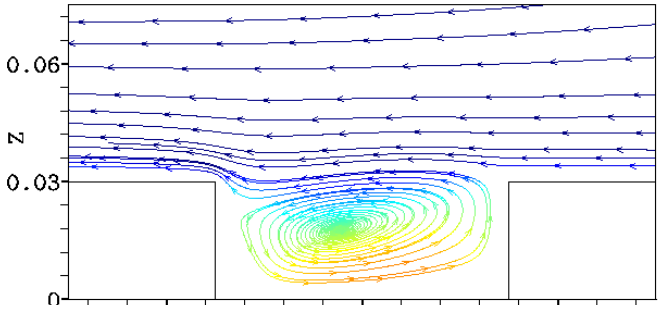

(d) Regime III : $Ra = 10^9$

Fig. V.12 Slice section near roughness elements at $y = 0.3125$ for 3 representative Ra numbers of mean 2D velocity streamlines colored with mean longitudinal velocity $\overline{u}$.

The transition between heat transfer regimes is supported by a change in the inner flow streamlines. As shown in figure (V.12), in regime I, the fluid is mainly at rest, i.e heated fluid is probably accumulated inbetween roughness elements and behave like a thermal resistance resulting in a reduced heat transport (this supports observation seen in figure (IV.15a)). In regime II, the rolls contribute in the mixing of the fluid, as the bulk flow has a moderate velocity magnitude, it allows the ejection process of heat in the outer zone, yields in better enhancement of the heat transfer. In regime III, the fluid in the inner zone is well mixed by means of the secondary flow but the heat is not released because the bulk flow is relatively intense, yield in a weak exhaust of thermal structures, it could be interpreted as another reason for which the growth rate of Nu number is pulled down.

V.3.3 Momentum and energy thicknesses

Figures (V.13) show the momentum and energy thicknesses as function of Ra number given in equations ((III.3.2),(III.3.2)). In regime I, both δ_u^M and δ_u^E decrease monotonically with a nearby magnitude order in all zones. In regimes II and III, as expected, the top of roughness is behaving like a the smooth top surface with δ_u^M and δ_u^E still decreasing. But, the measure reveals that momentum and energy thickness remain constants in the fluid zone, i.e. the sink of the momentum transport and kinetic energy in the boundary layer becomes independent from Ra number. We note that $\delta_u^M \approx \frac{1}{3}H_p$ and $\delta_u^E \approx \frac{1}{2}H_p$. It is not easy to explain whether this effect could be related to the heat transfer enhancement in regimes II and III. Further investigations are needed to clarify this point.

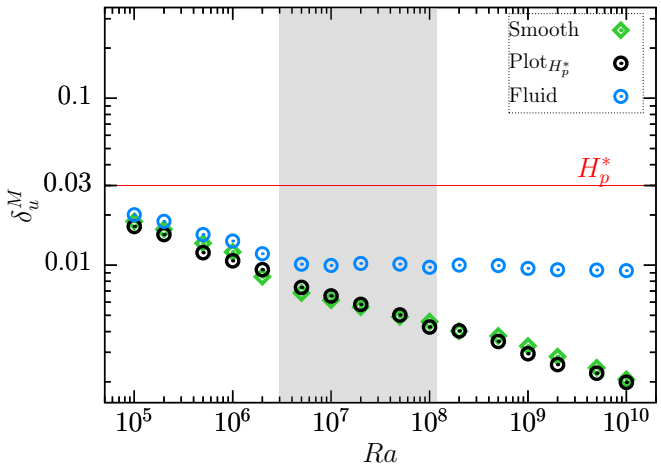

(a) Momentum thickness

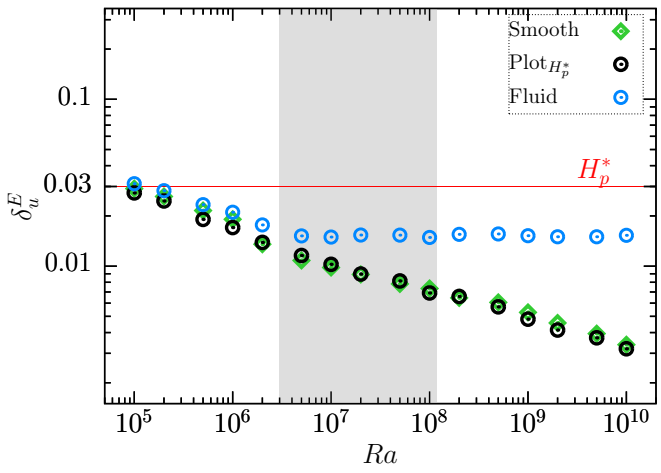

(b) Energy thickness

Fig. V.13 Momentum thickness δ^M and Energy thickness δ^E as a function of Rayleigh number Ra. Conditional spatial average is used to distinguish roughness (black) from fluid (blue) zones. The top smooth plate (green).

V.4 Effect of roughness on turbulent fluctuations

V.4.1 Boundary layer effect

Local temperature rms profiles are plotted in figure (V.14) for the 3 regimes. Intensity of the peaks is plotted in figure (V.15a) as a function of Ra. As the Ra increases, the intensity of θ_{rms} peak increases near the smooth plate. On the top of plots, intensity of θ_{rms} increases and reaches its maximum in regime II, then it remains nearly constant in regime III. For the fluid zone, intensity of the fluctuation in the outer zone (peak-1) increases during regime I and reaches also a maximum in regime II at around critical Rayleigh Ra_c. Additionally, a second peak appears in the inner region (peak-2) at the end of regime II with a growing-up intensity as the Ra increase beyond $Ra = 10^9$.

As shown in figure (V.15b), TBL thickness based on the location of the peak is plotted as function of Ra. In regimes I and II, δ_θ^{rms} shows a monotonic decrease in all zones. It remains consistent with the fact that $[\delta_\theta^{rms}]^{plot} < [\delta_\theta^{rms}]^{smooth} < [\delta_\theta^{rms}]^{fluid}$. In regime III, we determine two peaks. This phenomenon is due to a separation of BL in two layers : (i) the position of peak-2 as a TBL thickness in the inner region. We obtain a homogeneous TBL as $[\delta_\theta^{rms}]^{plot} \approx [\delta_\theta^{rms}]^{smooth} \approx [\delta_\theta^{rms}]^{fluid}_{peak-2}$. (ii) peak-1 is signature of mixing layer at $z \approx H_p$.

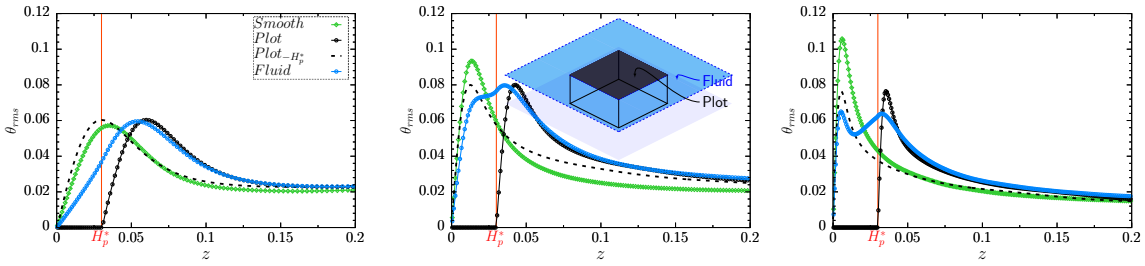

(a) Regime I : $Ra = 2 \times 10^6$ (b) Regime II : $Ra = 5 \times 10^7$ (c) Regime III : $Ra = 10^9$

Fig. V.14 Temperature rms profiles near plots, fluid and smooth surface. plot$_{H_p^*}$ profiles are the same profiles as near plots but shifted downward with H_p^*.

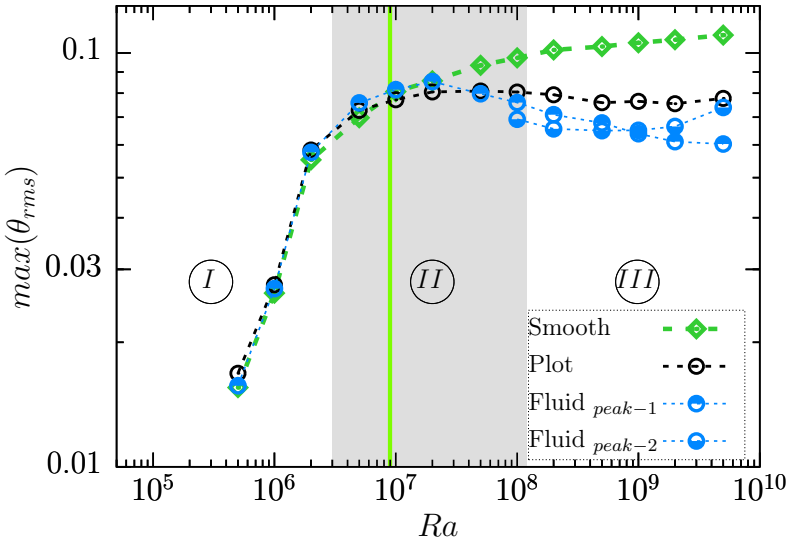

(a)

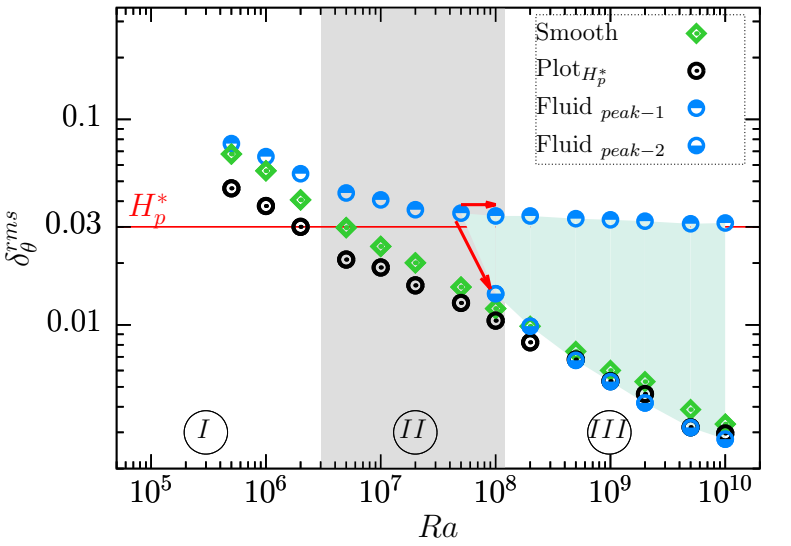

(b)

Fig. V.15 (a) Intensity of rms temperature peak. Vertical green line is Ra_c. (b) Thermal boundary layer thickness δ_θ as function of Ra number. Thicknesses are estimated using spatial conditional averaging over corresponding areas to smooth, plot or fluid zone and using peaks of rms temperature profiles. H_p^* is the height of plots.

Horizontal rms velocity profiles are plotted in figure (V.16). We can highlight two points. First, the distribution of fluctuation on the top of roughness and smooth plates is very similar. Secondly, a second peak appears in rms velocity fluctuation in the inner fluid zone in regime III. We believe that the appearance of double peak of velocity and temperature fluctuations are correlated and the delay that we can notice for the appearance of peak-2 kinetic BL is related to the Prandtl number.

In figure (V.17), we plot the turbulent flow BL thickness. In regime I and II, we see a monotonic decrease in all zones. Moreover, plot and smooth zones have practically the same intensity of fluctuations. In regime III, we can interpret the position of peak-2 as a KBL thickness in the inner fluid region. This inner BL is apparently thinner than in other zones.

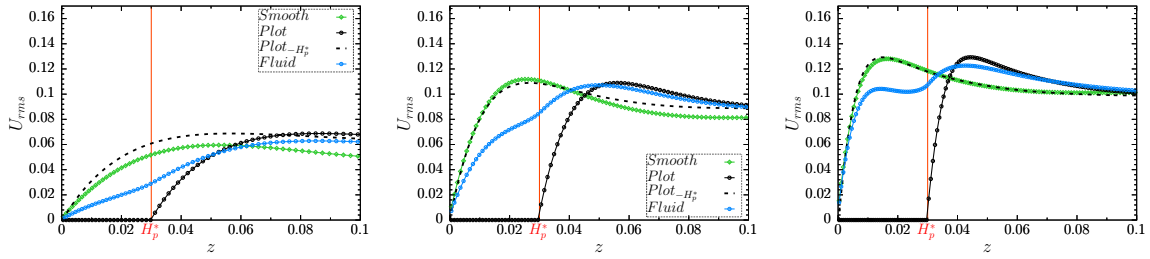

(a) Regime I : $Ra = 2 \times 10^6$ (b) Regime II : $Ra = 5 \times 10^7$ (c) Regime III : $Ra = 10^9$

Fig. V.16 Horizontal velocity rms $U_{rms} = \sqrt{u_{rms}^2 + v_{rms}^2}$ profiles near plots, fluid and smooth surface. plot$_{H_p^*}$ are the same profiles near plots shifted down with H_p^*.

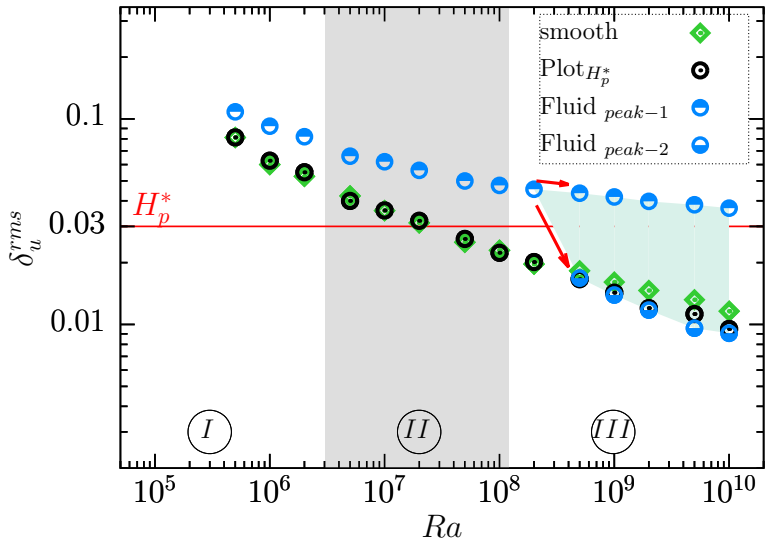

Fig. V.17 Kinetic boundary layer thickness δ_u as function of Ra. Thicknesses are estimated using spatial conditional averaging over corresponding areas to smooth, plot or fluid zone and using peaks of rms velocity profiles $U_{rms} = \sqrt{u_{rms}^2 + v_{rms}^2}$.

V.4.2 Reynolds number based on velocity fluctuation

Figure (V.18) shows the dependence of $Re_{w_{rms}}$ (equation (I.29)) on Ra number. The scaling exponent n decreases in regimes II and III for both smooth and fluid zone. $Re_{w_{rms}}$ is slightly larger for smooth plate rather than the fluid zone, but the differences decreases with increasing Ra. Otherwise, we observe that $Re_{w_{rms}} \geqslant 1$ in regime II nearby Ra_c. We may therefore suppose that turbulent advection is more important when $Ra \geqslant Ra_c$.

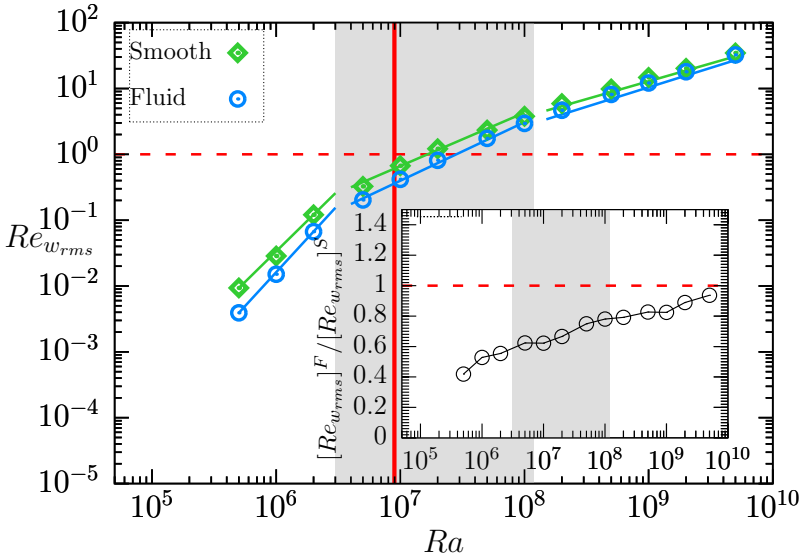

(a) $Re_{W_{rms}} = H_p^* w_{rms}|_{z=H_p^*}/\nu$

Fig. V.18 Reynolds number $Re_{W_{rms}}$ as a function of Ra in the R/S cavity. See table [V.4] for the fitted power laws.

Regime	smooth	fluid
	$Re_{w_{rms}\|_{z=H_p^*}} \sim Ra^n$	
(I)	$Ra^{1.85}$	$Ra^{2.05}$
(II)	$Ra^{0.81}$	$Ra^{0.89}$
(III)	$Ra^{0.54}$	$Ra^{0.59}$

Table V.4 Scaling law of the Reynolds number $Re_{w_{rms}}$ in regimes II and III regarding conditional average zones. It is defined as $Re = H w_{rms}|_{z=H_p^*}/\nu$ with f a reference velocity. $w_{rms}|_{z=H_p^*}$ is vertical rms velocity at $z = H_p^*$.

V.4.3 Global effect

Figure (V.15a) reveals that the maximum value of fluctuations is located near the smooth surface for $Ra > Ra_c$. But this does not reflect the global behavior near solid boundaries. We can also see relatively lower intensity of fluctuations for fluid zone, however, when going toward the bulk region, fluctuations remain intensive especially if we compare the profiles smooth/fluid in regime II (V.14b). To show better the influence of roughness, we compute the average of rms temperature over a half cavity volume V. We aim to figure out in which side of the cell (half top or bottom), temperature fluctuations are more intense. First, we perform an integration of $\theta_{rms}(z)$ in the vertical direction to get the mean intensity of temperature fluctuation relative to half rough or smooth sides.

$$\begin{cases} \text{Global/rough} & \dfrac{1}{V_R}\int_0^{H/2}\theta_{rms}dV \\ \text{Global/smooth} & \dfrac{1}{V_S}\int_{H/2}^{H}\theta_{rms}dV \end{cases} \tag{V.1}$$

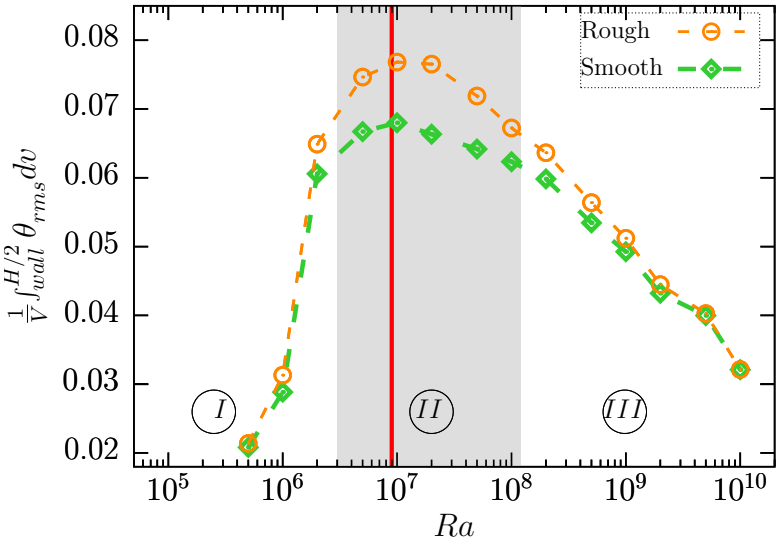

Fig. V.19 Integral of temperature rms profiles over a half cavity. Blue pentagons refers to spatial conditional integration in fluid zone applied also on the smooth plate. Orange circles and green diamond are used for an integration using all zones. Vertical green line in Ra_c.

As shown in figure (V.19), in regime II, we can qualitatively see a highest intensity of fluctuations in the bottom rough side comparing with regimes I and III. It also shows that intensity of θ_{rms} in the top and bottom sides is similar in regimes I and III, whereas in regime II the intensity of temperature fluctuations are more important near the rough side. The maximum is reached at Ra_c. We believe that more thermal plumes are likely emitted from top of roughness element as observed by Du and Tong (1998), yielding to an intensification of thermal fluctuations and contributing partially to the enhancement of the heat transfer and to a higher scaling exponent β.

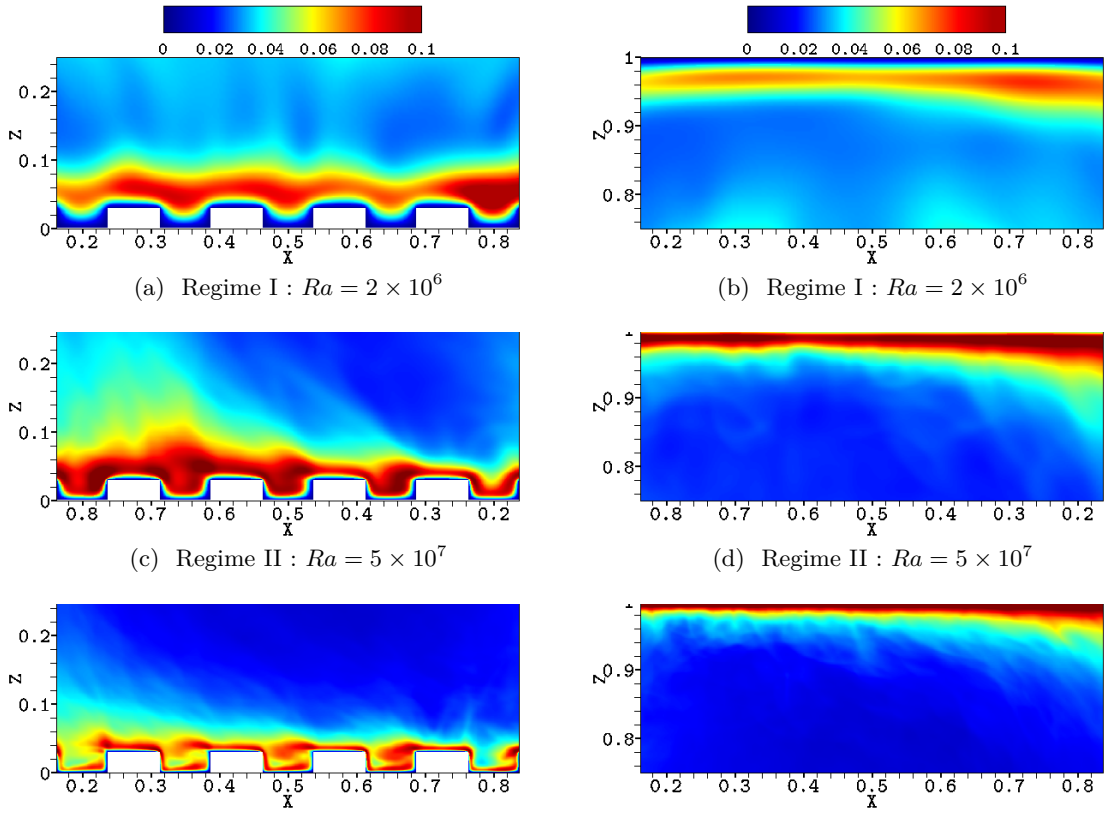

(a) Regime I : $Ra = 2 \times 10^6$ (b) Regime I : $Ra = 2 \times 10^6$

(c) Regime II : $Ra = 5 \times 10^7$ (d) Regime II : $Ra = 5 \times 10^7$

(e) Regime III : $Ra = 10^9$ (f) Regime III : $Ra = 10^9$

Fig. V.20 Vertical plane near roughness elements at $y = 0.3125$ for 3 representative Ra numbers in (a,b) regime I , (c,d) regime II and (e,f) regime III. Temperature rms field θ^{rms} near (a,c,e) rough plate (b,d,f) smooth plate.

We compare in figures (V.20) the temperature fluctuations fields near rough and smooth plates at particular Rayleigh numbers in the three regimes. We can highlight the highest level of intensity of thermal fluctuations in regime II comparing with regimes I and III on both plates. However, it is qualitatively larger in the bottom side which could be considered as another reason of the increase of heat transfer efficiency in regime II. In regime III, the recirculation eddies full-filling the cavities inbetween plots interact intensively with the bulk flow, this is the reason why two peaks of fluctuations are observed in the rms profiles of fluid zone, i.e, on one hand the inner peak is resulting from the interaction of those eddies directly with bottom surface, on the other hand, the outer peak is a result of the LSC interaction with roughness elements and recirculation eddies. The highest intensity could be understood as a signature of plumes detachment near the upper edges and entrained by the bulk flow. We also notice that fluctuations are getting concentrated near solid boundaries with decreasing intensity in comparison with regime II. This effect could be associated with the fact that scaling law exponent β in $Nu \sim Ra^{\beta}$ relation is reduced going back to the classical scaling law for smooth RBC.

V.5 Conclusion

We discussed the effect of roughness on the structure of both thermal and kinetic layers over a range of Rayleigh numbers and examine if these changes are connected with the regimes of heat transfer identified previously.The thicknesses of the different BL are estimated in different ways from statistical quantities such as mean profiles and rms values. These quantities are computed for each side globally but also locally, that is by separating the region above the roughnesses from that in between the roughnesses (fluid zone).

We find that the region above the roughness behaves like the smooth plate and that changes associated with the different heat regimes are detected only in the fluid zone. In the beginning of Regime II, the thermal BL thickness becomes thinner than roughness height, i.e $\delta_\theta^* \leqslant H_p$ in agreement with various experimental and numerical studies as Tisserand et al. (2011); Salort et al. (2014) and Stringano et al. (2006). In the beginning of Regime III, the kinetic BL thickness becomes thinner when comparing with the roughness height, i.e $\delta_U^* \leqslant H_p$, also consistent with experimental study of Xie and Xia (2017). The inhomogeneity of the flow statistics on the rough plate will be studied in more detail in the next chapter.

We then studied the characteristics of the thermal and velocity fluctuations for the different regimes. In the fluid zone, we showed that the double peak observed in both velocity and temperature rms values in regime III corresponds to the double interaction of small eddies with the roughness and large-scale circulation. We then integrated the thermal fluctuations over each side of the cavity (half-cavity). We found that on both sides, the intensities increase in Regime I, reach a maximum in Regime II for the Ra_c, and decrease in Regime III. A difference between the rough side and the smooth side, with an intensification for the rough side, is only observed in Regime II. The origin of the intensification of thermal fluctuations will be studied in more detail in Chapter (§ VII) with a focus on thermal plumes.

VI – DNS vs EXP : direct comparison of vertical temperature profiles

VI.1 Introduction

We have compared in section (§ IV.4) the heat transfer relative to the rough plate of our DNS with those measured in the experiments conducted at Lyon (Tisserand et al., 2011; Salort et al., 2014; Rusaouën et al., 2018) and at Hong Kong by Wei et al. (2014). Despite the fact that different shapes and sizes of roughness elements are used, we have seen that the comparison is possible if we consider the gap in turbulence intensity due to different range explored for Ra number. The enhancement of the heat transfer is mainly linked with the height H_p and rescaling all data with respect of critical Rayleigh number Ra_c should be made in order to take in account the difference between the range of explored Ra number.

It seems that comparison is possible, this encourages us to looks forward to discussing further details. In this chapter, we are interested in comparing the flow physics near roughness elements. Since the effects of the rough wall topology (shape,size,distribution,...) is crucial and implies different flow dynamics as proved in many works as Wagner and Shishkina (2015); Toppaladoddi et al. (2015); Xie and Xia (2017), it will be natural to choose a similar

configuration to our DNS such as of du Puits et al. (2017). On this basis, we first describe both DNS and EXP physical configurations and identify comparable Ra numbers. We then compare local temperature and rms profiles. We show that the profiles depend on the location and differences could be explained by the influence of the large scale circulation. Finally, we focus on the comparison of temperature rms profiles measured as the experiment.

VI.2 Description of the physical configurations

In the following work, we will compare experimental cases at different Ra numbers. We use the critical Rayleigh number to identify comparable Ra numbers in our DNS study.

VI.2.1 Barrel of Ilmenau rough cell set-up

du Puits et al. (2017) built a rectangular section into the large-scale Rayleigh-Bénard experiment "Barrel of Ilmenau" as shown in figure (VI.1). The Prandtl number used is $Pr = 0.7$ and the geometrical dimensions of the cavity are : $H = 2500mm$ (height), $H_p = 12mm$ (roughness height), $H_p^* = H_p/H = 0.0048$ and an aspect ratio $\Gamma_y = W/H = 1/4$.

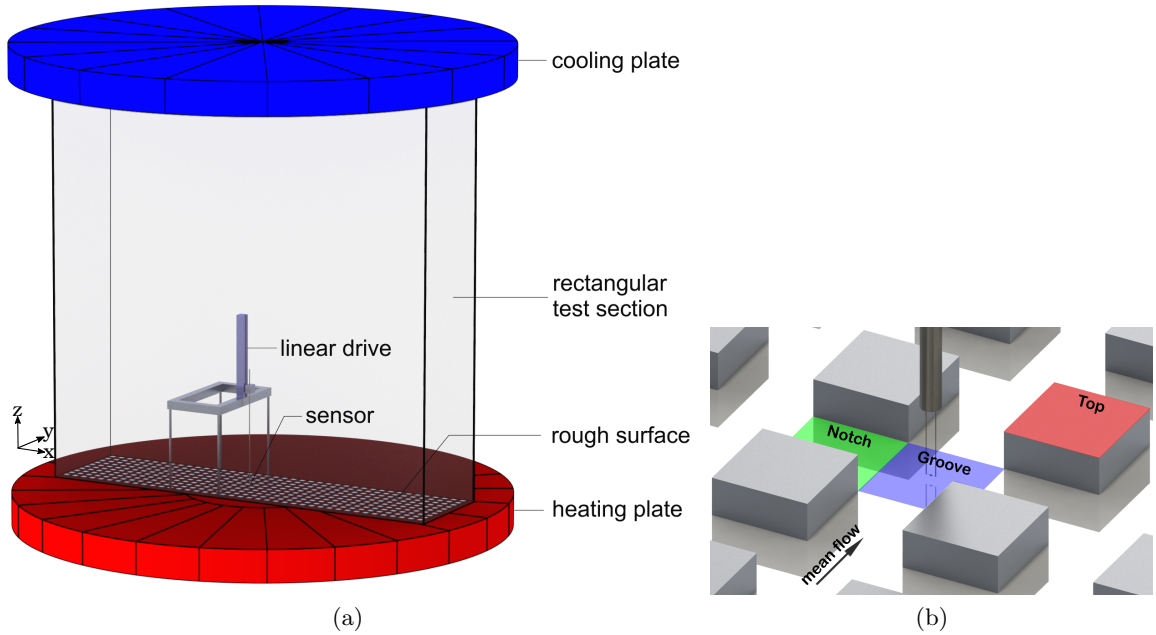

(a) (b)

Fig. VI.1 (a) Barrel of Ilmenau rough cavity from du Puits et al. (2017). Asymmetric cell with rough bottom and top smooth plates. Square based rectangular obstacles are used as roughnesses. The large scale circulation is a unique roll filling the box. (b) Measurements are performed at an area located near the center of the rough plate. A sensor is used to measure temperature above different zone : plot (red), notch (green) and groove (blue).

The idea is use as a reference the critical Rayleigh to scale our DNS with the experiment data. Following Tisserand et al. (2011), we consider the Rayleigh number for the rough plate based on the temperature difference between the rough wall and the bulk. We should note that du Puits et al. (2017) used the old prefactors of Grossmann and Lohse (2001) theory to estimate critical Rayleigh number $Ra_c = f_{GL}^{-1}(\frac{H}{2H_p}) = 5.6 \times 10^9$. Here, we estimate Ra_c using new data fit of Stevens et al. (2013) with updated prefactors founding that $Ra_c = f_{GL}^{-1}(\frac{H}{2H_p}) = 4.7917 \times 10^9$, which is slightly different. f_{GL} refers to the resolution of equations *I*.38, it implicitly takes into account the Prandtl number effects. Superscript "low" and "high" refer to experimental low and high Rayleigh numbers. The scaling with critical Ra_c as shown in figure (IV.10) is our key to compare with Ilmenau experiment. We note by α the ratio between the rough and critical Ra numbers.

For each of the cases, the parameters are

Low Rayleigh number :

$$\begin{cases} Ra^{low} & = 4.6 \times 10^9 \\ \Delta T_R^{low} & = 2(T_h - T_{bulk}) & = 2 \times (23.23 - 22.096) & = 2.268 \\ \Delta T & = 3 \\ Ra_R^{low} & = Ra^{low} \times \dfrac{\Delta T_R^{low}}{\Delta T} & = 3.478 \times 10^9 \\ \alpha^{low} & = \dfrac{Ra_R^{low}}{Ra_c} & = 0.72575 \end{cases} \tag{VI.1}$$

High Rayleigh number :

$$\begin{cases} Ra^{high} & = 4.7 \times 10^{10} \\ \Delta T_R^{high} & = 2(T_h - T_{bulk}) & = 2 \times (53.4 - 39.387) & = 28.026 \\ \Delta T & = 40 \\ Ra_R^{high} & = Ra^{high} \times \dfrac{\Delta T_R^{high}}{\Delta T} & = 3.293 \times 10^{10} \\ \alpha^{high} & = \dfrac{Ra_R^{high}}{Ra_c} & = 6.87241 \end{cases} \tag{VI.2}$$

VI.2.2 DNS rough cell set-up

We now define the critical Rayleigh in our DNS and determine the equivalent Ra comparing to the same values of α. In our simulation, the range of Rayleigh numbers covered is $[10^5 - 5 \times 10^9]$. The Prandtl number is fixed at $Pr = 4.38$ and geometrical parameters are setted up with a high $H = 1$, a roughness height $H_p = 0.03$, $H_p^* = H_p/H = 0.03$ and an aspect ratio of the cavity $\Gamma_y = 1/2$. Similarly, we estimate Ra_c using the unifying GL theory of scaling in thermal convection with updated prefactors (Stevens et al., 2013).

Table VI.1 Ratio between rough Ra numbers Ra_R^{DNS} of our simulations and the critical Rayleigh number $Ra_c = 8.9676 \times 10^6$. The closest α^{DNS} values to the experiments are highlighted with cyan.

Ra^{DNS}	Ra_R^{DNS}	$\alpha^{DNS} = \frac{Ra_R^{DNS}}{Ra_c}$
1×10^5	1.0041×10^5	0.011196
2×10^5	2.0030×10^5	0.022336
5×10^5	4.9727×10^5	0.055451
1×10^6	9.9078×10^5	0.110484
2×10^6	1.9642×10^6	0.219034
5×10^6	4.7685×10^6	0.531748
1×10^7	9.3651×10^6	1.044322
2×10^7	1.8075×10^7	2.015639
5×10^7	4.3207×10^7	4.818141
1×10^8	8.4110×10^7	9.379340
2×10^8	1.6397×10^8	18.28465
5×10^8	4.0297×10^8	44.93567
1×10^9	8.0237×10^8	89.47402
2×10^9	1.5996×10^9	178.3748
5×10^9	4.0193×10^9	448.1975
1×10^{10}	8.0000×10^9	892.1000

We found that $Ra_c = f_{GL}^{-1}(\frac{H}{2H_p}) = 8.9676 \times 10^6$. The idea is to find the closest ratios between rough and critical Ra numbers to those identified for du Puits et al. (2017). The table [VI.1] shows all α values corresponding to our DNS. A rapid comparison give us the closest value to α^{low} and α^{high} which are $\alpha^{low-DNS} = 0.532$ and $\alpha^{high-DNS} = 4.818$. By using α^{low} and α^{high}, we calculated the rough DNS Rayleigh numbers based on the same ratios α of the experiments and the critical Ra_c identified in our DNS.

$$\begin{cases} Ra_R^{low-DNS} = \alpha^{low} \times Ra_c = 6.51 \times 10^6 \\ \\ Ra_R^{high-DNS} = \alpha^{high} \times Ra_c = 6.16 \times 10^7 \end{cases} \tag{VI.3}$$

We take the nearest Ra^{DNS} numbers corresponding to $Ra_R^{low-DNS}$ and $Ra_R^{high-DNS}$, which give us $Ra^{DNS-low} = 5 \times 10^6$ and $Ra^{DNS-high} = 5 \times 10^7$ as the low and high Ra numbers. Therefore, we compare our DNS versus experimental Rayleigh numbers three decades higher. We suppose that low and high Ra cases are belonging to regime I and II respectively.

Since the Rayleigh numbers for which we have seen transitions of convection regimes based on Nu-Ra scaling. The first transition from regime I to II is around $Ra = 3 \times 10^6$ while the second one from regime II to III is founded to be around $Ra = 1 \times 10^8$. It appears that the low Rayleigh $Ra^{DNS-low}$ corresponds to the beginning of regime II while $Ra^{DNS-high}$ is around the middle of regime II.

VI.3 Comparison based on location

The experimental study of du Puits et al. (2017) is based on local temperature measurements near the rough plate. It distinguishes three different zone types : (i) plot, that is the top area of roughness, (ii) notch that is the zone in between the roughness in parallel with the bulk flow and (iii) grooves, that is the zone between lines of roughness elements. In order to compare with the experiments, we divided the rough plate in the DNS in a similar way as shown in figure (VI.2).

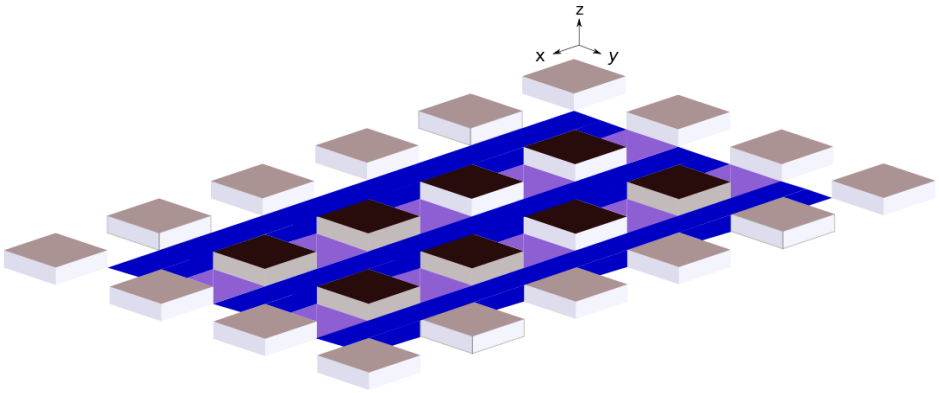

Fig. VI.2 Decomposition of the rough plate into three zone types : (i) plot in black, (ii) groove in blue and (iii) notch in magenta.

VI.3.1 Mean temperature profiles

We computed mean temperature profiles using spatial conditional average over each zone separately. Since the bulk temperature in the DNS and experiment is different, we take this effect into account and define a normalized mean temperature $\langle\overline{\Theta}\rangle(z)$ to rescale both DNS and EXP data

$$\langle\overline{\Theta}(z)\rangle = \frac{\langle\overline{\theta(z)}\rangle - \theta_{bulk}}{\theta_h - \theta_{bulk}} \tag{VI.4}$$

a) Spatial conditional averaging over each type of zone

First, we have considered all areas in the central zone to exclude side wall effects. The DNS results are averaged over all surfaces related either to groove, notch, plot or smooth surface. In the following figures (VI.3) are plotted the profiles of normalized mean temperature $\langle\overline{\Theta}\rangle$ by the bulk temperature versus the normalized distance $(z/H)/H_p^*$ from the plate for lower and higher Rayleigh numbers.

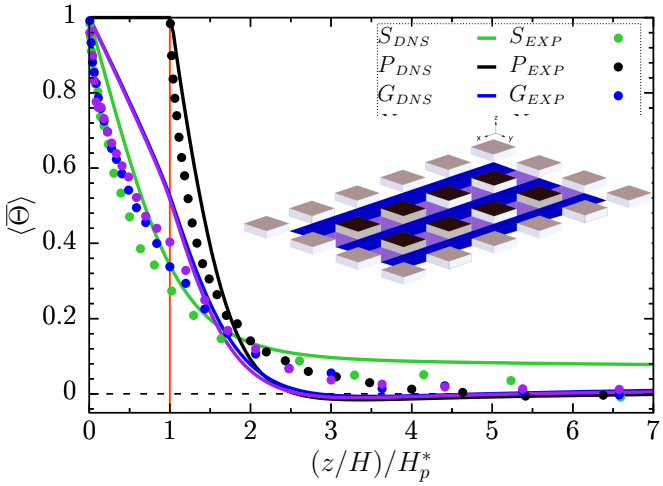

(a) $Ra^{EXP} = 4.6 \times 10^9$ versus $Ra^{DNS} = 5 \times 10^6$

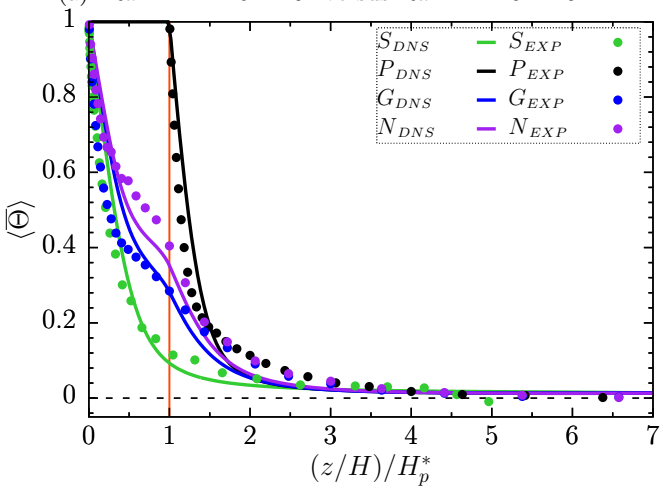

(b) $Ra^{EXP} = 4.7 \times 10^{10}$ versus $Ra^{DNS} = 5 \times 10^7$

Fig. VI.3 Normalized mean temperature $\langle\overline{\Theta}\rangle(z)$ profiles over plots (P), grooves (G), notches (N) and smooth (S) side for (a) low Ra number and (b) high Ra number. We use full symbols for du Puits et al. (2017) experimental data and lines for our DNS.

For lower Ra, the mean temperature field $\langle\overline{\Theta}\rangle|_{DNS}$ over plot and smooth surface are close to experimental data (EXP). However, we observe differences with experimental data in the grooves and notches especially in the inner zone where $z < H_p^*$. We slightly over estimate Θ. This suggests that the surrounding zones, i.e groove and notches are hotter according to DNS. For the higher Ra, a good agreement is obtained in all zones. We highlight that notches are relatively hotter than grooves. Therewith, the temperature of the notches and grooves is within the experimental differences in the inner zone. Generally, the DNS reproduces fairly the near rough wall temperature at different zones as the experiment, mainly the forms of the profiles. However, we highlight the differences of the magnitude orders due the gaps of Ra number. The boundary layer is thicker in Ra-DNS while the experiment shows more skewed profiles to the wall because of high turbulent flow.

b) Spatial conditional average over roughness size

Instead of averaging over the entire zones, we average over individual regions (as colored in figure (VI.4)) for each zone type to compare with the corresponding experimental data. The purpose of this conditional averaging over small areas is to check whether if the temperature field is homogeneous or not within the same zone type. In particular, we aim to highlight eventual dependency on the large scale effect but also to get closer to the measurement procedure employed in the experiment.

Comparison at low Ra number

As shown in figures (VI.4a, VI.4b, VI.4c), the individual behavior over each couple of plots or notches or along a groove is almost the same (in each sub-figure, color lines correspond to the colored surface used for averaged profiles). The overall differences are probably due to the gaps induced from the estimation of equivalent Ra and from the Pr number effects. Since temperature profiles $\langle\overline{\Theta}\rangle$ in the three grooves are exactly similar, we consider only the groove in the center that we decompose into two parts : (i) odd grooves are the zones in between notches where (ii) even groove are the zones in between plots regarding x-direction. As expected, figures (VI.4d,VI.4e) show that the profiles of $\langle\overline{\Theta}\rangle|_{\text{odd groove}}$ are more closer to the experiment data since du Puits et al. (2017) measure the temperature of the groove zone near the center of the plate in between notches.

Comparison at high Ra number

As shown in figures (VI.5a,VI.5b), profiles of $\langle\overline{\Theta}\rangle$ are sensitive to the local averaging area. Indeed, the DNS profiles corresponding to the plots and notches in the center of the plate (red regions) collapse well with the experimental data. Otherwise, the profiles over the regions where $x < 0.4$ differ from the experiment data. The mean temperature field is not homogeneous and demonstrate the dependence on the location of the measurement process. In this respect, we find that the temperature profiles over the the odd groove between notches are the nearest to experimental measures in particular in the center of the cavity $x = 0.5$. Overall, figures (VI.5d,VI.5e) show that $\langle\overline{\Theta}\rangle|_{\text{even groove}} > \langle\overline{\Theta}\rangle|_{\text{odd groove}}$ in the inner zone. It proves that the mean temperature in the groove zone is not homogeneous in spite of similarity for grooves shown in figure (VI.5c). Therefore, any comparison based on local measurements must take into account this inhomogeneity of the mean temperature field around roughness elements.

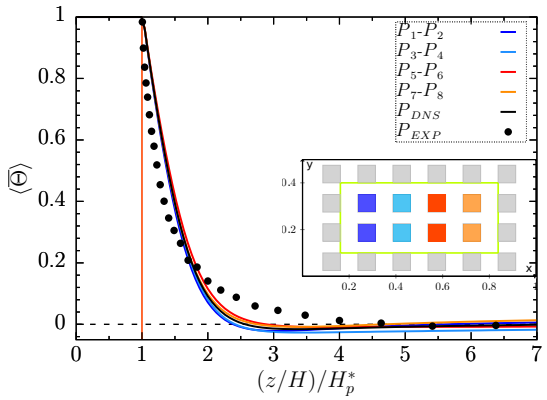

(a) Plots

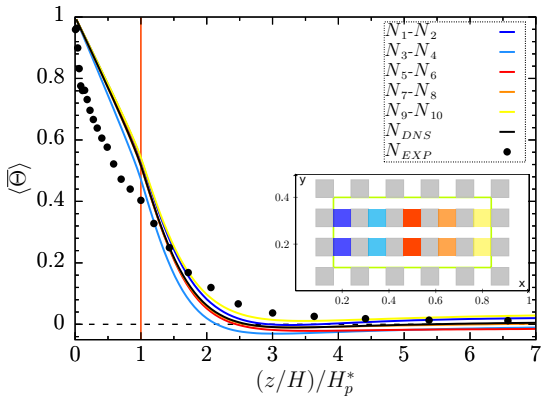

(b) Notches

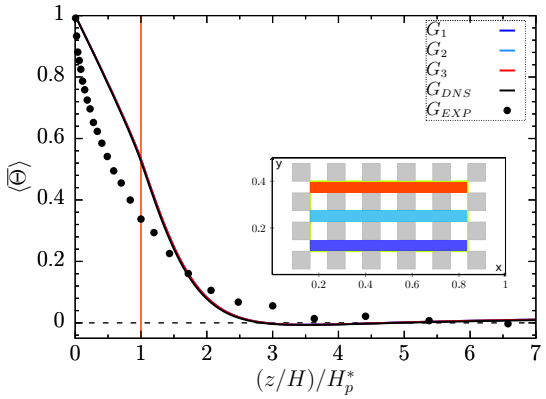

(c) Grooves

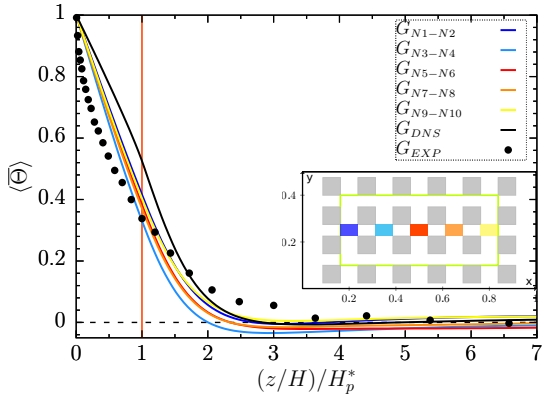

(d) Odd grooves

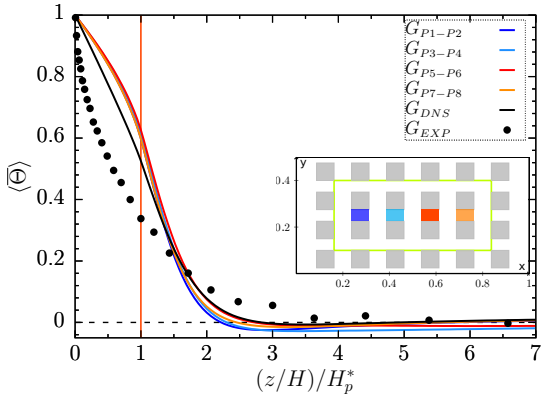

(e) Even grooves

Fig. VI.4 Conditional profiles of the temperature $\langle\overline{\Theta}\rangle$ over local zones : (a) plots (b) notches (c) grooves (d) local odd groove (e) local even grooves at $Ra^{DNS} = 5\times10^6$. Profiles are colored with respect to the map color given in inset of each figure. Black line is an average over the entire zone type. Black dots : experimental data.

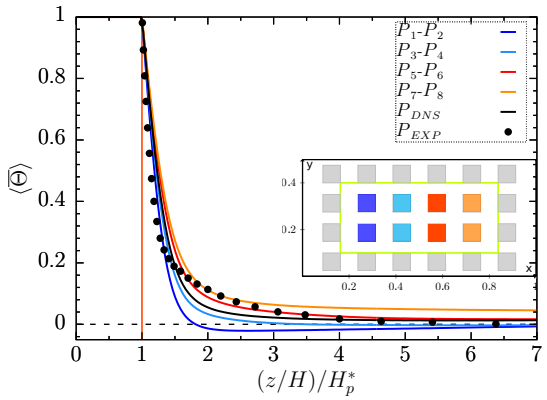

(a) Plots

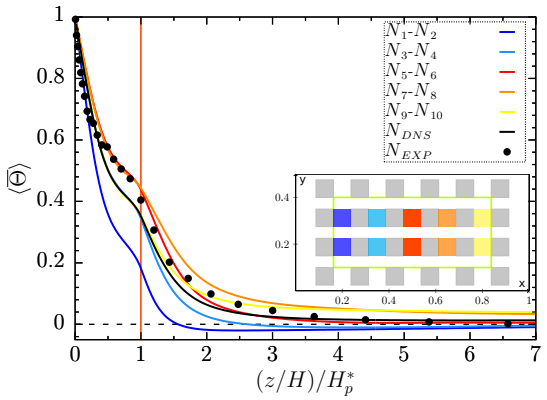

(b) Notches

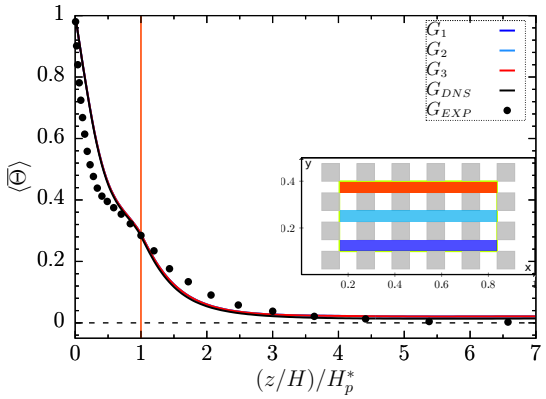

(c) Grooves

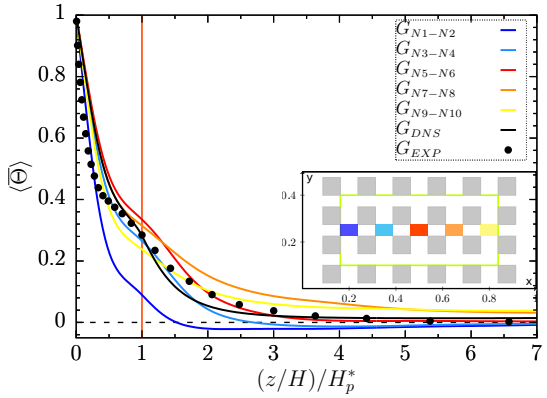

(d) Odd grooves

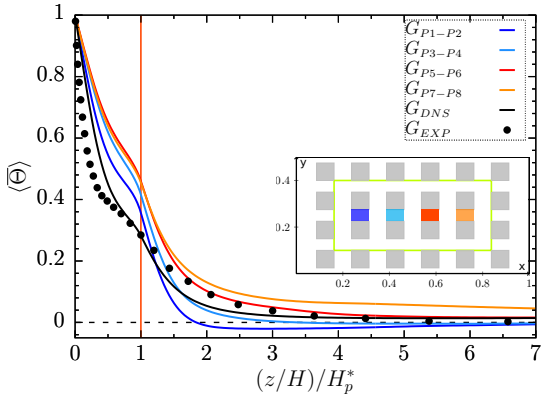

(e) Even grooves

Fig. VI.5 Conditional profiles of the temperature in different zones over (a) plots (b) notches (c) grooves (d) local odd groove (e) local even grooves at $Ra^{DNS} = 5\times10^7$. Profiles are colored with respect to the map color given in inset of each figure. Black line is an average over the entire zone type. Black dots : experimental data.

VI.3.2 Temperature rms profiles

In the following, we keep the spatial decomposition plot/notch/groove. We carried out normalized temperature local profiles Θ_{rms} for the equivalent lower and higher Rayleigh numbers of the experiments.

$$\Theta_{rms}(z) = \frac{\theta_{rms}(z)}{\theta_h - \theta_{bulk}} \tag{VI.5}$$

a) Spatial conditional average over the different regions

Local profiles of Θ_{rms} are plotted in figure (VI.6). At low Ra, we reproduce the global behavior in terms of order magnitude, with exception that Θ_{rms} is underestimated in the outer zone. On the contrary, for high Ra, we have $\Theta_{rms}|_{DNS} \geqslant \Theta_{rms}|_{EXP}$. This could be an effect of the intensity of turbulence which requires a second rescaling of our data. As this is not as straightforward as it might appears. We suppose that first rescaling of the Ra number based only on the gap with Ra_c is not sufficient. One should take into account the dependence of Θ_{rms} on the Ra number.

b) Spatial conditional average over individual regions

In addition to previous observations, figure (VI.7) shows that Θ_{rms} is sensitive to the location of averaging. Indeed, it seems that temperature fluctuations are more important close to the sides of the cell rather than the center of plate. However, we highlight that $\Theta_{rms}|_{EXP}$ collapse better with $\Theta_{rms}|_{\text{odd groove}}$ which support our point of view that data depend strongly on the localization of the sensor.

For high Ra, we can see through figure (VI.8) that changing average location brings a significant dispersion on Θ_{rms} profiles in particular the form at $z \approx H_p^*$. The order of magnitude of $\Theta_{rms}|_{DNS}$ differs highly from experiment data. On this basis, we first discuss in the next section about the behavior of LSC near roughness elements to clarify whether we have a similarities with the experiment or not, at least in shape and near flow properties. Then, we detail the necessity to rescale our DNS data regarding the dependence $\Theta_{rms} \sim Ra$.

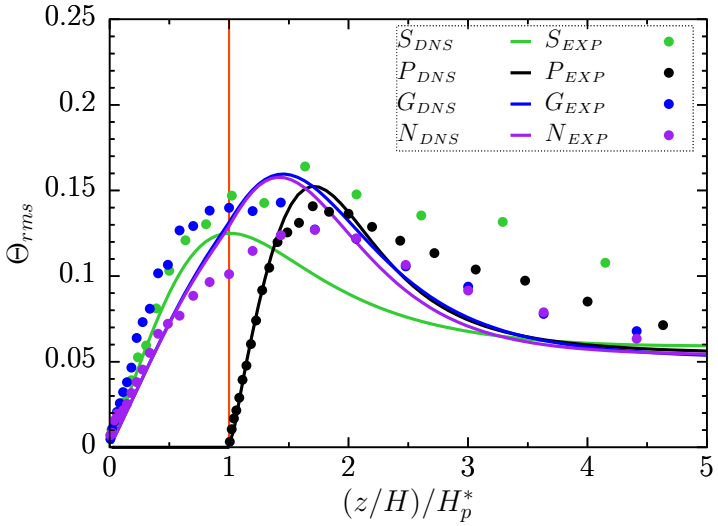

(a) $Ra^{EXP} = 4.6 \times 10^9$ versus $Ra^{DNS} = 5 \times 10^6$

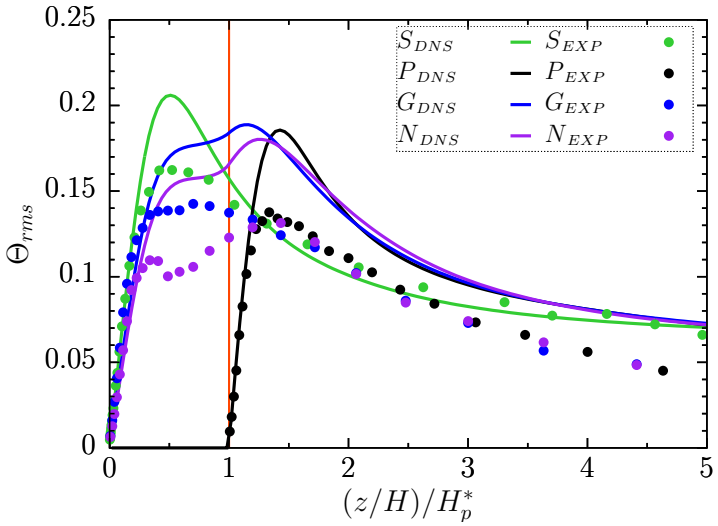

(b) $Ra^{EXP} = 4.7 \times 10^{10}$ versus $Ra^{DNS} = 5 \times 10^7$

Fig. VI.6 Profiles of Θ_{rms} over plots (P), grooves (G), notches (N) and smooth plate (S). Full symbols are for du Puits et al. (2017) experiment data and lines for our DNS.

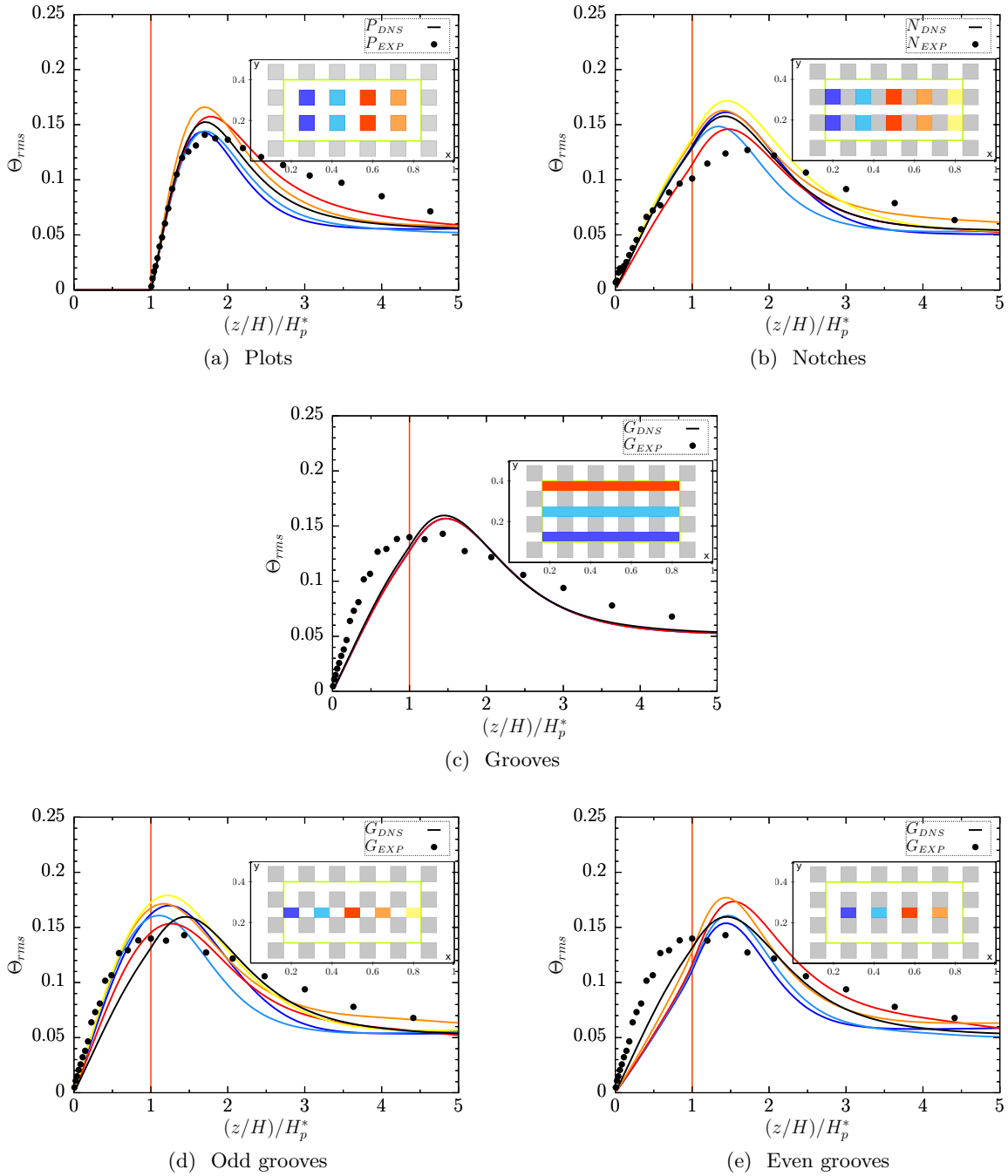

(a) Plots (b) Notches

(c) Grooves

(d) Odd grooves (e) Even grooves

Fig. VI.7 Conditional profiles of normalized temperature rms in different zones over (a) plots and (b) notches (c) grooves (d) local odd groove (e) local even grooves at $Ra = 5 \times 10^6$. Profiles are colored with respect to the map color given in inset of each figure. Black line is an average over the entire zone type. Black point : experimental data.

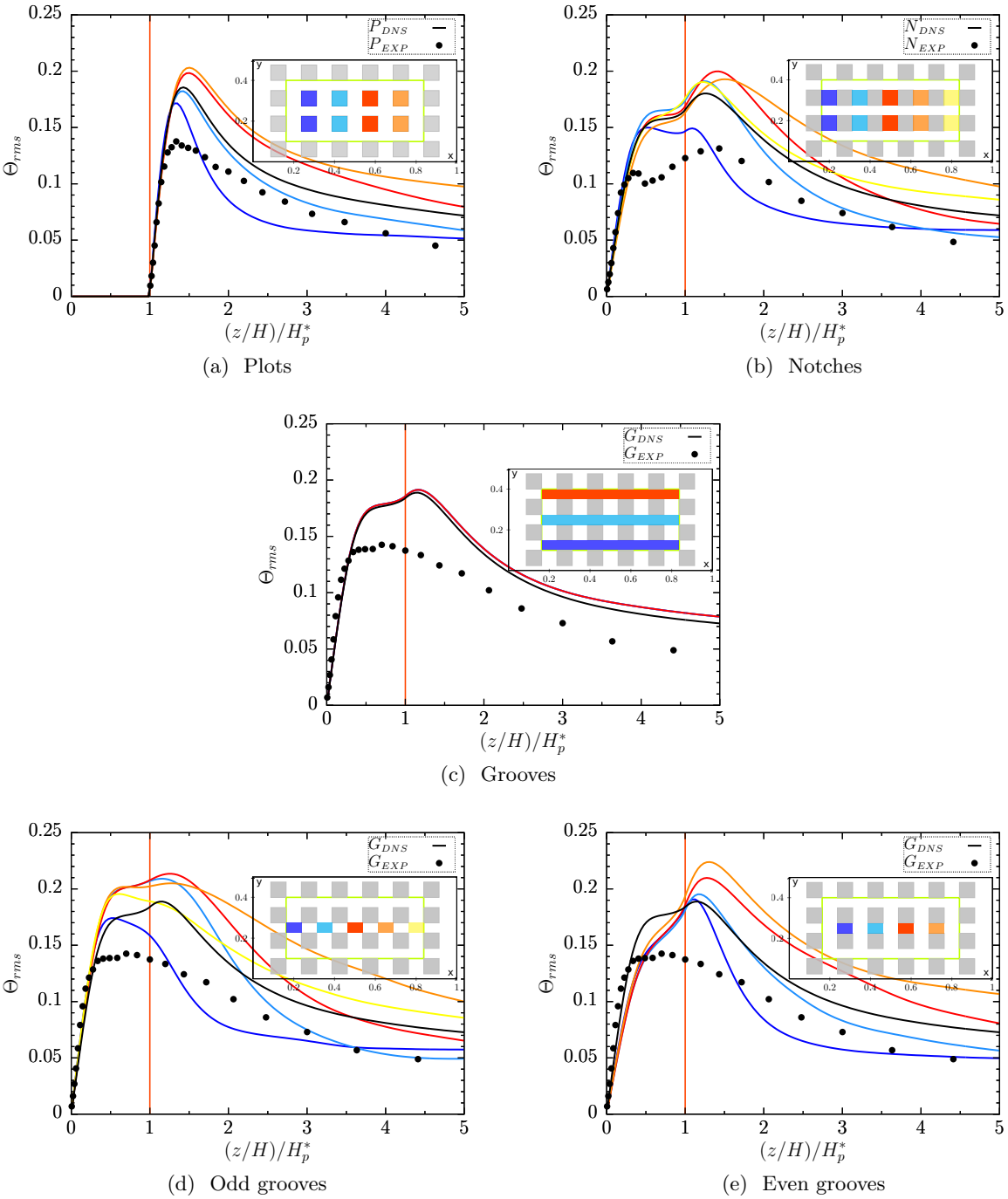

(a) Plots (b) Notches

(c) Grooves

(d) Odd grooves (e) Even grooves

Fig. VI.8 Conditional profiles of normalized temperature rms in different zones over (a) plots and (b) notches (c) grooves (d) local odd groove (e) local even grooves at $Ra = 5 \times 10^7$. Profiles are colored with respect to the map color given in inset of each figure. Black line is an average over the entire zone type. Black point : experimental data.

VI.4 Effects of the Large scale circulation filling the box

In order to perform a fair comparison with the experiment, we evaluate the influence of the large scale circulation on the measurements. Thus, it requires a characterization of the flow patterns near the rough plate in particular the orientation of the LSC. We used 8 probes placed over the roughness elements located at the center of the plate at a hight $z = 2H_p^*$ as shown in figure (VI.9).

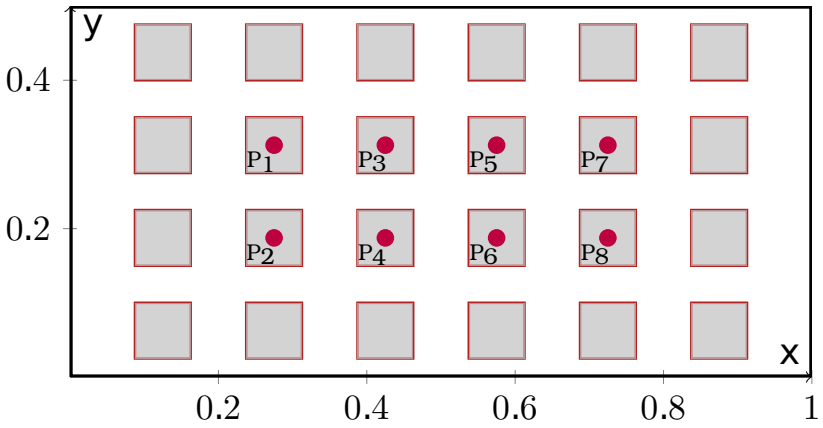

(a) Top view

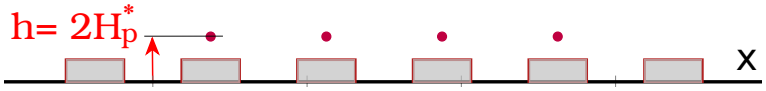

(b) Side view

Fig. VI.9 Locations of the 8 probes near the rough plate.

We adopted a simple methodology for the measurement of the direction of the LSC at an horizontal plan of the cell. By recording the longitudinal and transversal velocities with the 8 probes P_i with $i = 1 : 8$, we can construct the local direction magnitude time series $\varphi_{LSC}^{P_i}(t)$. The average of the 8 signals $\varphi_{LSC}^{8-P}(t)$ is considered as the direction of the flow near the rough plate.

$$\varphi_{LSC}^{8-P}(t) = \frac{1}{8}\sum_{i=1}^{8} Arctan(\frac{v_{|P_i}(t)}{u_{|P_i}(t)}) \tag{VI.6}$$

In figure (VI.10), we plot time series of $\varphi_{LSC}^{8-P}(t)$ for different Ra numbers. Figure (VI.11a) shows the absolute value of the time averaged of the LSC direction $|\overline{\varphi}_{LSC}^{8-P}|$. With increasing Ra until 10^6, the mean orientation of the LSC relative to $\overrightarrow{i}$ vector varies in $\approx [20°, 45°]$. Actually, in the case of the steady flows, i.e Ra ranging in $[10^5, 10^6]$, there is only one main roll filling the box in which the horizontal flow near roughness is almost diagonally oriented as shown in figures (VI.12a) and (VI.12b).

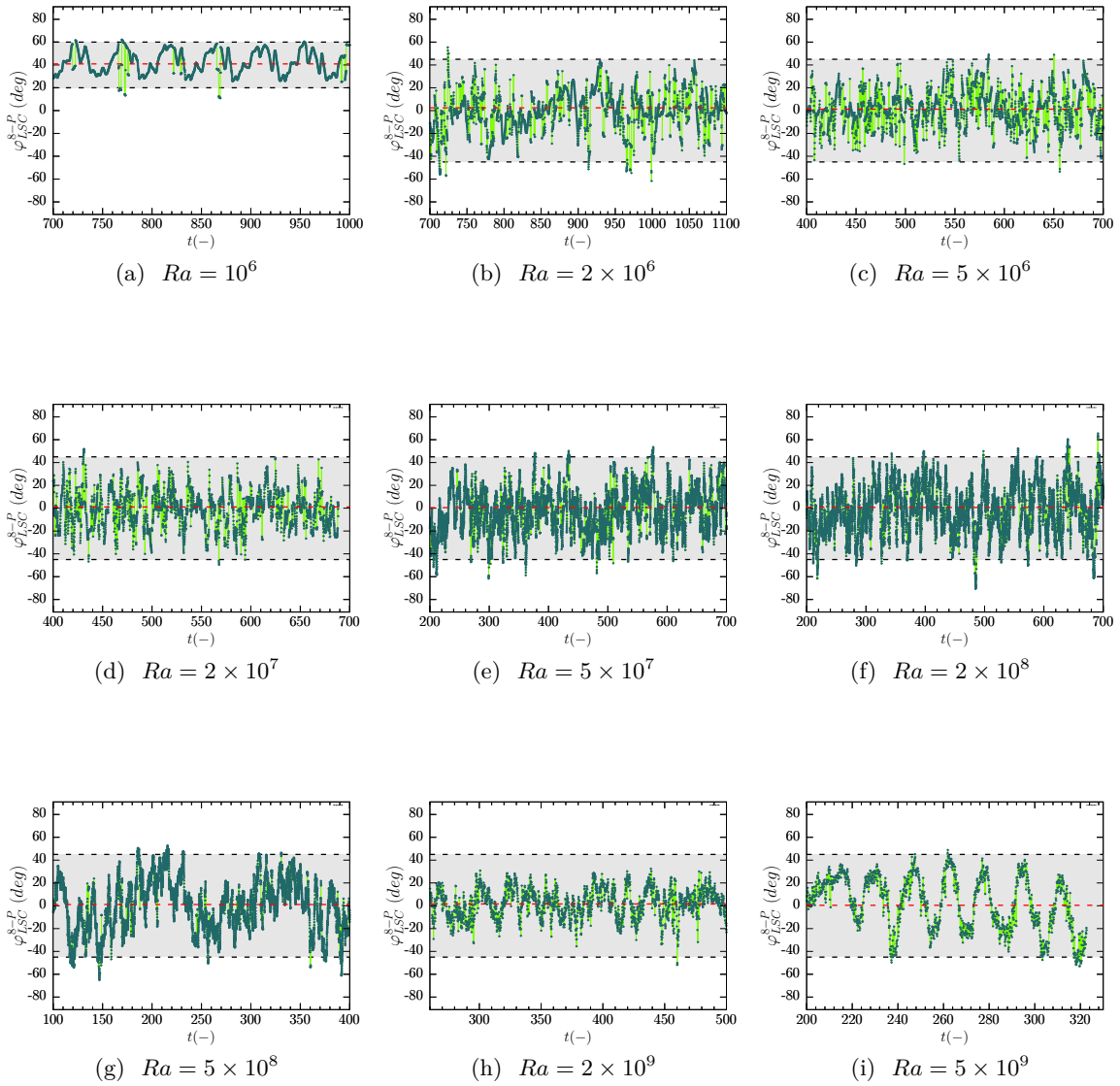

(a) $Ra = 10^6$ (b) $Ra = 2 \times 10^6$ (c) $Ra = 5 \times 10^6$

(d) $Ra = 2 \times 10^7$ (e) $Ra = 5 \times 10^7$ (f) $Ra = 2 \times 10^8$

(g) $Ra = 5 \times 10^8$ (h) $Ra = 2 \times 10^9$ (i) $Ra = 5 \times 10^9$

Fig. VI.10 Time series of the mean direction magnitude $\varphi_{LSC}^{8-P}(t)$ calculated using 8 probes located at the center of the rough plate (equation (VI.6)) at $z = 2H_p^*$ function of Ra. Red dashed lines represent the time averages of these series.

For $Ra \geqslant 2 \times 10^6$, the time series in figures ((VI.10b), (VI.10c), (VI.10d), (VI.10e), (VI.10f), (VI.10g), (VI.10h)) show that the LSC is oscillating within a range of $[-45°, 45°]$. As we have $|\overline{\varphi}_{LSC}^{8-P}| \approx 0$, thus the mean flow is statistically aligned with the $\overrightarrow{i}$ direction. The probability density functions of φ_{LSC}^{8-P} for $Ra \geqslant 2 \times 10^6$ are plotted in figure (VI.11b). It shows that φ_{LSC}^{8-P} is symmetrically distributed with respect to the zero degree axis which means that the mean flow near roughness is oriented parallelly to $\overrightarrow{i}$ vector.

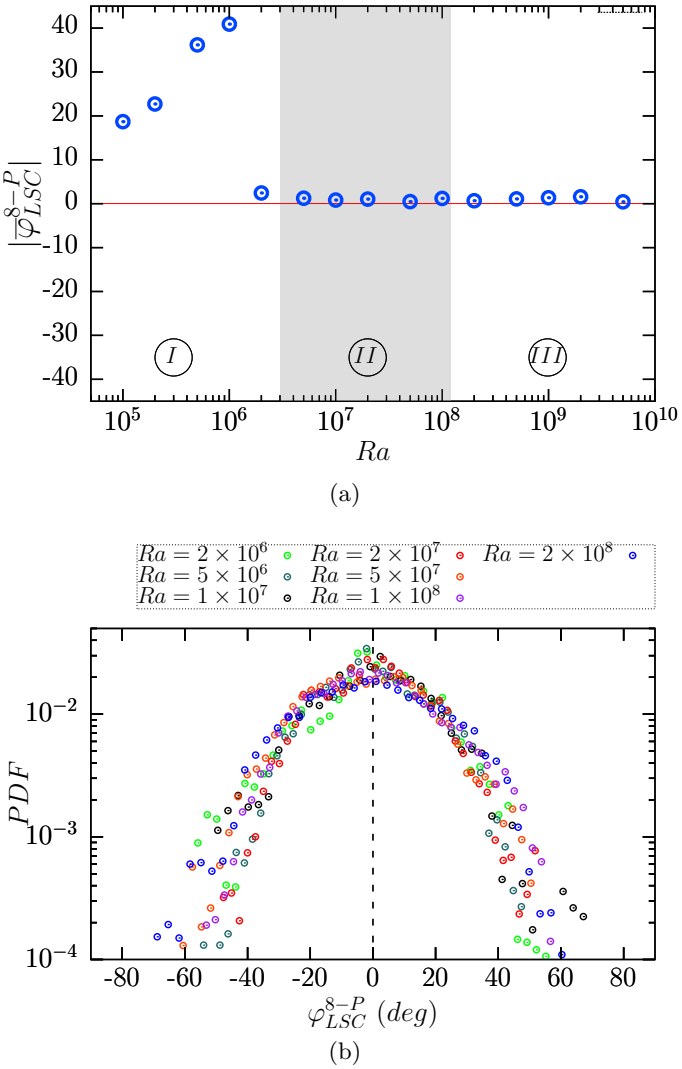

Fig. VI.11 (a) Time average of direction magnitude near rough plate as function of Rayleigh number. (b) Probability density function of the direction magnitude near rough plate at $z = 2H_p^*$ for different Rayleigh numbers.

However, this method can not determine whether the LSC is oriented in the clockwise or anticlockwise direction. The analysis of figure (VI.12c) and (VI.12d) reveal that the flow is organized in a set of multiple roll structures. We only highlight this behavior for particular range of Rayleigh number $2 \times 10^6 \leqslant Ra \leqslant 2 \times 10^7$. It is consistent with the observations reported by Wagner and Shishkina (2013). In this paper, they used a symmetric smooth cell S/S with an aspect ratio $\Gamma_y = 1/4$ and showed with a decomposition of the instantaneous flow fields into two-dimensional modes, i.e they estimate the number and type of the structure present in the cavity. These investigations reveal a mixture of different modes and the flow field tends to be organized into one to four rolls structure when $3 \times 10^6 \leqslant Ra \leqslant 2 \times 10^7$.

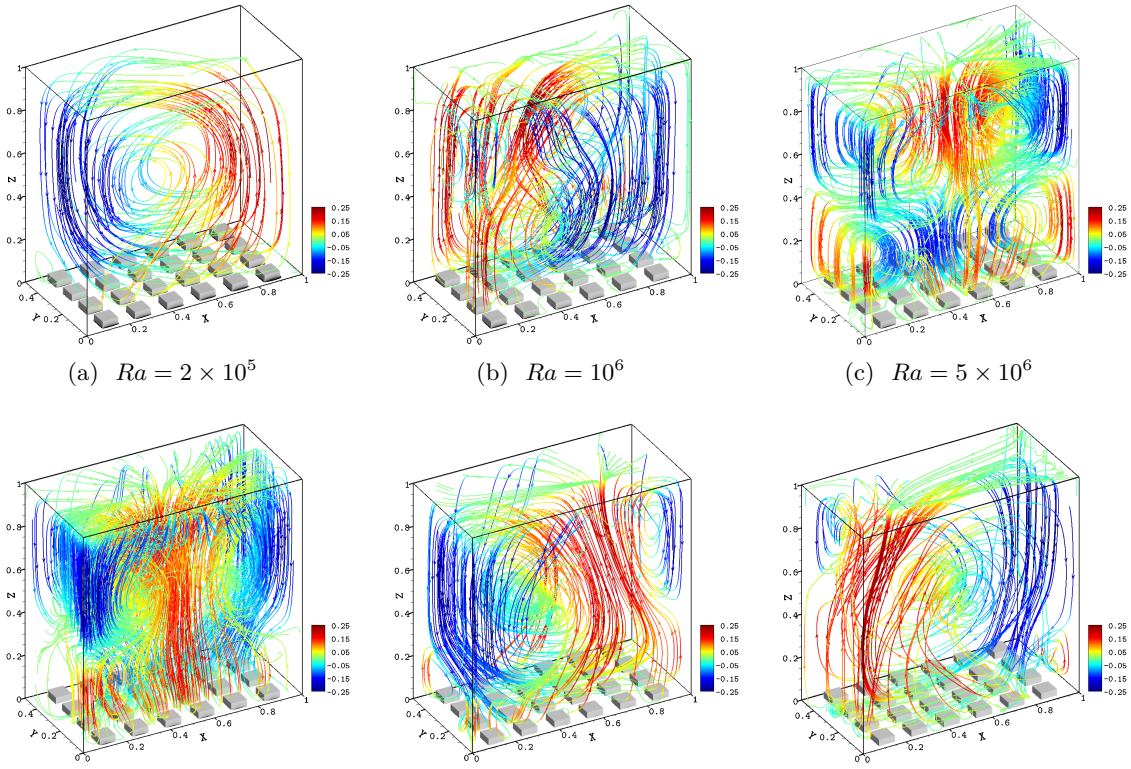

(a) $Ra = 2 \times 10^5$ (b) $Ra = 10^6$ (c) $Ra = 5 \times 10^6$

(d) $Ra = 10^7$ (e) $Ra = 5 \times 10^7$ (f) $Ra = 10^9$

Fig. VI.12 3D plot of the mean velocity streamlines colored with the vertical velocity $\overline{w}$.

It is more appropriate to look for the local direction magnitude at the 8 probes independently. We take into account the oscillations of $\varphi^{P_i}(t)$ in all possible directions in the horizontal plan. We use the following conditional definitions,

$$\begin{cases} if \quad (u_{|P_i}(t) > 0) \quad \text{then} \quad \varphi^{P_i}(t) \quad = Arctan(\dfrac{v_{|P_i}(t)}{u_{|P_i}(t)}) \\ if \quad (u_{|P_i}(t) < 0) \quad \text{then} \quad \varphi^{P_i}(t) \quad = Arctan(\dfrac{v_{|P_i}(t)}{u_{|P_i}(t)}) + \pi \end{cases} \tag{VI.7}$$

Since we are dealing with angles, it is better to express the direction magnitude properly in a two-dimensional polar coordinates. We make a change of the variables to switch to the new coordinate system. Therefore, the radial coordinate $t|_p$ will represent the time units where the azimuthal coordinate $\varphi^{P_i}|_p$ is the direction magnitude itself.

As sketched in figure (VI.13), the trigonometric circle is divided into four quadrants. The gray quadrants I and II represent the positive x-direction. Otherwise, if the angle $\varphi^{P_i}|_p$ is within the quadrants III and IV, it means that the flow is oriented towards negative x-direction. Furthermore, we can also check whether the flow is oriented parallelly to $\overrightarrow{i}$ vector or to a particular quadrant. In the following, we discuss three cases including the low and the high Ra numbers and at even higher Ra in the range of the experiments of du Puits et al. (2017). It is useful to improve the comparison between the DNS and EXP vertical profiles.

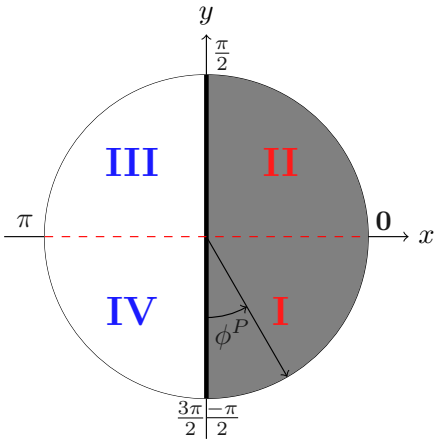

Fig. VI.13 (Color online) Sketch of a horizontal plan. The direction magnitude φ^{P_i} of the flow is defined in the four quadrants of trigonometric circle and ranging in $[\frac{-\pi}{2}\ \frac{3\pi}{2}]$.

a) Flow orientation in experimental cases

Since the experiment are conducted at $Ra > 10^9$. We check the with DNS the flow orientation for $Ra = 10^9$ at the same range as in the experiments, figure (VI.14) shows that the flow is totally oriented towards negative x-direction. It is statistically aligned with $\overrightarrow{i}$ because the oscillation of $\varphi|_p(t|_p)$ at all the probes are identified in quadrants III and IV are symmetrical.

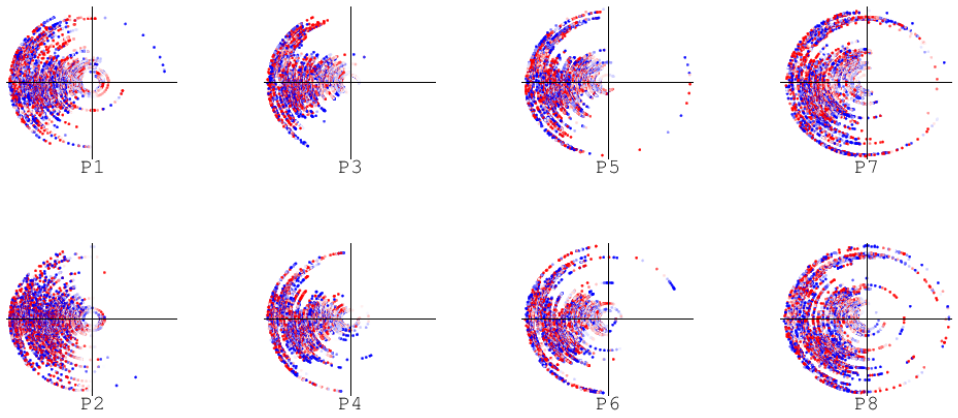

Fig. VI.14 Local direction magnitudes $\varphi^{P_i}|_p(t|_p)$ recorded near the rough plate with the probes P_i with $i = 1 : 8$ for Rayleigh number $Ra = 10^9$. Red and blue colors represent whether the intensity of the time derivative $\partial_t\varphi^{P_i}$ is positive (clockwise) or negative (anticlockwise).

b) Local direction magnitude for lower Rayleigh number $Ra = 5 \times 10^6$

As shown in figure (VI.15), the flow is divided into two cells in which the fluid is moving in opposite directions (figure (VI.12c)). According to the probes $P_{i=1,4}$, the LSC is oriented towards negative x-direction where $P_{i=5,8}$ indicate that the LSC is directed to positive x-direction. Overall, it seems that there is a trend for the flow to go toward corners in particular over $P_{1,2}$ respectively towards the quadrants III and IV while over $P_{7,8}$ it goes towards

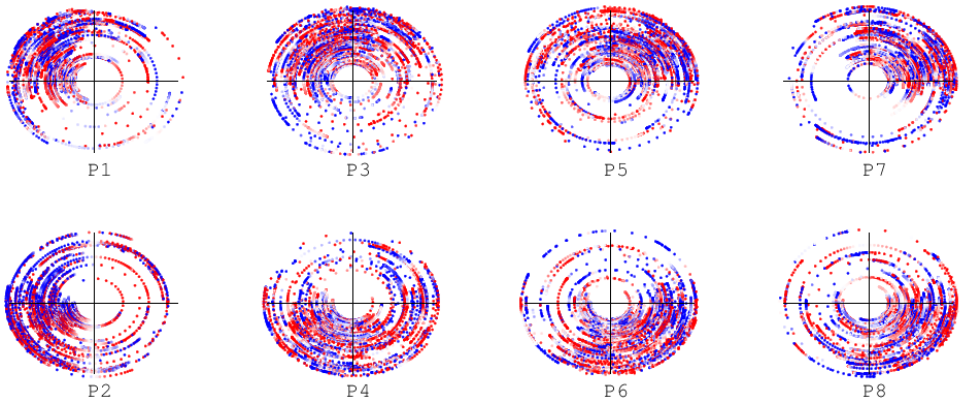

Fig. VI.15 Local direction magnitudes $\varphi^{P_i}|_p(t|_p)$ recorded near the rough plate with the probes P_i with $i = 1:8$ for lower Rayleigh number $Ra = 5 \times 10^6$.

quadrants II and I. The oscillations of $\varphi|_p(t|_p)$ over $P_{1,2}$ and $P_{7,8}$ are symmetrical, the flow is statistically parallel to $\overrightarrow{i}$ vector at $y = D/2$. These findings suggest that the measures for this low Ra should be performed near the left or right sides of the cell (close to $P_{7,8}$) to get as close as possible to experimental flow structure.

c) Local direction magnitude for higher Rayleigh number $Ra = 5 \times 10^7$

As shown in figure (VI.16), the LSC is oriented towards $\overrightarrow{i}$ direction. Indeed, $\varphi^{P_i}|_p$ is oscillating in the right quadrants I and II except near $P_{7,8}$ that oscillate in all quadrants because we have both the LSC and the counter-rotating corner eddies that sometimes widens and be within the probes $P_{7,8}$. Therefore, we suggest that measures in the center would more consistent with the experiment.

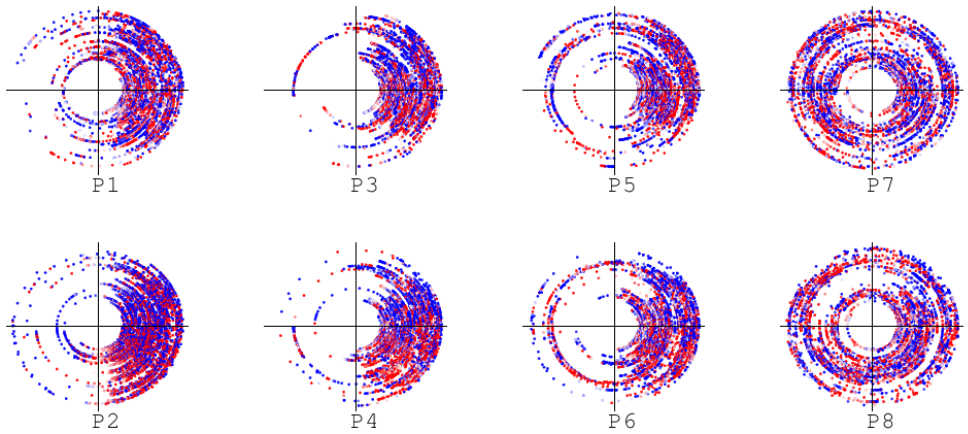

Fig. VI.16 Local direction magnitudes $\varphi^{P_i}|_p(t|_p)$ recorded near the rough plate with the probes P_i with $i = 1:8$ for higher Rayleigh number $Ra = 5 \times 10^7$.

VI.5 Comparison of temperature rms profiles along vertical lines

Figures (VI.17) and (VI.18) show the distribution of temperature rms over horizontal planes near the rough elements. It is clear that the intensity highly varies with the location. For low Ra, Θ_{rms} is relatively larger on the sides. For high Ra we could see the high intensity of fluctuation growing up around the left and right sides of the roughnesses. Otherwise near the front and back edges, the fluctuations are relatively less intense. These observations evince the sensibility of the mean vertical profiles of temperature rms to the averaging area. On the one hand, in order to show the differences of intensity fluctuation around the roughness, profiles of temperature rms are plotted in vertical direction at specific locations. The goal here is to reproduce the experimental measurement procedure with a temperature sensor. This methods makes clear the spatial dependence of the temperature fluctuations at various locations in the cell. On the other hand, the intensity of thermal fluctuation varies with increasing Ra number. In that respect, experimental work of Daya and Ecke (2001, 2002) shows the dependence of temperature fluctuations on Ra as $\Theta_{rms} \sim Ra^{-0.05}$ for $Pr = 3.25$ and $\Theta_{rms} \sim Ra^{-0.10}$ for $Pr = 5.47$. Also, Grossmann and Lohse (2004) based on their unifying theory get $\Theta_{rms} \sim Ra^{\gamma}$ with $-0.16 \leqslant \gamma \leqslant -0.11$. We used formula from Daya and Ecke (2001, 2002) to rescale the DNS profiles of Θ_{rms} with respect to the differences with the experimental work of du Puits et al. (2017) conducted at three decades of Ra numbers higher than our DNS cases.

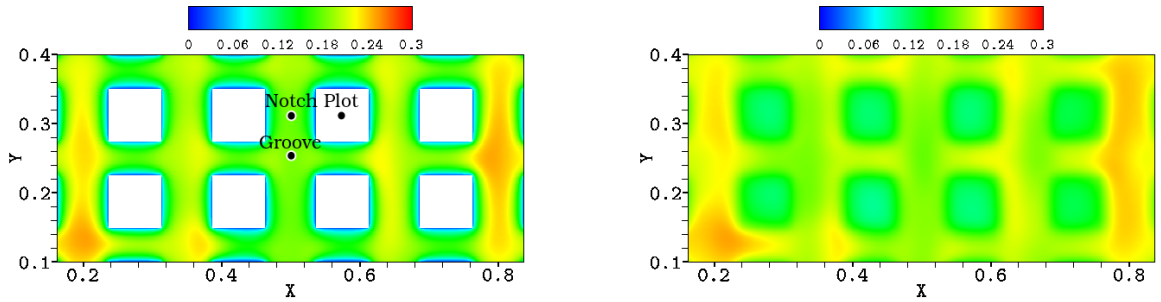

(a) $z = H_p^*$ (b) $z = \frac{4}{3}H_p^*$

Fig. VI.17 Time averaged field of Θ_{rms} near the plate for $Ra = 5 \times 10^6$.

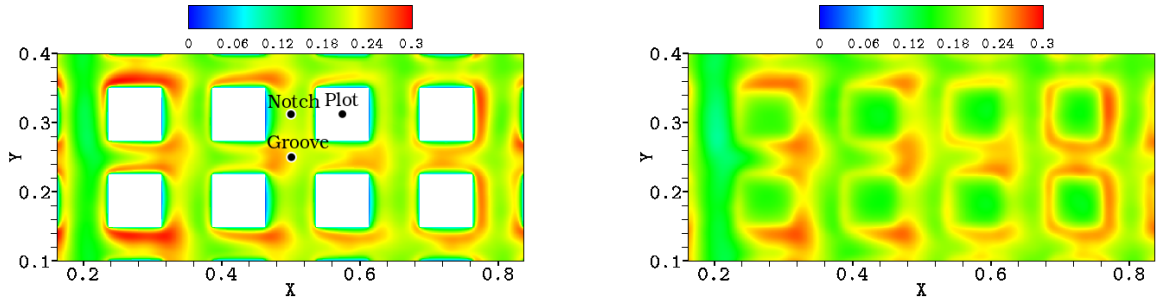

(a) $z = H_p^*$ (b) $z = \frac{4}{3}H_p^*$

Fig. VI.18 Time averaged field of Θ_{rms} near the plate for $Ra = 5 \times 10^7$.

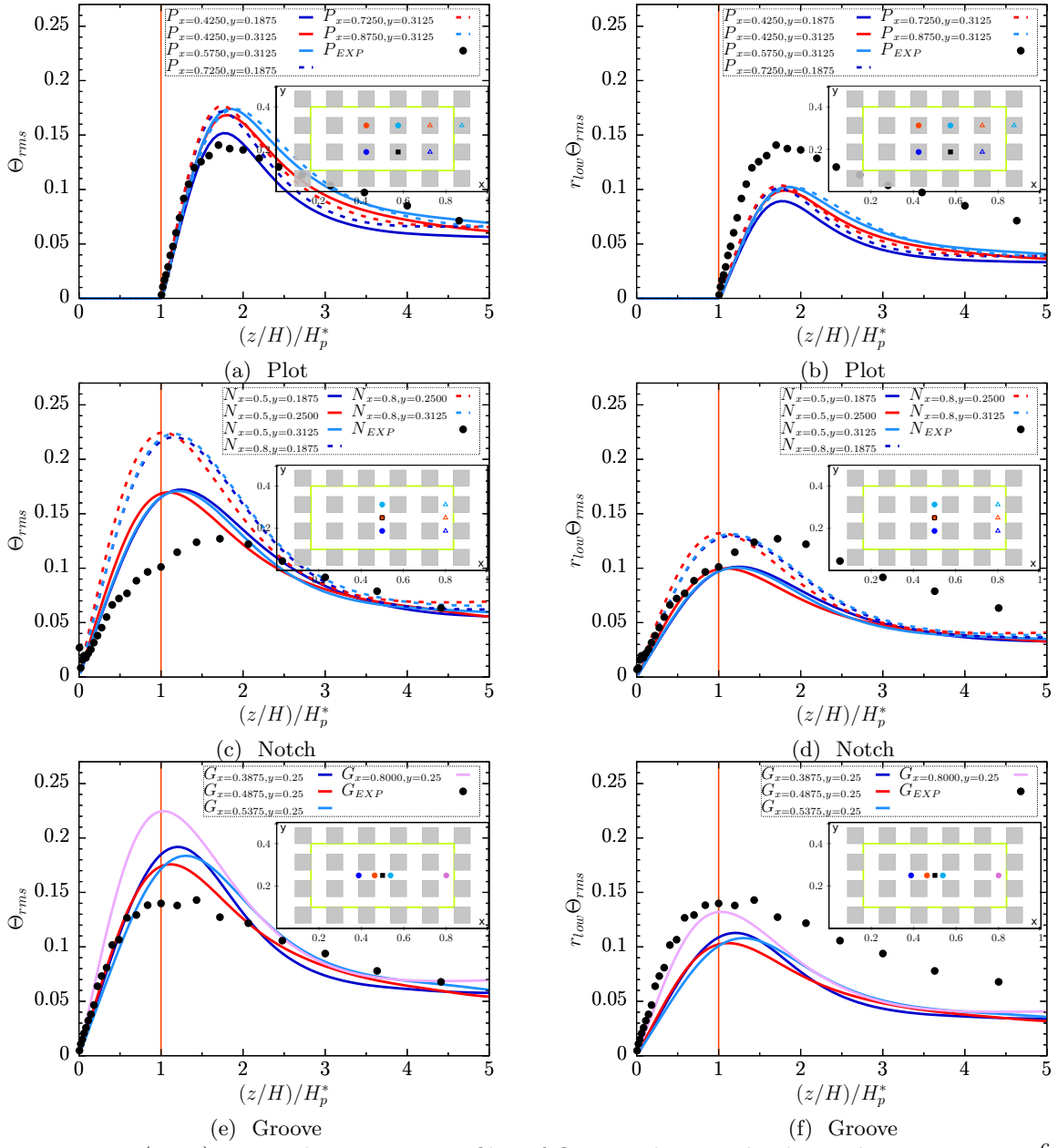

(a) Plot (b) Plot

(c) Notch (d) Notch

(e) Groove (f) Groove

Fig. VI.19 (a,c,e) Vertical pointwise profiles of Θ_{rms} at low Rayleigh number $Ra = 5 \times 10^6$. (b,d,f) are the compensated Θ_{rms} by the ratio $r_{low} = [Ra^{low-EXP}/Ra^{low-DNS}]^{-0.09}$. Profiles are colored with respect to the map color given in inset of each figure.

The DNS Θ_{rms} profiles are plotted against experimental data of lower Ra as shown in figure (VI.19). By adopting the same measurement technique as in experiment, we show that the intensity of $\Theta_{rms}|_{DNS}$ around $z = H_p^*$ is higher near the right side at $z = 0.8$, in particular over the groove and notches (figures (VI.19a), (VI.19c), (VI.19e)). This demonstrates the effects of the location on measurements. By taking into account the gap between Ra numbers, i.e DNS vs EXP, we rescale the DNS data and obtain practically the same intensity of the peak of Θ_{rms} profiles notably over notches and grooves at $z = 0.8$ where the flow structure is comparable with EXP case except over plot zone where $\Theta_{rms}|_{DNS}$ is overestimated.

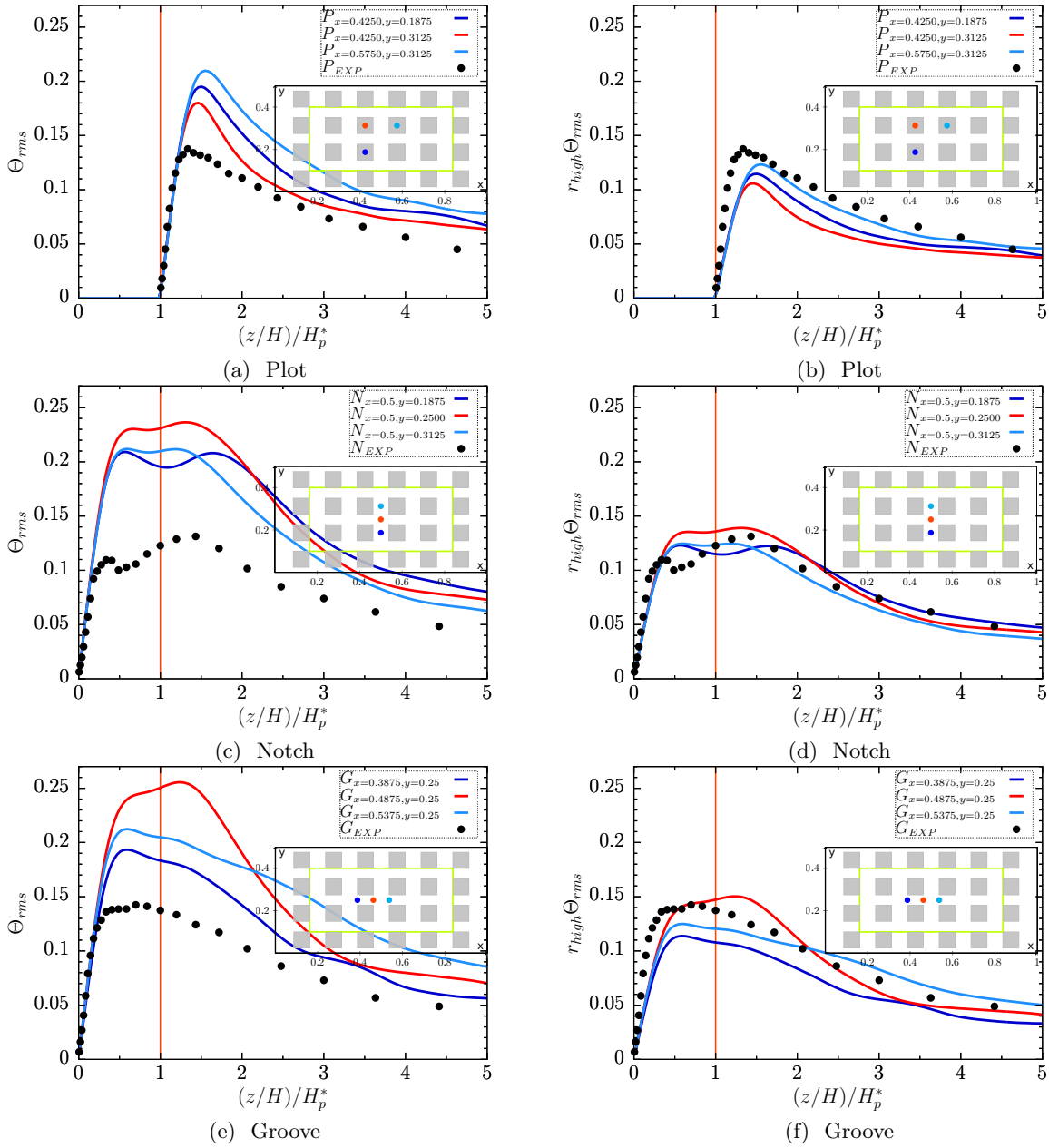

(a) Plot (b) Plot

(c) Notch (d) Notch

(e) Groove (f) Groove

Fig. VI.20 (a,c,e) Vertical pointwise profiles of Θ_{rms} at high Rayleigh number $Ra = 5 \times 10^7$. (b,d,f) are the compensated Θ_{rms} by the ratio $r_{high} = [Ra^{high-EXP}/Ra^{high-DNS}]^{-0.09}$. Profiles are colored with respect to the map color given in inset of each figure.

For higher Ra number, Θ_{rms} profiles are shown in figure (VI.20). We highlight the sensibility of the results to the location of the sensor in particular in the groove zone (figure (VI.20c). Indeed, intensity of Θ_{rms} is higher over the red pointwise which consistent with the flow structure shown in figure (VI.18a). Therefore, the locations of measures are chosen to be closer as possible to the experimental one. By taking into account the effects of Ra on the fluctuation intensity of temperature, the rescaled data mostly collapse with the EXP-data.

VI.6 Conclusion

A direct comparison for the asymmetric rough cell is conducted between our 3D DNS with the experimental work of du Puits et al. (2017). Despite the fact of inhomogeneity of the flow patterns due to the presence of the roughness elements, we looked for a robust method to compare the DNS and experimental measurements. Profiles of the vertical temperature in z-direction are available from EXP-data. The differences with the experiment are (i) the range of Rayleigh number explored three decades higher than in our DNS, (i) the size of roughness elements. This leads to a different Ra_c. We therefore introduced a scaling based on Ra_c in order to compare the results.

Since it is possible to identify equivalent Ra numbers to the experimented in terms of the regime of the heat transfer. The present method is based on the identification of a similar ratio between the rough and critical Rayleigh numbers. The discrepancy in Ra numbers also led to the introduce of a global rescaling of the temperature. We then calculated mean profiles of the temperature Θ using conditional spatial average over different locations. A good agreement is obtained when the region of averaging the DNS-data is closer to the position of the sensor in the experiment in particular in the groove zone.

The present DNS reveals that temperature fluctuations field is not homogeneous around roughness elements. It is strongly depended on the large scale circulation and the location of the measures. As a consequence, the comparison could be only conducted in a local way, i.e pointwise vertical profiles. Therefore, we identified the equivalent measurement positions to those in the experiment based on the similarity of the flow structure. In the experiment, means are made at different location. In the DNS, it is possible to make spatial averages. This allowed me to establish the influence of the LSC on the temperature measurements. When different factors were taken into account, a good agreement was observed especially at high Ra number. The present DNS vs EXP comparison is successful and approves the ability of the code to reproduce the flow physics with rough surfaces in spite of macroscopic size of the obstacles employed in the numerical modeling.

VII – Characterization of thermal plumes

VII.1 Introduction

We have seen that the presence of roughness on one side implies differences on the flow structure when comparing the rough and smooth plates. As seen in chapter (*III*), the symmetry is broken in terms of thermal fluctuations which are reinforced in the half bottom side but only during the intermediate regime II. The origin of this intensification is not well known and supposed to be linked with characteristics of thermal plumes. This will be the subject of the present chapter. Previous studies in classic RBC such as of Shang et al. (2003, 2004) have showed the role of thermal plumes in driving the large scale flow and in carrying the heat within the cavity. Zhou and Xia (2010) studied the physical and geometrical properties of thermal plumes and suggested that the plume number primarily determines the scaling law $Nu \sim Ra^{\beta}$ in particular the scaling exponent. As roughness can modify the flow dynamics as observed by Du and Tong (2000); Stringano et al. (2006), the question then arises of how roughness elements modify the initiation and the properties of the thermal plumes. First we compare the near wall dynamics between the hot rough and cold smooth plates of the asymmetric RBC in the three regimes of heat transfer described in Chapter (§ IV). We mainly discuss and compare plumes characteristics (amplitude, width,

size). By use of "numerical ombroscopy", we discuss about the qualitative aspects of the thermal structure near both plates. Finally, a method based on thermal dissipation is used to quantify the number of buoyant plumes.

VII.2 Plume analysis based on temperature and velocity time series

We compare the roughness effects on the flow dynamics at different regimes of heat transfer as identified in chapter (IV). The chosen Rayleigh numbers representative of each regime are (i) $Ra = 10^6$, (ii) $Ra = 5 \times 10^7$ and (iii) $Ra = 2 \times 10^9$. This choice is justified by the presence of a large scale circulation formed by a single roll filling the cavity as shown in figure (VI.12) for these three cases. In order to extract plume properties, local temperature and vertical velocity measurements are performed using a set of multiple probes placed symmetrically near the rough wall at a distance $z = 3H_p^*$ and the smooth plate at $z = 1 - 3H_p^*$. This vertical position is chosen to be higher than the thermal and viscous boundary layers thicknesses. Actually, among the three Ra, the ratio $3H_p/\delta_\theta^*$ is about 2 (for $Ra = 10^6$) to 10 (for $Ra = 2 \times 10^9$). Thus, we consider that the probes are placed "thermally" inside the bulk region. Likewise, the ratio $3H_p/\delta_u^*$ is about 2 to 5. Thus, we consider also that our probes are placed outside the viscous BL. However, we should note here that for $Ra = 10^6$, some effects would be expected since the probes are likely in the mixing layer.

As shown in figure (VII.1), a total of 7 probes placed at the center zone of the horizontal plane near each plate are sharing roughly the same physical behavior. Thus one could use them to gather as much as possible observations in order to get statistically converged results. The sampling is done each time step (Δt is given in table [III.1]). With all 7 probes gathered, we obtain about 1.4 to 4 million samples for each time series.

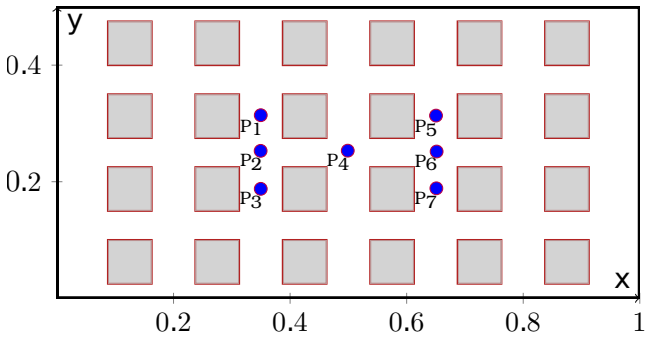

(a) Top view

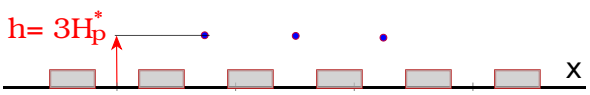

(b) Side view

Fig. VII.1 Locations of the 7 probes near the rough or the smooth plates [$(x = 0.35; 0.5; 0.65), (y = 0.1875; 0.25\ ; 0.3125)$].

VII.2.1 Histogram of time series

First, we show in figures (VII.2) and (VII.3) just an examples of time series of temperature fluctuations $\theta^{'}(t)$ and vertical velocity fluctuations $w^{'}(t)$ recorded at two symmetric probes placed at the center $(x, y) = (W/2, D/2)$. $(\theta^{'}, w^{'})$ are obtained by subtracting the time average of the complete set of time-series to the instantaneous value. We then calculate histograms based on time series monitoring on the 7 probes.

$$\theta^{'} = \theta - \overline{\theta} \tag{VII.1}$$

$$w^{'} = w - \overline{w} \tag{VII.2}$$

From figures (VII.2), we shortly describe the thermal fluctuations at 3 different regimes,

- Regime I : (figures (VII.2 a,b)), temperature fluctuations are weak near both sides $\theta^{'}|_R \cong \theta^{'}|_S$. Nevertheless, some intense fluctuations appear near rough wall from time to time but they remain infrequent.
- Regime II : (figures (VII.2 c,d)), we see the downward and upward spikes which are associated *a priori* with cold and hot thermal plumes detached from the upper and lower boundary layers respectively. Clearly, we observe a change of the flow dynamics near the rough wall as reported by Du and Tong (1998, 2000), i.e the peaks with large intensity $|\theta'| > 0.1$ are more frequent on the rough side. But both sides recover more comparable dynamics.
- Regime III : (figures (VII.2 e,f)), comparing with regime II, the intensity of $|\theta^{'}|$ is smaller. We still observe intense fluctuations in the order of $|\theta^{'}| > 0.5$ more importantly on the rough side.

Figures (VII.3) show the vertical velocity fluctuations. We called an overspeed velocity fluctuations that correspond to $(w - \overline{w}) \cdot \overline{w} > 0$ while an underspeed represent the fluctuations corresponding to $(w - \overline{w}) \cdot \overline{w} < 0$. These particular events are typical for thermal plumes. Depending on Ra number, We mainly observe in,

- Regime I : (figures (VII.3 a,b)), we can observe that the intensity of the velocity fluctuations is similar when comparing the rough and smooth sides. These fluctuations are in the order of $|w^{'}| \leqslant 0.07$ on both sides.
- Regime II : (figures (VII.3 c,d)). Intensive fluctuations comparing with regime I. Near the smooth plate, large positive and negative fluctuations are present, i.e they correspond to an overspeed and underspeed fluctuations. In contrast, close to the rough plate, fluctuations of overspeed type seem to be dominant.
- Regime III : (figures (VII.3 e,f)), close to the rough and smooth sides, we observe a similar behavior with frequent overspeed oscillations, i.e large $w^{'} > 0$ close to the rough plate while large $w^{'} < 0$ on the smooth plate.

For now, we highlighted observations on $\theta^{'}$ and $w^{'}$ time series. It seems that a change of the flow dynamic is remarkable. Next, we study the histograms of fluctuations and discuss about

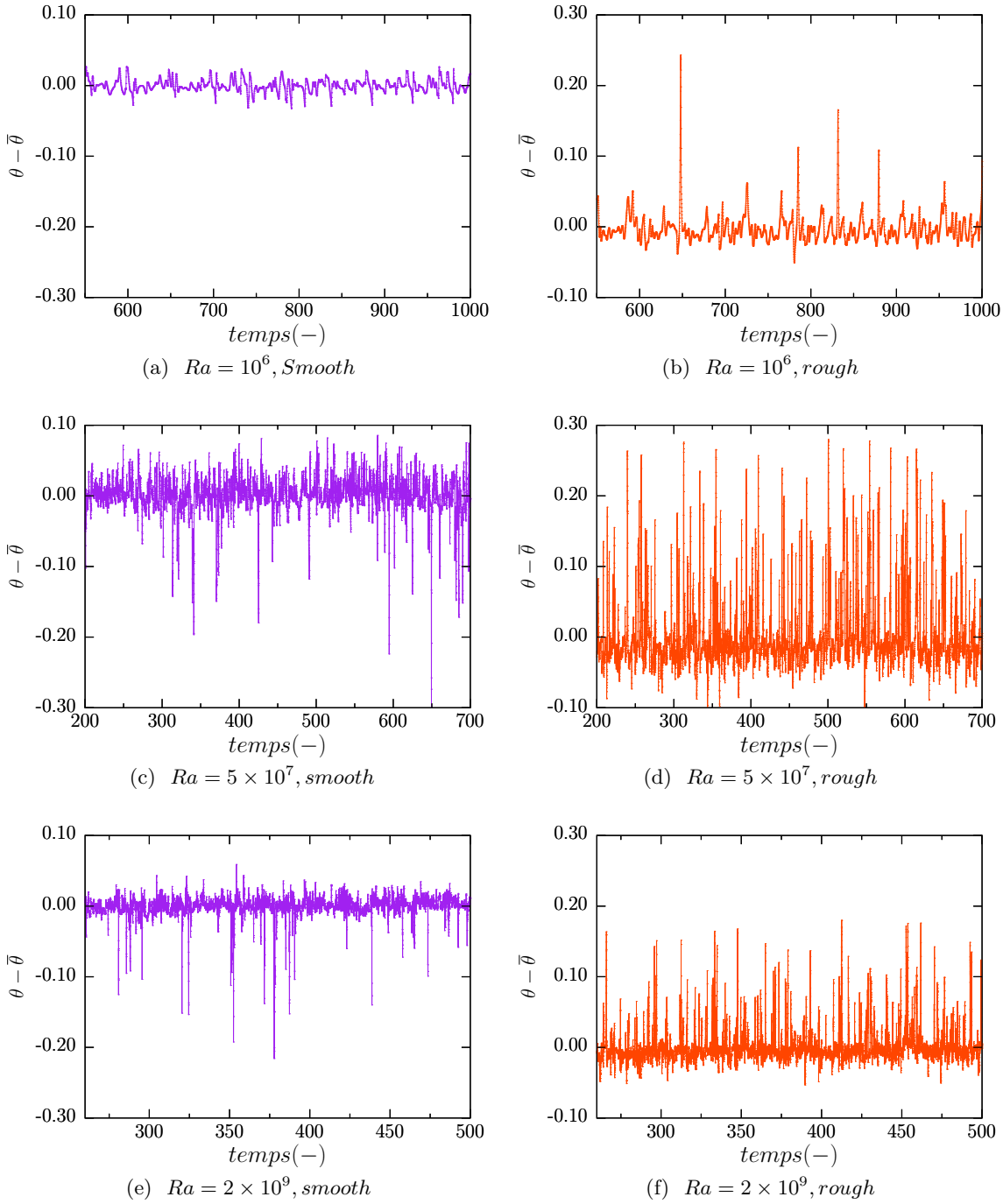

(a) $Ra = 10^6, Smooth$ (b) $Ra = 10^6, rough$

(c) $Ra = 5 \times 10^7, smooth$ (d) $Ra = 5 \times 10^7, rough$

(e) $Ra = 2 \times 10^9, smooth$ (f) $Ra = 2 \times 10^9, rough$

Fig. VII.2 Time series of the temperature fluctuations inside the asymmetric rough cell (R/S) recorded at $x = 0.5$, $y = 0.25$ near (a,b,c) the smooth plate at $z = 1 - 3H_p^*$ and (d,e,f) near the rough plates at $z = 3H_p^*$ in the three regimes of heat transfer. (a,d) regime I, $Ra = 10^6$, (b,e) regime II, $Ra = 5 \times 10^7$ and (c,f) regime III, $Ra = 2 \times 10^9$.

the relevant statistics.

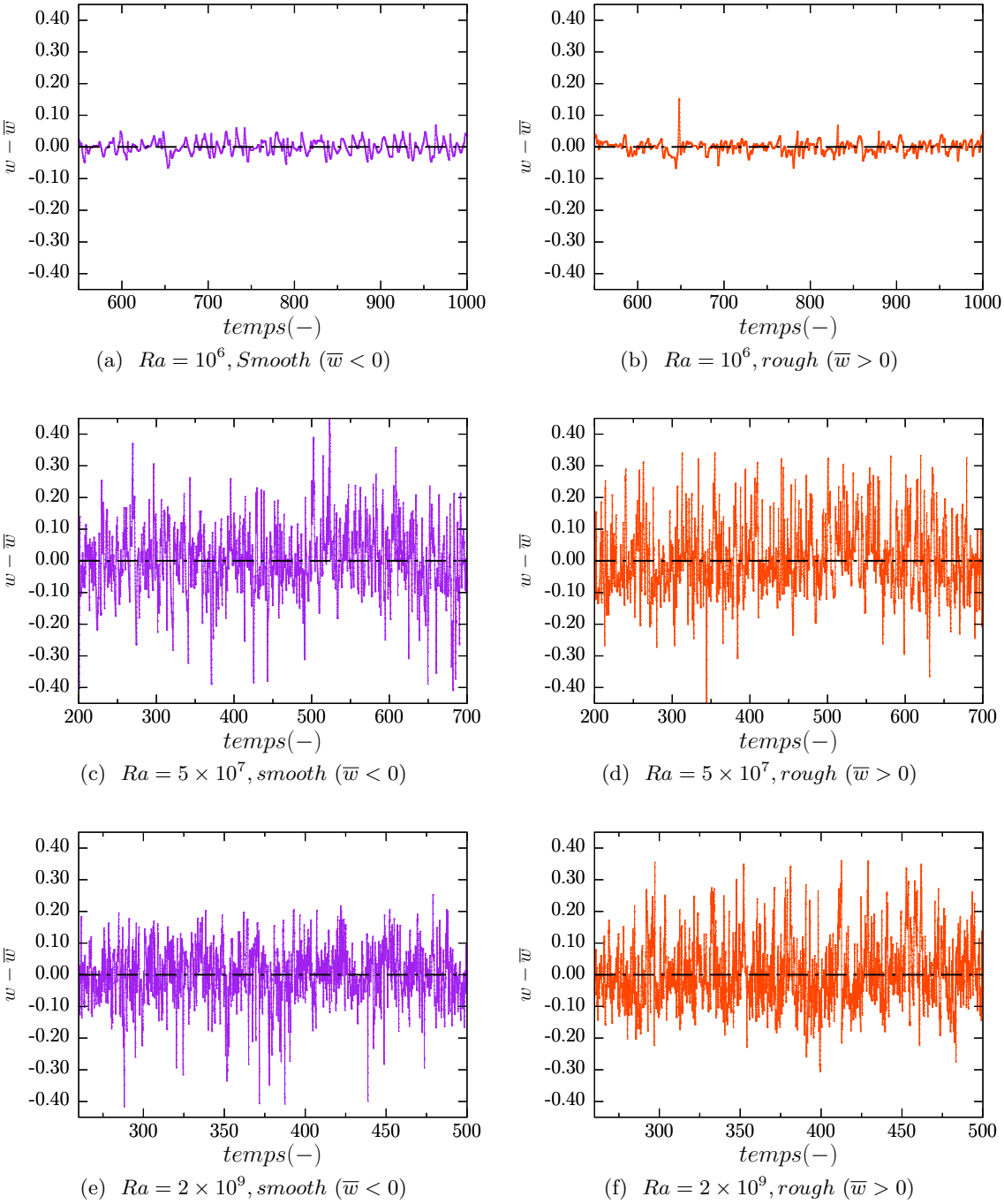

(a) $Ra = 10^6, Smooth\ (\overline{w} < 0)$ (b) $Ra = 10^6, rough\ (\overline{w} > 0)$

(c) $Ra = 5 \times 10^7, smooth\ (\overline{w} < 0)$ (d) $Ra = 5 \times 10^7, rough\ (\overline{w} > 0)$

(e) $Ra = 2 \times 10^9, smooth\ (\overline{w} < 0)$ (f) $Ra = 2 \times 10^9, rough\ (\overline{w} > 0)$

Fig. VII.3 Time series of the vertical velocity fluctuations inside the asymmetric rough cell (R/S) recorded at $x = 0.5$, $y = 0.25$ near (a,b,c) the smooth plate at $z = 1 - 3H_p^*$ and (d,e,f) near the rough plates at $z = 3H_p^*$ in the three regimes of heat transfer. (a,d) regime I, $Ra = 10^6$, (b,e) regime II, $Ra = 5 \times 10^7$ and (c,f) regime III, $Ra = 2 \times 10^9$.

We plot in figure (VII.4) the probability density functions (PDF) of temperature and vertical velocity fluctuations corresponding to the complete set of measurements gathering with all 7 probes. The PDF of $\theta^{'}|_S$ (resp. $w^{'}|_S$) relative to the smooth plate are inverted with respect to $\theta^{'} = 0$ (resp. $w^{'} = 0$) to compare more easily with the rough plate.

In regime I, figure (VII.4a) shows that the PDFs of θ' for the smooth and rough plates have a similar distribution. For $\theta^{'} \leqslant 0.1$, they display an almost symmetric distribution that we may attribute to turbulent background. However these PDFs deviate from the symmetrical distribution for $\theta^{'} \geqslant 0.1$ indicating more frequent hotter (colder) fluctuations which mark the presence of plumes (Zhou and Xia (2002); Shishkina and Wagner (2008)). Figure (VII.4b) shows the PDFs of $w^{'}$ near the smooth and the rough plates. They both have a slender Gaussian distributions. It seems that velocity fluctuations are quite similar when comparing the both plates.

In regime II, as shown in figure (VII.4c), the PDFs of thermal fluctuations are skewed towards hot (resp. cold) side for the rough (resp. smooth) plate. The PDFs show that thermal plumes with large intensity are detached more frequently from the rough surface. figure (VII.4d) shows that the PDFs of $w^{'}$ deviate from the Gaussian distributions. For both sides , similarly to temperature fluctuation, the intensive overspeed oscillations are more frequent indicate the presence of thermal plumes. Surprisingly, the PDF of $w^{'}_S$ close to smooth side is wider. Furthermore, fluctuation of underspeed type are more frequent as tail is clearly observed in PDF for $W^{'}|_S < -0.4$. This could be explained by an effect of the LSC or the presence of coherent structures flowing upwards close the smooth plate.

In regime III, figures (VII.4e) and (VII.4f) show that the PDFs of $\theta^{'}$ become again much similar and less wider than in regime II. Since we kept our monitoring probes at the same height, with increasing Ra number we move away from boundary layer, therefore the intensity of thermal fluctuations is being reduced to $\theta^{'} \leqslant 0.2$. The PDFs of $\theta^{'}$ still deviate for both the rough and smooth side, the large fluctuation ($\theta' > 0.05$) are more frequent close to the rough plate but the between PDFs of θ' is reduced when comparing with the regime II. Concerning the velocity fluctuation, figure (VII.4f) show that the PDFs of $w^{'}$ for both plates become again similar as in regime I. They are mostly fitted with Gaussian functions $G^R_w \approx G^S_w$. The tails shown in both PDF for $w^{'}|_S$ and $w^{'}|_R > 0.2$ is due to a few overspeed fluctuations. These deviations are markers of the rising and falling plumes from the bottom and upper plate respectively.

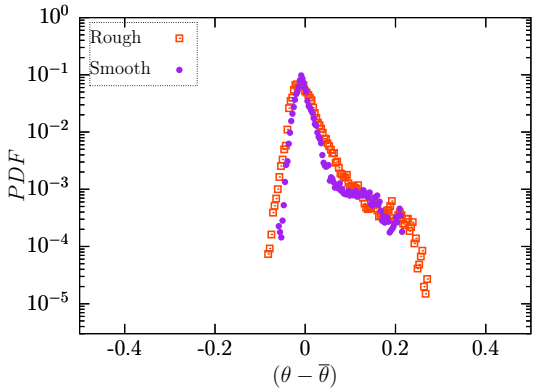

(a) **Regime I** : $Ra = 10^6$

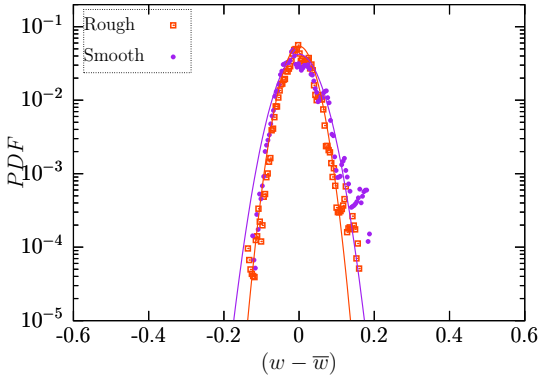

(b) **Regime I** : $Ra = 10^6$. The fit with centered Gaussian function : $G_w^R(\sigma \approx 0.0329)$; $G_w^S(\sigma \approx 0.0425)$

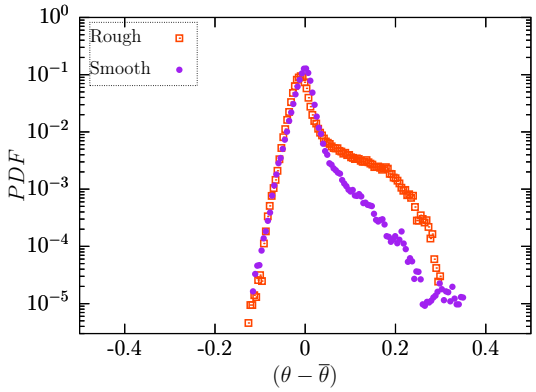

(c) **Regime II** : $5 \times Ra = 10^7$

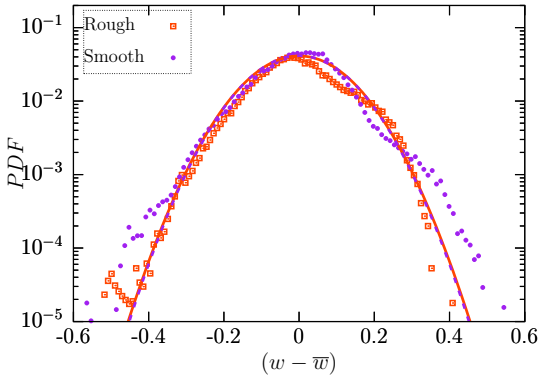

(d) **Regime II** : $5 \times Ra = 10^7$. The fit with centered Gaussian function : $G_w^R(\sigma \approx 0.1114)$; $G_w^S(\sigma \approx 0.1106)$

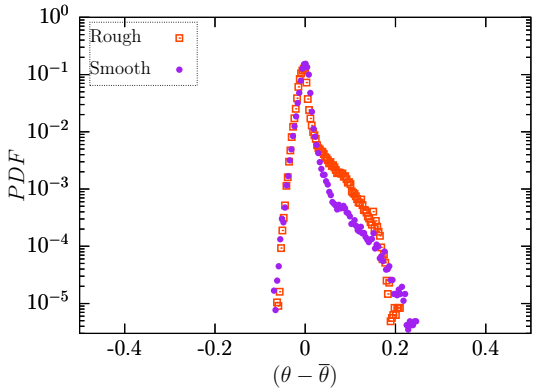

(e) **Regime III** : $2 \times Ra = 10^9$

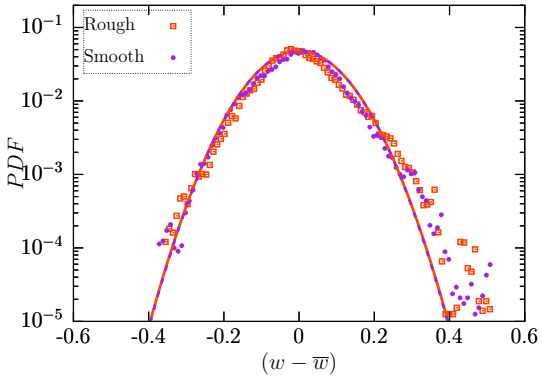

(f) **Regime III** : $2 \times Ra = 10^9$. The fit with centered Gaussian function : $G_w^R(\sigma \approx 0.0962)$; $G_w^S(\sigma \approx 0.0959)$

Fig. VII.4 Probability density function of (a,c,e) the temperature fluctuations $\theta' = (\theta - \overline{\theta})$ and (b,d,f) the vertical velocity fluctuations $w' = (w - \overline{w})$ near the rough plate (orange squares) at $z = 3H_p^*$ and near the smooth plate (magenta circles) at $z = 1 - 3H_p^*$. Orange and violet line are Gaussian fit of w' distribution. For the smooth plate, PDF of $\theta'|_S$ and $w'|_S$ are flipped with respect to $\theta' = 0$ and $w' = 0$ respectively.

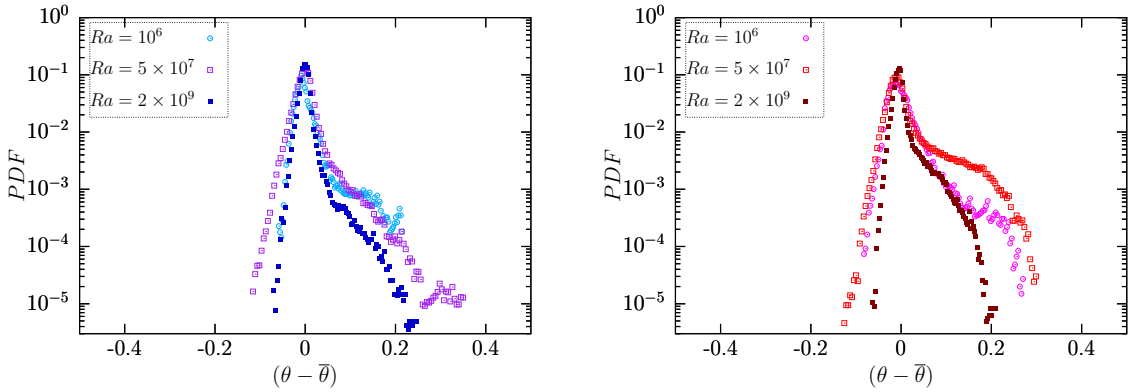

(a) Smooth (b) Rough

Fig. VII.5 (a) Comparison of probability density functions of the temperature fluctuation $(\theta - \overline{\theta})$ near (a) the rough plate at $z = 0.1$ and (b) the smooth plate at $z = 0.9$. PDF of $\theta^{'}|_S$ and $w^{'}|_S$ are flipped with respect to $\theta^{'} = 0$ and $w^{'} = 0$ respectively.

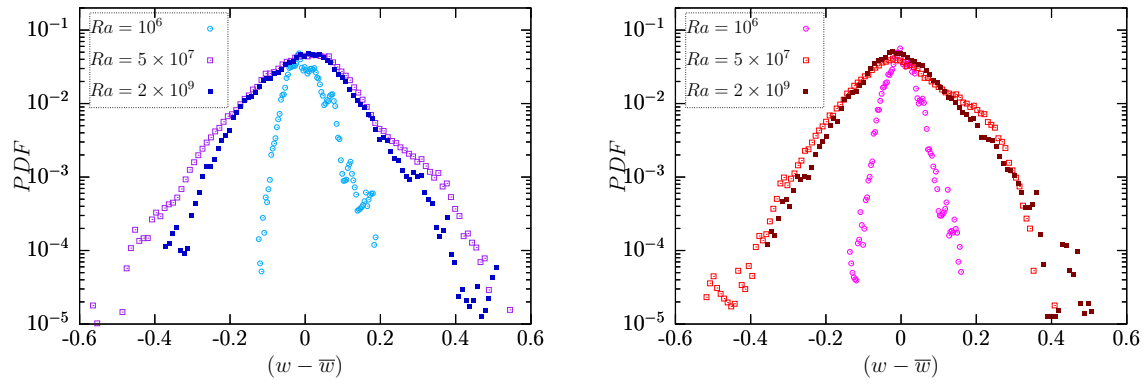

(a) Smooth (b) Rough

Fig. VII.6 (a) Comparison of probability density functions of the vertical velocity fluctuations $(w - \overline{w})$ near (a) the smooth plate at $z = 0.9$ and (b) the rough plate at $z = 0.1$. PDF of $\theta^{'}|_S$ and $w^{'}|_S$ are flipped with respect to $\theta^{'} = 0$ and $w^{'} = 0$ respectively

In figures (VII.5), we compare the PDFs of $\theta^{'}$ relative to the three regimes regarding the smooth or rough sides. In regime I and II, the PDF of smooth plate are comparable, the same deviations are observed from $\theta^{'} \approx 0.1$ which are signatures of plumes. Near the rough plate, the emission of thermal plumes that have large intensity $\theta^{'} \geqslant 0.1$ is more frequent in regime II. Then, it decreases with increasing Ra. This is very consistent with our previous discussion on the enhancement of temperature fluctuations in the half bottom side of the cavity in regime II as shown in figure (V.19).

As shown in figure (VII.6), the PDFs of $w^{'}$ close to the smooth plate become wider when Ra increases from regimes I to II. The distribution is even wider in regime II than in regime III where the large fluctuations $|w^{'}| > 0.2$ becomes less frequent. Near the rough plate, PDFs of $w^{'}$ are quite similar in regimes II and III, only a few large positive velocity fluctuations corresponding to an overspeed of plumes could be highlighted in regime III. Overall, whatever the plate, the PDFs are wider for thermal and kinetic fluctuations in regime II.

VII.2.2 Statistical properties of thermal plumes

a) Correlation between temperature and velocity fluctuations

We have seen a strong modification of the histograms of $\theta^{'}$ and $w^{'}$, depending on the heat transfer regime. Particularly in regime II, while the emission of plumes of large $\theta^{'}$ is more frequent near the rough plate, large velocity fluctuations $w^{'}$ are detected near the smooth plate too. We thus have an interest on studying the correlation between θ and w. We evaluate the bivariate Pearson correlation coefficient ϱ to measure the linear dependence between the temperature and vertical velocity fluctuations at different Ra regarding rough and smooth plates. It has a value between -1 and 1, where -1 is total negative linear correlation, 0 is no linear correlation, and 1 is total positive linear correlation. It is defined as

$$\varrho(\theta_i, w_j) \quad = \frac{1}{N-1} \sum_{n=1}^{N} \left(\overline{\frac{\theta_i(n) - \mu_{\theta_i}}{\sigma_{\theta_i}}} \right) \left(\overline{\frac{w_j(n) - \mu_{w_j}}{\sigma_{w_j}}} \right). \tag{VII.3}$$

Where N is the total of samples from the 7 probes; μ and σ are the mean and standard deviation of the considered variable.

Table VII.1 Coefficient $\varrho(\theta, w)$ of the correlation between the temperature and vertical velocity fluctuations calculated using the time series from all the 7 probes near the rough or smooth sides.

Side	$Ra = 10^6$	$Ra = 5 \times 10^7$	$Ra = 2 \times 10^9$
Rough	0.743	0.683	0.482
Smooth	0.710	0.584	0.400

The table [VII.1] shows that $\varrho(\theta, w)$ correlation between the temperature and vertical velocity decreases with increasing Ra for both sides under the effects of turbulence which promotes the mixing. Nevertheless, it also shows that $\varrho(\theta, w)_R \geqslant \varrho(\theta, w)_S$ which means that the temperature and vertical velocity time series are more correlated near the rough plate. This is particularly pronounced in regime II. Overall, we can see that $\varrho(\theta, w) \geqslant 0.4$: the fluctuations of θ and w can be considered as nearly correlated. Therefore, our next analysis concerning the properties of thermal plumes involves measurements of these two correlated variables.

b) Method of extraction of thermal plumes

We extract some characteristics of the thermal plumes under the effect of rough surface following the work of Zhou et al. (2016). We suppose that the cliff-ramp structures captured in the temperature or vertical velocity measurements as shown in figures (VII.7a) and (VII.7c) are signatures of plumes passing through our probes. We follow the plume extraction method described in their work. It consist on 3 steps :

1. We determine the time positions of t_0 (see figure (VII.7b)) when the temperature increment satisfies the criterion : $\theta(t+\tau) - \theta(t) > \zeta\theta_{rms}$. Where τ is a time interval chosen here as the time-step $\tau = \Delta t$, $\zeta = 0.15$ is a threshold.

2. We track the time positions of temperature extrema t_1 and t_2 which correspond to the positions of the local minimum and maximum temperatures surrounding t_0 (see figure (VII.7a)).

3. We apply a second criterion : the mean temperature between t_1 and t_2, $[\theta(t_1)+\theta(t_1)]/2$ should be greater than the average temperature over the time series.

We assume that the time interval between t_1 and t_2 represents the transit time for the plume passing through the monitoring probe, which is defined as the plume width ω,

$$\omega = t_2 - t_1 \tag{VII.4}$$

Accordingly, the absolute value of the temperature difference between those instants is defined as the plume amplitude A.

$$A = |\theta(t_2) - \theta(t_1)| \tag{VII.5}$$

We can apply the same process to extract thermal plumes based on the fluctuation of vertical velocity time series. The time positions t_0^* should satisfying the criterion : $w(t+\tau) - w(t) > \zeta w_{rms}$ (the same threshold value ζ as for the temperature fluctuation is used). The time positions of vertical velocity extrema are denoted by t_1^* and t_2^*. Similarly, we denote by ω^* the transit time for the plume passing across the probe. while A^* represents the amplitude of the vertical velocity of the plume as shown in figure (VII.7c).

$$\omega^* = t_2^* - t_1^* \tag{VII.6}$$

$$A^* = |w(t_2^*) - w(t_1^*)| \tag{VII.7}$$

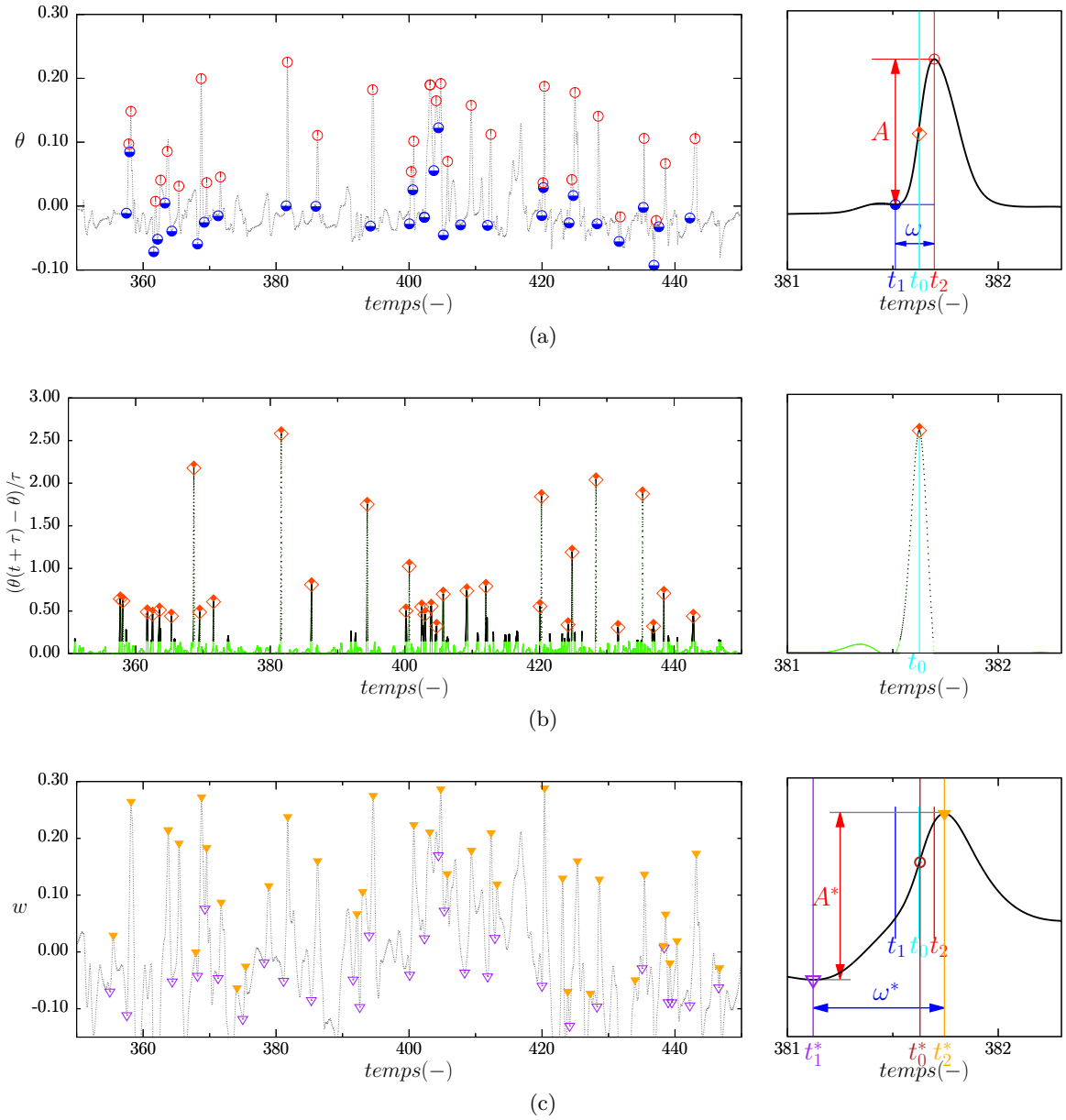

Fig. VII.7 On the left column : (a) Temperature time series (black dashed line) recorded near the rough plate at $x = 0.5$, $y = 0.25$, $z = 3H_p^*$ at $Ra = 5 \times 10^7$. This is an example illustrating the time recording at the 7 probes near roughness. Blue and red circles represent local minima at t_1 and maxima at t_2 of the temperature fluctuation around t_0 values (cyan line). (b) The corresponding time derivative of temperature signal. Orange diamonds show where the maximum increment of θ is reached and represents the values which verifying the selective criterion for t_0 (zoom view on a single peak). (c) Time series of the vertical velocity $w(t)$. On the right column : we show blow-up of the left figures at a particular time period.

c) Effect of roughness on plume's amplitude

We plot in figures (VII.8) the PDFs of normalized amplitudes $(A/\theta_{rms}, A^*/w_{rms})$ of thermal plumes near the rough and smooth plates. The large value of A/θ_{rms} could be associated to plumes in terms of transient increase of thermal potential energy while the large values of A^*/w_{rms} could be linked to plumes in terms of transient increase of local kinetic energy.

Here, we discuss about various observations that could be made on normalized amplitudes of thermal plumes in the different regimes as follows,

- Regimes I and III : (figures (VII.8 a,b,e,f) present the PDFs of A/θ_{rms} and A^*/w_{rms}. They have a well-shaped log-normal distribution $LN(\mu, \sigma)$ as suggested by Zhou and Xia (2002) and Zhou et al. (2016). They interpret this as an intrinsic feature of thermal plumes (see table [VII.2] for the mean and standard deviation). Moreover, the distributions associated with the rough plate are nearly similar to those of smooth one.

- Regime II : on figure (VII.8c), $A/\theta_{rms}|_S$ is well fitted with a LN distribution for the smooth plate. However, a deviation from the LN function is seen close to the rough plate for higher amplitudes $A/\theta_{rms}|_R > 0.3$. We estimate that the gap between the two PDFs is about 2% to 10% which exhibits a more frequent detachment of plumes containing larger potential energy. Likewise, figure (figures (VII.8d)) shows a deviation from the LN distribution for $A^*/w_{rms} > 2$ near the rough plate, which suggests a more frequent detachment of plumes with large kinetic energy content close the rough plate.

d) Effect of roughness on plume's width

We plot in figures (VII.9) the PDFs of plumes widths (ω, ω^*) near the rough and smooth plates. Actually, PDFs of ω and ω^* are quite similar for both sides and almost fitted with log-normal functions. The fit parameters shown in table [VII.2] are almost identical. If we compare the three regimes, it seems that the PDFs become narrower with increasing Ra, i.e the plume's widths ω and ω^* is decreasing. It means that the transit time of plumes becomes shorter near both the rough and smooth plates as Ra increases.

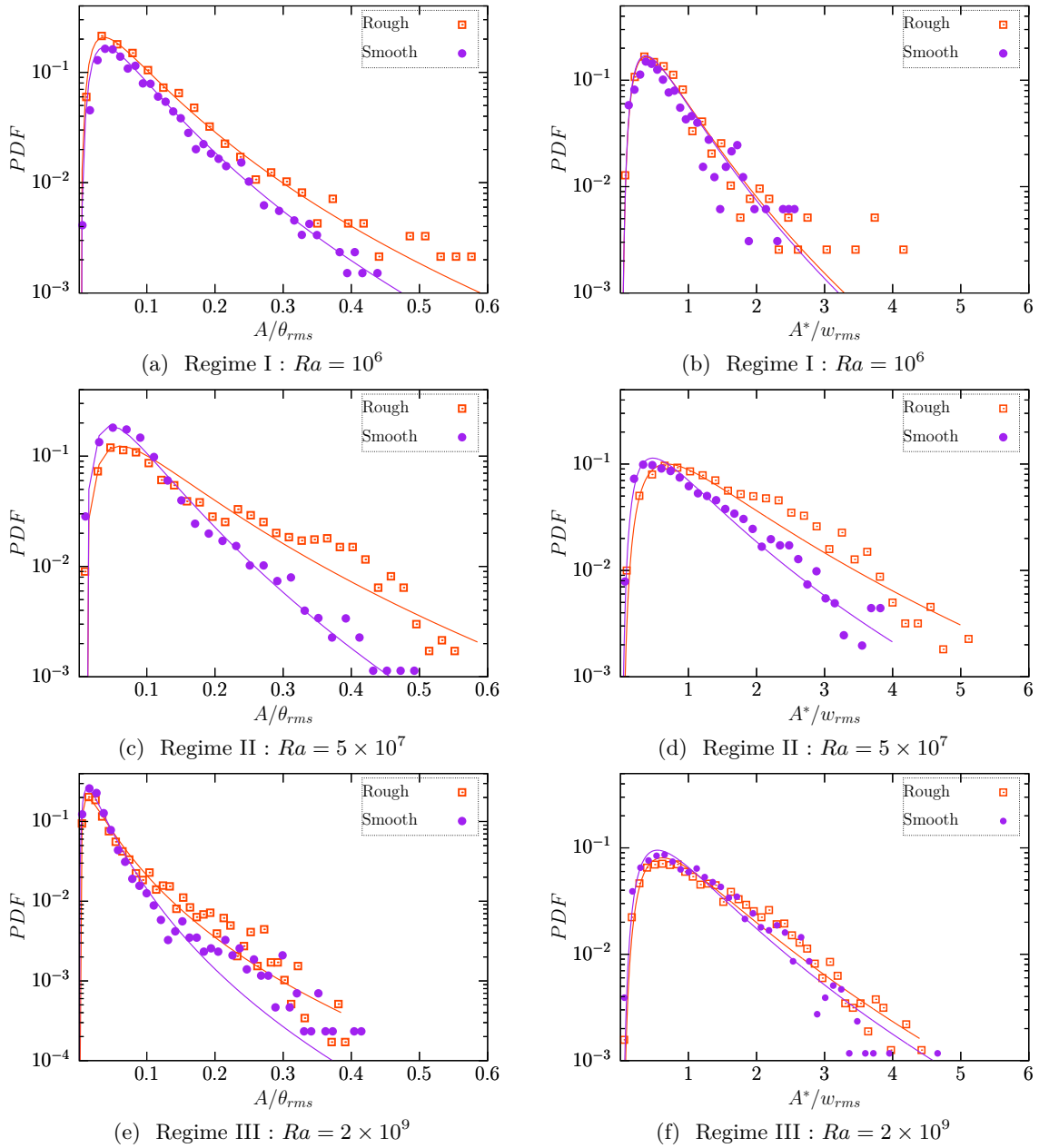

(a) Regime I : $Ra = 10^6$

(b) Regime I : $Ra = 10^6$

(c) Regime II : $Ra = 5 \times 10^7$

(d) Regime II : $Ra = 5 \times 10^7$

(e) Regime III : $Ra = 2 \times 10^9$

(f) Regime III : $Ra = 2 \times 10^9$

Fig. VII.8 Probability density function of normalized plume amplitudes (a,c,e) A/θ_{rms} and (b,d,f) A^*/w_{rms} extracted using temperature and vertical velocity time series recorded near the bottom rough plate at $z = 0.1$ and near the smooth plate at $z = 0.9$. Orange and violet lines are a log-normal fit with a mean μ and standard deviation ω given in table [VII.2].

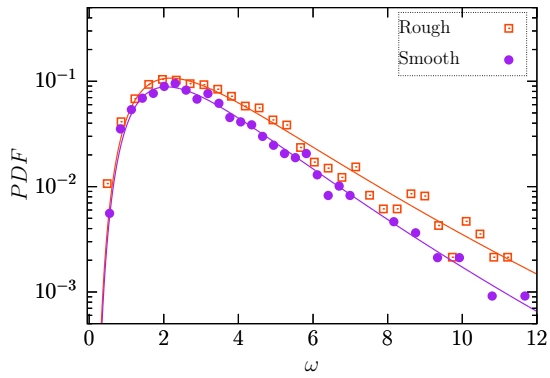

(a) Regime I : $Ra = 10^6$

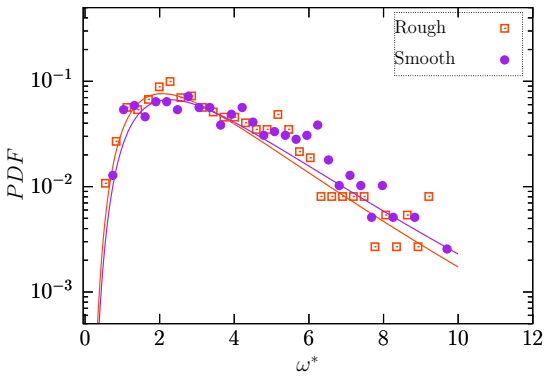

(b) Regime I : $Ra = 10^6$

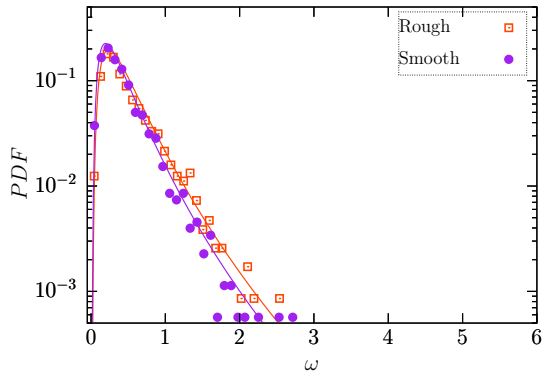

(c) Regime II : $Ra = 5 \times 10^7$

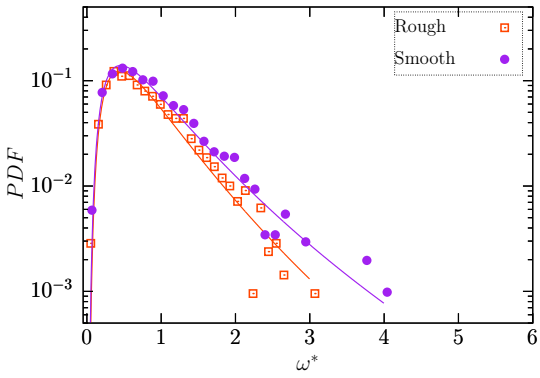

(d) Regime II : $Ra = 5 \times 10^7$

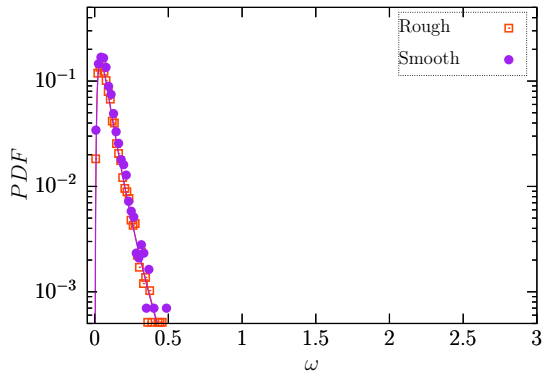

(e) Regime III : $Ra = 2 \times 10^9$

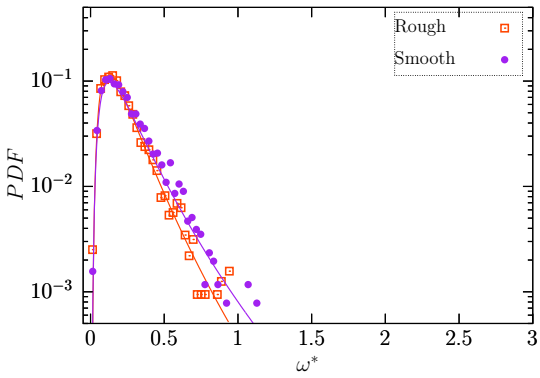

(f) Regime III : $Ra = 2 \times 10^9$

Fig. VII.9 Probability density function of normalized plume widths (a,c,e) ω and (b,d,f) ω^* extracted using temperature and vertical velocity time series recorded near the bottom rough plate at $z = 0.1$ and near the smooth plate at $z = 0.9$. Orange and violet lines are a log-normal fit with a mean μ and standard deviation ω given in table [VII.2].

Table VII.2 Log-normal functions with a mean μ and standard deviation σ of normalized amplitudes (see figures (VII.8)) and widths (see figures (VII.9)) distributions.

Side	$Ra = 10^6$		$Ra = 5 \times 10^7$		$Ra = 2 \times 10^9$	
	μ	σ	μ	σ	μ	σ
fit of normalized amplitude $PDF(log(A/\theta_{rms}))$						
Rough	-2.58	0.85	-2.18	0.79	-3.40	0.96
Smooth	-2.64	0.78	-2.56	0.70	-3.62	0.84
fit of the width $PDF(log(\omega))$						
Rough	1.12	0.58	-0.98	0.69	-2.75	0.71
Smooth	1.05	0.56	-1.13	0.70	-2.74	0.70
fit of normalized amplitude $PDF(log(A^*/w_{rms}))$						
Rough	-0.52	0.68	0.19	0.75	0.10	0.70
Smooth	-0.54	0.67	-0.17	0.75	-0.11	0.71
fit of the width $PDF(log(\omega^*))$						
Rough	1.05	0.57	-0.41	0.63	-1.74	0.62
Smooth	1.14	0.57	-0.33	0.67	-1.62	0.67

VII.3 Numerical Ombroscopy

As shown in previous section, roughness changes the flow dynamics near the wall namely by affecting the amplitude of thermal fluctuations particularly in the intermediate regime II. Shang et al. (2003, 2004) observed experimentally more frequent thermal plumes detached especially from the rough boundary layers towards the bulk. This effect has also been viewed for example in numerical work of Stringano et al. (2006) or recently by Jiang et al. (2018) using ratchets on the top and bottom plates. They reported a strong plume detachments at the tips of roughness elements. Optical technique such as ombroscopy is one of the methods largely used in experiments to visualize the coherent structures. However, it does not give a direct access to the temperature field but rather to the Laplacian of temperature. We study the instantaneous features of the thermal structures by reproducing this technique numerically. All needed quantities have been embedded in the Sunfluidh code to perform a spatial averaging in the depth direction during the computing instead of saving the complete 3D fields.

VII.3.1 Qualitative aspects of thermal plumes

Beside to the temperature and the velocity fields, we also compute the spatial averaging in transversal y-direction of the 2D Laplacian of the temperature and the thermal dissipation rate in the plan XZ as follows

$$\Delta^{\theta}_{xz} = \langle \frac{\partial^2 \theta}{\partial x^2} + \frac{\partial^2 \theta}{\partial z^2} \rangle_y \tag{VII.8}$$

$$\epsilon^{\theta}_{xz} = \kappa \langle (\frac{\partial \theta}{\partial x})^2 + (\frac{\partial \theta}{\partial z})^2 \rangle_y \tag{VII.9}$$

Figures (VII.10 a,c,e) show the 2D Laplacian of temperature Δ^{θ}_{xz} which is an indicator of the concave and convex thermal structures in the temperature field. Therefore it provides informations about the geometrical shape of thermal plumes. It allows to visualize clearly thermal plumes in a similar way as in experiments. As expected, we can view that the number of plumes increases while their size decreases when the Ra number increases.

Similarly, figures (VII.10 b,d,f) show the 2D averaged thermal dissipation fields ϵ^{θ}_{xz} at different Ra numbers. It reveals details of the dissipative structures which transport the heat. A high thermal dissipation is a good indicator to track and localize thermal plumes. The presence of those structures is more important and their sizes decreases with increasing Ra. However, difference between the top and the bottom plates is not obvious. We need a time monitoring to attempt a more quantitative study.

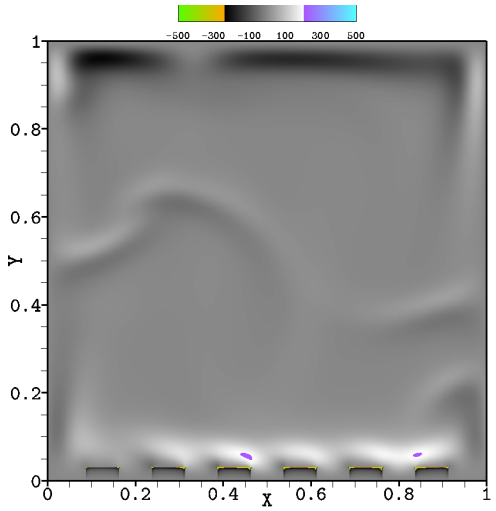

(a) Regime I : $Ra = 10^6$

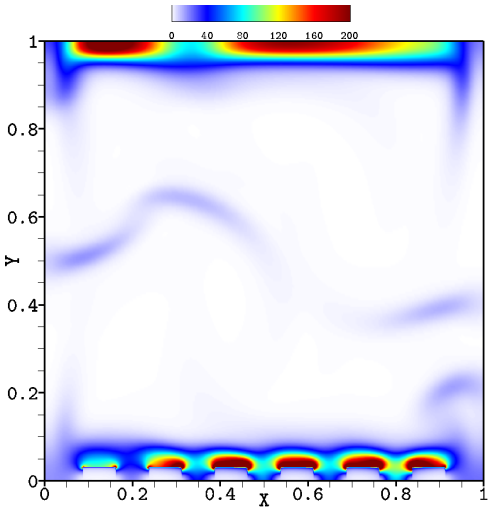

(b) Regime I : $Ra = 10^6$

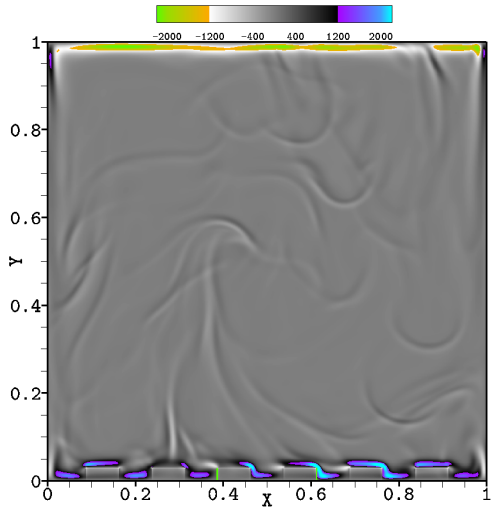

(c) Regime II : $Ra = 5 \times 10^7$

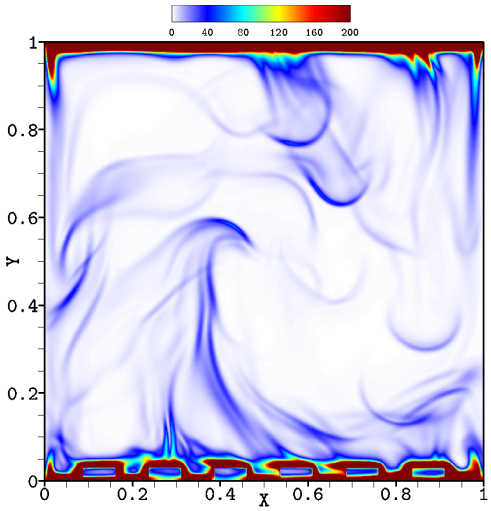

(d) Regime II : $Ra = 5 \times 10^7$

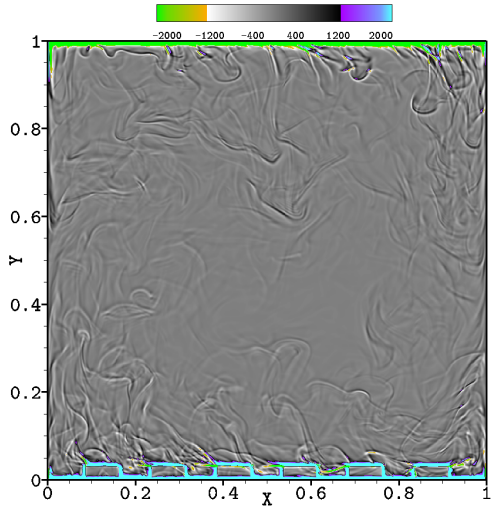

(e) Regime III : $Ra = 2 \times 10^9$

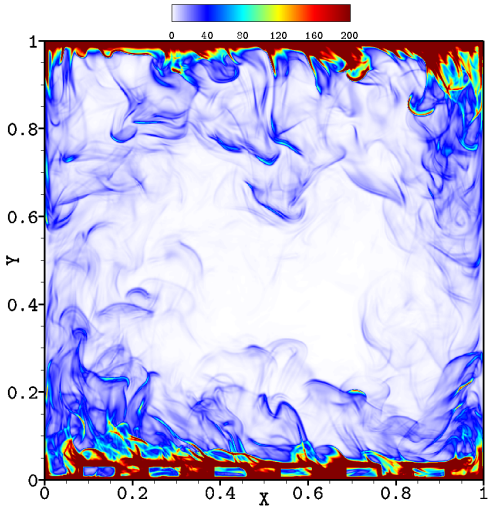

(f) Regime III : $Ra = 2 \times 10^9$

Fig. VII.10 Spatial averaged fields in transversal direction of instantaneous (a) 2D Laplacian of temperature Δ^{θ}_{xz} and (b) 2D thermal dissipation ϵ^{θ}_{xz}.

VII.3.2 Spatiotemporal analysis

In order to identify the detachment and the motion of thermal plumes, we consider two horizontal symmetric lines near the bottom rough plate (R) at $z = 3H_p^*$ and the top smooth one (S) at $z = (1-3H_p)$. The spatiotemporal diagrams of the temperature θ and normalized thermal dissipation per the Nusselt number $\epsilon_{xz}^{\theta}/Nu_{R/S}$ are shown in figures (VII.11 to 13) for the 3 regimes. In classic RBC, we have an exact relation between $Nu_{R/S}$ and ϵ_θ as given by the equation (I.23). So this normalization allows us to compare regions of high and low heat transfer)

In regime I, as shown in figures (VII.11), one may note oblique lines of high and of low temperatures near the hotter and the colder plates resp. We interpret these lines as markers of hot and cold thermal plumes crossing the monitoring lines and moving towards the bulk. We note that one or more thermal plumes could pass across the lines at the same time as we will see later in details. Qualitatively, the appearance of oblique lines is quasi-periodic near both the top and bottom plates. At the center $z = H/2$, spatiotemporal diagram of θ and $\epsilon_{xz}^{\theta}/Nu_{R/S}$ are symmetric with respect to $x = W/2$. Overall, we can see the same behavior whatever the plate which supports the idea of inactive roughness elements.

In regime II, as shown in figures (VII.12), hot structures are remarkably present near the rough plate comparing with the cold plumes detaching from the smooth side. Other viewpoint is illustrated by the spatiotemporal thermal dissipation. It shows that the dissipative structures are intensively present at the rough side. We also notice traces of relatively high temperature structures at the half cell $z = H/2$, particularly near the left vertical side of the cell, which indicates that hotter plumes are still rising upwards. This could explain the more efficient heat transfer observed in this regime.

In regime III, as shown in figures (VII.13), one may observe that the thermal plumes are similarly distributed from the smooth plate as much as from the rough one. There is no observable difference between the spatiotemporal diagrams of thermal dissipation. Moreover, these figures show a homogeneous bulk region at the half cell $z = H/2$, i.e there is no difference between the left and right side of the cavity. These observations could be understood as reasons for which in regime III we recover the classic $Nu \sim Ra^{\beta}$ scaling law as observed in regime I with an exponent close to $\beta = 1/3$ as shown in figure (IV.5b).

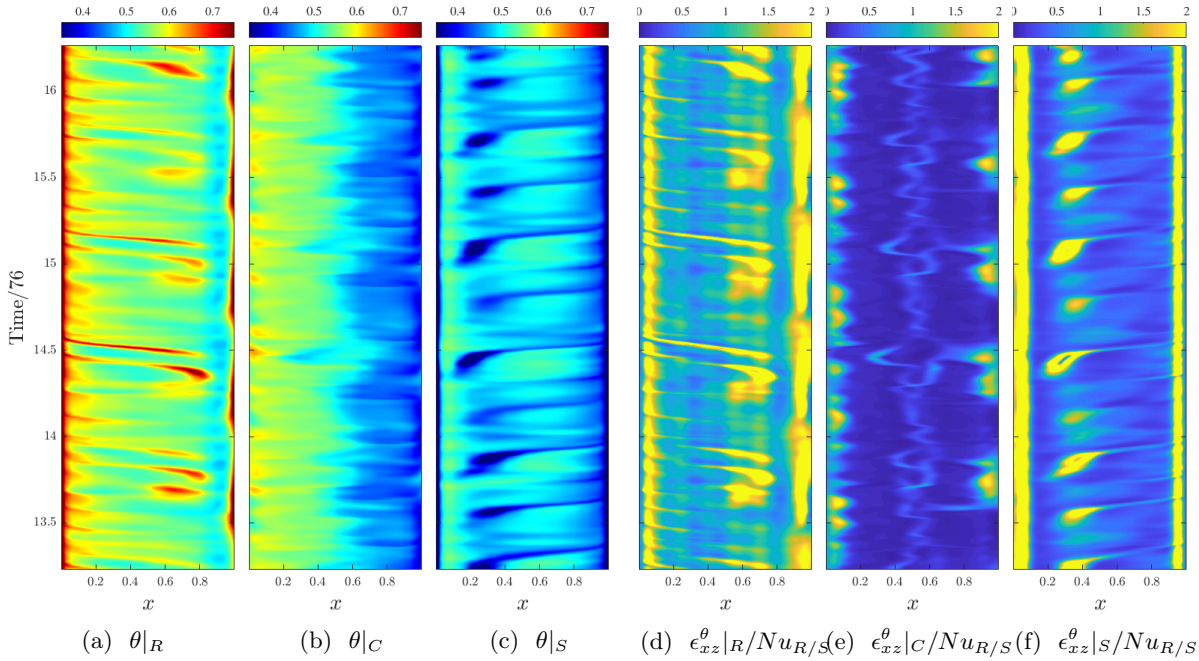

Fig. VII.11 Spatiotemporal diagram of averaged (a,b,c) temperature and (d,e,f) normalized 2D thermal dissipation at $Ra = 10^6$ (regime I).(a,d) $z = 3H_p^*$,(b,e) $z = H/2$,(c,f) $z = 1-3H_p^*$.

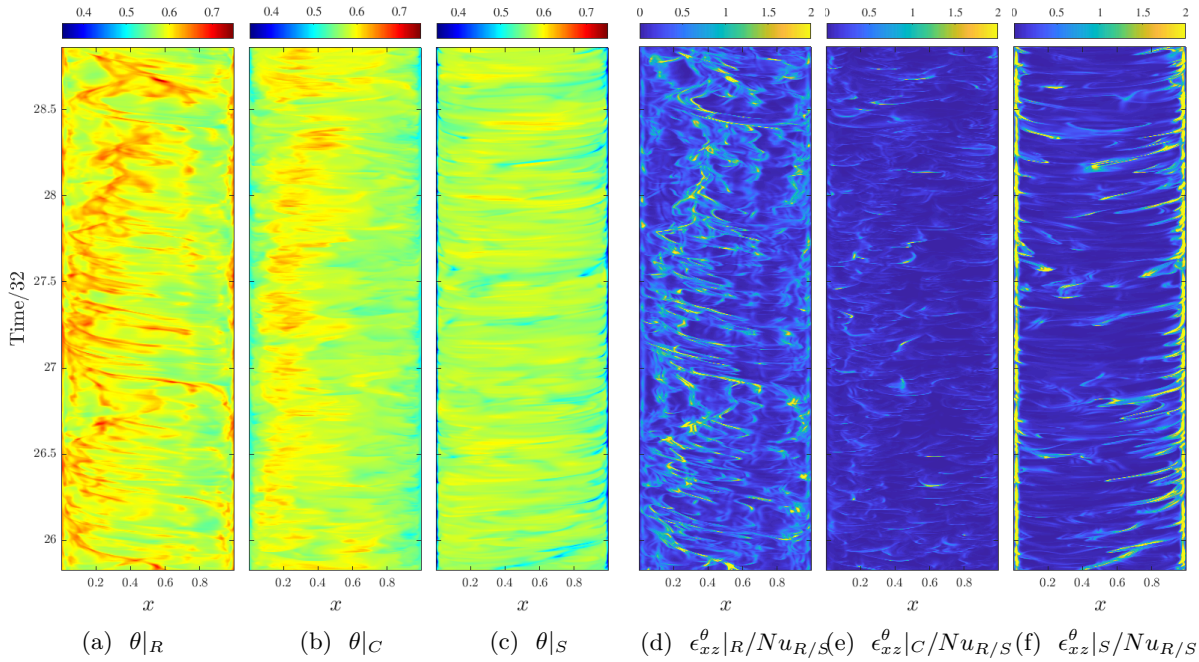

Fig. VII.12 Spatiotemporal diagram of averaged (a,b,c) temperature, (d,e,f) normalized 2D thermal dissipation at $Ra = 5\ 10^7$ (regime II).(a,d) $z = 3H_p^*$,(b,e) $z = H/2$,(c,f) $z = 1-3H_p^*$.

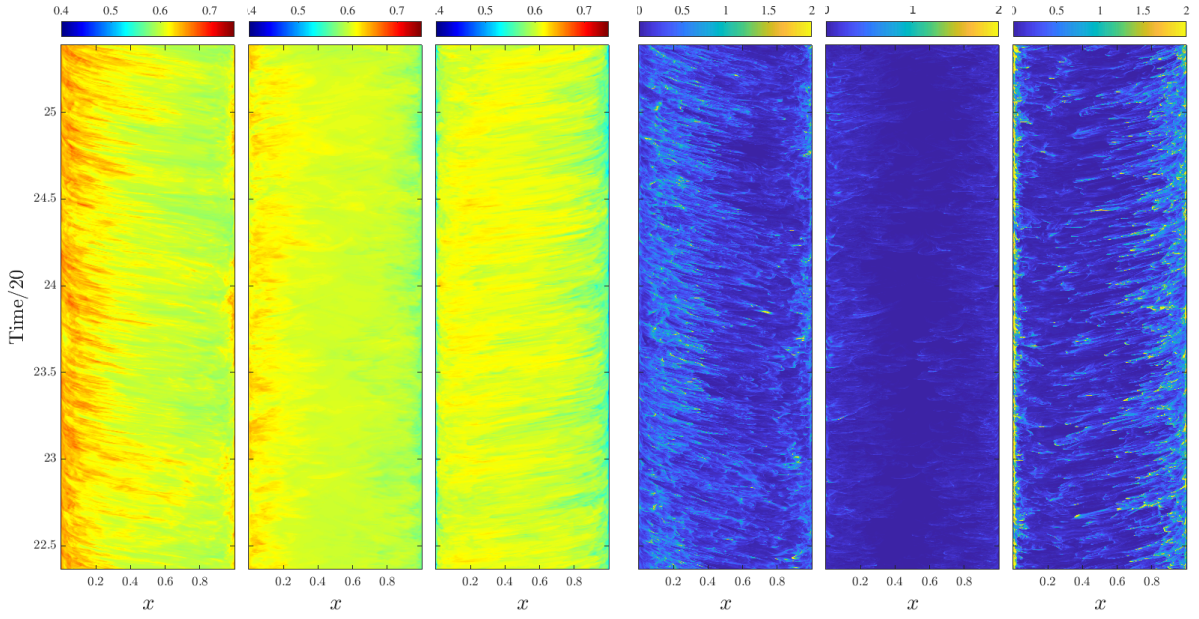

Fig. VII.13 Spatiotemporal diagram of averaged (a,b,c) temperature, (d,e,f) normalized 2D thermal dissipation at $Ra = 2\ 10^9$ (regime III).(a,d) $z = 3H_p^*$,(b,e) $z = H/2$,(c,f) $z = 1-3H_p^*$.

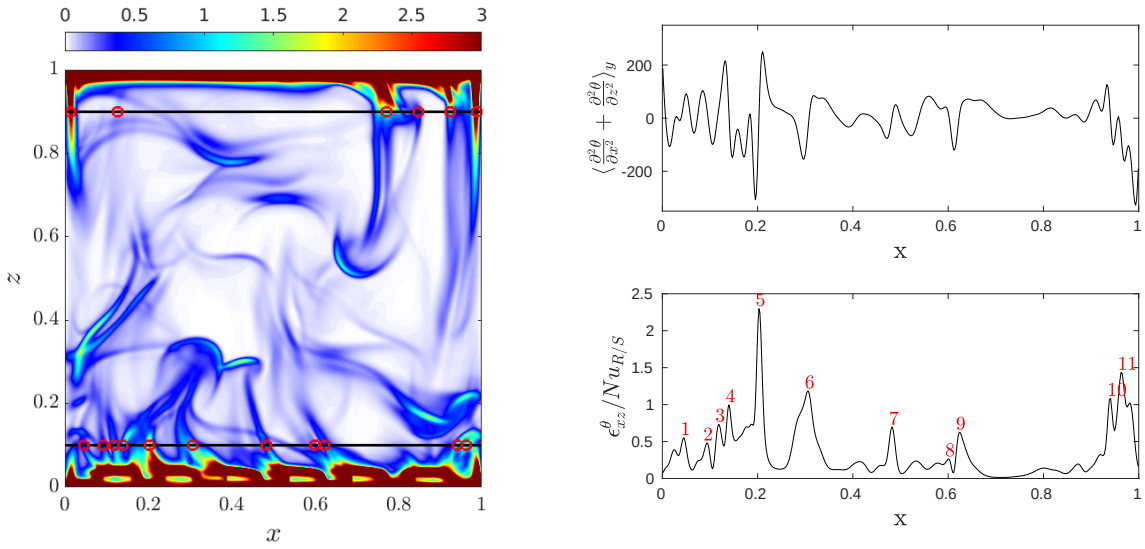

(a) (b)

Fig. VII.14 (a) Instantaneous spatial averaged fields in transversal y-direction of the normalized 2D thermal dissipation $\epsilon^\theta_{xz}/Nu_{R/S}$. The algorithm of quantification of the plume's number is applied at both horizontal black lines near the rough plate at $z = 3H^*_p$ and near the smooth one at $z = 1-3H^*_p$. (b) Corresponding 2D-Laplacian and normalized 2D thermal dissipation on the bottom line ($z = 3H^*_p$). In this example, the algorithm identifies 11 plumes on the $\epsilon^\theta_{xz}/Nu_{R/S}$ distribution near rough plate marked by red circles in figure (a).

VII.3.3 Quantification of the number of plumes

a) Methodology

Our goal is to compare the number of detached plumes from the rough and smooth plates. We used the two symmetric lines placed at a distance $3H^*_p$ from both sides as shown in figure (VII.14a). However, it is not obvious to extract the plumes, since the 2D spatial averaged field in y-direction is much noisy, i.e the various plumes present in transversal y-direction are being superimposed. One possibility is to capture the large impulsions in the signal of instantaneous 2D Laplacian of temperature (see the figure (VII.14b) on top). Rather, we use the integrated 2D dissipation signal (see the figure (VII.14b) on bottom). Since plumes are dissipative structures, the peaks in $\epsilon^\theta_{xz}/Nu_{R/S}$ distribution are markers of thermal plume. A selective criterion will be applied to choose whether each peak represents well a plume. The algorithm of plume quantification contains three steps :

1. Finding local maxima in the signal of $[\epsilon^\theta_{xz}/Nu_{R/S}](x)$. The reason of this normalization by $Nu_{R/S}$ is to take into account the dependence of ϵ^θ_{xz} on Ra number.
2. Applying a threshold $\zeta = 0.15$ to capture the highest peaks of $[\epsilon^\theta_{xz}/Nu_{R/S}](x)$. The choice of ζ is based on the mean intensity of $\langle\epsilon^\theta_{xz}\rangle_{x,t}/Nu_{R/S}$ time series.

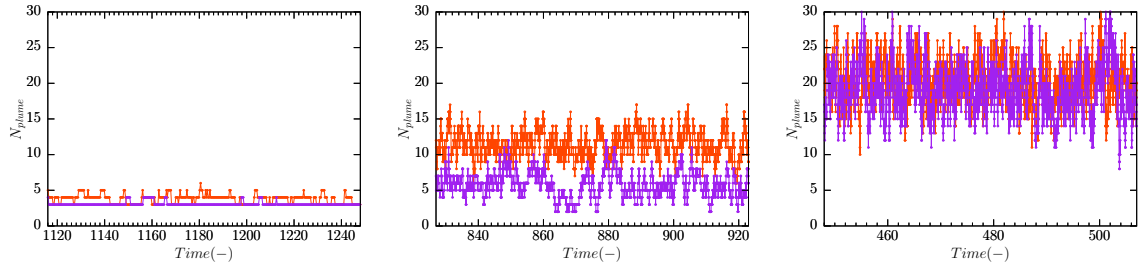

(a) Regime I : $Ra = 10^6$; $\overline{N^S_{plume}} = 3.11$, $\overline{N^R_{plume}} = 3.32$

(b) Regime II : $Ra = 5 \times 10^7$; $\overline{N^S_{plume}} = 5.79$, $\overline{N^R_{plume}} = 11.41$

(c) Regime III : $Ra = 2 \times 10^9$; $\overline{N^S_{plume}} = 18.96$, $\overline{N^R_{plume}} = 20.21$

Fig. VII.15 Time series of the number of plumes passing through the two symmetric lines placed at a distance $3H^*_p$ from the rough plate (orange) and the smooth plate (violet) for different Ra numbers. The threshold is $\zeta = 0.15$

The selective criterion of thermal plumes is based on the identification of the peaks in $(\epsilon^{\theta}_{xz}(x)/Nu_{R/S}(x)$ that have a prominence Δ (amplitude between the highest and lowest peaks) of at least ζ. We summarize the algorithm as follows

$$\begin{array}{lll|ll} & & & \text{Plume} & \\ \text{If} & \Delta\left(\dfrac{\epsilon^{\theta}_{xz}}{Nu_{R/S}}\right)_{peak} \geqslant \zeta & & \textit{yes} & N_{plume}(t,z) = N_{plume}(t,z) + 1 \\ \text{Else} & & & \textit{no} & / \end{array} \quad \text{(VII.10)}$$

The instantaneous number of thermal plumes is $N_{plume}(t, z) =$ number of retained peaks at specific time t and vertical distance z.

3. We estimate $\overline{N_{plume}}$, the time average of the number of plumes crossing the line placed at a distance z from the plate.

We note that this method does not identify the shape of thermal plume. It makes no difference between the plume head and stem but it can capture at least part of it. As shown in figure (VII.14b), the identified peaks correspond qualitatively to noticeable thermal plumes of figure (VII.14a).

b) Roughness effects on the number of plumes

Figure (VII.15) shows the time series of the number of thermal plumes passing through the horizontal lines. In regime I, $\overline{N_{plume}}$ is very low near both plates, it is about 3 to 5. In regime II, as expected, we see an enhancement of the plume's number near the rough plate about %70 higher than that near the smooth surface. With increasing Ra, $\overline{N_{plume}}$ increases in the regime III. However, no difference exist between the two rough and smooth sides which supports our previous observations on the spatiotemporal diagrams.

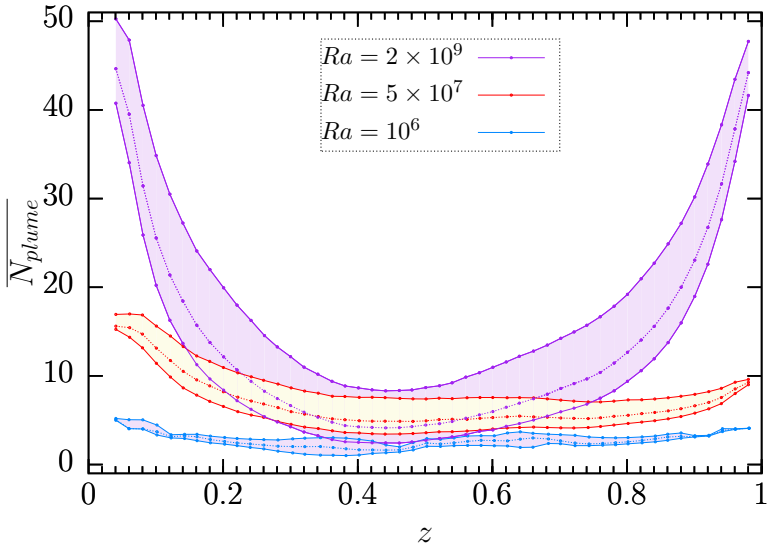

Fig. VII.16 Mean number of thermal plumes at a given vertical distance z from the bottom for three Ra numbers belonging to different regimes. Three thresholds are tested : $\zeta = 0.05, 0.10, 0.15$. Colors displays the area between the distributions relative to $\zeta = 0.15$ (lower curves) and $\zeta = 0.05$ (upper curves).

However, this previous analysis is based on constant height from the plates $z = 3H_p^*$. We are interested in extending this analysis to the regions of boundary layers and to the bulk. We focus now on the vertical distribution of $\overline{N_{plume}}$. Figure (VII.16), shows the variation of mean plumes number along the height of the cell. In order to check whether a dependence on the threshold ζ exists, we tested three different values, $\zeta = 0.15; 0.10; 0.05$. With decreasing ζ, we expected to identify more thermal plumes. Despite the fact of ζ values are different, we mainly observe :

- The increase of the number of plumes near the boundary layer regions on both sides as the Ra number increases. By going towards the bulk region this number decreases likely because of plume's merging and thermal dissipation,
- In regimes I and III : by comparing the rough and smooth sides, we can see an almost symmetric distribution of thermal plumes in the cavity,
- In regime II : we observe a remarkable increase of $\overline{N_{plume}}$ on the half rough bottom side of the cavity. We have $\frac{\overline{N_{plume}}_R}{\overline{N_{plume}}_{H/2}} > \frac{\overline{N_{plume}}_S}{\overline{N_{plume}}_{H/2}}$. Moreover, the number of plumes in the vertical center of the cell $z = H/2$ is relatively of the same order as in regime III, indicating the higher ability of plumes to flow across the bulk.

VII.4 Conclusion

We conducted a comparison between the flow dynamics near the rough and smooth plates within the same Rayleigh Bénard cavity for three different regimes of heat transfer. We focus on three particular Ra numbers.

In the first part, we performed a temporal monitoring near both sides using a couple of probes. The plumes analysis based on the temperature and velocity time series shows that roughness modifies the flow dynamics by changing the statistical properties of thermal plumes in agreement with the experiments namely of Shang et al. (2003, 2004), Du and Tong (2000) and numerical study of Stringano et al. (2006). Indeed, the temperature fluctuations with high intensity are more frequent near the rough plate, in particular in the intermediate regime II. However, in this regime, large vertical velocity fluctuations are found near the smooth plate rather than the rough one.

We extract the characteristics of thermal plumes such as amplitude and width near both the rough and smooth plates. In regime I and III, the PDFs of A/θ_{rms} and A^*/w_{rms} are quite similar and have a log-normal distribution in agreement with Zhou and Xia (2002); Zhou et al. (2016). In regime II, detachment of plumes that have a high potential and kinetic energy is more frequent close to rough plate.

In the second part, we conducted a numerical ombroscopy. The observation of spatiotemporal diagrams of the temperature and thermal dissipation shows that dissipative structures in regime II are not only more present near the rough side comparing with the smooth one but also in the center of bulk region. A quantification of the plumes number's supports this finding. Indeed, the presence of roughness leads to an increase of the thermal plumes number near roughness up to %70 comparatively to the smooth plate.

Conclusions and perspectives

In this work, we have studied the effects of rough surface in Rayleigh Bénard turbulence using a numerical model of a three dimensional asymmetric cell where an array of 24 plots modeled the roughness over the bottom plate. We focused on the heat transfer scaling regimes and the corresponding flow structure. Furthermore, we studied the roughness impact on boundary layers structure at different regimes. We compared the DNS results against experimental data in an attempt to provide a systematic quantitative comparison of the flow physics. Finally, we studied the influence of roughness on thermal plumes properties.

In Chapter § III, 3D rough Rayleigh Bénard cavity is designed. Roughnesses are embedded within the bottom hot surface using an immersed boundary method. The Prandtl number chosen corresponds to the water as working fluid. We perform numerical simulations for a wide range of Ra number covering five decades.

In Chapter § IV, examination of the Nusselt number scaling allowed us to identify three successive regimes of heat transfer in the R/S cavity, corresponding to modifications observed for the rough plate :

(i) In Regime I, heat transfer is reduced, corresponding to a thermally resistant state.
(ii) In regime II, heat is efficiently transferred with an increase of the power law exponent in the relation between Nu_R and Ra_R.
(iii) In Regime III, heat transfer is still enhanced but the classic scaling exponent of smooth boundaries $\beta = 1/3$ is recovered.

Through a decomposition into conductive and convective contributions to the Nusselt number relative to the rough plate, we showed that transitions between the regimes were associated with a modification of dominant mode of heat transfer from conductive in regime I to convective in regime III, while both modes are important in regime II. An equal contribution of the regimes corresponds to the critical Rayleigh number based on the height of roughness elements H_p. Moreover, a spatial decomposition of the heat flux on the rough plate based on the separate contributions from the top of roughness elements and the space between them (called fluid zone) shows a strong dependence of global scaling laws on the fluid zone.

In Chapter § V, the spatial decomposition was used to determine the effect of roughness on the structure of the thermal and kinetic boundary layers for the two regions. Global similarities between the plot and the smooth plate were reported while significant changes were detected in the fluid zone for the different regimes. The transition to regime II is linked with a thermal boundary layer thickness becoming thinner than roughness height, where the second transition to regime III is associated with a viscous boundary layer becoming thinner that the roughness height H_p, which is in agreement with the literature. We also found that thermal fluctuations are particularly intense in the rough side of the cavity in regime II.

In Chapter § VI, we compared our DNS with experimental data. Both studies were conducted in a box shaped asymmetric cavity with close aspect ratios. The roughness elements have an identical shape, i.e square based plot and their geometric organization is similar. However the relative size of roughness is much smaller in the experiment, and the experimental Ra range is 3 decades higher than in our DNS. This led us to introduce suitable rescalings by use of critical Rayleigh number in order to determine equivalent Rayleigh numbers. Profiles of the temperature measured in the vertical direction were compared at different locations corresponding to a decomposition of the rough plate into plots, grooves and notches zones. We established that the temperature fluctuations are not homogeneous around obstacles and that the flow structure is highly perturbed by the large scale circulation. A good agreement is finally obtained when spatial dependence is taken into account and the flow physics near roughness the experiment are fairly well reproduced by the DNS.

In Chapter § VII, we first studied the effect of roughness on the characteristics of thermal plumes. First, series of probes are placed near both the rough and smooth plates to study the instantaneous features of the local dynamics at different regimes of heat transfer. Near smooth boundaries, the log normal distribution is generally recognized in the PDF of the temperature and velocity fluctuations as an intrinsic mark of plume. We found a significant deviation of the distribution in regime II, corresponding to an intensification of the emission of hot and highly energetic plumes near the rough plate. No difference was found for the transit time of plumes between the smooth and rough plates. We then quantified the number of plumes for the different regimes, using spatiotemporal diagrams of the temperature and the thermal dissipation. The number of plumes increased with the Rayleigh number on both sides for all regimes. However, a symmetric distribution of plumes is found in regime I and III, while a significant increase and strong dissymmetry is highlighted in regime II with the presence of highly dissipative structures not only near roughness but also in the bulk of the cavity.

Perspectives

In this work, we used 3D DNS to characterize three successive regimes of heat transfer. Further directions of research could include the following aspects :

1. Thanks to the implementation of hybrid parallelization, the time of computing is significantly reduced, it would be interesting to increase the Ra number and check whether the heat transfer enhancement saturates back to the relative increase of heat exchange surface.
2. We showed the dependence of thermal and viscous boundary layer structure on the height of roughness. It might be interesting to study the impact of working fluid with Prandtl number smaller than unity which exhibits a viscous BL thinner than thermal BL to check whether this affect the mechanism of heat transfer enhancement and better understand thermal and viscous effects.
3. For highest Ra numbers, the interaction between the large scale circulation with different form of roughness is not well understood and need further investigations. It would be interesting to quantify the flow friction and check whether it has a role in the go back to the classic scaling law. Another point is to focus on the origin of the enhancement of thermal plumes number by analyzing in details the process of detachment and how plumes grip on the roughness side-borders.
4. The influence of the roughness geometry could be examined. An optimization of the roughness topology would be fruitful for improving the efficiency of turbulent heat transfer.

Bibliographie

Ahlers, G., Brown, E., Araujo, F. F., Funfschilling, D., Grossmann, S., and Lohse, D. (2006). Non-oberbeck-boussinesq effects in strongly turbulent Rayleigh-Bénard convection. *Journal of Fluid Mechanics*, 569 :409–445.

Ahlers, G., Grossmann, S., and Lohse, D. (2009). Heat transfer and large scale dynamics in turbulent Rayleigh-Bénard convection. *Rev. Mod. Phys.*, 81 :503–537.

Ahlers, G. and Xu, X. (2001). Prandtl-number dependence of heat transport in turbulent Rayleigh-Bénard convection. *Physical review letters*, 86 :3320–3.

Amati, G., Koal, K., Massaioli, F., Sreenivasan, K. R., and Verzicco, R. (2005). Turbulent thermal convection at high Rayleigh numbers for a Boussinesq fluid of constant Prandtl number. *Physics of Fluids*, 17 :121701.

Bailey, D. H., Bjørstad, P. E., Gilbert, J. R., Mascagni, M., Schreiber, R. S., Simon, H. D., Torczon, V., and Watson, L. T., editors (1995). *Parallel Processing for Scientific Computing*. SIAM.

Batchelor, G. K. (1959). Small-scale variation of convected quantities like temperature in turbulent fluid part 1. general discussion and the case of small conductivity. *Journal of Fluid Mechanics*, 5(1) :113–133.

Bergé, P. and Dubois, M. (1984). Rayleigh Bénard convection. *Contemporary Physics*, 25(6) :535–582.

Bouillaut, V., Lepot, S., Aumaitre, S., and Gallet, B. (2019). Transition to the ultimate regime in a radiatively driven convection experiment. *Journal of Fluid Mechanics*, 861 :R5.

Boussinesq, J. V. (1903). *Théorie analytique de la chaleur*. Gauthier-villars / CNRS Editions.

Brandt, A. (1977). Multi-level adaptive solutions to boundary-value problems. *Mathematics of Computation*, 31(138) :333–390.

Brown, P. N., Falgout, R. D., and Jones, J. E. (2000). Semicoarsening multigrid on distributed memory machines. *SIAM Journal on Scientific Computing*, 21(5) :1823–1834.

Burnishev, Y., Segre, E., and Steinberg, V. (2010). Strong symmetrical non-oberbeck-boussinesq turbulent convection and the role of compressibility. *Physics of Fluids*, 22(3) :035108.

Busse, F. (1978). The optimum theory of turbulence. *Adv. Appl. Mech*, 18 :77–121.

Bénard, H. (1900a). Etude expérimentale du mouvement des liquides propageant la chaleur par convection. régime permanent : tourbillons cellulaires. *Comptes Rendus des Séances de l'Académie des Sciences. Paris*, 130 :1004–1007.

Bénard, H. (1900b). Mouvements tourbillonnaires à structure cellulaire. etude optique de la surface libre. *Comptes Rendus des Séances de l'Académie des Sciences. Paris*, 130 :1065–1068.

Castaing, B., Gunaratne, G., Heslot, F., Kadanoff, L., Libchaber, A., Thomae, S., Wu, X.-Z., Zaleski, S., and Zanetti, G. (1989). Scaling of hard thermal turbulence in Rayleigh-Bénard convection. *Journal of Fluid Mechanics*, 204 :1–30.

Cebeci, T. and Bradshaw, P. (1984). *Physical and Computational Aspects of Convective Heat Transfer*. Springer-Verlag Berlin Heidelberg-New York-Tokyo.

Cernecky, J., Koniar, J., and Brodnianska, Z. (2014). The effect of heat transfer area roughness on heat transfer enhancement by forced convection. *Journal of Heat Transfer*, 136(4) :041901.

Chang, S., Liou, T.-M., Chiang, K., and Hong, G. (2008). Heat transfer and pressure drop in rectangular channel with compound roughness of v-shaped ribs and deepened scales. *International Journal of Heat and Mass Transfer*, 51(3) :457 – 468.

Chaumat, S., Castaing, B., and Chilla, F. (2002). Rayleigh-Bénard cells : influence of plate properties. *Advances in turbulence IX (ed. I. P. E. Hancock & T. G. Thomas) International Center for Numerical Methods in Engineering, CIMNE.*

Chavanne, X., Chilla, F., Casting, B., Hébral, B., Chabaud, B., and Chaussy, J. (1997). Observation of the ultimate regime in Rayleigh-Bénard convection. *Phys. Rev*, 79 :3648–3651.

Chavanne, X., Chillà, F., Chabaud, B., Castaing, B., and Hébral, B. (2001). Turbulent Rayleigh-Bénard convection in gaseous and liquid He. *Physics of Fluids*, 13(5) :1300–1320.

Chilla, F. and Schumacher, J. (2012). New perspectives in turbulent Rayleigh-Bénard convection. *Eur. Phys. J. E*, 35 :58.

Chorin, A. J. (1969). On the convergence of discrete approximations to the navier-stokes equations. *Mathematics of Computation*, 23(106) :341–353.

Chu, T. Y. and Goldstein, R. J. (1973). Turbulent convection in a horizontal layer of water. *Journal of Fluid Mechanics*, 60(1) :141–159.

Ciliberto, S. and Laroche, C. (1999). Random roughness of boundary increases the turbulent convection scaling exponent. *Phys. Rev. Lett.*, 82 :3998–4001.

Cioni, S., Ciliberto, S., and Sommeria, J. (1997). Strongly turbulent Rayleigh-Bénard convection in mercury : comparison with results at moderate prandtl number. *Journal of Fluid Mechanics*, 335 :111–140.

Daniels, P. G. (1993). Bénard cells and Taylor vortices. *Journal of Fluid Mechanics*, 253 :722–723.

Daya, Z. A. and Ecke, R. E. (2001). Does turbulent convection feel the shape of the container ? *Phys. Rev. Lett.*, 87 :184501.

Daya, Z. A. and Ecke, R. E. (2002). Prandtl-number dependence of interior temperature and velocity fluctuations in turbulent convection. *Phys. Rev. E*, 66 :045301.

Deardorff, J. W. and Willis, G. E. (1967). Investigation of turbulent thermal convection between horizontal plates. *Journal of Fluid Mechanics*, 28(4) :675–704.

Doering, C. and Constantin, P. (1996). Variational bounds on energy dissipation in incompressible flows. *Phys. Rev E*, 53 :5957–5981.

Du, Y.-B. and Tong, P. (1998). Enhanced heat transport in turbulent convection over a rough surface. *Phys. Rev. Lett.*, 81 :987–990.

Du, Y.-B. and Tong, P. (2000). Turbulent thermal convection in a cell with ordered rough boundaries. *Journal of Fluid Mechanics*, 407 :57–84.

du Puits, R., Loesch, A., Salort, J., and Chillà, F. (2017). Thermal boundary layers in turbulent Rayleigh-Bénard convection with rough surfaces. *ArXiv e-prints*.

Falgout, R. and Jones, J. (2000). *Multigrid on Massively Parallel Architectures*, volume vol 14. In : Dick E., Riemslagh K., Vierendeels J. (eds) Multigrid Methods VI. Lecture Notes in Computational Science and Engineering.

Falgout, R., Jones, J., and Yang, U. (2005). Pursuing scalability for hypre's conceptual interfaces. *ACM Transactions on Mathematical Software*, 31 (3) :326–350.

Falgout, R. D., Jones, J. E., and Yang, U. M. (2006). *Numerical Solution of Partial Differential Equations on Parallel Computers*. Springer Berlin Heidelberg, Berlin, Heidelberg.

Ferziger, J. H. and Peric, M. (2002). *Computational Methods for Fluid Dynamics*. Springer-Verlag Berlin Heidelberg.

Fleischer, A. S. and Goldstein, R. J. (2002). High Rayleigh number convection of pressurized gases in a horizontal enclosure. *Journal of Fluid Mechanics*, 469 :1–12.

Getling, A. V. (1998). *Rayleigh-Bénard Convection*. WORLD SCIENTIFIC.

Glazier, J., Segawa, T., Naert, A., and Sano, M. (1999). Evidence against 'ultrahard' thermal turbulence at very high Rayleigh numbers. *Nature*, 398 :307–310.

Goldstein, R. J., Chiang, H. D., and See, D. L. (1990). High Rayleigh number convection in a horizontal enclosure. *Journal of Fluid Mechanics*, 213 :111–126.

Grossmann, S. and Lohse, D. (2000). Scaling in thermal convection : a unifying theory. *Journal of Fluid Mechanics*, 407 :27–56.

Grossmann, S. and Lohse, D. (2001). Thermal convection for large Prandtl numbers. *Phys. Rev. Lett.*, 86 :3316–3319.

Grossmann, S. and Lohse, D. (2004). Fluctuations in turbulent Rayleigh-Bénard convection : The role of plumes. *Physics of Fluids*, 16(12) :4462–4472.

Grossmann, S. and Lohse, D. (2011). Multiple scaling in the ultimate regime of thermal convection. *Physics of Fluids*, 23(4) :045108.

Grötzbach, G. (1983). Spatial resolution requirements for direct numerical simulation of the Rayleigh-Bénard convection. *Journal of Computational Physics*, 49 :241–264.

Guermond, J., Minev, P., and Shen, J. (2006). An overview of projection methods for incompressible flows. *Computer Methods in Applied Mechanics and Engineering*, 195(44) :6011 – 6045.

Harlow, F. H. and Welch, J. E. (1965). Numerical calculation of time dependent viscous incompressible flow of fluid with free surface. *The Physics of Fluids*, 8(12) :2182–2189.

Haynsworth, E. V. (1968). Determination of the inertia of a partitioned hermitian matrix. *Linear Algebra and its Applications*, 1(1) :73 – 81.

He, X., Funfschilling, D., Nobach, H., Bodenschatz, E., and Ahlers, G. (2012b). Transition to the ultimate state of turbulent Rayleigh-Bénard convection. *Phys. Rev. Lett.*, 108 :024502.

Heslot, F., Castaing, B., and Libchaber, A. (1987). Transitions to turbulence in helium gas. *Phys. Rev. A*, 36 :5870–5873.

Howard, L. (1972). Bounds on flow quantities. *Annu. Rev. Fluid Mech*, 4 :473–494.

Jiang, H., Zhu, X., Mathai, V., Verzicco, R., Lohse, D., and Sun, C. (2018). Controlling heat transport and flow structures in thermal turbulence using ratchet surfaces. *Phys. Rev. Lett.*, 120 :044501.

Kaczorowski, M., Chong, K.-L., and Xia, K.-Q. (2013). Turbulent flow in the bulk of Rayleigh-Bénard convection : small-scale properties in a cubic cell. *J. Fluids Mech*, 722 :596–617.

Kaczorowski, M., Chong, K.-L., and Xia, K.-Q. (2014). Turbulent flow in the bulk of Rayleigh-Bénard convection : aspect-ratio dependence of the small-scale properties. *J. Fluid Mech*, 747 :73–102.

Kaewchoothong, N., Maliwan, K., Takeishi, K., and Nuntadusit, C. (2017). Effect of inclined ribs on heat transfer coefficient in stationary square channel. *Theoretical and Applied Mechanics Letters*, 7(6) :344 – 350.

Kerr, R. M. (1996). Rayleigh number scaling in numerical convection. *Journal of Fluid Mechanics*, 310 :139–179.

Kolmogorov, A. (1941). The local structure of turbulence in incompressible viscous fluid for very large reynolds' numbers. *Akademiia Nauk SSSR Doklady*, 30 :301–305.

Kraichnan, R. (1962). Turbulent thermal convection at arbritary prandlt number. *Physics of Fluids*, 5 :1374–1389.

Krishnamurti, R. (1973). Some further studies on the transition to turbulent convection. *Journal of Fluid Mechanics*, 60(2) :285–303.

Liot, O., Ehlinger, Q., Rusaouën, E., Coudarchet, T., Salort, J., and Chillà, F. (2017). Velocity fluctuations and boundary layer structure in a rough Rayleigh-Bénard cell filled with water. *Phys. Rev. Fluids*, 2 :044605.

Liot, O., Salort, J., Kaiser, R., du Puits, R., and Chillà, F. (2016). Boundary layer structure in a rough Rayleigh-Bénard cell filled with air. *Journal of Fluid Mechanics*, 786 :275–293.

Malkus, W. V. R. (1954). The heat transport and spectrum of thermal turbulence. *Proc. R. Soc. London A*, 225 :196–212.

Mutabazi, I., Wesfreid, J. E., and Guyon, E. (2006). *Dynamics of Spatio-Temporal Cellular Structures*. Springer.

Niemela, J. J., Skrbek, L., Sreenivasan, K. R., and Donnelly, R. J. (2000). Turbulent convection at very high Rayleigh numbers. *Nature*, 404 :837–840.

Pacheco, P. S. (1996). *Parallel Programming with MPI.* .

Paterson, A. R. (1976). Statistical fluid mechanics : mechanics of turbulence. *The Aeronautical Journal (1968)*, 80(781) :44–44.

Petschel, K., Stellmach, S., Wilczek, M., Lülff, J., and Hansen, U. (2013). Dissipation layers in Rayleigh-Bénard convection : A unifying view. *Phys. Rev. Lett.*, 110 :114502.

Petschel, K., Stellmach, S., Wilczek, M., Lülff, J., and Hansen, U. (2015). Kinetic energy transport in Rayleigh Bénard convection. *Journal of Fluid Mechanics*, 773 :395–417.

Pohlhausen, E. (1921). Der wärmeaustausch zwischen festen körpern und flüssigkeiten mit kleiner reibung und kleiner wärmeleitung. *ZAMM - Journal of Applied Mathematics and Mechanics / Zeitschrift für Angewandte Mathematik und Mechanik*, 1(2) :115–121.

Rayleigh, L. (1916). On the convective currents in a horizontal layer of fluid when the higher temperature is on the under side. *Phil. Mag.*, 32 :529–546.

Roche, P., Gauthier, F., Kaiser, R., and Salort, J. (2010). On the triggering of the ultimate regime of convection. *New Journal of Physics*, 12 :085014.

Roche, P.-E., Castaing, B., Chabaud, B., and Hébral, B. (2001). Observation of the $\frac{1}{2}$ power law in Rayleigh Bénard convection. *Phys. Rev. E*, 63 :045303.

Rusaouën, E., Liot, O., Castaing, B., Salort, J., and Chillà, F. (2018). Thermal transfer in Rayleigh-Bénard cell with smooth or rough boundaries. *Journal of Fluid Mechanics*, 837 :443–460.

Salort, J., Liot, O., Rusaouen, E., Seychelles, F., Tisserand, J.-C., Creyssels, M., Castaing, B., and Chillà, F. (2014). Thermal boundary layer near roughnesses in turbulent Rayleigh-Bénard convection : Flow structure and multistability. *Physics of Fluids*, 26(1) :015112.

Schaffer, S. (1998). A semicoarsening multigrid method for elliptic partial differential equations with highly discontinuous and anisotropic coefficients. *SIAM Journal on Scientific Computing*, 20(1) :228–242.

Schlichting, H. and Gersten, K. (2000). *Boundary layer theory.* Springer.

Schur, J. (1917). Über potenzreihen, die im innern des einheitskreises beschränkt sind. *Journal für die reine und angewandte Mathematik*, 147 :205–232.

Shang, X.-D., Qiu, X.-L., Tong, P., and Xia, K.-Q. (2003). Measured local heat transport in turbulent rayleigh-bénard convection. *Phys. Rev. Lett.*, 90 :074501.

Shang, X.-D., Qiu, X.-L., Tong, P., and Xia, K.-Q. (2004). Measurements of the local convective heat flux in turbulent rayleigh-bénard convection. *Phys. Rev. E*, 70 :026308.

Shen, Y., Tong, P., and Xia, K.-Q. (1996). Turbulent convection over rough surfaces. *Phys. Rev. Lett.*, 76 :908–911.

Shishkina, O., Stevens, R. J. A. M., Grossmann, S., and Lohse, D. (2010). Boundary layer structure in turbulent thermal convection and its consequences for the required numerical resolution. *New J. Phys*, 12 :075022.

Shishkina, O. and Wagner, C. (2008). Analysis of sheet-like thermal plumes in turbulent Rayleigh-Bénard convection. *Journal of Fluid Mechanics*, 599 :383–404.

Shishkina, O. and Wagner, C. (2011). Modelling the influence of wall roughness on heat transfer in thermal convection. *Journal of Fluid Mechanics*, 686 :568–582.

Shraiman, B. I. and Siggia, E. D. (1990). Heat transport in high-Rayleigh-number convection. *Phys. Rev. A*, 42 :3650–3653.

Siggia, E. D. (1994). High Rayleigh number convection. *Annual Review of Fluid Mechanics*, 26(1) :137–168.

Solomon, T. H. and Gollub, J. P. (1991). Thermal boundary layers and heat flux in turbulent convection : The role of recirculating flows. *Phys. Rev. A*, 43 :6683–6693.

Stevens, R., Clercx, H., and Lohse, D. (2010a). Boundary layers in rotating weakly turbulent Rayleigh-Bénard convection. *Physics of Fluids*, 22(8) :085103.

Stevens, R. J. A. M., Lohse, D., and Verzicco, R. (2011). Prandtl and Rayleigh number dependence of heat transport in high Rayleigh number thermal convection. *Journal of Fluid Mechanics*, 688 :31–43.

Stevens, R. J. A. M., van der Poel, E. P., Grossmann, S., and Lohse, D. (2013). The unifying theory of scaling in thermal convection : the updated prefactors. *Journal of Fluid Mechanics*, 730 :295–308.

Stevens, R. J. A. M., Verzicco, R., and Lohse, D. (2010b). Radial boundary layer structure and nusselt number in Rayleigh-Bénard convection. *Journal of Fluid Mechanics*, 643 :495–507.

Strang, G. (2007). *Computational Science and Engineering*. Wellesley-Cambridge Press.

Stringano, G., Pascazio, G., and Verzicco, R. (2006). Turbulent thermal convection over grooved plates. *Journal of Fluid Mechanics*, 557 :307–336.

Stringano, G. and Verzicco, R. (2006). Mean flow structure in thermal convection in a cylindrical cell of aspect ratio one half. *Journal of Fluid Mechanics*, 548 :1–16.

Subudhi, S. and Arakeri, J. H. (2012). Flow visualization in turbulent free convection over horizontal smooth and grooved surfaces. *International Communications in Heat and Mass Transfer*, 39(3) :414 – 418.

Threlfall, D. C. (1975). Free convection in low-temperature gaseous helium. *Journal of Fluid Mechanics*, 67(1) :17–28.

Tikadar, A., Najeeb, U., Paul, T. C., Oudah, S. K., Salman, A. S., Abir, A. M., Carrilho, L. A., and Khan, J. A. (2018). Numerical investigation of heat transfer and pressure drop in nuclear fuel rod with three-dimensional surface roughness. *International Journal of Heat and Mass Transfer*, 126 :493–507.

Tisserand, J.-C., Creyssels, M., Gasteuil, Y., Pabiou, H., Gibert, M., Castaing, B., and Chillà, F. (2011). Comparison between rough and smooth plates within the same Rayleigh-Bénard cell. *Physics of Fluids*, 23(1) :015105.

Toppaladoddi, S., Succi, S., and Wettlaufer, J. S. (2015). Tailoring boundary geometry to optimize heat transport in turbulent convection. *EPL (Europhysics Letters)*, 111(4) :44005.

Toppaladoddi, S., Succi, S., and Wettlaufer, J. S. (2017). Roughness as a route to the ultimate regime of thermal convection. *Phys. Rev. Lett.*, 118 :074503.

Tritton, D. (1977). *Physical Fluid Dynamics*. The Modern University in Physics Series. Springer Netherlands.

Urban, P., Hanzelka, P., Kralik, T., Musilova, V., Srnka, A., and Skrbek, L. (2012). Effect of boundary layers asymmetry on heat transfer efficiency in turbulent Rayleigh-Bénard convection at very high Rayleigh numbers. *Physical review letters*, 109 :154301.

Urban, P., Musilová, V., and Skrbek, L. (2011). Efficiency of heat transfer in turbulent Rayleigh-Bénard convection. *Phys. Rev. Lett.*, 107 :014302.

Ventola, L., Robotti, F., Dialameh, M., Calignano, F., Manfredi, D., Chiavazzo, E., and Asinari, P. (2014). Rough surfaces with enhanced heat transfer for electronics cooling by direct metal laser sintering. *International Journal of Heat and Mass Transfer*, 75 :58–74.

Verzicco, R. and Camussi, R. (2003). Numerical experiments on strongly turbulent thermal convection in a slender cylindrical cell. *Journal of Fluid Mechanics*, 477 :19–49.

Wagner, S. and Shishkina, O. (2013). Aspect-ratio dependency of Rayleigh-Bénard convection in box-shaped containers. *Physics of Fluids*, 25 :085110.

Wagner, S. and Shishkina, O. (2015). Heat flux enhancement by regular surface roughness in turbulent thermal convection. *Journal of Fluid Mechanics*, 763 :109–135.

Wagner, S., Shishkina, O., and Wagner, C. (2012). Boundary layers and wind in cylindrical Rayleigh-Bénard cells. *Journal of Fluid Mechanics*, 697 :336–366.

Wei, P., Chan, T.-S., Ni, R., Zhao, X.-Z., and Xia, K.-Q. (2014). Heat transport properties of plates with smooth and rough surfaces in turbulent thermal convection. *Journal of Fluid Mechanics*, 740 :28–46.

Wesseling, P. (1992). *An introduction to multigrid methods*. John Wiley & Sons Australia.

Wu, X.-Z. and Libchaber, A. (1992). Scaling relations in thermal turbulence : The aspect-ratio dependence. *Phys. Rev. A*, 45 :842–845.

Xi, H.-d., Lam, S., and Xia, K.-o. (2004). From laminar plumes to organized flows : the onset of large-scale circulation in turbulent thermal convection. *Journal of Fluid Mechanics*, 503 :47–56.

Xie, Y.-C. and Xia, K.-Q. (2017). Turbulent thermal convection over rough plates with varying roughness geometries. *Journal of Fluid Mechanics*, 825 :573–599.

Yann Fraigneau (2013). Principes de base des méthodes numériques utilisées dans le code sunfluidh pour la simulation des écoulements incompressibles et à faible nombre de mach. *Notes et documents .LIMSI.*

Zhang, Y.-Z., Sun, C., Bao, Y., and Zhou, Q. (2018). How surface roughness reduces heat transport for small roughness heights in turbulent Rayleigh-Bénard convection. *Journal of Fluid Mechanics*, 836 :R2.

Zhou, Q. and Xia, K.-Q. (2010). Physical and geometrical properties of thermal plumes in turbulent rayleigh - bénard convection. *New Journal of Physics*, 12 :075006.

Zhou, S.-Q. and Xia, K.-Q. (2002). Plume statistics in thermal turbulence : Mixing of an active scalar. *Phys. Rev. Lett.*, 89 :184502.

Zhou, S.-Q., Xie, Y.-C., Sun, C., and Xia, K.-Q. (2016). Statistical characterization of thermal plumes in turbulent thermal convection. *Phys. Rev. Fluids*, 1 :054301.

Zhu, X., Mathai, V., Stevens, R. J. A. M., Verzicco, R., and Lohse, D. (2018). Transition to the ultimate regime in two-dimensional Rayleigh-Bénard convection. *Phys. Rev. Lett.*, 120 :144502.

Zhu, X., Ostilla-Mónico, R., Verzicco, R., and Lohse, D. (2016). Direct numerical simulation of taylor–couette flow with grooved walls : torque scaling and flow structure. *Journal of Fluid Mechanics*, 794 :746–774.

Zhu, X., Stevens, R. J. A. M., Shishkina, O., Verzicco, R., and Lohse, D. (2019). $Nu \sim Ra^{1/2}$ scaling enabled by multiscale wall roughness in Rayleigh–Bénard turbulence. *Journal of Fluid Mechanics*, 869 :R4.

Zhu, X., Stevens, R. J. A. M., Verzicco, R., and Lohse, D. (2017). Roughness-facilitated local 1/2 scaling does not imply the onset of the ultimate regime of thermal convection. *Phys. Rev. Lett.*, 119 :154501.

Zocchi, G., Moses, E., and Libchaber, A. (1990). Coherent structures in turbulent convection, an experimental study. *Physica A : Statistical Mechanics and its Applications*, 166(3) :387 – 407.

Appendix A

Table A.1 Thickness of the zones outside the bulk region : h_R and h_S relative to rough and smooth sides as a function of Ra number.

Ra	h_R	h_S
1×10^5	0.37771	0.36331
2×10^5	0.36924	0.35801
5×10^5	0.27579	0.26296
1×10^6	0.21317	0.19910
2×10^6	0.20087	0.18666
5×10^6	0.18791	0.17386
1×10^7	0.18102	0.16765
2×10^7	0.16765	0.15703
5×10^7	0.15694	0.15138
1×10^8	0.15144	0.14688
2×10^8	0.14861	0.14397
5×10^8	0.14255	0.14031
1×10^9	0.14021	0.13889
2×10^9	0.13852	0.13751
5×10^9	0.13617	0.13415

Table A.2 Ra, Rayleigh number; θ_{bulk}, bulk temperature; $\theta center$ temperature of the horizontal plane at $z = H/2$; $\theta_h = 1$ and $\theta_c = 0$ are temperatures of hot and cold plates; $\chi = \frac{\theta_{bulk}-\theta_c}{\theta_h-\theta_{bulk}}$, ratio between temperature differences; $\Delta\theta_S = 2(\theta_{bulk} - \theta_c)$ and $\Delta\theta_R = 2(\theta_h - \theta_{bulk})$ are double the temperature difference between the hot rough (cold smooth) plate and the bulk region.

Ra	θ_{bulk}	θ_{center}	$\theta_{bulk} - \theta_c$	$\theta_h - \theta_{bulk}$	χ	$\Delta\theta_S$	$\Delta\theta_R$
1×10^5	0.49796	0.49678	0.49796	0.50203	0.99190	0.99593	1.00406
2×10^5	0.49923	0.49850	0.49923	0.50076	0.99694	0.99847	1.00152
5×10^5	0.50272	0.50194	0.50272	0.49727	1.01097	1.00545	0.99454
1×10^6	0.50460	0.50494	0.50460	0.49539	1.01860	1.00921	0.99078
2×10^6	0.50894	0.50653	0.50894	0.49105	1.03644	1.01789	0.98210
5×10^6	0.52314	0.50817	0.52314	0.47685	1.09709	1.04629	0.95370
1×10^7	0.53174	0.52616	0.53174	0.46825	1.13559	1.06349	0.93650
2×10^7	0.54811	0.54543	0.54811	0.45188	1.21294	1.09622	0.90377
5×10^7	0.56792	0.56531	0.56792	0.43207	1.31443	1.13585	0.86414
1×10^8	0.57944	0.57815	0.57944	0.42055	1.37783	1.15889	0.84110
2×10^8	0.59007	0.58890	0.59007	0.40992	1.43947	1.18015	0.81984
5×10^8	0.59703	0.59632	0.59703	0.40296	1.48160	1.19406	0.80593
1×10^9	0.59881	0.59859	0.59881	0.40118	1.49262	1.19763	0.80236
2×10^9	0.60010	0.60015	0.60010	0.39989	1.50063	1.20020	0.79979
5×10^9	0.59807	0.59794	0.59807	0.40192	1.48802	1.19614	0.80385

Table A.3 Ra, Rayleigh number ; $Nu_{R/S}$ Nusselt number of R/S cell ; Ra_S and Nu_S are the Rayleigh and Nusselt numbers relative to the smooth plate ; Ra_R and Nu_R are the Rayleigh and Nusselt numbers relative to the rough plate.

Ra	$Nu_{R/S}Ra^{-1/3}$	$Nu_S Ra_S^{-1/3}$	$Nu_R Ra_R^{-1/3}$
1×10^5	0.0814645337	0.0819080219	0.0810252307
2×10^5	0.0815892845	0.0817557416	0.0814234195
5×10^5	0.0798713985	0.0792938945	0.0804563034
1×10^6	0.0796549890	0.0786864084	0.0806446285
2×10^6	0.0797040489	0.0778412441	0.0816462910
5×10^6	0.0802093996	0.0755122821	0.0854428115
1×10^7	0.0825993203	0.0760904507	0.0901492098
2×10^7	0.0849521001	0.0751576367	0.0972214410
5×10^7	0.0865040202	0.0729913780	0.1050965853
1×10^8	0.0875266657	0.0719029414	0.1102407895
2×10^8	0.0871297529	0.0698632728	0.1135505169
5×10^8	0.0862141788	0.0680569524	0.1149516811
1×10^9	0.0858895067	0.0675318395	0.1151973483
2×10^9	0.0849165328	0.0665762595	0.1143806171
5×10^9	0.0845422552	0.0665825261	0.1131113538

Table A.4 Ra, Rayleigh number ; $Nu_{R/S}$ Nusselt number of R/S cell ; Ra_S and Nu_S are the Rayleigh and Nusselt numbers relative to the smooth plate ; Ra_R and Nu_R are the Rayleigh and Nusselt numbers relative to the rough plate ; Nu_{GL} is Nusselt number of GL theory.

Ra	$Nu_{R/S}$	Ra_S	Nu_S	Nu_S^{GL}	$\frac{Nu_S}{Nu_S^{GL}}$	Ra_R	Nu_R	Nu_R^{GL}	$\frac{Nu_R}{Nu_R^{GL}}$
1×10^5	3.7812	9.9594×10^4	3.7967	5.3118	0.7148	1.0041×10^5	3.7659	5.3218	0.7077
2×10^5	4.7713	1.9969×10^5	4,7786	6.2578	0.7636	2.0030×10^5	4.7641	6.2623	0.7608
5×10^5	6.3394	5.0273×10^5	6.3050	7.8406	0.8042	4.9727×10^5	6.3742	7.8200	0.8151
1×10^6	7.9655	1.0092×10^6	7.8927	9.3474	0.8444	9.9078×10^5	8.0396	9.3032	0.8642
2×10^6	10.0421	2.0357×10^6	9.8655	11.2091	0.8801	1.9642×10^6	10.2251	11.1048	0.9208
5×10^6	13.7156	5.2315×10^6	13.1087	14.3980	0.9105	4.7685×10^6	14.3815	14.0421	1.0242
1×10^7	17.7955	1.0635×10^7	16.7330	17.4689	0.9579	9.3651×10^6	19.0020	16.8654	1.1267
2×10^7	23.0595	2.1925×10^7	21.0354	21.3468	0.9854	1.8075×10^7	25.5148	20.2194	1.2619
5×10^7	31.8684	5.6793×10^7	28.0567	27.9208	1.0049	4.3207×10^7	36.8786	25.8179	1.4284
1×10^8	40.6263	1.1589×10^8	35.0560	34.2603	1.0232	8.4110×10^7	48.3013	31.2402	1.5461
2×10^8	50.9538	2.3603×10^8	43.1756	42.1283	1.0249	1.6397×10^8	62.1503	37.8988	1.6399
5×10^8	68.4282	5.9703×10^8	57.3067	55.4060	1.0343	4.0297×10^8	84.9059	49.3377	1.7209
1×10^9	85.8895	1.1976×10^9	71.7161	68.2517	1.0508	8.0237×10^8	107.0451	60.5312	1.7684
2×10^9	106.9881	2.4004×10^9	89.1417	84.2212	1.0584	1.5996×10^9	133.7691	74.4653	1.7964
5×10^9	144.5652	5.9807×10^9	120.8589	111.2819	1.0861	4.0193×10^9	179.8408	98.5245	1.8253

Table A.5 Thermal diffusive sublayer thickness δ_θ^g over plot , fluid and smooth plate as a function of Ra number. The estimation is made via the slope of temperature profile.

Ra	$plot_{H_p^*}$	$fluid$	$smooth$
1×10^5	0.0634616	0.2733794	0.1240535
2×10^5	0.0559297	0.2179784	0.0956353
5×10^5	0.0438244	0.1525443	0.0737215
1×10^6	0.0355309	0.1172348	0.0608554
2×10^6	0.0290055	0.0923687	0.0469630
5×10^6	0.0218098	0.0648780	0.0350810
1×10^7	0.0190130	0.0505137	0.0282019
2×10^7	0.0162183	0.0358586	0.0232753
5×10^7	0.0130265	0.0224400	0.0176032
1×10^8	0.0110706	0.0149699	0.0142554
2×10^8	0.0095575	0.0115942	0.0115217
5×10^8	0.0069165	0.0090009	0.0087817
1×10^9	0.0059302	0.0069954	0.0071651
2×10^9	0.0049977	0.0058654	0.0058152
5×10^9	0.0040331	0.0047255	0.0044810

Table A.6 RMS based thermal layer thickness δ_θ^{rms} over plot, fluid and smooth plate as a function of Ra number. The estimation is made via θ^{rms} peak position.

Ra	$plot_{H_p^*}$	$fluid_{peak-1}$	$fluid_{peak-2}$	$smooth$
5×10^5	0.0462254	0.0762254	/	0.067892861
1×10^6	0.0378930	0.0658821	/	0.056246210
2×10^6	0.0300179	0.0544011	/	0.040575422
5×10^6	0.0207904	0.0438798	/	0.029765012
1×10^7	0.0190243	0.0405755	/	0.024088187
2×10^7	0.0155693	0.0363689	/	0.020056034
5×10^7	0.0128011	0.0349909	/	0.015278629
1×10^8	0.0104986	0.0338841	0.0141869	0.012013751
2×10^8	0.0082287	0.0338841	0.0098581	0.009858138
5×10^8	0.0067922	0.0328937	0.0067235	0.007439112
1×10^9	0.0053358	0.0324657	0.0052960	0.006009132
2×10^9	0.0046130	0.0319657	0.0041743	0.005296069
5×10^9	0.0031779	0.0310517	0.0031658	0.003874306

Table A.7 Thermal displacement thickness δ_θ^* over plot , fluid and smooth zones.

Ra	$plot_{H_p^*}$	$fluid$	$smooth$
1×10^5	0.0521952	0.0567210	0.0550788
2×10^5	0.0413209	0.0488629	0.0439191
5×10^5	0.0319292	0.0424143	0.0341984
1×10^6	0.0268090	0.0385285	0.0296835
2×10^6	0.0226608	0.0342846	0.0238920
5×10^6	0.0175722	0.0303055	0.0180123
1×10^7	0.0147594	0.0272176	0.0149776
2×10^7	0.0120490	0.0236378	0.0122769
5×10^7	0.0098213	0.0190929	0.0098296
1×10^8	0.0083387	0.0168638	0.0082836
2×10^8	0.0069300	0.0146877	0.0070986
5×10^8	0.0054742	0.0129066	0.0056445
1×10^9	0.0046554	0.0112054	0.0048372
2×10^9	0.0040976	0.0100293	0.0042134
5×10^9	0.0033589	0.0086380	0.0033388

Table A.8 Kinetic diffusive sublayer thickness δ_u^g over plot , fluid and smooth plate as a function of Ra number. The estimation is made via the slope of horizontal velocity profile.

Ra	$plot_{H_p^*}$	$fluid$	$smooth$
1×10^5	0.0433017	0.1982611	0.0579171
2×10^5	0.0396853	0.1637633	0.0516270
5×10^5	0.0329516	0.1259554	0.0428847
1×10^6	0.0298203	0.1039112	0.0390541
2×10^6	0.0241218	0.0796685	0.0325058
5×10^6	0.0201503	0.0601460	0.0271973
1×10^7	0.0181830	0.0495482	0.0228620
2×10^7	0.0163540	0.0406657	0.0207628
5×10^7	0.0142150	0.0319933	0.0186109
1×10^8	0.0124337	0.0267347	0.0171198
2×10^8	0.0112654	0.0209949	0.0149259
5×10^8	0.0094333	0.0157326	0.0134987
1×10^9	0.0082942	0.0123100	0.0118313
2×10^9	0.0073537	0.0105481	0.0097429
5×10^9	0.0063419	0.0084965	0.0081043

Table A.9 RMS based viscous layer thickness δ_u^{rms} over plot, fluid and smooth plate as a function of Ra number. The estimation is made via U^{rms} peak position.

Ra	$plot_{H_p^*}$	$fluid_{peak-1}$	$fluid_{peak-2}$	$smooth$
5×10^5	0.1114159	0.1084159	/	0.0812576
1×10^6	0.0926182	0.0923096	/	0.0600177
2×10^6	0.0850320	0.0820320	/	0.0525824
5×10^6	0.0699326	0.0658821	/	0.0422152
1×10^7	0.0658821	0.0619448	/	0.0358014
2×10^7	0.0619448	0.0562464	/	0.0312397
5×10^7	0.0560596	0.0499068	/	0.0251392
1×10^8	0.0523424	0.0475049	/	0.0229545
2×10^8	0.0501203	0.0455165	/	0.0196640
5×10^8	0.0466126	0.0435249	0.0168048	0.0182475
1×10^9	0.0442913	0.0417622	0.0139169	0.0160830
2×10^9	0.0420032	0.0397482	0.0117524	0.0146389
5×10^9	0.0412479	0.0382630	0.0095921	0.0131951

Table A.10 kinetic displacement thickness δ_u^* over plot , fluid and smooth zones.

Ra	$plot_{H_p^*}$	$fluid$	$smooth$
1×10^5	0.0426333	0.0686786	0.0439426
2×10^5	0.0377550	0.0634600	0.0390582
5×10^5	0.0305732	0.0541737	0.0322945
1×10^6	0.0277116	0.0515249	0.0295276
2×10^6	0.0225997	0.0461147	0.0238558
5×10^6	0.0181354	0.0399843	0.0200883
1×10^7	0.0159220	0.0372434	0.0173784
2×10^7	0.0138195	0.0358604	0.0159217
5×10^7	0.0116467	0.0326096	0.0133979
1×10^8	0.0095974	0.0302954	0.0114929
2×10^8	0.0083823	0.0274538	0.0101826
5×10^8	0.0072672	0.0248335	0.0082895
1×10^9	0.0061601	0.0215200	0.0074744
2×10^9	0.0052890	0.0206601	0.0064202
5×10^9	0.0045277	0.0180147	0.0053625

Table A.11 Momentum thickness δ_u^M over plot and fluid zones.

Ra	$plot_{H_p^*}$	$fluid$	$smooth$
1×10^5	0.0170608	0.0200548	0.0182770
2×10^5	0.0152674	0.0183002	0.0164117
5×10^5	0.0118762	0.0152655	0.0135351
1×10^6	0.0106107	0.0139527	0.0119938
2×10^6	0.0093935	0.0117042	0.0085233
5×10^6	0.0073547	0.0101295	0.0068125
1×10^7	0.0065344	0.0099484	0.0061642
2×10^7	0.0058164	0.0102369	0.0055997
5×10^7	0.0050278	0.0101471	0.0049033
1×10^8	0.0042580	0.0097071	0.0045893
2×10^8	0.0040376	0.0100095	0.0040184
5×10^8	0.0034854	0.0099466	0.0037656
1×10^9	0.0029462	0.0095594	0.0032756
2×10^9	0.0025357	0.0093839	0.0028312
5×10^9	0.0022523	0.0093427	0.0024255

Table A.12 Energy thickness δ_u^E over plot and fluid zones.

Ra	$plot_{H_p^*}$	$fluid$	$smooth$
1×10^5	0.0274584	0.0311834	0.0291254
2×10^5	0.0245695	0.0283264	0.0261348
5×10^5	0.0190620	0.0233610	0.0215397
1×10^6	0.0170412	0.0210511	0.0190800
2×10^6	0.0138716	0.0176508	0.0135334
5×10^6	0.0115822	0.0151727	0.0108167
1×10^7	0.0102512	0.0149370	0.0098073
2×10^7	0.0089687	0.0153697	0.0089216
5×10^7	0.0081490	0.0153498	0.0078166
1×10^8	0.0069017	0.0148623	0.0073491
2×10^8	0.0065812	0.0155013	0.0064493
5×10^8	0.0057027	0.0155879	0.0060673
1×10^9	0.0048123	0.0152274	0.0052842
2×10^9	0.0041414	0.0150034	0.0045656
5×10^9	0.0037195	0.0150008	0.0039396

Appendix B

Effects of roughness on dissipation rates

As defined by Petschel et al. (2013, 2015), viscous and thermal dissipation layers thicknesses are identified by the vertical position where the local viscous and thermal dissipations rate equal their volume-averaged values.

Thermal dissipation layer

The thickness of thermal dissipation layer is defined by the vertical position where the local thermal dissipation rate equals its volume-averaged value.

$$\delta_{\theta}^{DL} = z(\langle\overline{\epsilon_{\theta}}\rangle_S \stackrel{!}{=} \langle\overline{\epsilon_{\theta}}\rangle_V) \tag{.11}$$

Using this definition, one can separate the flow into regions of high (above average) and low (below average) thermal energy dissipation. Since dissipation rates are related to the overall heat transport (see exact relations that relate dissipation rates with the Nusselt number from Siggia (1994)), one can proceed to a direct comparison between regions of either boundary layer or bulk dominant part (figure (A.1)).

Kinetic dissipation layer

The kinetic dissipation layer is defined by the vertical position where the local kinetic dissipation rate equal its volume-averaged value.

$$\delta_{u}^{DL} = z(\langle\overline{\epsilon_{u}}\rangle_S \stackrel{!}{=} \langle\overline{\epsilon_{u}}\rangle_V) \tag{.12}$$

Using this definition, one can separate the flow into regions of high (above average) and low (below average) kinetic energy dissipation. In the same way, we can derive an exact relation between kinetic dissipation rate and Nusselt number (Siggia, 1994).

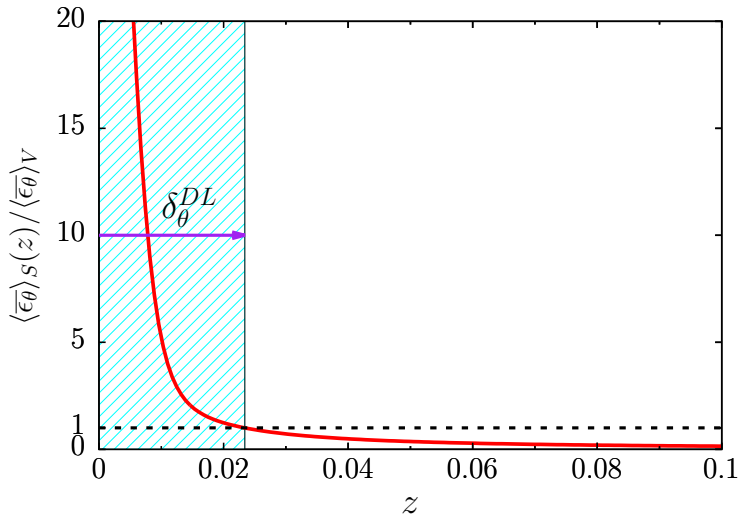

Fig. A.1 Definition of thermal dissipation layer thickness δ_θ^{DL}.

By using those definitions, one can separate the flow into regions of high (above average) and low (below average) kinetic and thermal energy dissipations. Since dissipation rates are related to the overall heat transport, we can proceed to a direct comparison between regions of either boundary layer or bulk dominant part. It is pointed out here the exact relations which could be derived from Siggia (1994).

$$\langle\overline{\epsilon_\theta}\rangle_{V_{fluid}} = \frac{\kappa(H-H_p)^2}{\Delta\theta^2}Nu \qquad \text{and} \qquad \langle\overline{\epsilon_u}\rangle_{V_{fluid}} = \frac{\nu 3}{(H-H_p)^4}(Nu-1)RaPr^{-2}$$

Figure (A.2) shows profiles of the mean thermal and kinetic dissipation rates normalized with their corresponding volume average. In regime I, we observe in the inner region ($z < H_p^*$) a layer with lower thermal and kinetic energy dissipations below the average. This could be related to high viscosity effect which may reduce the Nu number in the rough cell R/S. In regime II, it seems that bulk contribution dominates the thermal dissipation while the BL contribution dominates the viscous one. In smooth cavity, (Grossmann and Lohse, 2000, 2001) suggested that the scaling exponent in the $Nu \sim Ra^\beta$ law would be close to $\beta = 3/7$ for $Pr > 1$. It is fairly consistent with the scaling exponent that we found for R/S cell in regime II with $\beta = 0.42$. In regime III, we have both dissipation rates are above the average $\langle\overline{\epsilon_\theta}\rangle_S > \langle\overline{\epsilon_\theta}\rangle_V$ in the inner zone, which implies higher Nu number. As we have a uniform BL (see figures (A.3e),(A.3f)), this may interpreted as a BL dominated regime brings back the system to classical scaling with $\beta = 1/3$.

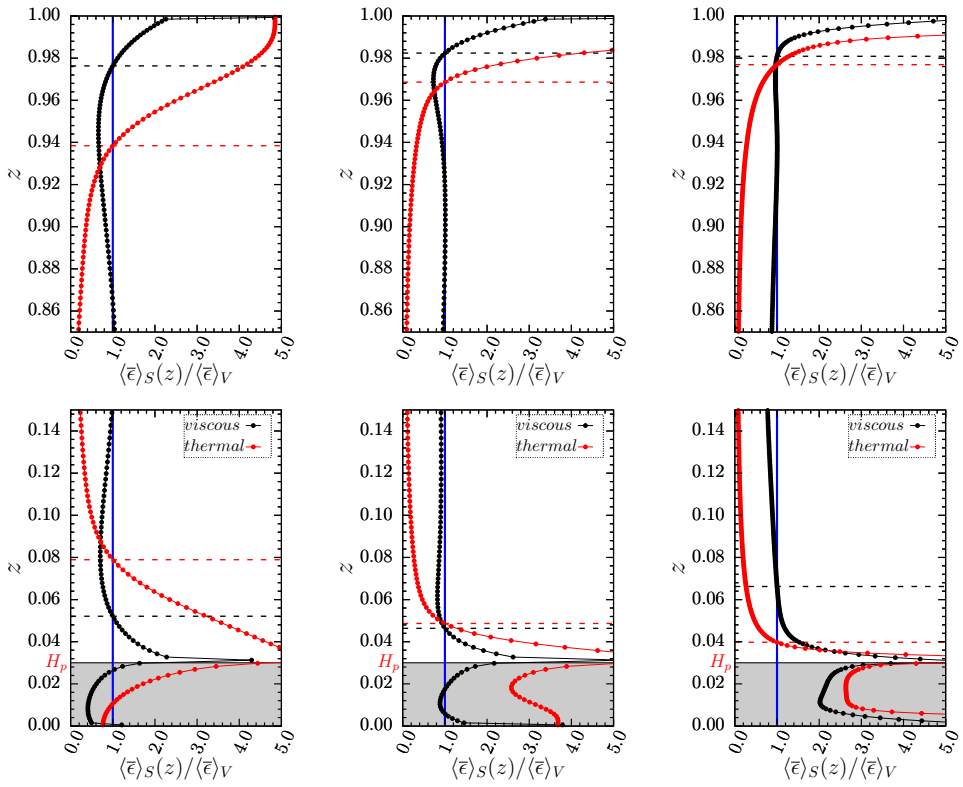

Fig. A.2 Temporally averaged profiles of the horizontally averaged viscous dissipation rate (black circles) and the thermal dissipation rate (red circles) for different Ra. The horizontal axis is scaled by the corresponding globally averaged dissipation rates (Eq.(VII.4)). The thickness of dissipation layers is illustrated for each Rayleigh number by black and red dashed lines and the blue vertical line show where the local viscous and thermal dissipations rate equal their volume-averaged values. From left to right Ra=10^6, 2×10^7 and 10^9, belonging to three different regimes.

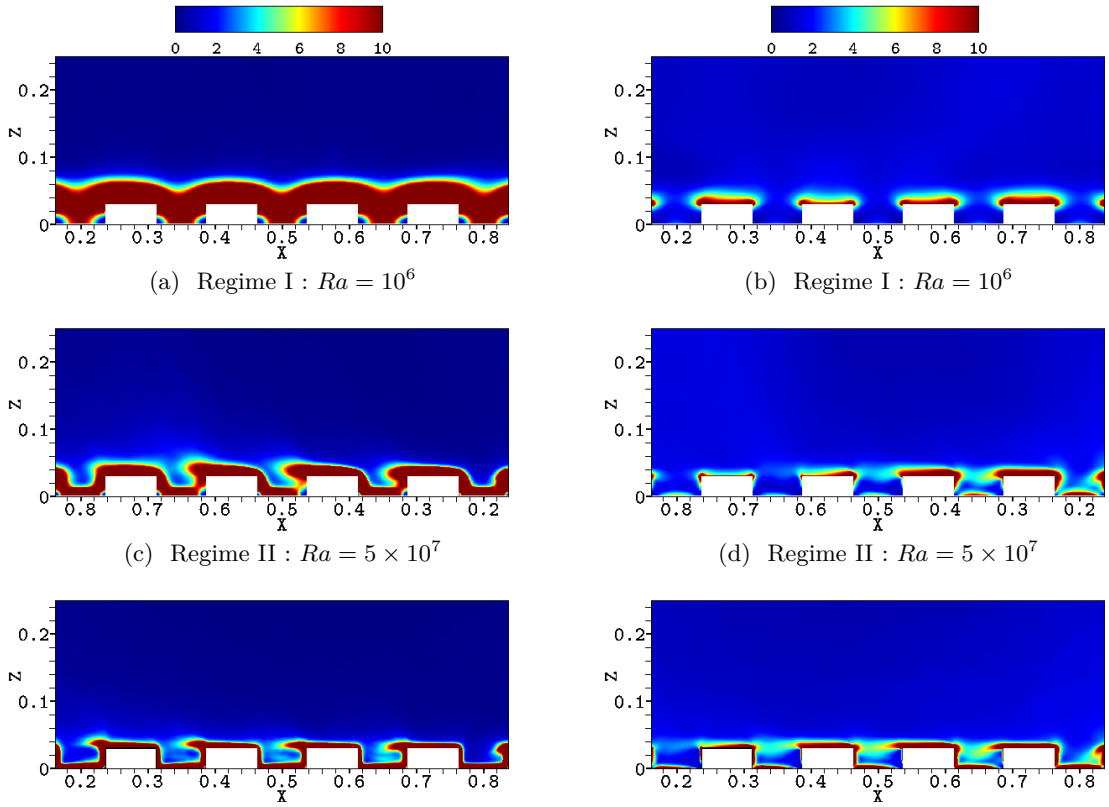

(a) Regime I : $Ra = 10^6$

(b) Regime I : $Ra = 10^6$

(c) Regime II : $Ra = 5 \times 10^7$

(d) Regime II : $Ra = 5 \times 10^7$

(e) Regime III : $Ra = 10^9$

(f) Regime III : $Ra = 10^9$

Fig. A.3 (a,c,e) Normalized thermal dissipation field $\overline{\epsilon_\theta}/Nu_{R/S}$. (b,d,f) normalized viscous dissipation field $\overline{\epsilon_u}/Nu_{R/S}$. Slice section at $y = 0.3125$.

In figure (A.3), we plotted time averaged thermal and viscous dissipation fields near roughness elements. We can observe a non-homogeneous distribution in regime I, i.e. dissipation is more intense above roughness rather than fluid zone. Otherwise, in regimes II and III, as Ra number increases, dissipation is significantly reduced and its distribution becomes uniform. However, the later observations need more investigations on the local thermal and kinetic dissipations near the immersed bodies.

Appendix C

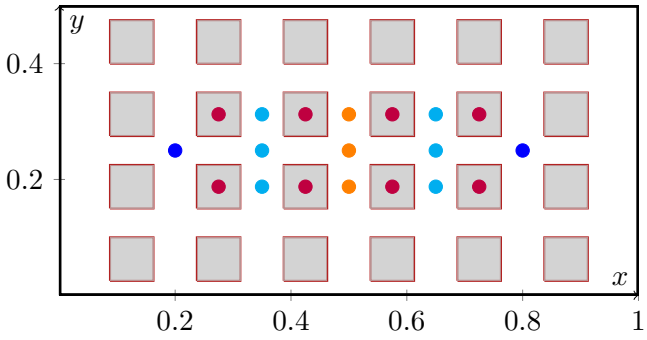

Fig. A.4 Horizontal locations of the probes in the R/S cavity.

Coordinates of the probes :

(●) : $\mathbf{x} = 0.500$, $\mathbf{y} = (0.1875\ ,\ 0.2500\ ,\ 0.3125)$
(■) : $\mathbf{x} = 0.350$, $\mathbf{y} = (0.1875\ ,\ 0.2500\ ,\ 0.3125)$
$\mathbf{x} = 0.650$, $\mathbf{y} = (0.1875\ ,\ 0.2500\ ,\ 0.3125)$
(●) : $\mathbf{x} = 0.275$, $\mathbf{y} = (0.1875\ ,\ 0.3125)$
$\mathbf{x} = 0.425$, $\mathbf{y} = (0.1875\ ,\ 0.3125)$
$\mathbf{x} = 0.575$, $\mathbf{y} = (0.1875\ ,\ 0.3125)$
$\mathbf{x} = 0.725$, $\mathbf{y} = (0.1875\ ,\ 0.3125)$
(●) : $\mathbf{x} = 0.200$, $\mathbf{y} = (0.2500)$
$\mathbf{x} = 0.800$, $\mathbf{y} = (0.2500)$

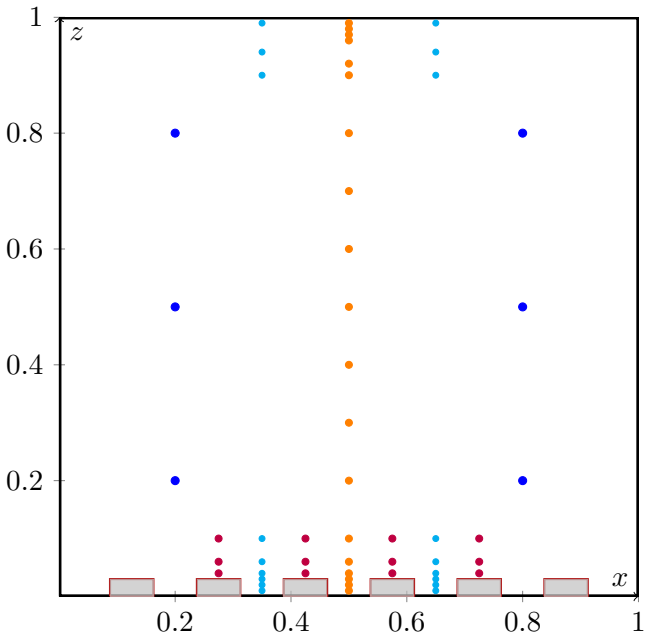

Fig. A.5 Vertical locations of the probes in the R/S cavity.

Coordinates of the probes :

(●) : $\mathbf{z}$ = (0.01, 0.02, 0.03, 0.04, 0.08, 0.1 ,0.2 ,0.3 ,0.4 ,0.5,
0.6 ,0.7 ,0.8 ,0.9 ,0.92 ,0.96, 0.98, 0.99)

(■) : $\mathbf{z}$ = (0.01, 0.02, 0.03, 0.04, 0.08, 0.1, 0.9, 0.94, 0.99)

(●) : $\mathbf{z}$ = (0.04, 0.08, 0.1)

(●) : $\mathbf{z}$ = (0.2, 0.5, 0.8)

Modélisation numérique des écoulements turbulents de Rayleigh-Bénard en présence d'une paroi rugueuse

Résumé : Les flux convectifs turbulents sur les surfaces rugueuses sont omniprésents dans les applications géophysiques mais aussi en ingénierie. Comprendre les mécanismes de ces interactions est crucial pour améliorer l'efficacité du transfert de chaleur. Dans ce travail, nous étudions les effets des rugosités sur la turbulence dans la cavité de Rayleigh Bénard. Des simulations numériques directes (DNS) tridimensionnelles sont effectuées en utilisant un code CFD parallèle employant das ressources informatiques intensives des supercalculateurs nationaux de haute performance. Les rugosités sont introduites sur une surface chaude en utilisant une méthode de frontières immergées. La configuration numérique permet l'identification de trois régimes successifs allant du thermiquement résistant jusqu'un régime du transfert de chaleur fortement intensifié. À travers une décomposition géométrique de la plaque rugueuse en partie solide et d'autre fluide, nous examinons leurs différents comportements, principalement leur contribution au transfert de chaleur. Nous analysons les effets de la rugosité sur les structures des couches limites thermiques et visqueuses et sur la physique de l'écoulement en proche parois. De plus, la comparaison avec les données expérimentales à l'échelle de rugosité met en évidence la non-homogénéité des fluctuations thermiques autour des obstacles. Nous nous sommes également intéressés aux effets des rugosités sur la dynamique de l'écoulement et les propriétés des panaches thermiques.

Mots clés : Convection, Rayleigh-Bénard, rugosité, turbulence, panache

Numerical modeling of turbulent convection in rough Rayleigh-Bénard cell

Abstract : Turbulent convective flows over rough boundaries are ubiquitous in geophysical and engineering applications. Understanding the mechanisms of these interactions is substantial for improving the heat transfer efficiency. In this work, we study the effects of wall roughness on the Rayleigh Bénard turbulence. Three dimensional direct numerical simulations (DNS) are performed using a parallel CFD code under the support of national high performance computers. The roughness elements are embedded over hotted surface using an immersed boundary method. The numerical configuration allows the identification of three successive regimes from a thermally resistant to highly enhanced heat transfer. Through a geometrical decomposition of the rough plate into plot and surrounding fluid, we examine their different behaviors, mainly the contribution to the heat transfer. We analyze the effects of roughness on thermal and viscous boundary layers structures and on the flow physics near the wall. Besides that, the comparison with experimental data at the roughness scale highlight the non homogeneity of thermal fluctuations around the obstacles. We also focused on the effects of roughness on the flow dynamics and on the properties of thermal plumes.

keywords : Convection, Rayleigh-Bénard, roughness, turbulence, plume

LIMSI CNRS, UPR3251, F-91405 Orsay, France,
Sorbonne Université, Collège Doctoral, ED391 SMAER, F-75006, Paris, France.